Fracture Mechanical Analysis of Failure Processes in Antarctic Ice Shelves

vom Fachbereich Maschinenbau und Verfahrenstechnik
der Technischen Universität Kaiserslautern
zur Verleihung des akademischen Grades
Doktor-Ingenieur (Dr.-Ing.)
genehmigte Dissertation

von
Dipl.-Ing. Carolin Plate
aus Lüdenscheid

Hauptreferent:	Prof. Dr.-Ing. Ralf Müller
Korreferenten:	Prof. Dr.-Ing. Dietmar Gross
	Prof. Dr. Angelika Humbert
Vorsitzender:	Prof. Dr.-Ing. Tilmann Beck
Dekan:	Prof. Dr.-Ing. Christian Schindler

Tag der Einreichung: 25.08.2015
Tag der mündlichen Prüfung: 01.10.2015

Kaiserslautern, 2015

D 386

Vorwort

Die vorliegende Arbeit entstand während meiner Tätigkeit als wissenschaftliche Mitarbeiterin am Lehrstuhl für Technische Mechanik der Technischen Universität Kaiserslautern.

Mein besonderer Dank gilt Herrn Prof. Dr.-Ing. Ralf Müller und Frau Prof. Dr. Angelika Humbert für die Ermöglichung dieser Arbeit sowie für die hervorragende Betreuung und Unterstützung sowohl von bruchmechanischer als auch von glaziologischer Seite. Ebenso danken möchte ich Herrn Prof. Dr.-Ing. Gross für sein Interesse an der Arbeit und für die Übernahme eines der Korreferate sowie Herrn Prof. Dr.-Ing. Beck für die Übernahme des Vorsitzes.

Herzlich bedanken möchte ich mich auch bei den Kolleginnen und Kollegen für die angenehme Atmosphäre sowohl während der Arbeitszeit als auch bei den zahlreichen außeruniversitären Aktivitäten. Besonders hervorzuheben sind meine Kollegen und ehemaligen Mitbewohner Charlotte Kuhn und Markus Klassen, für die Unterstützung in allen Lebenslagen sowie meine Zimmerkollegin Julia Christmann für die intensiven wissenschaftlichen Gespräche.

Zu guter Letzt möchte ich meiner Familie und meinem Freund für den Rückhalt und die fortwährende Unterstützung nicht nur während der Promotion danken.

Kaiserslautern, November 2015   Carolin Plate

Kurzfassung

Antarktische Schelfeise sind ein bedeutender Bestandteil des weltweiten Klimahaushalts. Die bis zu 500 m dicken schwimmenden Eisplatten sind das Bindeglied zwischen gegründetem Inlandeis und dem Ozean. Umgeben von Wasser auf der einen und Luft auf der anderen Seite, sind Schelfeise klimatischen Veränderungen direkt ausgesetzt. Studien der letzten Jahrzehnte zeigen, dass speziell die Schelfeise entlang der Antarktischen Halbinsel instabil werden und schließlich teilweise oder auch komplett zerbrechen.

Das Zerbrechen schwimmender Schelfeisteile oder ganzer Schelfeise trägt nicht direkt zu einer Erhöhung des Meeresspiegels bei. Studien von Rott et al. (2002), De Angelis (2003) und Scambos (2004) zeigen jedoch, dass mit Zerbrechen des Larsen B Schelfeises, die Fließgeschwindigkeiten der dahinter liegenden Gletscher erheblich zunahm und somit verstärkt Eis aus dem Inland dem Ozean zugeführt wird. Für den sehr pessimistischen Fall eines komplett eisfreien Antarktischen Kontinents prognostizieren Fretwell et al. (2013) einen weltweiten Anstieg des Meeresspiegels um 58 m. Jedoch wird auch ein Anstieg des Meeresspiegels um nur wenige Meter, wie z.B. durch das Kollabieren des Westantarktischen Eisschilds (Bamber et al., 2009b), weitreichende Konsequenzen auf die Infrastruktur entlang der Küsten haben. Es ist daher wichtig die Zusammenhänge zu verstehen, welche zu verstärktem Zerbrechen der Schelfeise führen.

Im Rahmen einer bruchmechanischen Finite Elemente Analyse untersucht diese Arbeit daher verschiedene Risssituationen in Antarktischen Schelfeisen. Basierend auf Messungen von Rist et al. (2002), werden die Materialeigenschaften des Eises für die kurze Zeitdauer des Bruchvorgangs als linear elastische angenommen. Der Lasteintrag erfolgt quasi-statisch über verschiedene Arten von Randbedingungen und Volumenkräfte. Die Bewertung der Risssituationen erfolgt über die Berechnung von Konfigurationskräften, basierend auf der grundlegenden Arbeit von Eshelby (1951). Im Zusammenspiel mit Finiten Elementen ist die Verwendung von Konfigurationskräften eine effektive und flexible Methode für die Berechnung von Energiefreisetzungsraten. Diese können dann in die im Ingenieurwesen für die Bewertung von Rissen üblichen Spannungsintensitätsfaktoren umgerechnet werden. Die Unterscheidung, ob ein Riss wächst oder nicht, erfolgt für Modus I Belastungen durch Vergleich mit gemessenen kritischen Werten für Spannungsintensitätsfaktoren welche zum Beispiel in Rist et al. (2002) und Christmann et al. (2015) zu finden sind.

Die Lösung des zweidimensionalen linear elastischen Randwertproblems erfolgt unter Einsatz des kommerziellen Finite Elemente Programms COMSOL. Die Kon-

figurationskräfte werden in Postprocessing Routinen in MATLAB berechnet. Durch die Verwendung von Dreieckselementen mit quadratischen Ansatzfunktionen können die erwarteten Spannungssingularitäten an Rissspitzen nicht korrekt abgebildet werden. Die gerne zur Rissbewertung herangezogene diskrete Konfigurationskraft an der Rissspitze stellt die tatsächlich vorhandene Energiefreisetzungsrate daher nur ungenau dar. Eine erhebliche Verbesserung des Ergebnisses kann durch in Denzer et al. (2003) vorgeschlagenes Aufsummieren der diskreten Knotenkonfigurationskräfte in einem Bereich um die Rissspitze erzeugt werden. Bei Problemen mit Volumenkräften, belasteten Rissflanken, räumlich verteilten Materialparametern oder unsymmetrischen Geometrien und Belastungen führt die Summation jedoch zu weiteren Fehlern, welche das Ergebnis verfälschen. Nur durch die Berechnung weiterer Flächenintegrale zur Berücksichtigung von Volumenkräften und räumlich verteilten Materialparametern sowie zusätzlicher Linienintegrale entlang der Flanken zur Einbeziehung von Druckspannungen im Inneren des Risses und gemischten Belastungsmodi, können hohe Genauigkeiten bei der Berechnung der Energiefreisetzungsrate erzielt werden. Mit dieser Implementierung wird der relative Fehler der berechneten Energiefreisetzungsrate im Vergleich zu analytischen Beispielen auf weniger als ein Promille reduziert.

Die implementierten Algorithmen werden zunächst für die Analyse der Spannungsintensitätsfaktoren vertikaler trockener Einzelrisse in Schelfeisen verwendet. Die Datengrundlage hierfür liefern Satellitenbilder verschiedener Aufbruchereignisse am Wilkins Schelfeis. Die Untersuchung des Einflusses der geometrischen Parameter Länge und Mächtigkeit der betrachteten idealisierten Schelfeisgeometrie sowie des Rissöffnungswinkels auf die Spannungsintensitätsfaktoren an der jeweiligen Risstiefe steht in direktem Zusammenhang mit der Betrachtung verschiedener Randbedingungen für die Belastung der vertikalen Ränder, sowie der Abbildung des tiefenabhängigen Wasserdrucks an der Schelfeisunterseite. Hierbei zeigt sich, dass die in bisherigen semi-analytischen Studien von z.B. Van Der Veen (1998a) oder Rist et al. (2002) gerne verwendeten Spannungsrandbedingungen entlang der vertikalen Ränder zumindest für geringe Risstiefen ähnliche Resultate liefern, wie die in dieser Arbeit bevorzugten Verschiebungsrandbedingungen. Besonders hervorzuheben ist der Einfluss des Rissöffnungswinkels, welcher bei bisherigen Veröffentlichungen zu Rissen in Schelfeisen komplett vernachlässigt wurde. Weitere Untersuchungen mit verschiedenen Dichteprofilen, dickenabhängigem Elastizitätsmodul und verschiedenen konstanten Werten für die Querkontraktionszahl zeigen, dass speziell die für schnelle Bruchvorgänge berechtigte Annahme kompressiblen Materialverhaltens (Schulson and Duval, 2009) zu deutlichen tieferen Rissen führt als das in der überwiegenden Anzahl bisheriger Studien verwendete inkompressible Materialverhalten.

Im Folgenden wird die Analyse vertikaler Einzelrisse auf wassergefüllte Spalten ausgedehnt. Dabei werden sowohl von Schmelzwasser oder Brine gefüllte Spalten an der Eisoberfläche, als auch die von Meerwasser gefüllten Bodenspalten betrachtet. Der zusätzliche Wasserdruck auf den Rissflanken sorgt bei gleicher Last

an den äußeren Rändern für wesentlich tiefer wachsende Risse als in den bisherigen Rechnungen mit unbelasteten Rissflanken. Dies führt, je nach äußerer Last, und unter Annahme von kompressiblem Materialverhalten, zu einem vollständigen Durchreißen ursprünglich stabiler Risse bei einem Wasserstand von etwa der halben Risstiefe. Frühere Studien mit inkompressiblem Materialverhalten von z.B. Van Der Veen (1998a) benötigen nahezu komplett gefüllte Spalten, um vollständiges Durchreißen zu erzeugen.

Ein größerer, mit einem Temperatursturz einher gehender Aufbruchvorgang am Wilkins Schelfeis, motiviert die Betrachtung von Frostsprengung als möglichen Auslöser. Für die bruchmechanische Modellierung von Frostsprengung werden zunächst mit einer thermodynamischen Simulation mögliche Eisdicken auf der Wasseroberfläche einer mit Schmelzwasser gefüllten Spalte berechnet. Der durch Phasentransformation im abgeschlossenen Spalteninneren entstehende Druck dient dann als Last für die bruchmechanische Auswertung. Die Simulationen zeigen, dass unter Voraussetzung einer abgeschlossenen Spalte, realistische Eisdicken zu einem vollständigen Durchreißen ursprünglich stabiler wassergefüllter Spalten führen.

Mit einem auf Konfigurationskräfte basierenden Algorithmus zur Ermittlung der wahrscheinlichsten Rissausbreitungsrichtung untersucht die vorliegende Arbeit auch horizontal wachsende Risse in Schelfeisen. Anders als im vorherigen Fall werden dafür die Belastungen im kompletten Schelfeis, oder zumindest in großräumigen Teilen um die betrachteten Risse benötigt. Mit einem neuen Ansatz, aufbauend auf Gleichgewichtsüberlegungen für ein viskoelastisches Fluid, werden daher die aus gemessenen Geschwindigkeitsfeldern berechneten viskosen Fliessspannungen in so genannte viskose Volumenkräfte überführt. Diese dienen dann als Last für die bruchmechanische Simulation. Angewendet auf Risswachstum in der Pine Island Gletscherzunge und im Wilkins Schelfeis liefert der verwendete Algorithmus gute Übereinstimmung im Vergleich zu beobachteten Rissverläufen. Die Ergebnisse sind bemerkenswert, da keine Informationen über die räumliche Verteilung der Materialeigenschaften des Eises benötigt werden. Ein Nachteil der Methode ist die starke Abhängigkeit der Ergebnisse von der Qualität des gemessenen Geschwindigkeitsfeldes sowie den teilweise nur unzulänglich bekannten Randbedingungen. Im Fall von hoch aufgelösten Geschwindigkeitsfeldern können aus der Berechnung der viskosen Volumenkräfte aktive Risse als Stellen mit extremen Spannungsgradienten ermittelt werden. Bei bekanntem Rissverlauf ist es darüber hinaus auch möglich, aus den Simulationsergebnissen Rückschlüsse auf mögliche Randbedingungen zu ziehen, welche dann in weiteren Analysen verwendet werden können.

Für zukünftige Modellierungen von Rissen in Schelfeisen ist die Ausweitung der Algorithmen auf viskoelastisches Materialverhalten möglich. Auch eine Kopplung von Bruchmechanik und eisdynamischen Simulationen ist wünschenswert. Für eine bessere Unterscheidung von vertikal wachsenden Oberflächenspalten und horizontal wachsenden Rissen ist darüber hinaus eine Simulation des drei-dimensionalen Problems denkbar.

Abstract

Antarctic ice shelves are important elements of the climate system. As link between the grounded ice sheet and the ocean, the up to 500 m thick floating plates are surrounded by water, on one side and by the atmosphere on the other side. These conditions make ice shelves very vulnerable to climate change. Recent publications indicate that, especially along the Western Antarctic Peninsula, ice shelves become unstable and eventually disintegrate.

The disintegration of floating ice shelf parts or entire ice shelves does not directly contribute to sea level rise. However, studies of Rott et al. (2002), De Angelis (2003) and Scambos (2004) show, that the disintegration of the Larsen B Ice Shelf considerably accelerated the flow velocities of the inflowing glaciers. This results in an increased drainage of grounded ice into the ocean. In the very pessimistic scenario of a completely ice-free Antarctic continent, Fretwell et al. (2013) predict a global sea level rise of about 58 m. However, a sea level rise of only a few meters, as forecast by Bamber et al. (2009b) for the collapse of the West Antarctic Ice Sheet, also leads to serious consequences for the infrastructure along the continental coasts. Therefore it is of major importance to understand the processes that lead to an accelerated disintegration of ice shelves.

The presented work analyses different failure scenarios in Antarctic ice shelves using fracture mechanical concepts together with finite element simulations. According to the study of Rist et al. (2002), linear elastic material behavior during the short fracturing process is applied. Neglecting concepts of dynamic crack propagation, the loading conditions are quasi-static using different types of boundary conditions and volume forces.

The estimation of crack criticality is based on the computation of configurational forces following the approach of Eshelby (1951). In conjunction with finite elements, configurational forces are an effective and flexible method for the evaluation of energy release rates, which are then transformed into stress intensity factors, a common measure for crack criticality in engineering. The comparison of computed stress intensity factors to measured values of critical stress intensity factors allows to determine whether crack growth continues. Critical stress intensity factors for mode I opening can be found in Rist et al. (2002) or Christmann et al. (2015).

The two-dimensional linear elastic boundary value problem is solved in the commercial finite element program COMSOL . The computation of the configurational forces follows in postprocessing routines in MATLAB . By applying triangular finite elements with standard quadratic shape functions, the expected stress singularities at the crack tip cannot be mapped. Therefore, the discrete configurational force at

the crack tip node, frequently used to compute the energy release rate, only provides an inaccurate measure for crack criticality. Denzer et al. (2003) therefore propose the summation of all nodal configurational forces in a region around the crack tip to considerably enhance the result. However, in the case of applied volume forces, spatially distributed elastic parameters, loaded crack faces or mixed crack opening modes, the inclusion of nodal configurational forces around the crack tip leads to further errors. Only by computing additional area integrals for applied volume forces and inhomogeneous material parameters, as well as additional line integrals along the crack faces to incorporate crack face loads and mixed opening modes, very accurate results can be achieved. The presented algorithm shows a relative error of less than one per-mil in comparison to analytical computations.

The fracture mechanical simulations first concentrate on the computation of stress intensity factors for dry single surface cracks in the ice shelf bulk. The input data for the simulations is based on satellite imagery of different fracture scenarios in the Wilkins Ice Shelf. The analysis of the influence of the geometric parameters length and thickness of the idealized ice shelf geometry, as well as of the crack opening angle is closely connected to the study of different boundary conditions for the remote loading along the vertical lateral boundaries on the one hand and for the mapping of the depth-dependent buoyancy force at the ice shelf bottom on the other hand. It appears that, at least for shallow cracks, former semi-analytical studies of e.g. Van Der Veen (1998a) or Rist et al. (2002) with stress boundary conditions along the vertical lateral boundaries are in good agreement with the results presented here, which are predominantly computed using displacement boundary conditions. The most influencing geometric parameter is the crack opening angle, which has been completely ignored in previous studies of cracks in ice shelves. Further simulations with various density profiles, depth-dependent Young's moduli and different constant Poisson's ratios show that the assumption of compressible material behavior, as motivated by e.g. Schulson and Duval (2009) for short-term fracture processes, leads to considerably deeper cracks than the use of incompressible material behavior, which is predominantly used in previous studies.
In a next step, the examination of vertical single cracks is expanded to surface crevasses, filled by meltwater or brine, as well as to cracks at the ice shelf bottom. For equal lateral loading, the simulations with additional water pressure on the crack flanks lead to significantly deeper cracks than the previous studies without crack face loads. Without additional lateral loading and under assumption of compressible material behavior, a water filling of about half of the crack depth results in a complete penetration of initially stable crevasses. Previous studies with incompressible material behavior (Van Der Veen, 1998a) and equal external loading need almost completely filled crevasses for a total penetration.
A break-up event at the Wilkins Ice Shelf that coincided with a major temperature drop motivates the consideration of frost wedging as triggering mechanism for ice shelf disintegration. Prior to the fracture mechanical analysis of frost wedging, a thermodynamic simulation investigates possible ice lid thicknesses that can form on

a water-filled crevasse due to given external temperatures. The additional pressure resulting from the phase transformation within the sealed crevasse then serves as loading for the fracture mechanical simulation. The analyses show, that reasonable ice lid thicknesses can lead to a complete penetration of an initially stable water-filled crevasse.

An algorithm for the evaluation of the most probable crack propagation direction, based on configurational forces, is used to analyze the horizontal propagation of rifts in ice shelves. Unlike in the previous models, now the stress state in the complete ice shelf or at least in an extended area around the rifts is needed for the simulation. Using equilibrium considerations for a viscoelastic fluid, a new method is introduced to compute so-called viscous volume forces from viscous surface stresses. The viscous surface stresses are evaluated using measured ice shelf velocities from satellite imagery. The resulting viscous volume forces then serve as loading for the fracture mechanical analysis. Applied to rifts in the Pine Island Glacier tongue and at Wilkins Ice Shelf, the resulting crack paths agree well to observed crack patterns. This is remarkable, as no information on e.g. the spatial distribution of ice parameters is needed. A disadvantage of the method is the strong dependence on the quality and the resolution of the measured velocity field, as well as on the boundary conditions, which for the most part are insufficiently known. If high-resolution velocity fields are provided, the locations of active rifts, as regions with strong stress gradients, follow as by-product of the evaluation of the viscous volume forces. Furthermore, if the final crack path is known from satellite data, the simulations can be used to deduce likely boundary conditions for further studies.

For future simulations of cracks in ice shelves, the linear elastic model could be extended to viscoelastic material behavior. A coupling of the fracture mechanical analysis to ice dynamical simulations is also desired. Furthermore, a three-dimensional model could help to better distinguish between vertically growing surface cracks and horizontally growing rifts.

Contents

Contents

1 Introduction

1.1 Motivation and background

Antarctica is the fifth largest continent on Earth. Approximately 98 percent of the landmass is covered with ice. New measurements by Fretwell et al. (2013) show, that the total volume of ice in Antarctica is about 27 Mio km^3 which corresponds to 70 percent of the worlds fresh water. The Transantarctic Mountains divide the continent into a larger eastern side and a smaller western side including the Antarctic Peninsula. The predominant part of the ice masses is concentrated in East Antarctica, where the ice thickness reaches more than 4000 m. The ice masses covering West Antarctica are comparably small. Nonetheless, especially the Antarctic Peninsula is of great scientific interest. It is the region extending furthest north from
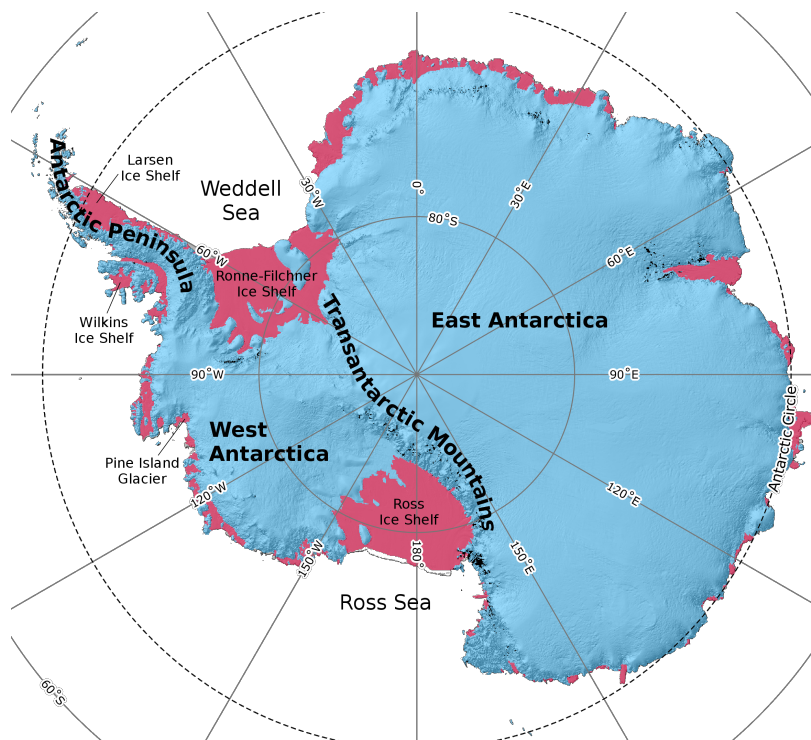

Figure 1.1: Overview of the Antarctic continent with distinction between ice shelves (red) and grounded ice (blue) applying the ALBMAP masks (Le Brocq et al., 2010) overlaid on a hillshade of the surface digital elevation model of Bamber et al. (2009a) with the help of Quantarctica as provided by the Norwegian Polar Institute

the pole with a climate that is considerably influenced by the warming ocean and hence comparatively mild. Glaciologists assume that with ongoing climate warming, the processes observable now along the Antarctic Peninsula will sooner or later affect the West Antarctic Ice Sheet (Joughin and Alley, 2011) and possibly the entire Antarctic continent.

An illustrative number to grasp the amount of ice in Antarctica is the potential sea level rise of 58 m associated with the collapse of the entire Antarctic Ice Sheet as published by Fretwell et al. (2013). The amount of eustatic sea level rise resulting from a collapse of only the West Antarctic Ice Sheet is given by Bamber et al. (2009b). With 3.3 m their value is considerably lower than the value by Fretwell et al. (2013) for the entire Antarctic Ice Sheet. In both cases, not only smaller flat islands, but also a considerable amount of the world's continental coastlines would be covered with water. Therefore, it is of great importance to understand the mechanisms that influence glaciological processes in Antarctica and to be able to correctly interpret signs that indicate an acceleration of the mass loss (Rignot et al., 2011b).

The Antarctic Ice Sheet gains new ice mass by snow accumulation. Ice loss occurs due to ablation and, for the main part, due to drainage through the many glaciers across the grounding line into the ocean. When the glaciers reach the open water, the ice masses start to float and build so called ice shelves (Fig. 1.1). Larger ice shelves are fed by several glaciers and can reach up to several $100\,000\,km^2$ in size. The most prominent large ice shelves are the Ross Ice Shelf in the Ross Sea with an area of even $487\,000\,km^2$ and the Filchner-Ronne Ice Shelf in the Weddell Sea with an area of $430\,000\,km^2$. Smaller ice shelves can be found along the complete Antarctic coastline. The total number of ice shelves in Antarctica listed by Rignot et al. (2013) is 66, from which some already partly or fully collapsed.

Since ice shelves are floating on the water, their melting or collapse does not directly contribute to sea level rise. Nevertheless, ice shelves play an important role as buttressing barriers that decelerate the glacier flow and hence the drainage of ice from the Antarctic Ice Sheet into the ocean. Rott et al. (2002), De Angelis (2003) and Scambos (2004) report considerable thinning and increase of the velocities of the tributary glaciers after the collapse of the Larsen B Ice Shelf. Since eight of twelve ice shelves along the Antarctic Peninsula retreated or disintegrated in the past decades (Braun et al., 2009; Cook and Vaughan, 2010), it is essential to gain a better understanding of the mechanisms that lead to ice shelf collapse.

Fracturing of weakened polycrystalline ice is the governing process for all calving or break-up events in ice shelves. The term calving denotes the continuous breaking of smaller ice fragments from ice shelves or glaciers (small scale calving), as well as the braking of large tabular icebergs from ice shelves. Both processes are substantial parts of the mass balance of an ice sheet. Break-up or disintegration events, on the other hand, describe the collapse of ice shelf parts or entire ice shelves into many small fragments. Prominent examples are the complete disintegration of the Larsen B Ice Shelf (Glasser and Scambos, 2008) or the break-up events at the Wilkins Ice Shelf (Braun et al., 2009). Break-up or disintegration events are most likely linked

to climate warming.

Initial cracks, as basis for all fracture events in ice shelves, form due to tensile bending stresses at the surface, originate at shear margins or result from large tensile flow stresses e.g. downstream of ice rises (Van Der Veen, 2002). With ongoing flowing of the ice shelf, some of these cracks might stabilize or close. Due to additional load or changes in the boundary condition, others can become critical and eventually penetrate the ice shelf, either vertically or horizontally. Several authors (Glasser and Scambos, 2008; Scambos et al., 2009; Banwell et al., 2014) argue, that increased surface melt due to a general warming of the atmosphere results in a large number of melt ponds and water-filled surface crevasses. The additional load of the water pressure inside the crevasse then leads to the penetration of initially stable cracks and eventually to larger break-up events.

One major difficulty for the analysis of cracks in ice shelves is the determination of appropriate geometric scales, material parameters and boundary conditions for the finite element (FE) simulation. The remoteness of the area of study, together with the extreme climatic conditions make measurements of the ice properties and observations of crack growth very difficult or even impossible. Most knowledge on geometry and boundary conditions is therefore obtained from satellite data. Satellite images recorded in visible light give information on the real surface structure. Unfortunately, since the study area lies close to the poles, visible light is only available during half of the year. Coverage by clouds also reduces the applicability of this kind of data. Further space borne instruments use Synthetic Aperture Radar (SAR) to resolve the surface structure of ice shelves. The big advantage of SAR data lies in the independence of daylight and cloud coverage, as well as in the high resolution of the image products. Disadvantages can be found in the more complex post-processing and the expertise needed to analyze and interpret the data.

High-resolution satellite images document the horizontal extent of surface crevasses. The lengths of the crevasses reach up to several 10s of kilometers. The crevasse width is more difficult to determine as it often covers only very few pixels. Possible crevasse widths therefore range from 10s of centimeters to 10s of meters. The crevasse depths remain unknown, which makes it difficult to clearly distinguish between vertically propagating surface crevasses and horizontally propagating rifts. With additional processing of the satellite images, the position of the grounding line, and hence the horizontal extent of the ice shelf, as well as surface velocities with the resulting surface stresses, are available. However, it is difficult to obtain precise information on the boundary conditions. Even though the position of features with rather constrained boundaries, such as the grounding line and ice rises, can be evaluated to some extent, the type of constraint and the degree of restriction can only be anticipated.

Knowledge on material parameters is obtained from ice cores that are drilled during expeditions. The huge amount of resources (fuel, manpower, money) needed for drilling expeditions only allows for data acquisition at few locations. The material parameters in other regions therefore have to be evaluated using interpolation based

on measurable environmental parameters. For these reasons, a meaningful fracture mechanical analysis of cracks in ice shelves should depend only on few parameters whose influence on the simulation results can be evaluated for a relevant range of values.

Ice, on the long time scale, behaves as viscous fluid. However, fracture in ice happens on a very short time scale during which ice can be regarded as a brittle solid (Rist et al., 2002). Although the qualification of a linear elastic model to describe the ice rheology for fracture mechanical purposes is still the subject of discussion and controversy within the glaciological community, linear elastic fracture mechanics (LEFM) is well established and widely used for the analysis of vertically, as well as horizontally propagating cracks (Weertman, 1973; Van Der Veen, 1998a; Rist et al., 2002; Larour et al., 2004a).

Fracture mechanical methods can be used to investigate crack criticality by, for example, determining the stress intensity factor K_I at the crack tip and comparing it with critical values of K_{Ic}, obtained experimentally (Rist et al., 2002; Christmann et al., 2015). A well-established and comfortable method for the computation of K_I in the context of a FE simulation is the use of configurational forces, which goes back to the work of Eshelby (1951). Configurational forces can be used as indicator for crack criticality and crack propagation direction for a wide range of material behavior, for static and dynamic crack propagation, small and large deformations and also in combination with mesh refinement or multi scale material simulations (Näser et al., 2009; Kuhn et al., 2015; Gurtin and Shvartsman, 1997; Müller and Maugin, 2002; Khalaquzzaman et al., 2012). However, publications on configurational forces in combination with volume forces, loaded crack faces or spatially distributed material parameters are rare, especially in combination with the computation of resulting configurational forces as introduced by Denzer et al. (2003). The presented algorithm for fracture analysis in linear elastic materials therefore extends the standard implementation for the evaluation of configurational forces towards problems with volume forces, loaded crack faces and depth-dependent Young's moduli. Additionally, a method is shown to allow the computation of resulting configurational forces also for mixed mode loading situations without loss of accuracy, depending on the area of influence. The simulations are restricted to static loading. Crack initiation is excluded from the analysis by assuming the existence of starter cracks.

The work at hand analyses vertical cracks in ice shelves using parameters that mimic the conditions in the Wilkins Ice Shelf (WIS). Due to its partial disintegration since 1991 (Braun et al., 2009; Cook and Vaughan, 2010) with the collapse of the ice shelf bridge in 2009 (Humbert et al., 2010), surface changes on the WIS are very well captured by satellite imagery. High-resolution images of WIS after the break-up event in 1998 or 1999, as shown in Braun et al. (2009), reveal a considerable amount of surface crevasses and rifts and motivate the presented analysis. Recent publications on surface cracks in ice shelves link larger break-up and disintegration events to surface water that fills existing crevasses and triggers crack propagation (Scambos et al., 2009). The correlation of the observed break-up event with a mea-

4

sured surface temperature drop at research stations close to the WIS motivates the analysis of a more complex frost wedging scenario as possible reason for the partial disintegration in February 2009. Therefore, also the coupled thermodynamics - fluid flow problem with phase transition is analyzed to estimate the possible ice layer thickness in a water-filled crevasse that builds due to a severe temperature drop. In a following step, the fracture process with ice layer is simulated.

Horizontally propagating rifts are analyzed at the floating tongue of Pine Island Glacier (PIG) and at WIS. A new method is introduced to transfer the viscous surface stresses of the entire ice shelf, evaluated using measured ice shelf velocities, into an appropriate loading for the LEFM analysis. Previous approaches by e.g. Hulbe et al. (2010) or Larour et al. (2004a,b) were either restricted to small ice shelf excerpts or did not explicitly solve the linear elastic problem.

PIG is only constrained along the lateral margins, without further boundaries due to ice rises acting as pinning points. Additionally, the number of active and hence propagating rifts is usually small. This and the well captured repeatedly occurring major calving events make PIG an interesting first subject for the analysis of rift propagation. A more complex situation is found at WIS. Clamped between several islands and pinned by an extraordinary large number of ice rises, the stress state in the WIS is much more complex. As a result, considerably more active rifts or cracks can be seen leading to ongoing calving of larger ice shelf parts. For the analysis of rift propagation in the WIS therefore also crack merging and calving processes are included in the simulation.

1.2 Overview

The thesis is composed of seven chapters. Fundamental kinematics and balance equations of continuum mechanics, which are relevant for the fracture mechanical analysis of ice, are briefly summarized in the next chapter.

Basic principles of linear elastic fracture mechanics with a focus on energy criteria for crack propagation leading to the concept of configurational forces follow in chapter 3. Special attention is paid to the expansion of the well-established configurational force approach to problems with volume forces, material inhomogeneities and loaded crack faces. Different strategies for the evaluation of the most probable direction of crack propagation are introduced.

Chapter 4 covers the implementation of the presented methods within the framework of the finite element software COMSOL[1] together with post-processing routines in MATLAB[2]. Besides the standard numerical integration within the element, additional routines for the computation of configurational forces due to pressurized crack faces and mixed mode loading along the crack faces are introduced. This allows a more precise computation of the resulting configurational crack tip force,

---

[1] www.comsol.com
[2] www.mathworks.com

which is the sum of all nodal configurational forces within a defined region. Moreover, this chapter introduces the crack propagation algorithm under mixed mode loading, later used for the evaluation of horizontal rift paths. Six benchmark examples are used to compare the performance of the implemented algorithms to semi-analytical results or literature values. The examples consider the type and the refinement of the mesh around the crack tip, loaded crack faces, problems with volume forces, inhomogeneous Young's moduli and various combinations of mixed mode loading with a static crack tip, as well as the crack propagation algorithm with one and two cracks.

In chapter 5, the presented methods are applied for the analysis of stress intensity factors for vertical single cracks in ice shelves. The situation found at the WIS in 2008 is used to identify a set of meaningful parameters. First concentrating on dry single cracks emerging from the ice shelf surface, the impact of the geometric model scales and boundary conditions, as well as the influence of the density, Young's modulus and Poisson's ratio are analyzed. In order to compare the presented approach to the study of Rist et al. (2002), the simulation is also run with input data from Ronne Ice Shelf. The focus is then shifted towards different setups of water-filled single cracks, emerging from the top or from the bottom of the ice shelf. The chapter closes with a thorough analysis of a possible frost wedging process at the WIS. To this end, the growth of an ice lid in a water-filled crevasse is first modeled using a coupled thermodynamic-fluid flow simulation. Therefore, the built-in COMSOL module is extended for the computation of phase transition, using the heat capacity method as presented by Ogoh and Groulx (2010). The resulting ice lid thicknesses are then applied to a fracture mechanical analysis of a frost wedging process.

Chapter 6 analyses the propagation of horizontal rifts in ice shelves. Unlike in the previous chapter, where only a small cutout of the ice shelf is considered, now the spatial distribution of the stresses in the entire ice shelf is needed. Instead of using a cumbersome time-dependent viscoelastic simulation to capture ice shelf flow and crack propagation, a method is presented that transforms the viscous surface stresses into in-plane loads for the linear elastic fracture mechanical analysis. The viscous surface stresses are computed using ice shelf velocities resulting from satellite imagery. The performance of the method is first shown for an idealized ice shelf with simulated velocities. Then, two velocity fields of PIG are used to simulate the rift propagation that led to the 2013 calving event. Finally, the method is applied to simulate the horizontal propagation of cracks in the WIS using a velocity field of autumn 2008. Therefore, a method is presented to reduce unphysically high stresses resulting from jumps in the velocity field of various origins.

Chapter 7 gives a short conclusion and an outlook on future work.

2 Continuum mechanics

The aim of the following introduction to linear elasticity, as well as ice dynamics, is to set a common basis necessary for the understanding of the implemented models and the consequent fracture mechanical evaluation. For more detailed information on continuum mechanics, as well as the application to ice shelf flow, several good books are available. Without claim of completeness, the reader is referred to Becker and Gross (2002) or Sadd (2005) for details on elasticity, to Altenbach (2012) or Holzapfel (2000) for a general overview on continuum mechanics and to Greve and Blatter (2009) for application to ice dynamics.

2.1 Kinematics

The motion of a deformable continuous body $\mathscr{B}$ from its reference configuration $\mathscr{R}_0$ at time t_0 to the current configuration $\mathscr{R}$ at time t is described by the smooth and invertible mapping χ. The position x of a material point in the current configuration is given by $x = \chi(X, t)$ at each time t, where X denotes the position of the material point in the reference configuration. The displacement vector

$$u = x - X \tag{2.1}$$

is defined as the connecting vector between a material point and its map in the reference and in the actual configuration, respectively. The displacement field can be written as a function of the material point in the reference configuration $u = u(X, t) = \chi(X, t) - X$ which is called the Lagrangian description. This formulation is commonly used in solid mechanics and will be used for the fracture mechanical analysis. For the characterization of fluids, e.g. glacier flow, a formulation in the current configuration, called Eulerian description is often more appropriate. Here the displacement is formulated as $u = u(x, t)$.

The deformation gradient $\mathbf{F}$, defined as

$$\mathbf{F} = \frac{\partial x}{\partial \mathbf{X}} \quad \text{or} \quad F_{iJ} = \frac{\partial x_i}{\partial X_J}, \tag{2.2}$$

in index notation, maps a line element $\mathrm{d}X$ in the reference configuration to the respective line element $\mathrm{d}x = \mathbf{F}\mathrm{d}X$ in the current configuration. The indices $i = 1, 2, 3$ and $J = 1, 2, 3$ indicate Cartesian components of vectors or tensors in the current or reference configuration, respectively.

Invertibility of the motion as well as preservation of orientation at all times implies
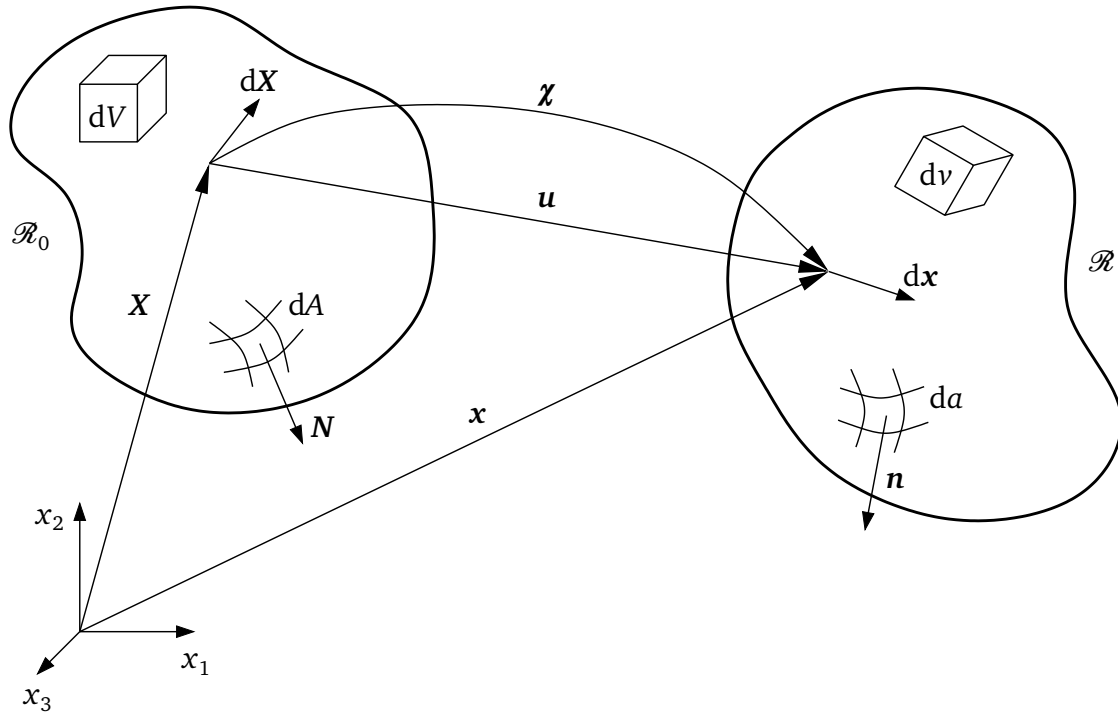
Figure 2.1: Mapping $\boldsymbol{\chi}$ between reference configuration $\mathscr{R}_0$ and current configuration $\mathscr{R}$

that $J = \det \mathbf{F} > 0$. Insertion of $\boldsymbol{x} = \boldsymbol{X} + \boldsymbol{u}$ in Eq. (2.2) yields

$$\mathbf{F} = \frac{\partial (\boldsymbol{X} + \boldsymbol{u})}{\partial \mathbf{X}} = \mathbf{1} + \mathbf{H}$$

where $\mathbf{1}$ denotes the second-rank identity tensor and $\mathbf{H}$ the displacement gradient defined as

$$\mathbf{H} = \frac{\partial \boldsymbol{u}}{\partial \boldsymbol{X}}. \tag{2.3}$$

A common symmetric deformation measure is the Green-Lagrange strain tensor, which can be given in terms of the displacement gradient as

$$\mathbf{E} = \frac{1}{2} \left(\mathbf{H} + \mathbf{H}^T + \mathbf{H}^T \mathbf{H} \right). \tag{2.4}$$

It describes the difference between the squares of the length of line elements $\mathrm{d}S$ and $\mathrm{d}s$ in reference and current configuration, respectively, in Lagrangian formulation. In the case of small displacement gradients, as will be assumed in the following, the reference and the current configuration coincide and

$$|H_{iJ}| = \left| \frac{\partial u_i}{\partial X_J} \right| = \left| \frac{\partial u_i}{\partial x_j} \right| \ll 1. \tag{2.5}$$

Hence, the quadratic terms in **H** become negligibly small and the Green-Lagrange strain tensor can be simplified, yielding the linearized strain tensor

$$\boldsymbol{\varepsilon} = \frac{1}{2}\left(\mathbf{H} + \mathbf{H}^T\right) \quad \text{or} \quad \varepsilon_{ij} = \frac{1}{2}\left(\frac{\partial u_i}{\partial x_j} + \frac{\partial u_j}{\partial x_i}\right) \tag{2.6}$$

in index notation. No further distinction between X and x is necessary.

The velocity field, in the Eulerian description is defined as

$$\boldsymbol{v} = \boldsymbol{v}(\boldsymbol{x}, t) = \frac{\mathrm{d}\boldsymbol{x}(X, t)}{\mathrm{d}t}, \tag{2.7}$$

where $\mathrm{d}(\ )/\mathrm{d}t$ denotes the material time derivative. The velocity gradient or strain-rate tensor

$$\mathbf{L} = \frac{\partial \boldsymbol{v}(\boldsymbol{x}, t)}{\partial \boldsymbol{x}} \tag{2.8}$$

is the spatial derivative of the velocity field. It can be additively decomposed into a symmetric and an antisymmetric part

$$\mathbf{D} = \frac{1}{2}(\mathbf{L} + \mathbf{L}^T) \quad \text{and} \quad \mathbf{W} = \frac{1}{2}(\mathbf{L} - \mathbf{L}^T). \tag{2.9}$$

An important quantity in the modeling of the material behavior of flowing ice is the square root of the second invariant of the symmetric strain-rate tensor,

$$d_e = \sqrt{II_D} = \sqrt{\frac{1}{2}\left[\mathrm{tr}(\mathbf{D}^2) - (\mathrm{tr}\,\mathbf{D})^2\right]}, \tag{2.10}$$

also called effective strain rate.
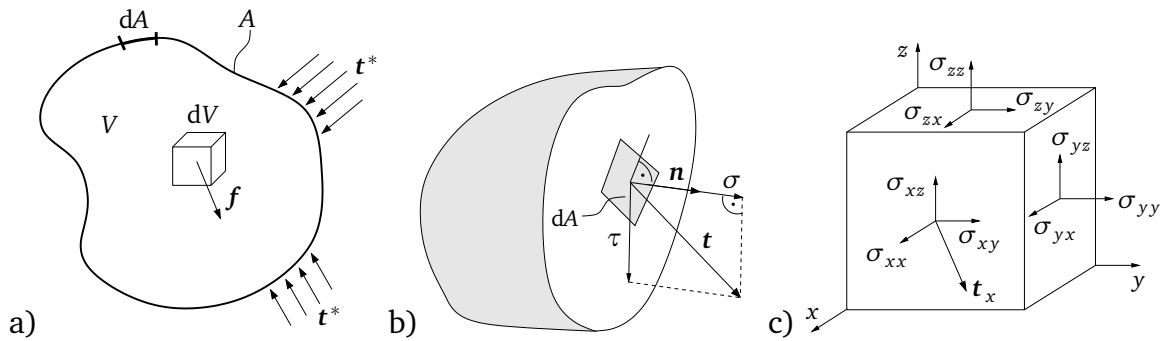
2.2 Balance Equation and Stress Measures

Figure 2.2: a) A body in equilibrium; b) internal forces in an arbitrary cut; c) elements of the Cauchy stress tensor in Cartesian coordinates

The balance of linear momentum indicates that a body is in equilibrium if

$$\int_{\partial V} \boldsymbol{t}^* \mathrm{d}A + \int_V \boldsymbol{f} \mathrm{d}V = 0, \tag{2.11}$$

with $\boldsymbol{t}^*$ representing external loads acting on the surface A of the body (Fig. 2.2 a) and $\boldsymbol{f}$ representing the loads per volume element $\mathrm{d}V$. These external forces cause internal stresses $\boldsymbol{t}$, which can be inferred by an arbitrary fictitious cut through the body (Fig. 2.2 b). The stress vector $\boldsymbol{t}$ depends on the direction of the cut represented by the outward pointing unit normal vector $\boldsymbol{n}$. The component of $\boldsymbol{t}$ in direction of $\boldsymbol{n}$, $\sigma = \boldsymbol{t} \cdot \boldsymbol{n}$, is called the normal stress, the component vertical to $\boldsymbol{n}$, $\tau = \sqrt{t^2 - \sigma^2}$, is called shear stress. If the body is cut along planes orthogonal to the axis of the Cartesian coordinate system (Fig. 2.2 c), the components of the resulting three stress vectors $\boldsymbol{t}_x$, $\boldsymbol{t}_y$, $\boldsymbol{t}_z$ constitute the elements of the symmetric Cauchy stress tensor $\boldsymbol{\sigma}$,

$$\boldsymbol{\sigma} = \begin{pmatrix} \boldsymbol{t}_x \\ \boldsymbol{t}_y \\ \boldsymbol{t}_z \end{pmatrix} = \begin{pmatrix} \sigma_{xx} & \sigma_{xy} & \sigma_{xz} \\ \sigma_{yx} & \sigma_{yy} & \sigma_{yz} \\ \sigma_{zx} & \sigma_{zy} & \sigma_{zz} \end{pmatrix}. \tag{2.12}$$

The first index of the stress components σ_{ij} points to the direction of the cut, the second index indicates the direction of the components of $\boldsymbol{t}_x$, $\boldsymbol{t}_y$ and $\boldsymbol{t}_z$, respectively. Balance of angular momentum for the volume element in Fig. 2.2 c) reveals the symmetry of the Cauchy stress tensor, hence $\sigma_{ij} = \sigma_{ji}$. With the use of Cauchy's theorem, $\boldsymbol{\sigma n} = \boldsymbol{t}$, integration by parts and the divergence theorem, Eq. (2.11) can be rewritten in the local form as

$$\mathrm{div}\,\boldsymbol{\sigma} + \boldsymbol{f} = \boldsymbol{0} \quad \text{or} \quad \sigma_{ij,j} + f_i = 0. \tag{2.13}$$

2.2.1 Linear elasticity

For the short-term fracture mechanical analysis, the generally complex material behavior of ice is assumed as linear elastic. The relation between the Cauchy stress tensor $\boldsymbol{\sigma}$ and the linearized strain tensor $\boldsymbol{\varepsilon}$ therefore reads

$$\boldsymbol{\sigma} = \mathbb{C}\boldsymbol{\varepsilon}, \tag{2.14}$$

where $\mathbb{C}$ is the fourth-rank stiffness-tensor. In case of isotropic material behavior, the components of $\mathbb{C}$ can be given in terms of the Lamé-constants λ and μ and Eq. (2.14) is rewritten as

$$\boldsymbol{\sigma} = \lambda \mathrm{tr}(\boldsymbol{\varepsilon})\mathbf{1} + 2\mu\boldsymbol{\varepsilon} \quad \text{or} \quad \sigma_{ij} = \lambda \varepsilon_{kk} \delta_{ij} + 2\mu \varepsilon_{ij}, \tag{2.15}$$

with the use of Kronecker's delta stating $\delta_{ij} = 1$ for $i = j$ and $\delta_{ij} = 0$ for $i \neq j$.

An important quantity for the successive fracture mechanical analysis is the work per unit volume W done during the deformation from the undeformed configuration to the actual state with the strain $\boldsymbol{\varepsilon}$,

$$W = \int_{\mathbf{0}}^{\boldsymbol{\varepsilon}} \boldsymbol{\sigma} \, \mathrm{d}\tilde{\boldsymbol{\varepsilon}}. \tag{2.16}$$

In an elastic body, W, also called strain energy density or specific elastic potential, only depends on $\boldsymbol{\varepsilon}$ and is independent of the deformation path. Hence, the increment

$$\mathrm{d}W = \sigma_{ij} \mathrm{d}\varepsilon_{ij} = \frac{\partial W}{\partial \varepsilon_{ij}} \mathrm{d}\varepsilon_{ij}$$

is a total differential and the stress can be computed via

$$\sigma_{ij} = \frac{\partial W}{\partial \varepsilon_{ij}}. \tag{2.17}$$

In case of quasi-static loading, the potential of internal work results from the strain energy density

$$\Pi^i = \int_V W \, \mathrm{d}V, \tag{2.18}$$

and the potential of conservative external loads reads

$$\Pi^e = -\int_V \boldsymbol{f} \cdot \boldsymbol{u} \, \mathrm{d}V - \int_{\partial V} \boldsymbol{t}^* \cdot \boldsymbol{u} \, \mathrm{d}A. \tag{2.19}$$

The total potential then follows as

$$\Pi = \Pi^i + \Pi^e. \tag{2.20}$$

Plane stress, plane strain

The dimensions of an ice shelf (80-500m thickness, several hundreds of kilometers in length and width) motivate two-dimensional approaches of the general three-dimensional system. Figure 2.3 a) illustrates crack propagation in the $(x, y$-plane), where the equations of the plane stress state yield a good approximation of the problem. Common mechanical applications for a plane stress analysis are plates, whose thickness is much smaller than the in-plane dimensions and which only support in-plane loads. In this case the components σ_{zz}, σ_{xz} and σ_{yz} of the Cauchy stress tensor, as well as the components ε_{xz} and ε_{yz} of the linearized strain tensor
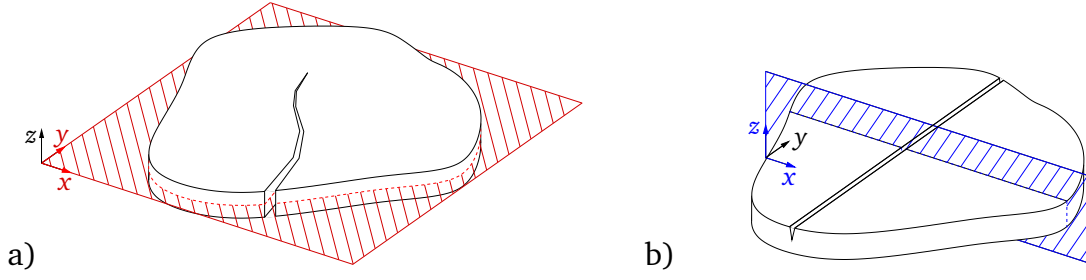
Figure 2.3: a) Horizontal crack propagation, plane stress conditions; b) vertical crack propagation, plane strain conditions

vanish and the remaining components are independent of z. Using the relations

$$\lambda = \frac{E\nu}{(1+\nu)(1-2\nu)} \quad \text{and} \quad \mu = \frac{E}{2(1+\nu)}, \tag{2.21}$$

with Young's modulus E and Poisson's ratio ν, Eq. (2.15) reduces to

$$
\begin{aligned}
\sigma_{xx} &= \frac{E}{1-\nu^2}\varepsilon_{xx} + \frac{E\nu}{1-\nu^2}\varepsilon_{yy}, \\
\sigma_{yy} &= \frac{E\nu}{1-\nu^2}\varepsilon_{xx} + \frac{E}{1-\nu^2}\varepsilon_{yy}, \\
\sigma_{xy} &= \frac{E}{1+\nu}\varepsilon_{xy}.
\end{aligned}
\tag{2.22}
$$

Independence of depth for the in-plane components of the stress and strain tensor is a valid assumption for ice shelves, whereas the extinction of σ_{zz} does not match reality, where in general, the compression due to gravity plays an important role. However, the influence of σ_{zz} can be neglected for the analysis of in-plane processes. Vertical crack propagation (Fig. 2.3 b) demands for an analysis of the processes in the vertical ice-shelf plane, the x,z-plane. The problem can be approximated by the equations of the plane strain state, which hold for situations where the displacements in one direction (here the y-direction) vanish. The applicability to vertical cracks in ice shelves follows from the presumption of an infinite extent of the ice shelf in y-direction, justified by the mentioned ice-shelf dimensions. In case of plane strain, Eq. (2.15) can be written as

$$
\begin{aligned}
\sigma_{xx} &= \frac{E(1-\nu)}{(1+\nu)(1-2\nu)}\varepsilon_{xx} + \frac{E\nu}{(1+\nu)(1-2\nu)}\varepsilon_{yy}, \\
\sigma_{yy} &= \frac{E\nu}{(1+\nu)(1-2\nu)}\varepsilon_{xx} + \frac{E(1-\nu)}{(1+\nu)(1-2\nu)}\varepsilon_{yy}, \\
\sigma_{xy} &= \frac{E}{1+\nu}\varepsilon_{xy}.
\end{aligned}
\tag{2.23}
$$

2.2.2 Glen's Flow Law

Shear experiments of polycrystalline ice indicate a complex nonlinear relation between the shear angle γ_{xz} and time (Fig. 2.4), (Glen, 1958). Whereas elastic deformation characterizes the short-term behavior of ice, the long-term properties are dominated by viscous creep. The secondary creep regime with a constant shear rate $\dot{\gamma}$ appropriately describes glacier and ice shelf flow (Greve and Blatter, 2009; Cuffey and Paterson, 2010).
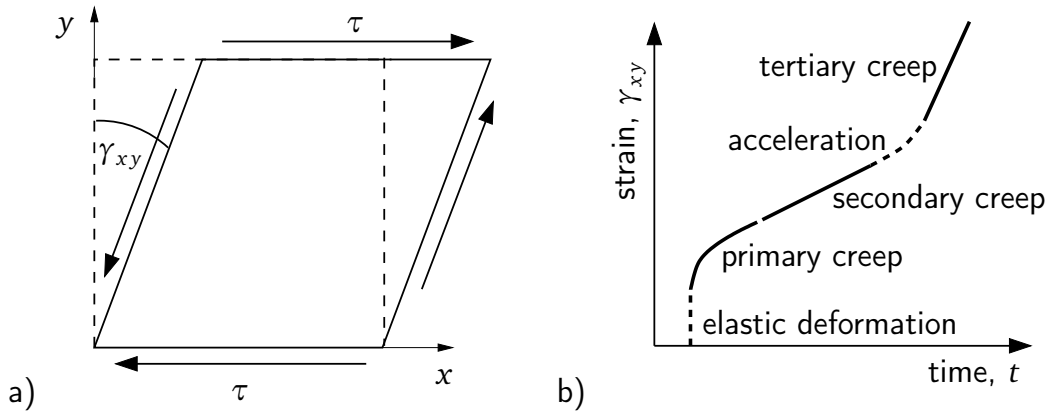
Figure 2.4: a) Simple shear experiment; b) nonlinear shear angle vs. time behavior of ice, (Greve and Blatter, 2009)

The relation between $\dot{\gamma}$ and the shear stress τ for secondary creep is best described by a non-linear viscous fluid,

$$\dot{\gamma} = \frac{1}{\eta(T, p, |\tau|)} \tau, \tag{2.24}$$

where the viscosity η is a function of the temperature T, the pressure p and the absolute shear stress $|\tau|$. Regarding the long term flow behavior, ice can be idealized as incompressible and $d\rho/dt = 0$. Therefore, the conservation of mass,

$$\frac{\partial \rho}{\partial t} + (\nabla \rho) \cdot \boldsymbol{v} + \rho \operatorname{div} \boldsymbol{v} = 0 \quad \text{with} \quad \frac{\partial \rho}{\partial t} + (\nabla \rho) \cdot \boldsymbol{v} = \frac{d\rho}{dt}, \tag{2.25}$$

reduces to

$$\operatorname{div} \boldsymbol{v} = \operatorname{tr} \mathbf{L} = \operatorname{tr} \mathbf{D} = 0. \tag{2.26}$$

In addition it can be shown for polycrystalline ice, that the strain rate is a function of the stress deviator $\boldsymbol{\sigma}_f^D$ defined as

$$\boldsymbol{\sigma}_f^D = \boldsymbol{\sigma}_f + p\mathbf{1} \quad \text{with} \quad p = -\frac{1}{3}\operatorname{tr}(\boldsymbol{\sigma}_f), \tag{2.27}$$

with $\boldsymbol{\sigma}_f$ being the viscous Cauchy stress (subscript f indicates flow). This leads to the expression for the stress - strain rate - relation in tensorial form

$$\mathbf{D} = \frac{1}{2\eta(T, p, \sigma_e^D)} \boldsymbol{\sigma}_f^D. \tag{2.28}$$

As a result, the strain rate tensor $\mathbf{D}$ is also deviatoric. The fluidity, $1/\eta$, can be rewritten as

$$\frac{1}{\eta(T, p, \sigma_e^D)} = 2A(T, p)(\sigma_e^D)^{n-1} \tag{2.29}$$

with the Arrhenius-type rate factor $A(T, p)$ and the effective deviatoric stress

$$\sigma_e^D = \sqrt{II_{\boldsymbol{\sigma}_f^D}} = \sqrt{\frac{1}{2}\left[\text{tr}(\boldsymbol{\sigma}_f^{D\,2}) - (\text{tr}\boldsymbol{\sigma}_f^D)^2\right]} = \sqrt{\frac{1}{2}\text{tr}(\boldsymbol{\sigma}_f^{D\,2})}, \tag{2.30}$$

since the trace of a deviatoric tensor equals zero. Following Cuffey and Paterson (2010), the power exponent n is usually set to $n = 3$. Solving Eq. (2.28) for the stress leads to the inverse flow law and consequently to a constitutive equation for the deviatoric stress

$$\boldsymbol{\sigma}_f^D = A(T, p)^{-1/n} d_e^{-\frac{n-1}{n}} \mathbf{D}. \tag{2.31}$$

Usually, the shear stresses $\sigma_{f\,xy}$ and $\sigma_{f\,yz}$ are considerably smaller than the vertical normal stress $\sigma_{f\,zz}$ and can be neglected in the vertical momentum balance (Greve and Blatter, 2009). Therefore, $\sigma_{f\,zz}$ can directly be computed yielding

$$\sigma_{f\,zz} = -\rho_I g(H - z), \tag{2.32}$$

with a upward pointing z-coordinate starting at the bottom of an ice shelf with the thickness H and the constant ice density ρ_I. The deviatoric vertical normal flow stress is then expressed as

$$\sigma_{f\,zz}^D = -\rho_I g(H - z) + p. \tag{2.33}$$

With this and the trace of the deviatoric flow stress, which by definition equals zero, the pressure p can be redefined as

$$\begin{aligned} p &= p - 0 = p - \sigma_{f\,xx}^D - \sigma_{f\,yy}^D - \sigma_{f\,zz}^D \tag{2.34} \\ &= \rho_I g(H - z) - \sigma_{f\,xx}^D - \sigma_{f\,yy}^D. \tag{2.35} \end{aligned}$$

The resulting equations for components of the flow stress tensor therefore read

$$\begin{aligned} \sigma_{f\,xx} &= B d_e^{\frac{1-n}{n}} (2D_{xx} + D_{yy}) - \rho_I g(H - z), \\ \sigma_{f\,yy} &= B d_e^{\frac{1-n}{n}} (D_{xx} + 2D_{yy}) - \rho_I g(H - z), \tag{2.36} \\ \sigma_{f\,xy} &= B d_e^{\frac{1-n}{n}} D_{xy}, \end{aligned}$$

where $B = A(T,p)^{-1/n}$. The surface stresses are computed for $z = H$ hence the last summand in Eq. (2.36) vanishes.

2.2.3 Principal stresses and their directions

Since fracture in ice shelves predominantly occurs perpendicular to the direction of the principal flow stress, principal stresses and the corresponding principal directions are introduced in the following. Principal directions denote a particular orthogonal coordinate system, characterized by the fact that cuts perpendicular to the principal directions feature only normal stresses σ, and no shear stresses occur. In other words, the stress vector in those cuts has the same direction as the normal vector, hence $\mathbf{t} = \sigma\mathbf{n}$. The latter property together with Cauchy's theorem can be used to compute the principal stresses. With $\boldsymbol{\sigma}\boldsymbol{n} = \sigma\boldsymbol{n}$, the formulation of an eigenvalue problem follows:

$$(\boldsymbol{\sigma} - \sigma\mathbf{1})\boldsymbol{n} = \mathbf{0}. \tag{2.37}$$

The three eigenvalues σ_i, called principal stresses, are the nontrivial solutions of the characteristic polynomial

$$\sigma^3 - I_\sigma \sigma^2 - I\!I_\sigma \sigma - I\!I\!I_\sigma = 0 \tag{2.38}$$

where I_σ, $I\!I_\sigma$ and $I\!I\!I_\sigma$ denote the invariants

$$I_\sigma = \mathrm{tr}\,\boldsymbol{\sigma}, \qquad I\!I_\sigma = \frac{1}{2}\left(\mathrm{tr}(\boldsymbol{\sigma}^2) - (\mathrm{tr}\,\boldsymbol{\sigma})^2\right) \quad \text{and} \quad I\!I\!I_\sigma = \det\boldsymbol{\sigma}. \tag{2.39}$$

The corresponding eigenvectors form the principal directions $\boldsymbol{n}_i$. In the two-dimensional case, Eqs. (2.38) and (2.39) simplify and the principal stresses (here in case of the Cauchy stress tensor) can be computed using the equation

$$\sigma_{1,2} = \frac{\sigma_{xx} + \sigma_{yy}}{2} \pm \sqrt{\left(\frac{\sigma_{xx} + \sigma_{yy}}{2}\right)^2 + \sigma_{xy}} \tag{2.40}$$

with $\sigma_1 \geq \sigma_2$. The angles of the principal directions follow from

$$\tan 2\varphi^* = \frac{2\sigma_{xy}}{\sigma_{xx} - \sigma_{yy}} \quad \text{and} \quad \varphi^{**} = \varphi^* \pm \frac{\pi}{2}. \tag{2.41}$$

The maximum shear stress,

$$\tau_{\mathrm{max}} = \sqrt{\left(\frac{\sigma_{xx} + \sigma_{yy}}{2}\right)^2 + \sigma_{xy}}, \tag{2.42}$$

occurs in cuts rotated by 45° to the principal directions.

3 Linear elastic fracture mechanics

Classical failure criteria have a long tradition in the evaluation of calving and break-up situations in glaciers and ice shelves. The most common failure criteria compare an effective stress to an ice specific yield stress (Nye, 1955). These methods appeal with simplicity and yield a good approximation for many situations. However, they cannot be applied at locations with stress singularities, as are e.g. the tips of crevasses. Here, classical fracture mechanics comes into play.

Ice is a polycrystalline material for which micro cracks initiate and propagate along lattice planes of the crystals or along grain boundaries. These characteristics lead to brittle failure on the macro scale (Rist et al., 1999, 2002). For brittle materials, the amount of inelastic deformations before failure is negligible. As micro mechanical processes leading to crack nucleation are not covered by the theory of classical fracture mechanics, the material is regarded as pre-damaged or interspersed with micro cracks. The single crystal on the micro scale is anisotropic. Nevertheless, the polycrystalline continuum on the macro scale will be treated as isotropic.

Once a crack is initiated, crack growth can occur unstable or stable, depending first of all on the geometry and boundary conditions (stress boundary conditions versus displacement boundary conditions), secondary on material properties. Stable crack growth is characterized by the need for additional load for the crack to grow further, while unstable crack growth occurs spontaneously without additional loads.

Cracks can grow with a speed up to the sonic velocity of the material, designated as fast crack growth. This behavior has also been reported for cracks in ice shelves. The opposite behavior, called slow or subcritical crack growth is predominantly found for cyclic loading, leading to crack growth velocities of one mm per second or less. Though subcritical crack growth has been discussed as mechanism for iceberg calving (Weiss, 2004) it will be ignored for the present analysis. Also inertia effects will be excluded, hence the loading and crack growth occur quasi-static.

For further reading on failure criteria, micro mechanical effects and crack growth the reader is referred to the textbooks of e.g. Gross and Seelig (2002) and Kuna (2008) which are the foundation of the following introduction into linear elastic fracture mechanics.
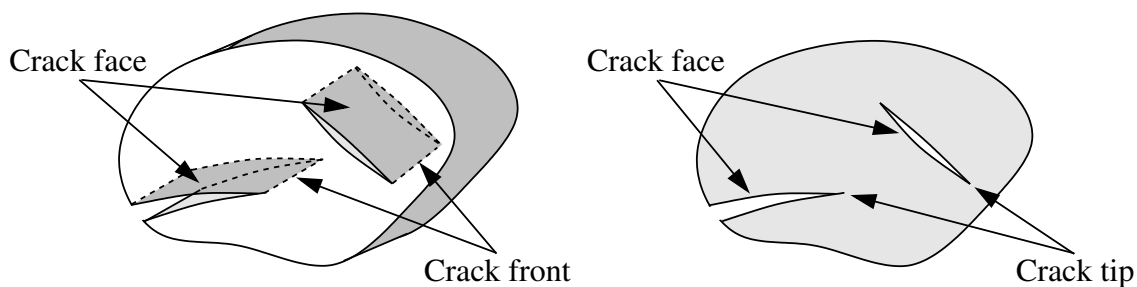
Crack face

Crack front

Crack face

Crack tip

Figure 3.1: Nomenclature for 3D and 2D cracks

3.1 Model assumptions

From the continuum point of view, a crack is an ideally sharp cut into a body, either emanating from the boundary of the body or located inside. The dimension of a crack is one dimension lower than the dimension of the body. Hence, in a three-dimensional body, a crack is formed by two surfaces and ends in one or two lines representing the crack front. In a two-dimensional setting, the crack surfaces reduce to lines and the crack front to a point, the crack tip. The opposite surfaces (3D) or lines (2D) are called crack faces or crack flanks. The opening of a crack can be

Mode I

Mode II

Mode III
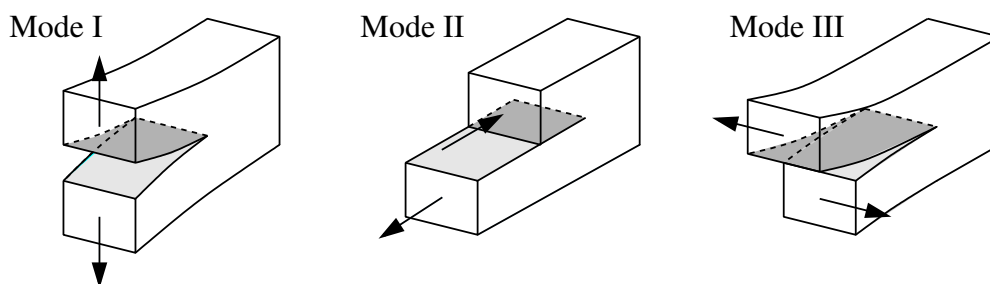
Figure 3.2: Crack opening modes

distinguished into three opening modes as illustrated in Fig. 3.2. Mode I describes a symmetric opening of the crack normal to the crack faces. It is the most common opening mode in practical applications and will predominantly be used in the context of ice shelf fractures. Mode II describes tangential sliding of crack faces towards and away from the crack front. The tearing mode III describes the tangential sliding of the crack faces parallel to the crack front. All modes can occur separately or in various combinations.

The concept of linear elastic fracture mechanics requires linear elastic material behavior in the fractured body. Hence, the so called inelastic process zone in which the complex and generally nonlinear micro-mechanical processes leading to crack growth take place has to be negligibly small in comparison to the geometric scale of the examined body. This is the case for most brittle materials and thus applies for cracks in ice in the examined scope.

3.2 Stress intensity factors and configurational forces

3.2.1 *K*-concept

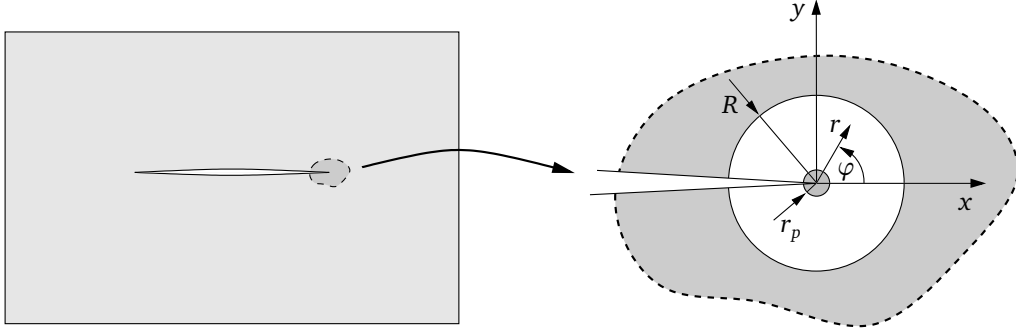Figure 3.3: Near-tip field

While the singularities at the crack tip do not influence the stress field in a sufficient distance from the tip, the stresses close to the tip are dominated by the near-tip field, defined as a small area of radius R around the crack tip. Since nonlinear processes in direct vicinity of the tip are not covered by the near-tip equations, R has to be significantly larger than the process zone (radius r_p). For simplified geometries and boundary conditions, the stresses of the near-tip field can be resolved in an analytical or semi-analytical procedure using the complex potential method introduced by Kolosov (1909) and refined by Muskhelishvili (1975). The order of the stress singularity at the crack tip depends on the crack opening angle α, depicted in Fig. 3.4. Without further derivation, the eigenvalue problem for the evaluation of the order of singularity in case of mode I and mode II opening modes reads

$$\sin(\lambda_e 2\beta) = \pm\lambda_e \sin(2\beta), \tag{3.1}$$

with $\beta = \pi - \alpha$. The dominant stress state at the crack tip shows singularities of the form $\sigma_{ij} \sim r^{\lambda_e - 1}$. Figure 3.4 b) illustrates the resulting eigenvalues λ_e with respect to β. For the valuation of the singularity, the smaller eigenvalue (dashed line) has to be considered. It can be seen that for the ideally sharp crack ($\alpha = 0$), also called Griffith crack, $\lambda_e = 1/2$ hence $\sigma_{ij} \sim 1/\sqrt{r}$. The resulting stresses for the different loading modes read

Mode I:

$$\begin{Bmatrix} \sigma_x \\ \sigma_y \\ \tau_{xy} \end{Bmatrix} = \frac{K_I}{\sqrt{2\pi r}} \cos(\varphi/2) \begin{Bmatrix} 1 - \sin(\varphi/2)\sin(3\varphi/2) \\ 1 + \sin(\varphi/2)\sin(3\varphi/2) \\ \sin(\varphi/2)\cos(3\varphi/2) \end{Bmatrix}, \tag{3.2}$$
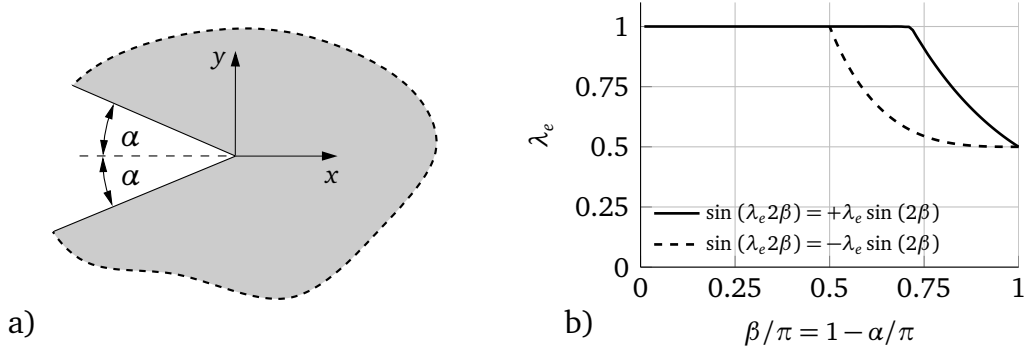
Figure 3.4: a) Crack opening angle α; b) order of singularity λ_e for different $\beta(\alpha)$

Mode II:

$$\begin{Bmatrix} \sigma_x \\ \sigma_y \\ \tau_{xy} \end{Bmatrix} = \frac{K_{II}}{\sqrt{2\pi r}} \begin{Bmatrix} -\sin(\varphi/2)\left[2+\cos(\varphi/2)\cos(3\varphi/2)\right] \\ \sin(\varphi/2)\cos(\varphi/2)\cos(3\varphi/2) \\ \cos(\varphi/2)\left[1-\sin(\varphi/2)\sin(3\varphi/2)\right] \end{Bmatrix}. \tag{3.3}$$

For small opening angles $0 < \alpha < \pi/10$, the change in the order of the singularity is negligible and the results for the ideally sharp crack meet the requirements. It is important to notice that the presented concepts only hold for sharp cracks and notches. If the tip is rounded, stress concentrations instead of stress singularities have to be considered.

The quantities K_I and K_{II} in Eqs. (3.2) and (3.3) are the so called stress intensity factors, introduced by Irwin (1957). Depending only on the geometry of the body and the crack, as well as on the applied load, the stress intensity factors quantify the intensity of the stress singularity at the crack tip. They can be used to establish fracture criteria and to evaluate if a crack will propagate once a material specific critical value K_c is reached. The fracture criteria read

$$K_I = K_{Ic}, \quad \text{and} \quad K_{II} = K_{IIc} \tag{3.4}$$

for the different pure modes I and II, respectively. For mixed loading, the fracture criterion takes the more general form

$$f(K_I, K_{II}) = 0. \tag{3.5}$$

Loading cases including a mode III opening demand for a three-dimensional analysis and will not be considered in the presented scope.

Depending on the model geometry and the applied load, there exist analytical or semi-analytical formulas for the evaluation of K_I and K_{II}. Figure 3.5 shows the load, the geometry and the resulting K_I and K_{II} as presented in Tada et al. (1973) for two exemplary situations, which will be used as benchmarks in the following studies.

$$K_I = \sigma\sqrt{\pi a}\sqrt{\frac{2b}{\pi a}\tan\frac{\pi a}{2b}}C_1(a/b)$$

$$C_1 = \frac{0.752 + 2.02\frac{a}{b} + 0.37(1 - \sin\frac{\pi a}{2b})^3}{\cos\frac{\pi a}{2b}}$$

$$\begin{Bmatrix} K_I \\ K_{II} \end{Bmatrix} = \begin{Bmatrix} \sigma \\ \tau \end{Bmatrix}\sqrt{\pi a}$$
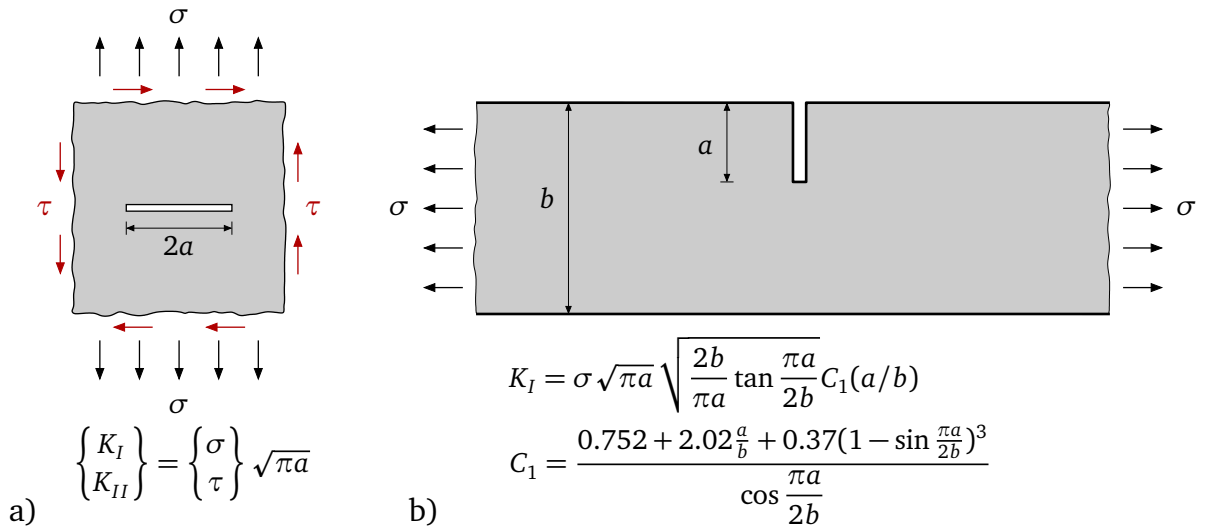
a)   b)

Figure 3.5: a) Straight crack of length $2a$ in an infinite plate under uniaxial remote stress σ and/or remote shear stress τ; b) single edge crack of length a in infinitely long plate of width b under uniaxial remote stress σ

3.2.2 Energy balance – the Griffith criterion

For simplified geometries and loading conditions, semi-analytical values for K_I and K_{II} can be computed to analyze the criticality of a crack. However, complex geometries, boundary conditions and loads, require the application of more advanced concepts for the analysis of the cracked body. The experiment in Fig. 3.6 illustrates the energy release $-\Delta\Pi$ resulting from a crack growth of an increment Δa. A pre-cracked body (crack length a) is loaded by a point displacement $\hat{u}$. The
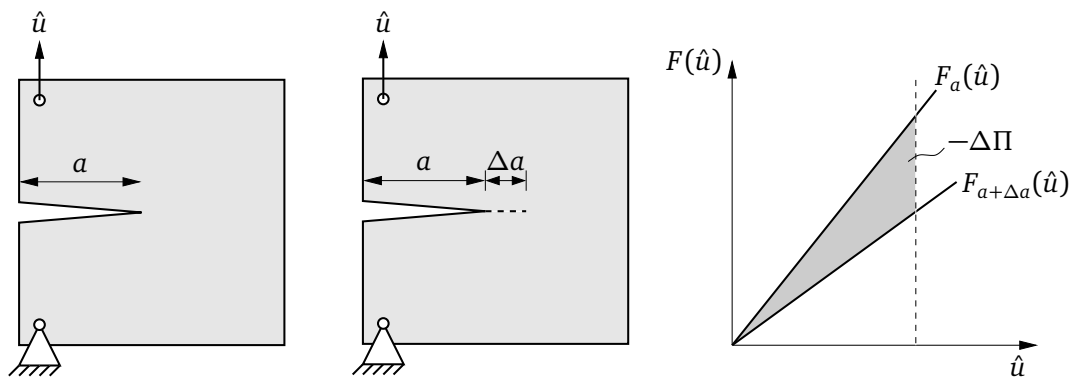
Figure 3.6: Energy release for crack growth

resulting reaction force $F(\hat{u})$ at the loading point is plotted with respect to the load. The experiment is repeated with an enlarged crack length of $a + \Delta a$. The comparison of the plotted reaction force yields a lower slope for a larger crack length. The difference $-\Delta\Pi = \Pi_a - \Pi_{a+\Delta a}$ yields the energy release of the system due to a crack growth of the increment Δa. Reducing the increment Δa to an infinitesimal crack

growth increment da leads to the definition of the energy release rate

$$\mathcal{G} = -\frac{\mathrm{d}\Pi}{\mathrm{d}a},\tag{3.6}$$

with the dimension force per unit thickness. Other names for $\mathcal{G}$, referring to the physical dimension, are crack extension force or crack driving force. For straight growing cracks, the crack driving force can be used to compute stress intensity factors using the relation

$$\mathcal{G} = \frac{K_I^2 + K_{II}^2}{E'},\tag{3.7}$$

where $E' = E$ in the case of plane stress and $E' = E/(1 - v^2)$ in the 3D case and under plane strain assumptions.

For pure loading modes a fracture criterion equivalent to Eq. (3.4) can be set up yielding

$$\mathcal{G} = \mathcal{G}_c.\tag{3.8}$$

This energy based fracture criterion, proposed by Griffith (1920) in a slightly modified form, states that a crack propagates if the energy release during crack growth equals the required energy. However, Griffith formulated his original criterion for crack initiation and not for its evolution.

3.2.3 J-integral and configurational forces
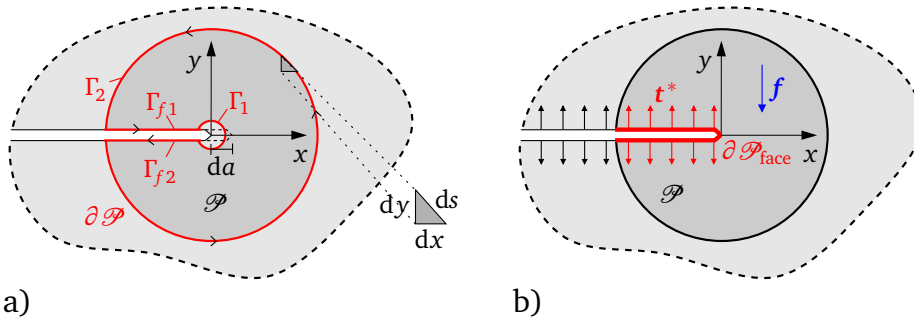
Figure 3.7: a) Contour around crack tip for evolution of J-integral; b) loaded crack faces

A well-established method for the computation of the energy release rate is the evaluation of the J-integral. In an elastic material, the J-integral computed for a straight crack along the x-axis of a two-dimensional homogeneous body without body loads and crack face tractions is defined as

$$J = \int_{\Gamma_2} W \mathrm{d}y - \mathbf{t} \cdot \frac{\partial \mathbf{u}}{\partial x} \mathrm{d}s\tag{3.9}$$

and was independently introduced by Rice (1968) and Cherepanov (1967). The

equivalence to $\mathscr{G}$ holds for infinitesimal crack growth increments $\Delta a \to 0$,

$$J = \lim_{\Delta a \to 0} -\frac{\Delta\Pi}{\Delta a} = -\frac{d\Pi}{da} = \mathscr{G}. \tag{3.10}$$

It can be shown that under the mentioned presumptions, the J-integral of any closed curve (Fig. 3.7 a) without enclosed singularity equals zero, hence

$$J = \int_{\partial\mathscr{P}} [\ ] = \int_{\Gamma_1} [\ ] + \int_{\Gamma_{f1}} [\ ] + \int_{\Gamma_2} [\ ] + \int_{\Gamma_{f2}} [\ ] = 0 \tag{3.11}$$

with $[\ ] = W\,dy - \boldsymbol{t} \cdot \dfrac{\partial\boldsymbol{u}}{\partial x}\,ds$. Since $dy = 0$ on Γ_{f1} and Γ_{f2}, in case of straight and traction free crack faces Eq. (3.11) can be reformulated to

$$\int_{\Gamma_1} [\ ] = -\int_{\Gamma_2} [\ ], \tag{3.12}$$

and path independence of Eq. (3.9) is demonstrated. Following Gradin (1985) and Wilson and Yu (1979), path independence for loaded crack faces and applied body loads (Fig. 3.7 b) can be preserved by including the crack face integrals and adding an extra area integral yielding

$$J = \int_{\Gamma_2} W\,dy - \boldsymbol{t} \cdot \frac{\partial\boldsymbol{u}}{\partial x}\,ds - \int_{\Gamma_{f1}+\Gamma_{f2}} \boldsymbol{t} \cdot \frac{\partial\boldsymbol{u}}{\partial x}\,ds - \int_{\mathscr{P}} \boldsymbol{f} \cdot \frac{\partial\boldsymbol{u}}{\partial x}\,dA. \tag{3.13}$$

Knowles and Sternberg (1972) introduce a more general form of Eq. (3.9) resulting in the components of the J-integral vector

$$J_k = \int_{\Gamma_2} (W\delta_{kj} - \sigma_{ij}u_{i,k})n_j\,ds. \tag{3.14}$$

For problems without volume forces or loaded crack faces, the component J_1 equals the just introduced path independent J-integral. The component J_2 is zero in case of a straight crack under pure mode I and pure mode II loading. For mixed mode loading or curved cracks J_2 is non-zero and always path dependent. It can be evaluated by contracting the contour Γ_2 to the crack tip or by including the crack face integrals into the computation.

The link between J_1, J_2 and the previously presented stress intensity factors K_I and K_{II} can be found in Bergez (1974) reading

$$J_1 = \frac{1-\nu^2}{E}(K_I^2 + K_{II}^2) \quad \text{and} \quad J_2 = -\frac{2(1-\nu^2)}{E}(K_I K_{II}) \tag{3.15}$$

in case of plane strain.

The integral in Eq. (3.9) can be computed on a path in sufficient distance from the crack tip, not taking into account the difficult computation of the field variables close to the tip. Limited to straight cracks under pure mode loading in absence of volume forces and crack face loading, Eq. (3.9) therefore provides a comfortable way to compute stress intensity factors in the context of numerical methods. Without the mentioned prerequisites, extra effort is needed for the computation or Γ_2 has to be contracted to the crack tip to fulfill Eq. (3.10) and the just mentioned benefits do no longer hold.

A popular method linked to J-integrals is the concept of configurational or material forces. It was introduced by Eshelby (1951) as a way to compute the "in a sense fictitious" forces acting on a singularity. Material or configurational forces must not be confused with physical forces but can rather be understood as a measure for energy changes in a system due to a change in the singularity. A multitude of different approaches exist for the computation of configurational forces. Examples can be found in the textbooks of Maugin (1993), Kienzler and Herrmann (2000), Müller (2006), Steinmann and Maugin (2010) and Maugin (2010). The method presented here follows an adaption of Eshelby's original procedure by Kuhn (2013). The basis of this approach is the computation of the gradient of the energy density, $W,_{\boldsymbol{x}}$. In this case, $W = \tilde{W}(\boldsymbol{\varepsilon}, \boldsymbol{x}, \boldsymbol{x}^{\text{tip}})$ is regarded as a function of the linearized strain tensor $\boldsymbol{\varepsilon}$, the coordinate $\boldsymbol{x}$ and the position of the crack tip $\boldsymbol{x}^{\text{tip}}$. The explicit dependence on $\boldsymbol{x}$ is necessary to account for possible inhomogeneities in the material. The gradient is computed by using the chain rule of differentiation,

$$W,_{\boldsymbol{x}} = \frac{\partial \tilde{W}}{\partial \boldsymbol{\varepsilon}} \boldsymbol{\varepsilon},_{\boldsymbol{x}} + \frac{\partial \tilde{W}}{\partial \boldsymbol{x}}\bigg|_{\text{expl.}} + \frac{\partial \tilde{W}}{\partial \boldsymbol{x}^{\text{tip}}}(\boldsymbol{x}^{\text{tip}}),_{\boldsymbol{x}} \, ,$$

or in index notation

$$W,_k = \frac{\partial \tilde{W}}{\partial \varepsilon_{ij}} \varepsilon_{ij,k} + \frac{\partial \tilde{W}}{\partial x_k}\bigg|_{\text{expl.}} + \frac{\partial \tilde{W}}{\partial x_i^{\text{tip}}}(x_i^{\text{tip}}),_k . \tag{3.16}$$

With the use of Eq. (2.17), the symmetry of the Cauchy stress tensor, the symmetry of second derivatives and the product rule of differentiation, the first summand of Eq. (3.16) takes the form

$$\frac{\partial \tilde{W}}{\partial \varepsilon_{ij}} \varepsilon_{ij,k} = \sigma_{ij} u_{i,jk} = \sigma_{ij} u_{i,kj} = (\sigma_{ij} u_{i,k}),_j - \sigma_{ij,j} u_{i,k}. \tag{3.17}$$

Exchanging the stress divergence $\sigma_{ij,j}$ in Eq.(3.17) with volume loads using the local balance law (Eq. 2.13) and insertion of Eq. (3.17) into Eq. (3.16) leads to

$$W,_k = (\sigma_{ij} u_{i,k}),_j + f_i u_{i,k} + \frac{\partial \tilde{W}}{\partial x_k}\bigg|_{\text{expl.}} + \frac{\partial \tilde{W}}{\partial x_i^{\text{tip}}}(x_i^{\text{tip}}),_k . \tag{3.18}$$

Rearrangement yields

$$(W\delta_{jk} - \sigma_{ij}u_{i,k})_{,j} - f_i u_{i,k} - \left.\frac{\partial \tilde{W}}{\partial x_k}\right|_{\text{expl.}} - \frac{\partial \tilde{W}}{\partial x_i^{\text{tip}}}(x_i^{\text{tip}})_{,k} = 0, \tag{3.19}$$

where the term in brackets forms a second order tensor,

$$\Sigma_{kj} = W\delta_{jk} - \sigma_{ij}u_{i,k}, \tag{3.20}$$

commonly named Eshelby stress tensor, which already appeared in Eq. (3.14). The remaining terms of Eq. (3.19) form the so called configurational volume force

$$g_k = -f_i u_{i,k} - \left.\frac{\partial \tilde{W}}{\partial x_k}\right|_{\text{expl.}} - \frac{\partial \tilde{W}}{\partial x_i^{\text{tip}}}(x_i^{\text{tip}})_{,k} = g_k^{\text{vol}} + g_k^{\text{inhom}} + g_k^{\text{tip}}. \tag{3.21}$$

In analogy to the physical force balance (Eq. 2.13), the so called material or configurational force balance can now be deduced from Eq. (3.19) reading

$$\Sigma_{kj,j} + g_k = 0 \quad \text{or} \quad \text{div}\boldsymbol{\Sigma} + \boldsymbol{g} = \boldsymbol{0}. \tag{3.22}$$

Special attention is given to the summands of the configurational volume force. Here, the first term accounts for physical volume forces, the second term includes possible material inhomogeneities. Since the only inhomogeneities considered in the following are spatial dependencies of the stiffness tensor, g_k^{inhom} can be written as

$$g_k^{\text{inhom}} = -\left.\frac{\partial \tilde{W}}{\partial x_k}\right|_{\text{expl.}} = -\frac{1}{2}\varepsilon_{ij}\frac{\partial \mathbb{C}_{ijnm}}{\partial x_k}\varepsilon_{nm}. \tag{3.23}$$

The last contribution to Eq. (3.21) represents a volume force, concentrated at the crack tip.
The integral of g_k^{tip} over any control volume $\mathscr{P}$ including the crack tip but no further singular points yields the point force acting on the tip,

$$G_k^{\text{tip}} = \int_{\mathscr{P}} g_k^{\text{tip}} \mathrm{d}A = -\int_{\mathscr{P}} \frac{\partial \tilde{W}}{\partial x_i^{\text{tip}}}(x_i^{\text{tip}})_{,k} \, \mathrm{d}A. \tag{3.24}$$

Since a direct computation of Eq. (3.24) is rather complicated, Eqs. (3.21) and (3.22) are solved for g_k^{tip} reading

$$g_k^{\text{tip}} = -\Sigma_{kj,j} - g_k^{\text{vol}} - g_k^{\text{inhom}}. \tag{3.25}$$

Hence

$$G_k^{\text{tip}} = \int_{\mathscr{P}} \left(-\Sigma_{kj,j} + f_i u_{i,k} + \left.\frac{\partial \tilde{W}}{\partial x_k}\right|_{\text{expl.}} \right) \mathrm{d}A \tag{3.26}$$

provides a comfortable way for the evaluation of the configurational crack tip force, which can be embedded in commonly used numerical schemes for the solution of

the displacement field. In case of loaded crack faces, curved cracks or mixed mode loading, the region of integration $\mathscr{P}$ has either to be shrunk to the crack tip or a correction term including the crack face contributions has to be added. The latter leads to the form

$$G_k^{\text{tip}} = \int_{\mathscr{P}} \left(-\Sigma_{kj,j} + f_i u_{i,k} + \left.\frac{\partial \tilde{W}}{\partial x_k}\right|_{\text{expl.}} \right) \mathrm{d}A - \int_{\partial \mathscr{P}_{\text{face}}} \left(W n_k - t_i u_{i,k} \right) \mathrm{d}s \qquad (3.27)$$

for the computation of the configurational crack tip load.

The link to the previously introduced J-integral and energy release rate follows through the scalar multiplication of $\boldsymbol{G}^{\text{tip}}$ with the crack tangential vector $\boldsymbol{e}_x$ reading

$$J = - \boldsymbol{G}^{\text{tip}} \boldsymbol{e}_x. \qquad (3.28)$$

In comparison to the J-integral method, the configurational force approach for the evaluation of crack criticality strikes not only by the straightforward incorporation into finite element routines, but also by the adaptability to problems with body loads and inhomogeneous material constants. Furthermore, the use of configurational forces exceeds the application to fracture mechanical problems as the method is used for mesh refinement, motion of phase boundaries, as well as for the analysis of various types of inclusions and defects (Müller et al., 2002; Gross et al., 2003; Müller et al., 2004; Miehe et al., 2007) and can be expanded to diverse material laws and dynamical problems (Gurtin and Podio-Guidugli, 1996; Kolling and Müller, 2004).

3.3 Crack growth direction for mixed loading situations

So far, the cracks considered were aligned horizontally and a local crack tip coordinate system, with the crack normal and the crack tangential vector as basis, coincided with the illustrated x, y-coordinate system. In the following, cracks pointing in arbitrary directions under mixed mode loading will be considered. Therefore, a local crack tip coordinate system as illustrated in Fig. 3.8 with $\boldsymbol{e}_1$ pointing in the crack tangential direction and $\boldsymbol{e}_2$ pointing in the crack normal direction is introduced.

Concentrating on the superposition of mode I and mode II loading, a mixed mode fracture criterion follows Eq. 3.5.

Depending on the material and the microscopic failure mechanisms, a multitude of different functions $f(K_I, K_{II})$ exist to match experimental results. In addition, cracks can propagate at an angle θ to the tangential direction of the crack tip, in the following called crack deflection angle.

A popular principle for the evaluation of crack criticality under mixed loading is the criterion of maximum circumferential stress by Erdogan and Sih (1963). With the

circumferential stress given as

$$\sigma_\varphi = \frac{1}{4\sqrt{2\pi r_c}}\left[K_I\left(3\cos\frac{\varphi}{2}+\cos\frac{3\varphi}{2}\right)-K_{II}\left(3\sin\frac{\varphi}{2}+3\sin\frac{3\varphi}{2}\right)\right], \tag{3.29}$$

it postulates that the crack propagates in the direction θ such that σ_φ is maximized. Crack advance happens if $\sigma_{\varphi,\max}$ in a distance r_c from the crack tip equals the critical stress for mode I loading,

$$\sigma_{\varphi,\max}=\sigma_\varphi(\theta)=\frac{K_{Ic}}{\sqrt{2\pi r_c}}. \tag{3.30}$$

This results in the equations

$$K_I\sin\theta + K_{II}(3\cos\theta - 1) \;=\; 0 \tag{3.31}$$

$$K_I\left(3\cos\frac{\theta}{2}+\cos\frac{3\theta}{2}\right)-K_{II}\left(3\sin\frac{\theta}{2}+3\sin\frac{3\theta}{2}\right) \;=\; 4K_{Ic} \tag{3.32}$$

for the computation of θ and the subsequent evaluation whether the crack growths or not. Another principle by Sih (1973b), called *S*-criterion, motivates to use the strength S of the strain energy density $W(r,\varphi)$ for the computation of the crack angle θ and for the evaluation whether crack growth occurs. With

$$\begin{aligned}
S(\varphi) \;&=\; Wr = a_{11}K_I^2 + 2a_{12}K_IK_{II} + a_{22}K_{II}^2,\\
a_{12} \;&=\; (1+\cos\varphi)(\kappa-\cos\varphi)/(16\pi\mu),\\
a_{11} \;&=\; \sin\varphi(2\cos\varphi-\kappa+1)/(16\pi\mu),\\
a_{22} \;&=\; ((\kappa+1)(1-\cos\varphi)+(1+\cos\varphi)(3\cos\varphi-1))/(16\pi\mu),
\end{aligned}$$

and $\kappa = 3-4\nu$ in case of plane strain, the deflection angle θ is computed using the relations

$$\left.\frac{\mathrm{d}S}{\mathrm{d}\varphi}\right|_{\varphi=\theta}=0 \quad\text{and}\quad \left.\frac{\mathrm{d}^2S}{\mathrm{d}\varphi^2}\right|_{\varphi=\theta}>0. \tag{3.33}$$

Further methods use the direction of the maximum energy release rate (Cotterell, 1965; Hussain et al., 1974; Ichikawa and Tanaka, 1982; Lo, 1978; Nuismer, 1975) or the maximum dissipated energy (Gurtin and Podio-Guidugli, 1998). A comparative overview of the different approaches can be found in Richard et al. (2005).

An alternative technique for the evaluation of the crack path under mixed mode loading follows by the use of the direction of the generalized J-integral vector, which can be deduced from the components of the configurational force vector $\boldsymbol{G}^{\mathrm{tip}}$. The crack deflection angle can then be computed using $\theta_J = \arctan\frac{J_2}{J_1}$. A popular benchmark example for mixed mode loading with known analytic solution is the straight crack in an infinite domain under mixed loading. Figure 3.5 a) illustrates the loading conditions and resulting analytic stress intensity factors. With $\sigma = k\cdot\tau$ and hence $K_I = k\cdot K_{II}$, the components of the J-integral vector, J_1 and J_2, follow using

Eqs. (3.15) and read

$$J_1 = \frac{(k^2+1)(1-\nu^2)}{E}\sigma^2\pi a \quad \text{and} \quad J_2 = \frac{k(1-\nu^2)}{E}\sigma^2\pi a \tag{3.34}$$

in case of plane strain. Figure 3.8 compares the crack deflection angles resulting from the circumferential stress criterion, as well as the S-criterion with the one resulting from the direction of J for different values of k. It shows, that for $K_I/K_{II} > 2$ the three criteria match very well. For $K_I/K_{II} < 1$ the direction of J is not suitable as indicator crack deflection. However, benchmark examples in Sec. 4.6.5 show, that a step-wise computation of J with consequent crack growth by small increments in the direction of J leads to an overall crack growth direction that coincides with the deflection angle computed according to Eq. (3.32) after very few steps.
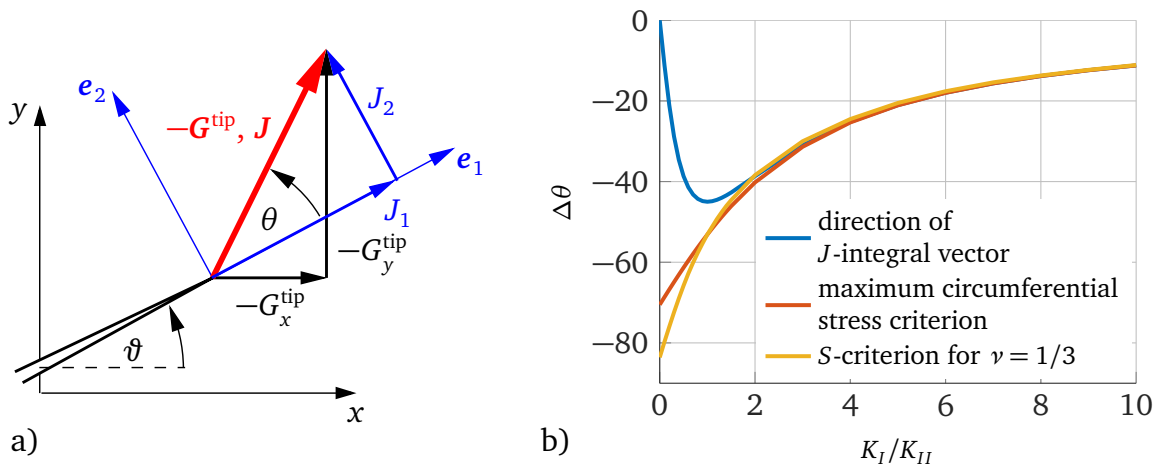

Figure 3.8: a) Global $x-y$-coordinate system and local crack tip coordinate system (e_1, e_2), distinction between G_x^{tip} and G_y^{tip}, as well as J_1 and J_2; b) crack deflection angle θ for straight crack in an infinite domain under mixed mode loading using different criteria

4 Finite element implementation

The linear elastic boundary value problem is solved using the commercial finite element code COMSOL. The nodal displacements and the mesh are exported to MATLAB, where the evaluation of the configurational forces follows in postprocessing routines. Information on changes of the geometry due to crack growth is then given back to COMSOL, where the new problem is solved. To facilitate automatic remeshing by the COMSOL mesh generator independent of the complexity of the ice shelf geometries, triangular elements are used. For brevity, the following summary is constricted to the implementation of discrete configurational forces. Details on the implementation of the elastic boundary value problem can be found in various textbooks as e.g. Wriggers (2008), Zienkiewicz and Taylor (2000) or Hughes (2000).

4.1 Weak form

For simplicity, the following derivations are performed in index notation where in the 3D case the indices j and k run from 1 to 3. The basis for the computation of discrete configurational forces is the weak form of the configurational force balance. Therefore, Eq. (3.22) is multiplied with an arbitrary vectorial virtual test function μ_k. Integration over the domain Ω leads to

$$\int_\Omega \left(\Sigma_{jk,j} + g_k\right)\mu_k \, \mathrm{d}V = \int_\Omega \left(\Sigma_{jk,j}\mu_k + g_k\mu_k\right)\mathrm{d}V = 0 \quad \forall \mu_k. \tag{4.1}$$

Application of the product rule of differentiation to the first summand in Eq. 4.1 yields

$$\Sigma_{jk,j}\mu_k = \left(\Sigma_{jk}\mu_k\right)_{,j} - \Sigma_{jk}\mu_{k,j}. \tag{4.2}$$

Insertion of Eq. (4.2) into Eq. (4.1) and application of the Gaußian theorem yields

$$\int_\Omega \left[\left(\Sigma_{jk}\mu_k\right)_{,j} - \Sigma_{jk}\mu_{k,j} + g_k\mu_k\right]\mathrm{d}V = \int_{\partial\Omega} \Sigma_{jk}\mu_k n_j \mathrm{d}A - \int_\Omega \left(\Sigma_{jk}\mu_{k,j} - g_k\mu_k\right)\mathrm{d}V = 0. \tag{4.3}$$

Most literature on the implementation of configurational forces uses virtual test functions that vanish on the complete boundary $\partial\Omega$. In order to consider loaded crack faces and mixed mode loading, the present formulation splits $\partial\Omega$ into an area with prescribed displacements $\partial\Omega_u$ and an area with prescribed stresses $\partial\Omega_t$.

Only on $\partial\Omega_u$, the test functions vanish. The right hand side of Eq. (4.3) can be transformed to

$$\int\limits_{\partial\Omega_t}(W\delta_{jk}-\sigma_{ij}u_{i,k})n_j\mu_k\,\mathrm{d}A-\int\limits_\Omega\left(\Sigma_{jk}\mu_{k,j}-g_k\mu_k\right)\mathrm{d}V\ =\ 0, \tag{4.4}$$

$$\int\limits_{\partial\Omega_t}Wn_k\mu_k\,\mathrm{d}A-\int\limits_{\partial\Omega_t}t_i^*u_{i,k}\mu_k\,\mathrm{d}A-\int\limits_\Omega\left(\Sigma_{jk}\mu_{k,j}-g_k\mu_k\right)\mathrm{d}V\ =\ 0\quad\forall\mu_k. \tag{4.5}$$

4.2 Discretization

The evaluation of discrete configurational forces is implemented for 2D geometries. The lower case indices, referring to the component of a variable, now run from 1 to 2 whereas capital indices refer to the global or local node number. In addition, the integration with respect to the volume $\mathrm{d}V$ reduces to an integration over the area $\mathrm{d}A$ and the integration over area elements in 3D reduces to an integration along line elements $\mathrm{d}s$. Within the framework of the FE method, the virtual test functions and their gradients can be approximated using the interpolations

$$\mu_k\approx\mu_k^h=\sum_{I=1}^N\mu_k^IN^I\quad\text{and}\quad\mu_{k,j}^h=\sum_{I=1}^N\mu_k^IN_{,j}^I \tag{4.6}$$

with the scalar shape functions N^I and the nodal values μ_k^I. The summation is performed for all N nodes of the FE mesh. Here and in the following, the superscript h is used to identify approximated quantities. Insertion of Eq. (4.6) into Eq. (4.5) and exchanging summation and integration yields

$$\sum_{I=1}^N\int\limits_{\partial\Omega_t}\left(Wn_k-u_{i,k}t_i^*\right)\mu_k^IN^I\,\mathrm{d}s-\sum_{I=1}^M\int\limits_\Omega\left(\Sigma_{jk}\mu_k^IN_{,j}^I-g_k\mu_k^IN^I\right)\mathrm{d}A\ =\ 0$$

$$\sum_{I=1}^N\mu_k^I\left(\int\limits_{\partial\Omega_t}\left(Wn_k-u_{i,k}t_i^*\right)N^I\,\mathrm{d}s-\int\limits_\Omega\left(\Sigma_{jk}N_{,j}^I-g_kN^I\right)\mathrm{d}A\right)\ =\ 0\quad\forall\mu_k^I,$$

exploiting the independence of the nodal values of the test functions μ_k^I of the spatial coordinates x and y. Arbitrariness of the nodal values μ_k^I of the virtual test functions leads to the discretized form of the configurational force balance,

$$\int\limits_{\partial\Omega_t}\left(Wn_k-u_{i,k}t_i^*\right)N^I\,\mathrm{d}s-\int\limits_\Omega\left(\Sigma_{jk}N_{,j}^I-g_kN^I\right)\mathrm{d}A=0.$$

Substitution of the configurational volume force with its components in Equ. (3.21) and solution for the crack tip force yields

$$
\begin{aligned}
G_k^{I,\text{tip}} &= \int_\Omega g_k^{\text{tip}} N^I \mathrm{d}A \\
&= \int_\Omega \left(\Sigma_{jk} N_{,j}^I - g_k^{\text{vol}} N^I - g_k^{\text{inhom}} N^I \right) \mathrm{d}A - \int_{\partial\Omega_t} \left(W n_k - u_{i,k} t_i^* \right) N^I \mathrm{d}s. \quad (4.7)
\end{aligned}
$$

The vector $\underline{G}_k^{\text{tip}}$ comprises the crack tip contribution to the configurational force for every node in the FE mesh. It is obvious that only for crack tip nodes or nodes in the proximity of crack tips the force can be interpreted as discrete crack driving force. For all other nodes in the bulk, $\underline{G}_k^{\text{tip}}$ is a measure for the inhomogeneity introduced by the discretization and should be very small compared to the result at the crack tip. Values for $\underline{G}_k^{\text{tip}}$ of intermediate amount can be found at boundary nodes, as boundaries represent a strong discontinuity in the system. However, these configurational boundary forces are considerably smaller than those at the tip of a loaded crack.

Exploiting the benefits of the isoparametric concept, the test functions, the displacement field and the global coordinates are approximated by the same element shape functions N^I, defined within the element e, and the element nodal values μ_k^I, u_k^I
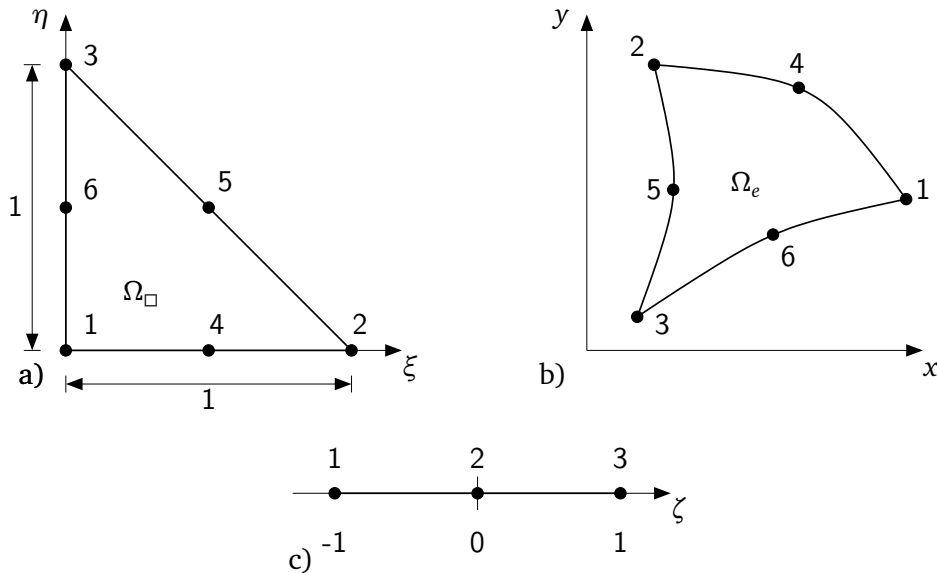

Figure 4.1: a) Isoparametric 2D reference element with local coordinates ξ and η; b) deformed 2D element with global coordinates, c) 1D reference line/edge element with the local coordinate ζ

and x_k^I. The approximations read

$$\mu_k \approx \mu_k^h = \sum_{I=1}^{M} \mu_k^I N^I, \qquad u_k \approx u_k^h = \sum_{I=1}^{M} u_k^I N^I \quad \text{and} \quad x_k \approx x_k^h = \sum_{I=1}^{M} x_k^I N^I, \qquad (4.8)$$

where M indicates the number of nodes per element.

Following the notation in Wriggers (2008), isoparametric quadratic shape functions N^I for triangular elements as depicted in Fig. 4.1 a) and b) are defined as

$$\begin{aligned} N^1 &= \lambda(2\lambda - 1) & N^4 &= 4\xi\lambda \\ N^2 &= \xi(2\xi - 1) & N^5 &= 4\xi\eta \\ N^3 &= \eta(2\eta - 1) & N^6 &= 4\eta\lambda \end{aligned} \qquad (4.9)$$

using the local coordinates ξ, η and $\lambda = 1 - \xi - \eta$. The relation between points on the edges of the 2D reference element in $\xi - \eta$-coordinates and the reference line element as shown in Fig. 4.1 c) follows in a similar manner,

$$\xi \approx \xi^h = \sum_{I=1}^{P} \xi^I \tilde{N}^I \quad \text{and} \quad \eta \approx \eta^h = \sum_{I=1}^{P} \eta^I \tilde{N}^I \qquad (4.10)$$

with the quadratic shape functions

$$\tilde{N}^1 = \frac{1}{2}(\zeta - 1)\zeta, \quad \tilde{N}^2 = 1 - \zeta^2 \quad \text{and} \quad \tilde{N}^3 = \frac{1}{2}(\zeta + 1)\zeta. \qquad (4.11)$$

The derivatives of N^I with respect to the global coordinates x and y follow using chain rule differentiation for the derivatives of N^I with respect to the local coordinates ξ and η,

$$\begin{aligned} \frac{\partial N^I(\xi,\eta)}{\partial \xi} &= \frac{\partial N^I(\xi,\eta)}{\partial x}\frac{\partial x}{\partial \xi} + \frac{\partial N^I(\xi,\eta)}{\partial y}\frac{\partial y}{\partial \xi} \\ \frac{\partial N^I(\xi,\eta)}{\partial \eta} &= \frac{\partial N^I(\xi,\eta)}{\partial x}\frac{\partial x}{\partial \eta} + \frac{\partial N^I(\xi,\eta)}{\partial y}\frac{\partial y}{\partial \eta}, \end{aligned}$$

or short

$$\begin{bmatrix} N_{,\xi}^I \\ N_{,\eta}^I \end{bmatrix} = \underbrace{\begin{bmatrix} x_{,\xi} & y_{,\xi} \\ x_{,\eta} & y_{,\eta} \end{bmatrix}}_{\boldsymbol{J}_e} \begin{bmatrix} N_{,x}^I \\ N_{,y}^I \end{bmatrix}. \qquad (4.12)$$

The derivatives in $\boldsymbol{J}_e$ are computed by use of the isoparametric approximation of the global coordinates,

$$x_{k,j} \approx x_{k,j}^h = \sum_{I=1}^{M} x_k^I N_{,j}^I. \qquad (4.13)$$

Solving Eq. (4.12) for the unknown $N^I_{,\boldsymbol{x}}$ yields

$$\begin{bmatrix} N^I_{,x} \\ N^I_{,y} \end{bmatrix} = \frac{1}{\det \boldsymbol{J}_e} \begin{bmatrix} y_{,\eta} & -y_{,\xi} \\ -x_{,\eta} & x_{,\xi} \end{bmatrix} \begin{bmatrix} N^I_{,\xi} \\ N^I_{,\eta} \end{bmatrix}. \tag{4.14}$$

Using Eq. (4.14), the gradient of u_k can be approximated by

$$u^h_{k,j} = \sum_{I=1}^{M} u^I_k N^I_{,j}. \tag{4.15}$$

This leads to the approximate expression for the linearized strain tensor,

$$\varepsilon^h_{kj} = \frac{1}{2} \sum_{I=1}^{M} \left(u^I_k N^I_{,j} + u^I_j N^I_{,k} \right), \tag{4.16}$$

which is necessary for the computation of the Cauchy stress tensor, the strain energy, and the Eshelby stress tensor as defined in Eqs. (2.15), (2.16) and (3.20).
Insertion of Eqs. (4.15) and (4.16) into Eq. (4.7) and separation of the individual summands yields the element contributions to the nodal configurational crack tip force

$$G^{I,\text{elast}}_{k,e} = \int_{\Omega_e} \Sigma^h_{jk} N^I_{,j} \, \mathrm{d}A \tag{4.17}$$

$$G^{I,\text{vol}}_{k,e} = -\int_{\Omega_e} g^{\text{vol}}_k N^I \, \mathrm{d}A = \int_{\Omega_e} f_i u^h_{i,k} N^I \, \mathrm{d}A, \tag{4.18}$$

$$G^{I,\text{inhom}}_{k,e} = -\int_{\Omega_e} g^{\text{inhom}}_k N^I \, \mathrm{d}A = \int_{\Omega_e} \frac{1}{2} \varepsilon^h_{ij} \frac{\partial \mathbb{C}_{ijnm}}{\partial x_k} \varepsilon^h_{nm} N^I \, \mathrm{d}A, \tag{4.19}$$

and

$$G^{I,\text{boun}}_{k,e} = -\int_{\partial \Omega_t} \left(W^h n_k - u^h_{i,k} t^*_i \right) N^I \, \mathrm{d}s, \tag{4.20}$$

hence

$$G^{I,\text{tip}}_{k,e} = G^{I,\text{elast}}_{k,e} + G^{I,\text{vol}}_{k,e} + G^{I,\text{inhom}}_{k,e} + G^{I,\text{boun}}_{k,e}. \tag{4.21}$$

It should to be noted that Eq. (4.20) is only computed for element edges along the crack face. The contribution of the boundary stress is evaluated by using the applied stress $\boldsymbol{t}^*$, not the resulting stress $\boldsymbol{t} = \boldsymbol{\sigma} \boldsymbol{n}$.
The crack tip load of a six-node element e with the nodes $I = 1,\ldots,6$ is formed by the shares of the respective element nodes,

$$\underline{\mathbf{G}}^{\text{tip}}_{k,e} = \begin{bmatrix} G^{1,\text{tip}}_{k,e} & G^{2,\text{tip}}_{k,e} & G^{3,\text{tip}}_{k,e} & G^{4,\text{tip}}_{k,e} & G^{5,\text{tip}}_{k,e} & G^{6,\text{tip}}_{k,e} \end{bmatrix}^T. \tag{4.22}$$

The assembly $\bigcup$ of all n_e elements leads to

$$\underline{G}_k^{\text{tip}} = \bigcup_{e=1}^{n_e} \underline{G}_{k,e}^{\text{tip}} = \begin{bmatrix} G_k^{1,\text{tip}} & G_k^{2,\text{tip}} & \cdots & G_k^{N,\text{tip}} \end{bmatrix}^T, \tag{4.23}$$

the global discrete crack tip force, with n_e being the total number of elements. Herein, the global crack tip force of a specific node I is formed by summation of the corresponding element nodal forces of elements adjacent to the node I.

4.3 Gauß quadrature

The integrals in Eq. (4.19) of the form

$$\int_{\Omega_e} f(x,y)\,\mathrm{d}A \quad \text{and} \quad \int_{\partial\Omega_e} f(x,y)\,\mathrm{d}s$$

will be approximated using a Gaußian quadrature scheme where the integration points, also called Gauß points, and weights are given for the reference elements in Fig. 4.1 a) and c), respectively. The evaluation of Eqs. (4.19) on the 2D reference element necessitates a coordinate transformation reading

$$\int_{\Omega_e} f(x,y)\mathrm{d}A = \int_0^1 \int_0^{1-\xi} \tilde{f}(\xi,\eta)\det\mathbf{J}_e\mathrm{d}\xi\mathrm{d}\eta \tag{4.24}$$

with $\mathbf{J}_e$ being the Jacobian as introduced in Eq. (4.12). The transformed integral is approximated by

$$\int_0^1 \int_0^{1-\xi} f(\xi,\eta)\det\mathbf{J}_e\mathrm{d}\xi\mathrm{d}\eta \approx \sum_{p=1}^{n_{\text{int}}} f(\xi_p,\eta_p)\det\mathbf{J}_e(\xi_p,\eta_p)w_p \tag{4.25}$$

with ξ_p, η_p and w_p being the coordinates of the Gauß points and the weights, respectively. The following simulations use triangular elements with three internal Gauß points. The corresponding coordinates and weights for the reference element in Fig. 4.2 a) take the values given in Fig. 4.2 b). This approximation enables an exact integration of polynomials $\xi^q\eta^r$ with $q+r \leq 2$.

The domain edge integral is transformed and approximated reading

$$\int_{\partial\Omega_e} f(x,y)\,\mathrm{d}s = \int_{-1}^1 f\left(\xi(\zeta),\eta(\zeta)\right)\frac{l}{2}\mathrm{d}\zeta \approx \sum_{p=1}^{n_{\text{int}}} f\left(\xi(\zeta_p),\eta(\zeta_p)\right)\frac{l}{2}w_p \tag{4.26}$$

p	ξ_p	η_p	w_p
1	1/6	1/6	1/6
2	2/3	1/6	1/6
3	1/6	2/3	1/6.

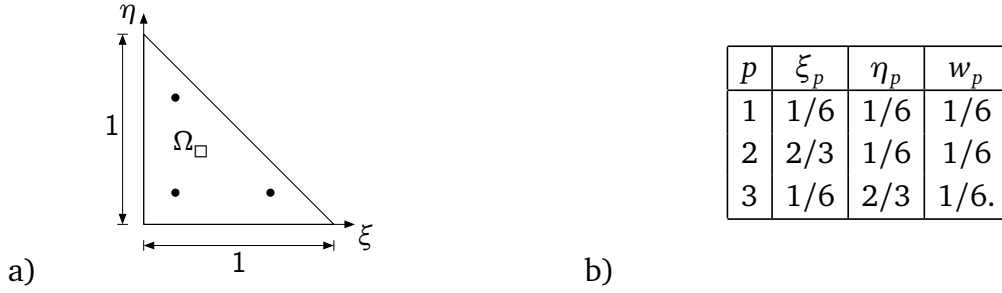a)   b)

Figure 4.2: a) Location of Gauß points in isoparametric reference element; b) associated Gauß point coordinates and weights

with the length of the edge element l. For the computation of the integral, two Gauß points are needed. The corresponding coordinates and weights for the reference element in Fig. 4.1 c) are

p	ζ_p	w_p
1	$-1/\sqrt{3}$	1
2	$1/\sqrt{3}$	1

enabling an exact integration of polynomials ζ^q with $q \leq 3$.

4.4 Evaluation of a resulting configurational crack tip force

Triangular elements with quadratic shape functions are not able to fully represent the singular stress field at the crack tip. Hence, the computation of the configurational crack tip force by only taking into account the crack tip node underestimates the correct solution, despite any kind of mesh refinement. Denzer et al. (2003) motivate the summation of the discrete configurational crack tip contributions within a small region, called influence area, enclosing the crack tip to considerably emend the outcome of the computation. The area can be defined in a geometric sense, e.g. comprising all nodes inside a circle of radius r_i around the crack tip, or, as presented here, by hierarchical considerations, following the original approach by Denzer et al. (2003). Figure 4.3 shows the hierarchical levels used to compute the crack tip configurational force. The index $m = 1$ indicates that the nodes in the elements adjacent to the crack tip (yellow area) are summed to compute the crack tip contribution. The next level, $m = 2$, sums the nodes of elements in the yellow and in the orange area. Level three appends the nodes in the red area and so on. If $m = 0$ only the configurational force at the crack tip node (green dot) is considered. The equation for the computation of the resulting configurational crack tip load therefore reads

$$G_k^{\text{tip}} = \sum_{i=1}^{m} \bigcup_{e=1}^{n_i} \underline{G}_{k,e}^{\text{tip}}. \tag{4.27}$$
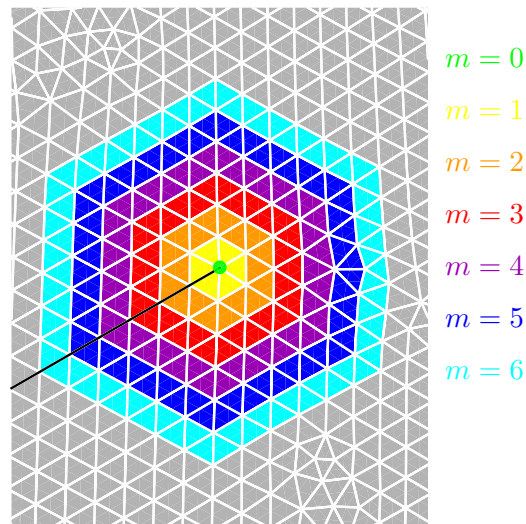
Figure 4.3: Summation levels for the computation of the crack tip configurational force

Denzer et al. (2003) only consider mode I loading and exclude the discussion about the path dependence of J_2. The here presented evaluation of J_1 and J_2 includes the crack surface contributions and therefore allows using resulting configurational forces also for the computation of J_2 in cases of mixed mode loading. The only restriction to the influence area is that it must not include further inhomogeneities as could be kinks in the crack faces or external boundaries. Inhomogeneous but smoothly varying material parameters are allowed due to the comprehension of spatially dependent material parameters in Eq. (4.19). The convergence of J_1 and J_2 or G_x^{tip} and G_y^{tip} with respect to growing level index m is shown in the benchmark examples following Sec. 4.5.

4.5 Crack propagation algorithm for mixed mode loading

Several publications describe the use of configurational forces for crack path prediction. A first qualitative result for a linear elastic material is shown by Müller and Maugin (2002), where the reverse direction of the configurational crack tip force at the crack tip node is used as indicator for the direction of crack propagation. The onset is set by a constant factor. Miehe and Gürses (2007) and Miehe et al. (2007) show a configurational force based crack growth implementation with a r-adaptive crack segment reorientation scheme. For this approach the initial mesh has to be sufficiently fine within the expected crack propagation area since no new elements are added at the new crack tip. The method is implemented for geometric linear and non-linear elasticity and compared to standard benchmark tests for

mixed mode loading, showing good results for fine meshes. Since the nodal configurational force at the crack tip shows rather unstable deflections, the application of an resultant configurational force as sum over all nodal configurational forces within an influence domain of radius r_i around the crack tip following Denzer et al. (2003) is discussed. The resulting configurational force is compared to the nodal crack tip force for mode I load cases. Zimmermann (2008) connects a configurational force driven crack propagation scheme to h-adaptive mesh refinement techniques. Again, the crack tip propagation follows the direction of a resulting configurational force based on an influence domain around the crack tip. No limitations are made to the integration domain with regard to mixed mode loading cases and the consequent path dependence of J_2. The hitherto presented methods use constant crack propagation increments. In order to be able to reproduce benchmark examples, these increments have to be very small. Hence, many increments are needed to form a complete crack path. Schütte (2009) and Schütte (2010) demonstrate an innovative predictor corrector scheme based on configurational forces together with spline type increments for crack propagation of curved cracks. This allows using larger crack growth increments and therefore less propagation steps. For the computation of the crack normal configurational force J_2, the use of an influence domain is investigated. Schütte (2009) further analyzes the trend of $J_2(r_i)$ and motivates an extrapolation scheme of $J_2(r_i > 0)$ towards $r_i = 0$ resulting in a sufficiently accurate limit value for $J_2(r_i = 0)$. The resulting crack path is compared to the popular benchmark example of Bittencourt et al. (1996).

The here presented implementation of the crack propagation algorithm follows the flowchart sketched in Fig. 4.4 and is similar to the algorithm proposed by Zimmermann (2008). Parameters to be set are the maximum element length at the crack tip, Δx_{el}, the radius of the influence area r_i, the threshold $\mathcal{G}_c$ and the crack propagation parameters $\Delta \lambda_t$ and $\Delta \lambda_n$. Zimmermann (2008) chooses a constant value $1/2 \Delta \lambda_t = \Delta \lambda_n = 0.025 h_{\mathrm{max}}$ with h_{max} being the maximum element edge length of the mesh. However, this results in a rather inadequate local crack opening angle at the tip and might cause incorrect values of $\underline{G}^{\mathrm{tip}}$. The algorithm in Fig. 4.4 sets $\Delta \lambda_t$ depending on the change of the crack direction $\Delta \theta$ in the form

$$\Delta \lambda_t = \begin{cases} \Delta \lambda_{\mathrm{max}}, & \text{if} \quad \Delta \theta < \theta_1 \\ a_1 \Delta \lambda_{\mathrm{max}}, & \text{if} \quad \theta_1 \leq \Delta \theta < \theta_2 \\ \dots \\ a_n \Delta \lambda_{\mathrm{max}}, & \text{if} \quad \Delta \theta \geq \theta_n. \end{cases} \tag{4.28}$$

The number of differentiations, the constants a_1 to a_n and the limit angles θ_1 to θ_n have to be chosen with respect to the simulated problem. The constant crack width is $2\Delta \lambda_n$ with $\Delta \lambda_n = \frac{1}{25} \min(\Delta \lambda_t) = \frac{1}{400} \Delta \lambda_{\mathrm{max}}$. The parameter $\Delta \lambda_{\mathrm{max}}$ has to be set with respect to the characteristic length scales of the problem, accounting for the geometry a well as inhomogeneities. In the finite element program COMSOL, the maximum element edge length along the crack faces is bound by the distance be-

set up geometry with initial crack
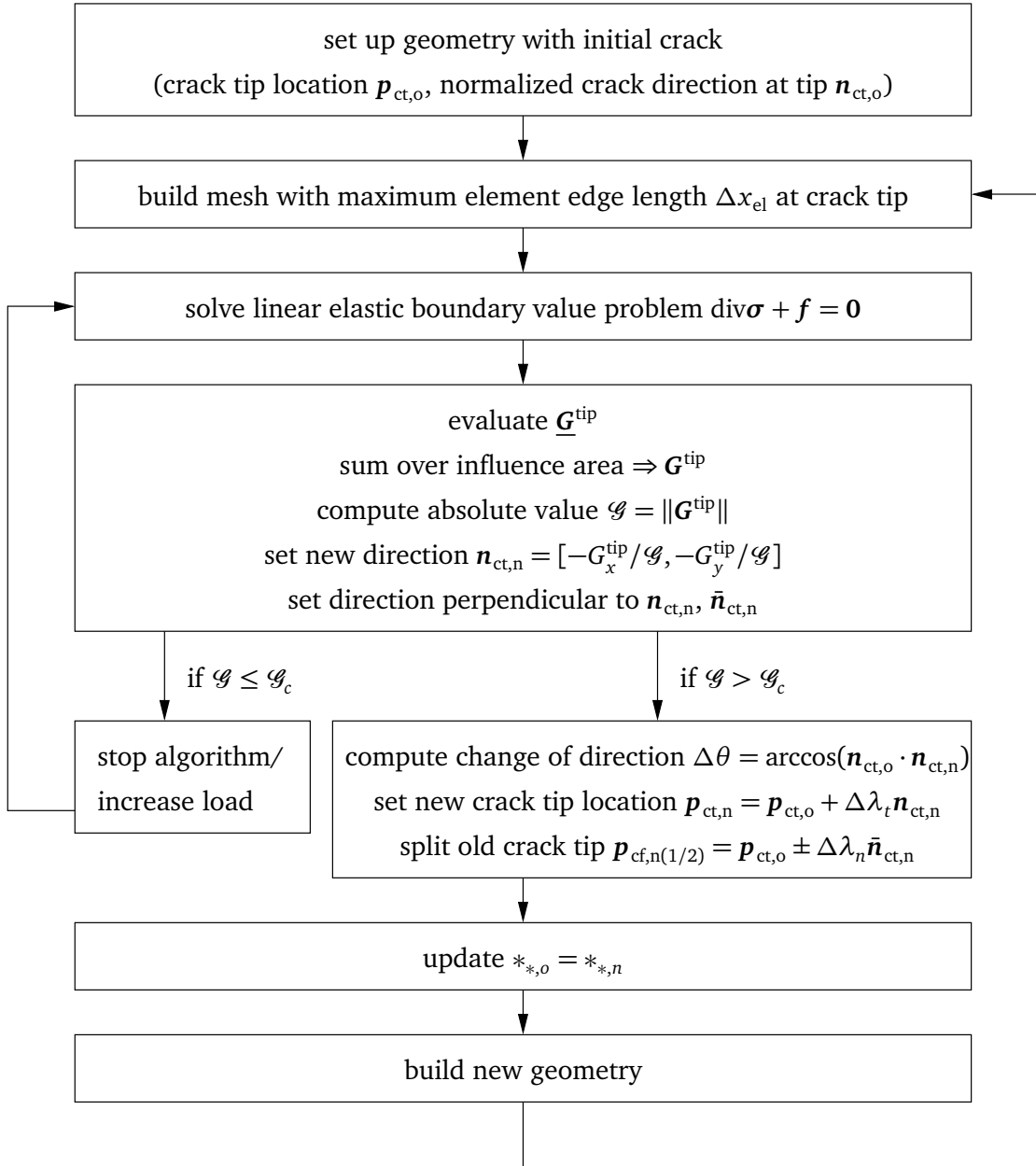
(crack tip location $\boldsymbol{p}_{\mathrm{ct,o}}$, normalized crack direction at tip $\boldsymbol{n}_{\mathrm{ct,o}}$)

build mesh with maximum element edge length Δx_{el} at crack tip

solve linear elastic boundary value problem $\mathrm{div}\boldsymbol{\sigma} + \boldsymbol{f} = \mathbf{0}$

evaluate $\underline{\boldsymbol{G}}^{\mathrm{tip}}$

sum over influence area $\Rightarrow \boldsymbol{G}^{\mathrm{tip}}$

compute absolute value $\mathscr{G} = \|\boldsymbol{G}^{\mathrm{tip}}\|$

set new direction $\boldsymbol{n}_{\mathrm{ct,n}} = [-G_x^{\mathrm{tip}}/\mathscr{G}, -G_y^{\mathrm{tip}}/\mathscr{G}]$

set direction perpendicular to $\boldsymbol{n}_{\mathrm{ct,n}}$, $\bar{\boldsymbol{n}}_{\mathrm{ct,n}}$

if $\mathscr{G} \leq \mathscr{G}_c$

if $\mathscr{G} > \mathscr{G}_c$

stop algorithm/ increase load

compute change of direction $\Delta\theta = \arccos(\boldsymbol{n}_{\mathrm{ct,o}} \cdot \boldsymbol{n}_{\mathrm{ct,n}})$

set new crack tip location $\boldsymbol{p}_{\mathrm{ct,n}} = \boldsymbol{p}_{\mathrm{ct,o}} + \Delta\lambda_t \boldsymbol{n}_{\mathrm{ct,n}}$

split old crack tip $\boldsymbol{p}_{\mathrm{cf,n(1/2)}} = \boldsymbol{p}_{\mathrm{ct,o}} \pm \Delta\lambda_n \bar{\boldsymbol{n}}_{\mathrm{ct,n}}$

update $*_{*,o} = *_{*,n}$

build new geometry

Figure 4.4: Flowchart of propagation algorithm for a single crack in a 2D setup

tween points on the polygon that defines the crack. Large deflection angles result in small crack growth increments and hence fine meshes that remain even if the crack tip has propagated several further steps. Zimmermann (2008) introduces an algorithm, which deletes old crack face nodes if the length of crack face segments falls below a certain threshold. The here presented algorithm also aims to reduce the overall number of elements by deleting polygon points along the crack face. The decision whether points are deleted or not however depends on the actual deflection angle and the change of the deflection angle compared to the previous step. The
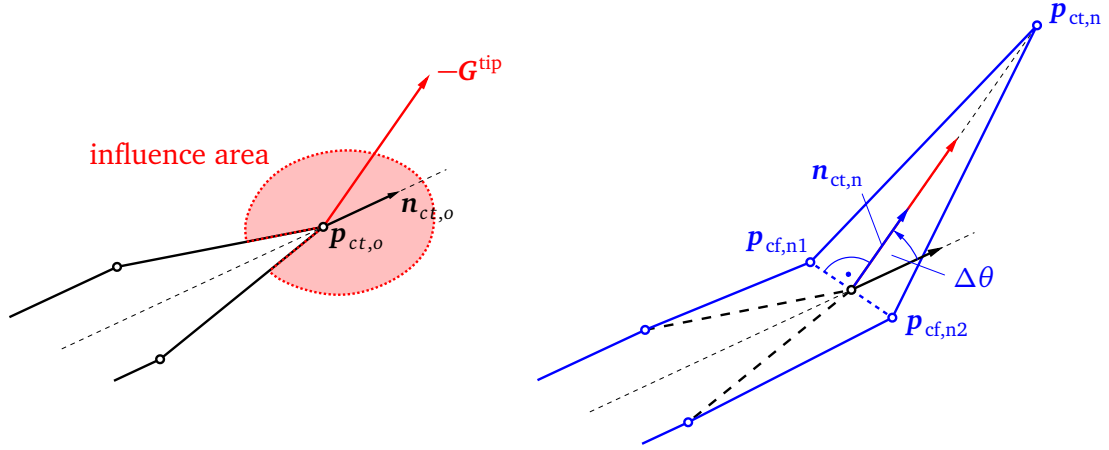
Figure 4.5: Update of crack geometry with left, the old crack tip (subscript o) with the resulting configurational crack tip force and right, the new inserted crack tip and the doubling of the old crack tip node into two new crack face nodes (subscript n)

pseudo code of the algorithm reads

$$
\begin{array}{llll}
\text{if} \quad \Delta\theta^i < 2° \quad \text{AND} \quad \Delta\theta^{i-1} > 2° & \Rightarrow & \text{delete} & p_{cf,n}^{i-1} \\
\text{else} & \Rightarrow & \text{keep} & p_{cf,n}^{i-1}
\end{array}
$$

with the superscript i indicating the actual step and $i-1$ the previous step. This results in a considerably reduced number of elements after several crack growth increments in comparison to a propagation simulation without crack face point removal. Since strongly curved parts of the crack with successive small increments remain untouched by the algorithm, changes in the overall crack path are negligibly small.

4.6 Benchmarks

4.6.1 Benchmark a: mesh characteristics and size

The appropriate mesh size with respect to the size of the geometry is evaluated by comparing the simulation results for a standard single edge notch tension test with results from Tada et al. (1973). Figure 4.6 shows the model geometry with the applied boundary conditions. The variables a, b and L denote the crack depth, the thickness of the specimen and its length, respectively. The model is loaded by a uniform tensile stress σ at the vertical boundary. For symmetric geometries and loads it suffices to simulate only one part and apply symmetry boundary conditions along the line of symmetry, visualized by the dashed line. Special attention is needed for the computation of the discrete configurational forces for nodes along the line of symmetry. Here, the components of the discrete configurational force in the direction of the dashed line have to be doubled, those perpendicular to the
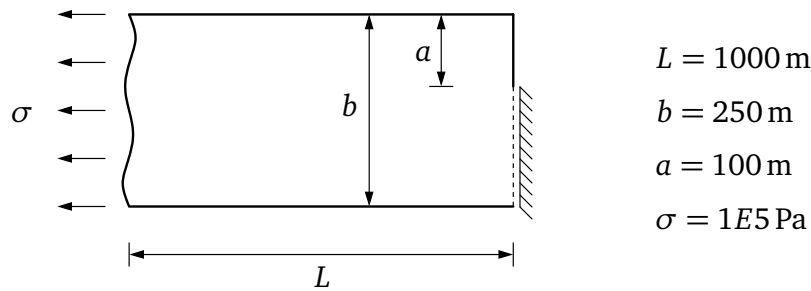
4 Finite element implementation

Figure 4.6: Model geometry for single edge notch tension test

$L = 1000\,\mathrm{m}$

$b = 250\,\mathrm{m}$

$a = 100\,\mathrm{m}$

$\sigma = 1E5\,\mathrm{Pa}$

dashed line have to be erased. This correction results from the missing assembly of the symmetric counterpart. Figure 4.7 shows different meshing strategies for the crack tip region. The mesh in Fig. 4.7 a) is built by placing squares over and under the crack tip (indicated by the red dot). Then these squares are meshed using quadrilateral elements and a defined number of elements n per square edge. In a next step the quadrilateral elements are split yielding the required triangular mesh inside the squares. The remaining geometry is freely meshed with triangular elements. The mesh in Fig. 4.7 b) differs from the one in a) by the orientation of the inserted triangles. For the mesh in Fig. 4.7 c), the quadrilateral mesh is split by two diagonals. The mesh in Fig. 4.7 d) uses a defined maximum element edge length Δx at the crack tip. This is induced by placing an additional point, indicated by the black dot, at the desired distance from the crack tip.

Figures 4.8 b) and c) show resulting stress intensity factors relative to the semi-analytical result of Tada et al. (1973) for different mesh refinements (parameter n), mesh types (line style) and summation levels (line color) for the problem as depicted in Fig. 4.6. Tada et al. (1973) presents several formulas with differing accuracy for the computation of the stress intensity factors K_I for the single edge notch tension test. The formula used as reference for the mesh size evaluation (Fig. 3.5 b) has an accuracy $> 0.5\%$ for any value of a/b and $L/b > 1$. Figures 4.8 b) and c) show converging results for finer discretizations for all mesh cases as well as summation levels. Crack tip meshes based on the mapped mesh show a smoother
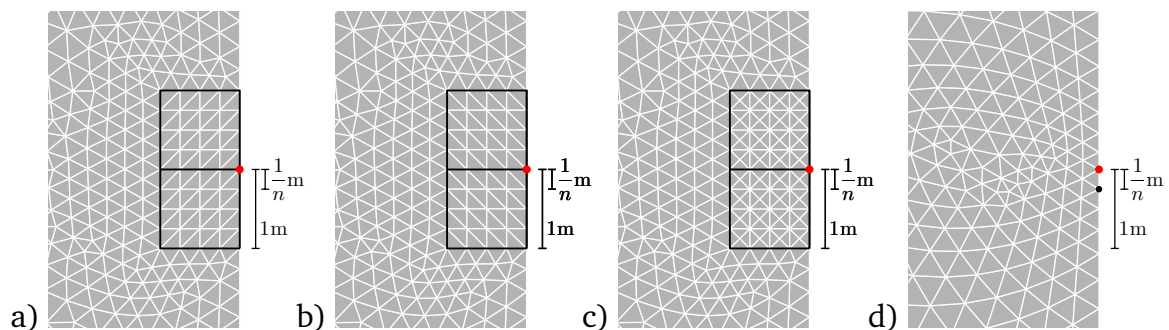

Figure 4.7: a) Mapped mesh with standard diagonal; b) mapped mesh with switched diagonal; c) mapped mesh with two diagonals; d) free mesh with additional point to define mesh size at crack tip
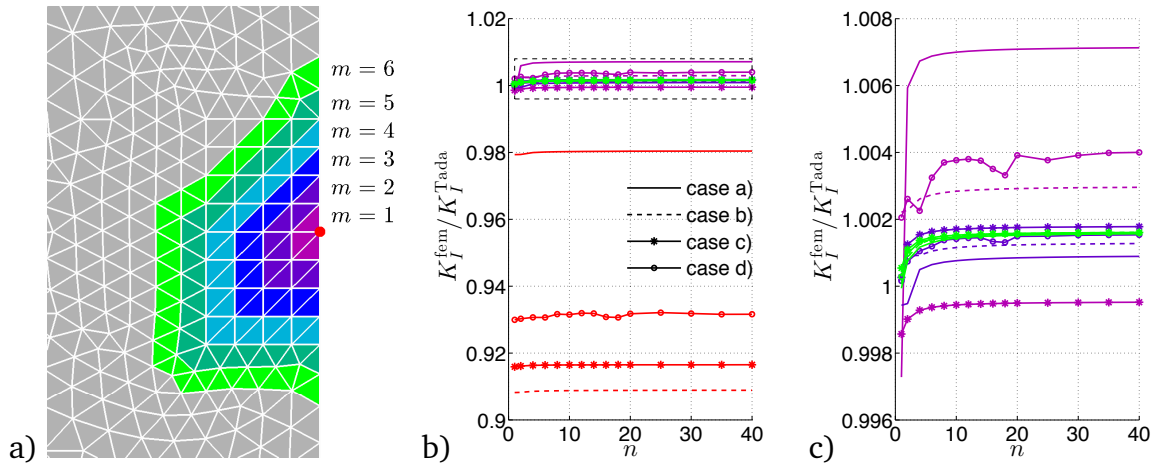
Figure 4.8: a) Summation levels for the computation of the crack tip configurational force; b) relative stress intensity factors for different mesh types, discretizations and summation levels; c) zoom into dashed box in b)

performance than the free triangular mesh, constrained by the additional point. An even stronger influence on the accuracy of the computed stress intensity factors results from the different summation levels. Whereas the computations without summation yield two to three percent deviation at their best and nine percent deviation for the most unfavorable mesh type, the inclusion of only one summation level yields less than one percent deviation for all mesh types and refinements. For six summation levels (green lines), the difference between the mesh cases is negligibly small. Furthermore, Fig. 4.8 c) shows, that the approximation formula of Tada et al. (1973) slightly underestimates the outcome of the FE simulation.

4.6.2 Benchmark b: loaded crack faces
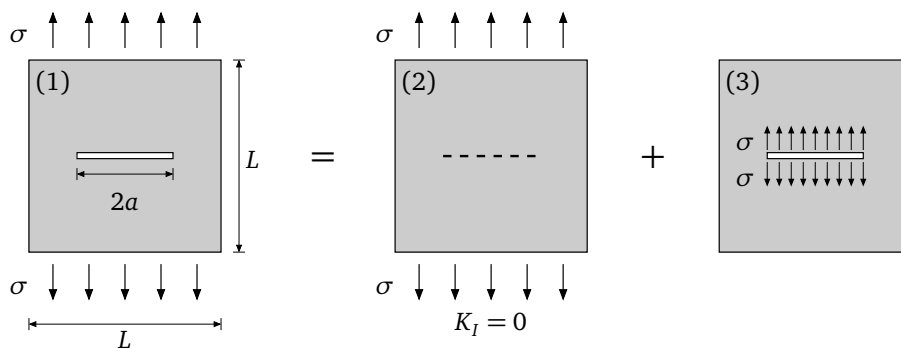
Figure 4.9: Superposition for evaluation of stress intensity factor for straight crack in infinite domain with pressurized crack faces

In case of linear elasticity, the superposition scheme illustrated in Fig. 4.9 serves to demonstrate that the stress intensity factor for a straight crack in an infinite domain

	m	0	1	2	3	4	5	6
$a)$	$\bar{G}^{\text{tip}}$	0.8788	1.0054	1.0002	1.0005	1.0006	1.0006	1.0006
$b)$	$\bar{G}^{\text{tip}}$	0.8788	1.0054	1.0002	1.0005	1.0005	1.0005	1.0006
	$\bar{G}^{\text{elast.}}$	0.8307	0.8131	0.7265	0.6600	0.5998	0.5431	0.4886
	$\bar{G}^{\text{boun. } t^*}$	0.0482	0.1925	0.2740	0.3407	0.4010	0.4577	0.5122
	$\bar{G}^{\text{boun. } W}$	−0.0001	−0.0002	−0.0002	−0.0003	−0.0003	−0.0003	−0.0003

Table 4.1: Resulting contributions $\bar{G}^* = G^*/G_{\text{analyt.}}$ to the normalized configurational crack tip force for different summation levels m

with pressurized crack faces in test (3) equals those of the straight crack in an infinite domain under uniaxial loading in test (1). Before verifying the implementation for test (3), the results of the FE simulation of test (1) are compared to the known analytical solution, $-G_{\text{analyt.}} = J_{1,\text{analyt.}} = \sigma^2 \pi a (1 - \nu^2)/E$ as shown in Fig. 3.5 a) for different values of the domain length L. Figure 4.10 a) shows the contributions of elastic and boundary components to the normalized total configurational crack tip load for different summation levels and ratios a/L. It shows that a too large ratio a/L (dotted line) overestimates the analytic result for the infinite plane. The dashed line and the solid line overlap and lead to sufficiently accurate results. Therefore, $a/L \leq 0.025$ will be used in the following studies. As to be expected for test (1), the contributions of the crack face integrals to the configurational crack tip load, represented by the pink and the green line, vanish, also in case of $m \geq 0$, hence $G^{\text{tip}} = G^{\text{elast.}}$. The first line in Tab. 4.1 shows that with $m = 0$, the computed value for G^{tip} strongly underestimates the analytical result. Two additional summation levels ($m = 2$) suffice to compute configurational crack tip loads with a relative error of less than one per mil.
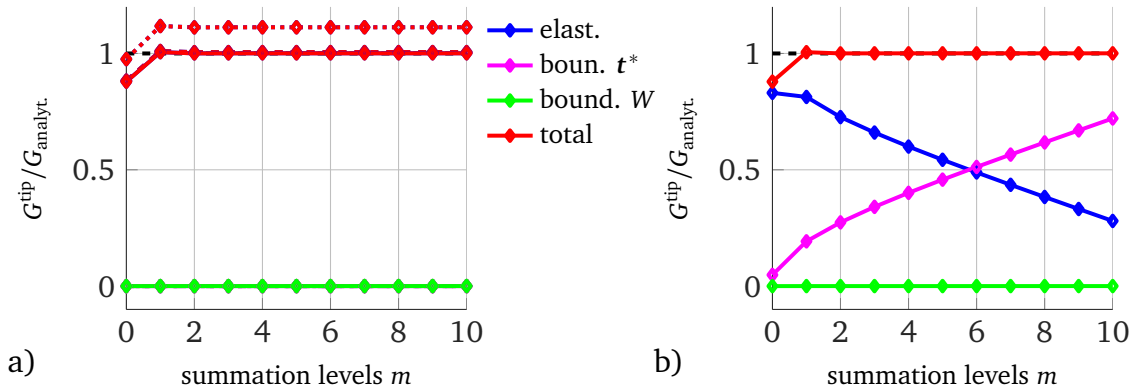

Figure 4.10: Contributions of elastic and boundary components to the normalized total configurational crack tip load versus summation levels for a straight crack in an approximated infinite domain under a) uniaxial loading and b) an equivalent normal pressure on the crack faces. The line style indicates the ratio a/L with $a/L = 0.1$ for the dotted lines, $a/L = 0.025$ for the solid lines and $a/L = 0.0125$ for the dashed lines.

The contributions to the configurational crack tip load in case of loaded crack faces are illustrated in Fig. 4.10 b). The elastic contribution to G_x^{tip} (blue line) now strongly depends on the area of integration and reduces for growing m. The contribution of the crack face load (pink line) is also path-dependent and increases with growing m. Since the crack is not ideally sharp ($\alpha \approx 0.06°$) small contributions of W on the crack faces have to be considered to get a total configurational crack tip load equivalent to case a). The individual contributions for different summation levels m are listed in Tab. 4.1. It is important to note that even for $m = 0$, the error due to a negligence of $G^{\text{boun. }t^*}$ is considerable ($\approx 10\%$). This emphasizes that the consideration of the crack face integrals in case of loaded crack faces is important. Again it shows that $m = 2$ suffices to compute very accurate results.

4.6.3 Benchmark c: volume forces
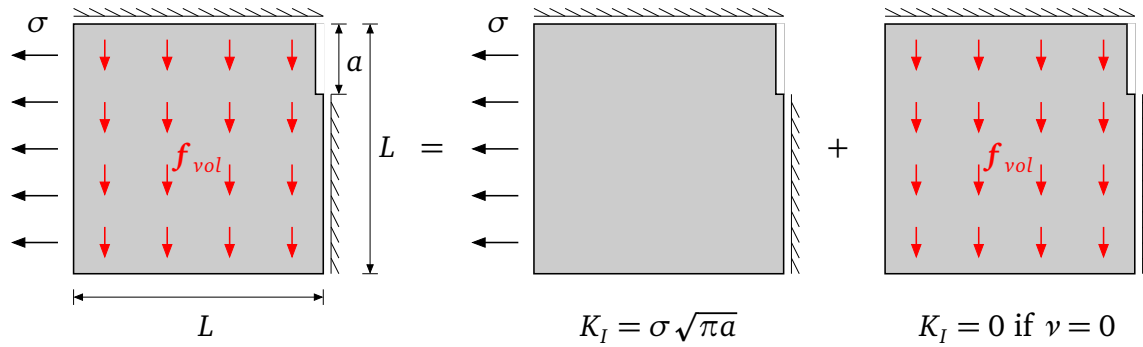
Figure 4.11: Superposition of uniaxial tension test and loading due to volume forces and resulting K_I for $\nu = 0$

Due to the lack of analytical solutions, as well as published results in case of applied volume forces, a rather scientific setup as illustrated in Fig. 4.11 has to serve as benchmark for the implementation of the volume force contribution to the configurational crack tip force. Similar to the previous example, superposition can be used to split the problem into one with only uniaxial loading and the known resulting configurational crack tip load from the previous example and one with only volume forces acting on the domain. For $\nu = 0$, transverse deformation is suppressed and the influence of the volume forces on stress concentrations at the crack tip disappears. In this case, the evaluation of the complete problem must result in the same configurational crack tip force as the problem with uniaxial loading. The plot in 4.12 a) illustrates the individual contributions to G^{tip} for $a/L = 0.025$. In the present example, the volume forces increase the elastic contribution to G^{tip} with growing summation levels. By adding the direct share due to volume forces G^{vol}, the total configurational crack tip force converges and independence on the size of the domain is preserved. The numbers in Tab. 4.2 indicate, that only one additional circle of elements suffices to compute configurational crack tip loads with a relative error of less than one per mil.
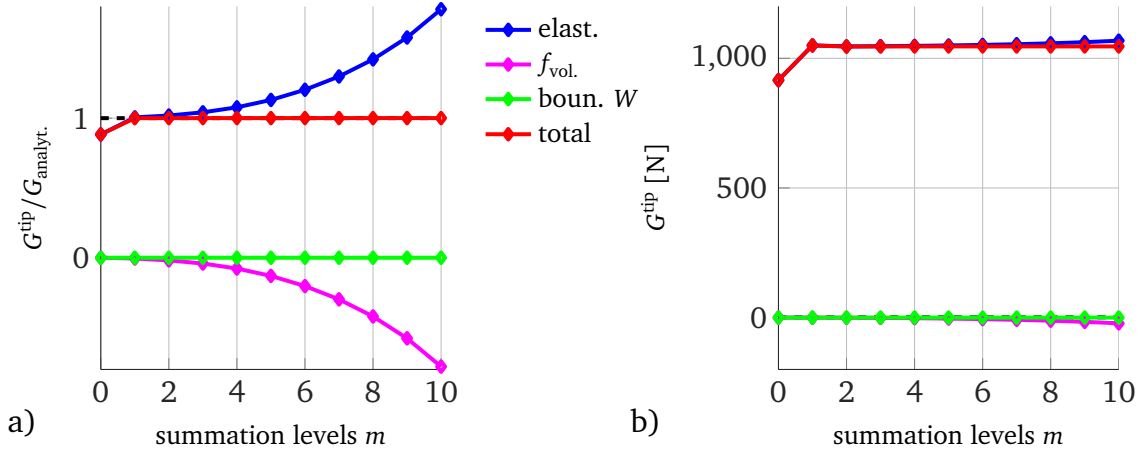
Figure 4.12: a) Resulting contributions to the normalized configurational crack tip force for different summation levels m and $\nu = 0$; b) contributions to the configurational crack tip force for different m and $\nu = 0.3$

Also in case of $\nu \neq 0$ the total configurational crack tip force converges for increasing m. Figure 4.12 b) shows the individual contributions to G^{tip} for $\nu = 0.3$, $\sigma = 100\,\text{kPa}$ and $f_{\text{vol}} = \rho g$ for $g = 10\,\text{m/s}^2$ and $\rho = 1000\,\text{kg/m}^3$. Unlike for $\nu = 0$, it appears that the contribution of the volume force correction is very small, even for larger m. Further simulations indicate that this trend is independent of the intensity of the volume force. As in the previous examples, $m = 0$ underestimates the correct result whereas $m = 2$ suffices to evaluate G^{tip} with a relative error of less than one per mil in comparison to the result for $m = 10$.

m	0	1	2	3	4	5	6
$\bar{G}^{\text{tip}}$	0.8834	1.0001	1.0001	1.0005	1.0005	1.0006	1.0006
$\bar{G}^{\text{elast.}}$	0.8834	1.0055	1.0187	1.0418	1.0775	1.1305	1.2034
$\bar{G}^{f_{\text{vol}}}$	-0.0000	-0.0053	-0.0186	-0.0413	-0.0770	-0.1299	-0.2028

Table 4.2: Resulting contributions $\bar{G}^* = G^*/G_{\text{analyt.}}$ to the crack tip configurational force for different summation levels m and $\nu = 0$

4.6.4 Benchmark d: inhomogeneous Young's moduli

There exists a multitude of papers on the analysis of stress intensity factors for functionally graded materials (FGMs). Erdogan (1995) and Erdogan and Wu (1997) present a semi-analytical approach for the computation of K_I in a functionally graded beam with single edge crack under different loading situations. The results are verified by Kim and Paulino (2002) who show different FE strategies for the evaluation of K_I such as a J-integral computation. Mahnken (2008) implemented a material force approach with different meshing strategies for the computation of K_I for $a/b = 1/2$ and compared the results to those of Kim and Paulino (2002). In

the present study, only loading by an uniaxial tensile stress will be considered as illustrated in Fig. 4.13. In analogy to the mentioned publications, $L/b = 4$ will be used. The variance of material parameters is constricted to Young's modulus which takes the form

$$E(z) = E_0\, e^{-z/b \ln \kappa_E} \tag{4.29}$$

with $\kappa_E = E(z = -b)/E_0$. Herein, z is the vertical coordinate with the origin located at the upper side of the domain. Resulting distributions of $E(z)/E_0$ are shown in Fig. 4.14 a).

Figure 4.14 b) compares own values of normalized K_I with a summation level of $m = 2$ to the findings in the mentioned publications. It appears that the J-integral approach, the material force approach by Mahnken (2008) and the presented evaluation of K_I via configurational forces lead to very similar results. The semi-analytical values of Erdogan and Wu (1997) are in good agreement for the most part of the analyzed setups. Only small κ_E and deep cracks lead to slightly higher K_I for the semi-analytical evaluation. Fig-ure 4.14 b) does not indicate a clear trend for K_I

Figure 4.13: Setup with depth-dependent Young's modulus

versus growing or decreasing E with depth. Only for deeper cracks, a trend towards higher K_I for decreasing E with depth and lower K_I for increasing E is evident.

Not only the ratio between E_0 and $E(z = -b)$ but also the characteristic trend of $E(z)$ considerably influences the resulting normalized K_I. Figure 4.15 b) illustrates result-ing normalized K_I for $\kappa_E = 0.1, 1$ and 10 as well as for different characteristic trends as plotted in Fig. 4.15 a). In comparison to Fig. 4.14 b) it appears that the dif-ferences in K_I due to the slope of $E(z)$ for equal κ_E are within the same order of magnitude as the differences due to different κ_E.
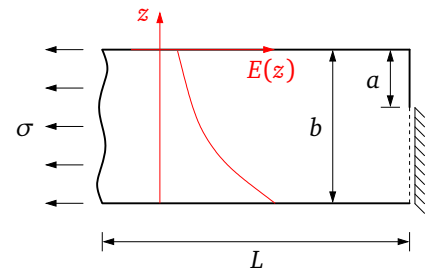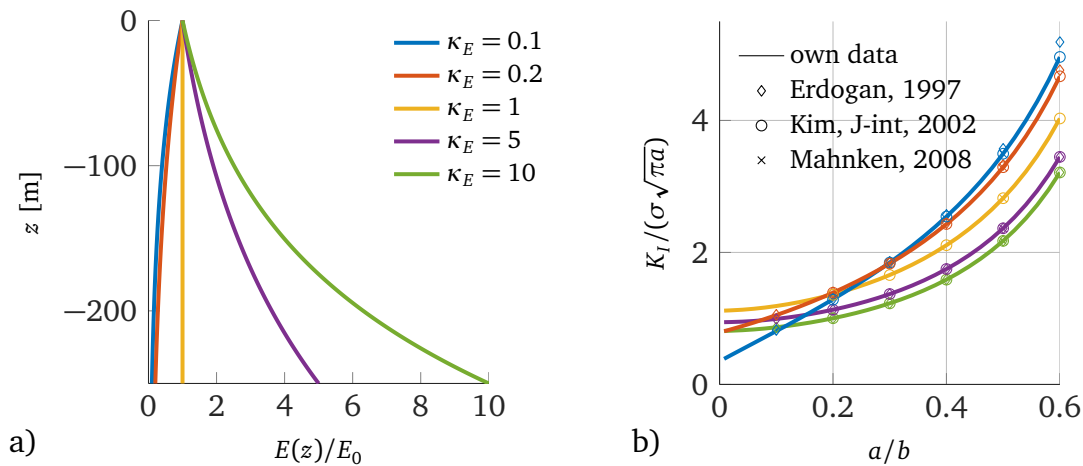

Figure 4.14: a) Normalized Young's modulus versus depth for different κ_E; b) resulting normalized K_I for single edge tension test in comparison to literature findings
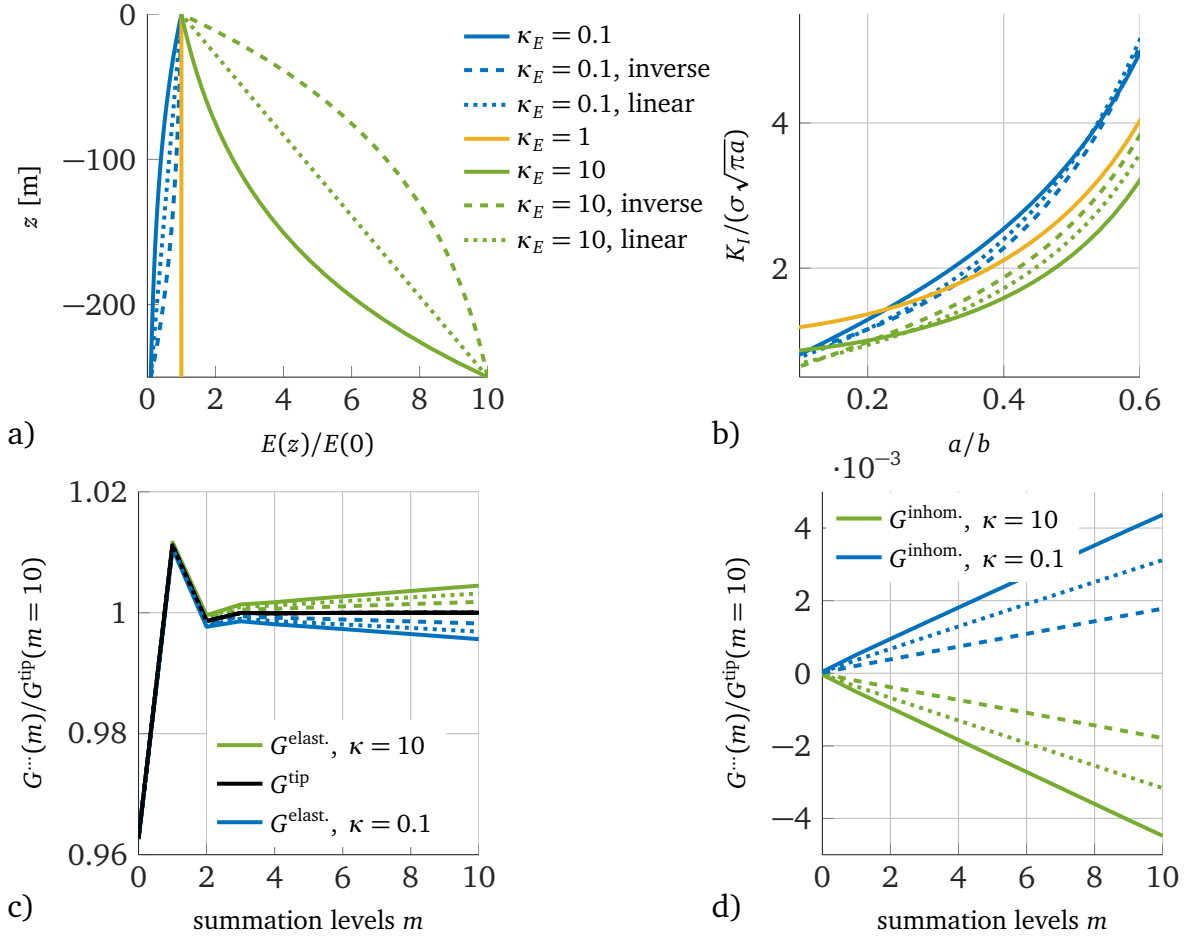
Figure 4.15: a) Normalized Young's modulus versus depth for different κ_E and characteristic trends; b) resulting normalized K_I versus normalized crack depth; normalized elastic (c) and inhom. (d) contribution to configurational crack tip force for different summation levels, characteristic trends and κ_E

The influence of the summation level m on the different contributions to the configurational crack tip force is illustrated in Fig. 4.15 c) and d). The results are normalized using the respective configurational crack tip force for $m = 10$. As in previous benchmarks, the relative error of G^{tip} with respect to an optimum value for $m = 10$ becomes small for $m \geq 2$. The error invoked by only taking the elastic contribution to G^{tip} is smaller than in the previous examples. Nevertheless a clear trend towards larger differences between G^{tip} and $G^{\text{elast.}}$ for stronger gradients in $E(z)$ appears. Hence, the results in Fig. 4.15 d) correspond well to Eq. (4.19), where the contribution of inhomogeneities in the material parameters is introduced as a function of the spatial derivative of the stiffness tensor.

4.6.5 Benchmark e: mixed mode loading, static crack tip

In order to demonstrate the good agreement of the numerically computed resulting configurational force vector with the analytically evaluated J-integral vector, the

benchmark example of the straight crack in an infinite domain under mixed mode loading (Sec. 3.3) will be used. Since the previous benchmarks showed the very good agreement between numerically computed values of J_1 and analytic results depending on m, the focus is now directed on the performance of J_2 with respect to m. The solid lines in Fig. 4.16 a) show corrected values of the different contributions to the configurational crack tip force ($G_y^{\text{elast.}}, G_y^{\text{boun.,W}}$) as well as the resulting configurational crack tip force G_y^{tip} for different sizes of the influence area specified by the summation levels m for $\sigma = \tau$, hence $K_I = K_{II}$ and $J_1 = J_2$. Corrected in this sense means, that contributions to $G_y^{\text{boun.,W}}$ of nodes on edge elements adjacent to the crack tip and of the crack tip itself are ignored. The dashed and the dotted lines illustrate results for $G_y^{\text{boun.,W}}$ and G_y^{tip} comprising all nodes, or ignoring only the crack tip node, respectively. Unlike in the previous examples, where the contribution of $G_x^{\text{boun.,W}}$ was negligibly small independent on the size of the influence area, Fig. 4.16 a) now illustrates the importance to include crack face contributions if resulting configurational forces are computed for mixed mode loading. In addition, the difference between a summation of nodal configurational forces within at least one element ring around the crack tip and solely taking the crack tip nodal configurational force appears even more pronounced than in previous benchmarks with mode I loading. Since the area covered by a certain number of element rings is related to the mesh size around the crack tip, the error by only taking $\boldsymbol{G}^{\text{elast.}}$ versus summation levels m reduces for finer discretizations. In Fig. 4.16 b), the numerically computed deflection angle $\theta = \text{atan}(J_2/J_1)$ is compared to the analytical result for different values of K_I/K_2. Both lines are in very good agreement. However, the illustrated precision of the numerical results can only be achieved with a very fine
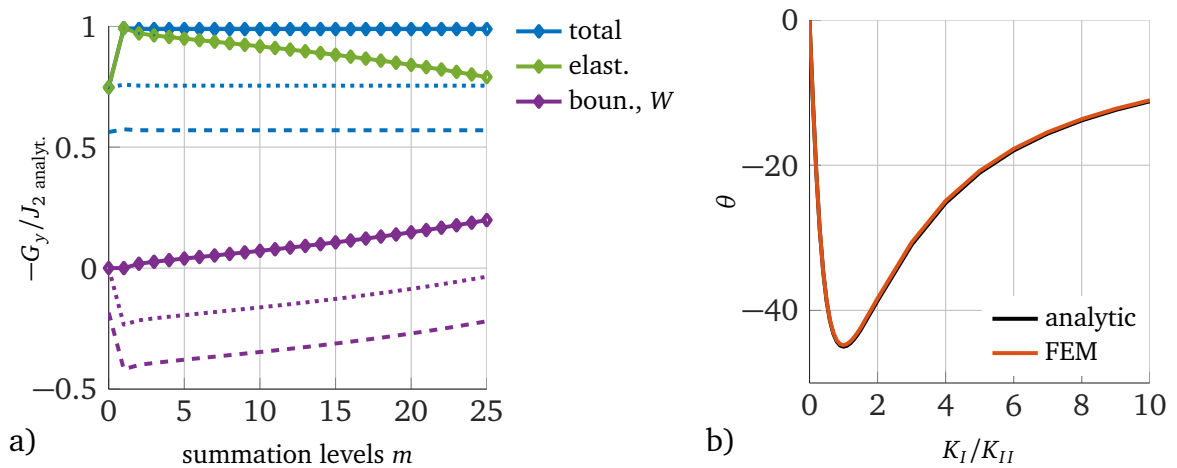

Figure 4.16: a) Contributions to resulting configurational crack tip force and total configurational crack tip force versus different summation levels m for straight crack in infinite domain under mixed loading ($\tau = \sigma$), $\boldsymbol{G}^{\text{boun.,W}}$ without correction (dotted line), ignoring crack tip node contribution (dashed line), ignoring nodes on crack adjacent element edge (solid line); b) crack deflection angle θ resulting from analytic and numerical computation of J_1 and J_2 for varying K_I/K_2
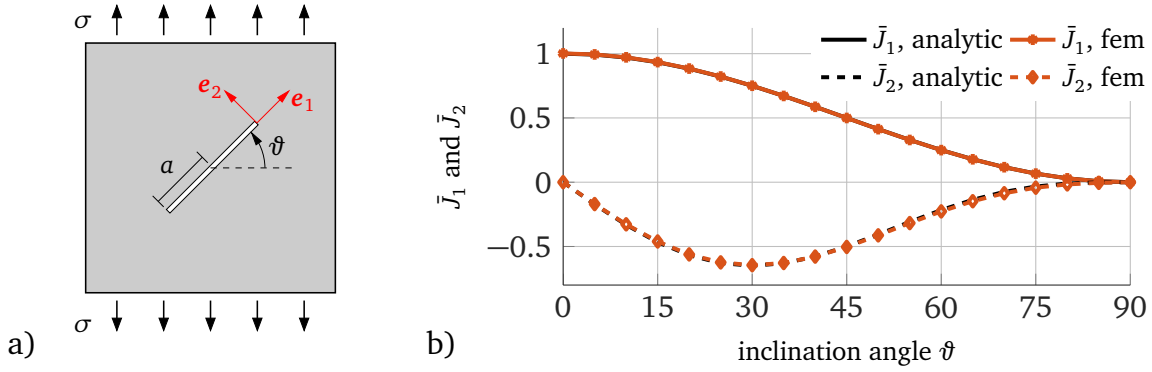
Figure 4.17: a) Setup of inclined straight crack in infinite domain under uniaxial tension following Kienzler et al. (2010); b) analytic and FE-based resulting normalized J_1 and J_2 for different inclination angles ϑ

and uniform mesh around the crack tip.

Thus far, mixed mode conditions were forced by external loading while the crack was oriented in horizontal direction. The sketch in Fig. 4.17 a) illustrates the setup of a benchmark with an inclined straight crack in an infinite domain under uniaxial tension as published by Kienzler et al. (2010). Resulting normalized values $\bar{J}_1$ and $\bar{J}_2$ with

$$\bar{J}_i = \frac{J_i E}{\pi a \sigma^2 (1 - \nu^2)}$$

are plotted in Fig. 4.17 b). The analytic components of the generalized J-integral are computed using

$$K_I = \sigma \sqrt{\pi a} \sin^2(\pi/2 - \vartheta) \quad \text{and} \quad K_{II} = \sigma \sqrt{\pi a} \sin(\pi/2 - \vartheta) \cos(\pi/2 - \vartheta). \quad (4.30)$$

A fine and uniform mesh at the crack tip provided, the numerical findings are in very good agreement with analytical results.

4.6.6 Benchmark f: mixed mode loading, crack propagation

A very demanding and often employed benchmark for crack propagation algorithms has been proposed by Bittencourt et al. (1996). As visualized in Fig. 4.18 a) the geometry consists of a two-dimensional homogeneous block with three holes and an initial crack at the lower left boundary. The bearing and the load are consistent with those of a three point bending test. Figures 4.18 b) and c) show digitized photographs of experimental crack trajectories found by Bittencourt et al. (1996) for two setups with $a = 5$m and $b = 1.5$m (in b) and $a = 6$m and $b = 1$m (in c). A replication of the crack path in Fig. 4.18 c) can easily be achieved and is relatively insensitive with respect to changes in the maximum crack propagation increment or the minimum mesh size. The simulation follows the work flow in Fig. 4.4 without checking if a threshold for crack propagation is reached. The results are plotted in Fig. 4.19 b) together with the digitized crack trajectory of the experiment by
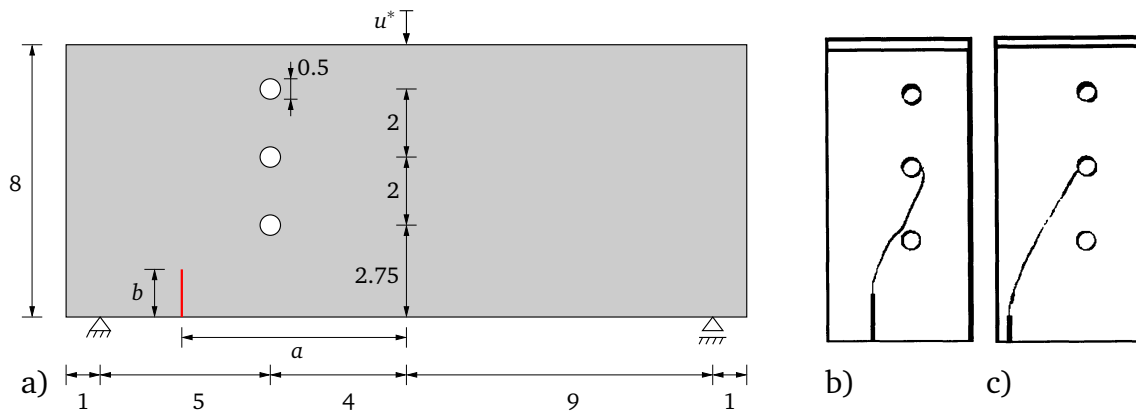
Figure 4.18: a) Setup for the benchmark test by Bittencourt et al. (1996) with length scales in [m]; b+c) digitized photographs of experimental crack trajectory taken from Bittencourt et al. (1996) with $a = 5$m and $b = 1.5$m (in b) and $a = 6$m and $b = 1$m (in c)

Bittencourt et al. (1996). As to be expected, small values of $\Delta\lambda_{\text{max}}$ are better able to reproduce the experimental result. Nevertheless also large $\Delta\lambda_{\text{max}}$ lead to the crack growing into the second hole with only 15 propagation steps, as visualized by the red line. The crack path in Fig. 4.18 b) is much more difficult to reproduce and imposes higher demands on $\Delta\lambda_{\text{max}}$ as well as on the maximum mesh size. Figure 4.19 a) illustrates modeled crack paths for varying $\Delta\lambda_{\text{max}}$. If the maximum crack growth increment is chosen too large, the crack passes the second hole on the right side and propagates towards the centre of the upper boundary where the load is introduced (light blue curve, overlapped by dark blue curve). Intermediate values of $\Delta\lambda_{\text{max}}$ can by chance be able to reproduce the crack path with a comparatively low number of steps required (green and red curve, overlapped by purple curve)
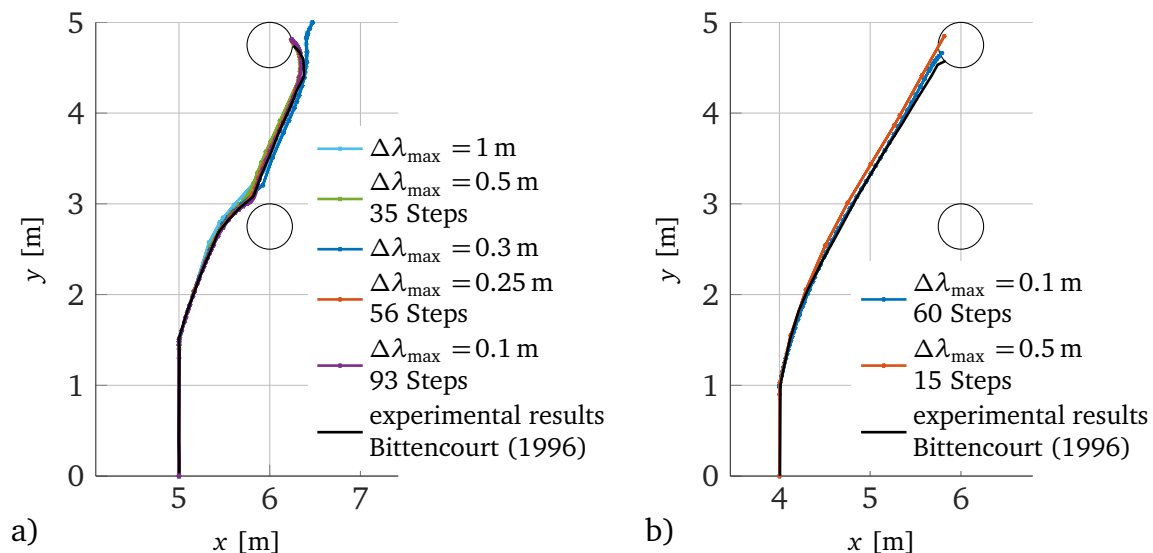

Figure 4.19: Simulated crack path in comparison to experimental result by Bittencourt et al. (1996) for different maximum crack propagation increments $\Delta\lambda_{\text{max}}$ using a) $a = 5$m and $b = 1.5$m or b) $a = 6$m and $b = 1$m

but may also fail if the new crack tip is set outside of what might be called an area of convergence around the correct solution (dark blue curve). If $\Delta\lambda_{\max}$ is below a certain threshold, all cracks hit the second hole from the right side as requested by the experimental results. The illustrated paths have been evaluated using

$$\Delta\lambda_t = \begin{cases} \Delta\lambda_{\max}, & \text{if} \quad \Delta\theta < 0.5° \\ \frac{1}{2}\Delta\lambda_{\max}, & \text{if} \quad 0.5° \leq \Delta\theta < 1° \\ \frac{1}{4}\Delta\lambda_{\max}, & \text{if} \quad 1° \leq \Delta\theta < 2° \\ \frac{1}{8}\Delta\lambda_{\max}, & \text{if} \quad 2° \leq \Delta\theta < 3° \\ \frac{1}{16}\Delta\lambda_{\max}, & \text{if} \quad \Delta\theta \geq 3°. \end{cases} \tag{4.31}$$

The resulting number of steps is considerably larger than the number needed by Schütte (2010) using curved crack path increments and a predictor corrector scheme. However, this is acceptable regarding the simplicity of the applied algorithm.

In order to demonstrate the behavior of the algorithm for multiple cracks, a benchmark first published by Bouchard et al. (2003) is used. The setup with two holes as visualized in Fig. 4.20 is symmetric to the center of the domain and comprises two cracks originating from the lateral boundaries. The horizontal boundaries are clamped and shifted by a constant displacement $\Delta u_y \boldsymbol{n}$ in vertical direction. As proposed by Bouchard et al. (2003), the crack deflection angle and the propagation increment for both crack tips is evaluated for every propagation step, hence the cracks grow simultaneously. In his paper, Bouchard et al. (2003) compared different criteria for the evaluation of the crack deflection angle (the maximum circumferential stress criterion, the maximum strain energy release rate criterion and the maximum strain energy density criterion) in combination with a mesh refinement algorithm. He showed that for the presented problem, the criteria used led to similar general
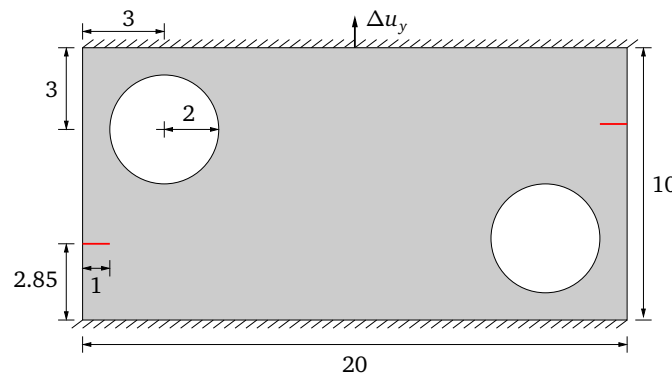

Figure 4.20: Setup for benchmark test following Bouchard et al. (2003) with length scales in [m]
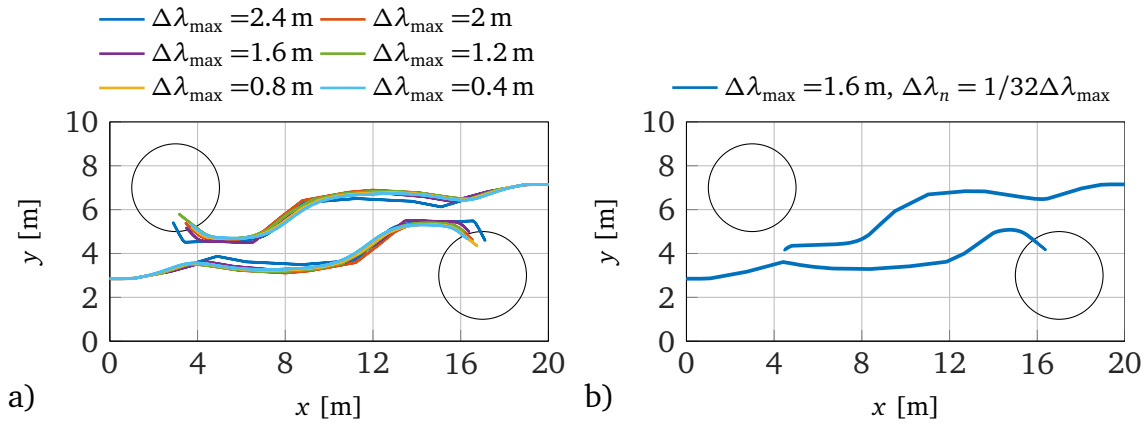
Figure 4.21: Simulated crack paths for the benchmark example of Bouchard et al. (2003) a) using different maximum crack propagation increments and $\Delta\lambda_n = 1/400\Delta\lambda_{\max}$, b) using $\Delta\lambda_n = 1/32\Delta\lambda_{\max}$

crack paths. Both cracks are first attracted by the neighboring hole then realign to grow towards the hole in front. After about two fifth of the domain length the cracks start approaching each other, but do not coalesce along the shortest path. The crack tips run around each other and would merge after some distance if they were not drawn by the holes which they eventually penetrate. This pattern is very well reproduced by the simulated crack paths for a wide range of crack propagation increments as shown in Fig. 4.21 a). A sensitivity due to larger opening angles at the tip invoked by taking $\Delta\lambda_n = 1/32\Delta\lambda_{\max}$ instead of $\Delta\lambda_n = 1/400\Delta\lambda_{\max}$ as in the previous plot is shown in Fig. 4.21 b), where the upper crack propagates towards the lower crack instead of penetrating the hole. By using smaller crack propagation increments, this misdirection can be remedied.
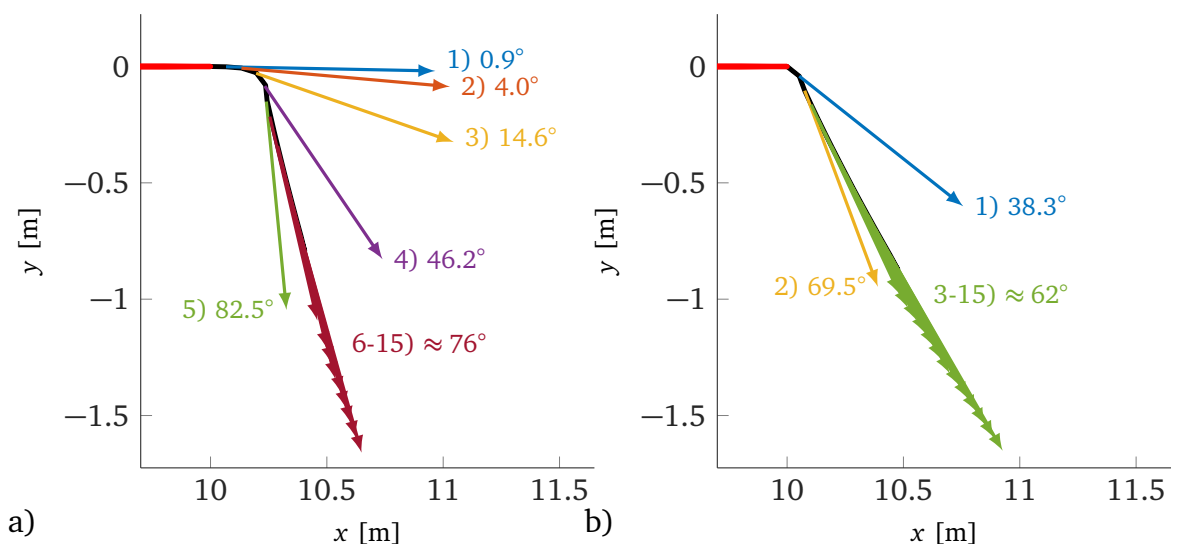

Figure 4.22: Crack propagation direction for straight crack in infinite domain for the first 15 propagation steps using a) pure mode II loading and b) mixed-mode loading with $K_I/K_{II} = 0.5$, initial crack tip marked in red

Figure 3.8 b) demonstrates that the direction of the generalized J-integral vector is not suitable to predict the crack deflection angle unless $K_I \gg K_{II}$. Figure 4.16 b) shows that the configurational force approach is able to very accurately compute the components of J for wide range of the ratio K_{II}/K_I.

In a last setup it will therefore be shown that the presented implementation of the configurational force approach is able to approximate the crack deflection angle predicted by the *S*-criterion for $\nu = 0.3$ and the maximum circumferential stress criterion (MCS-cirterion) also for $K_{II} \gg K_I$ by application of an incremental crack propagation algorithm after very few crack propagation steps. Therefore, the benchmark example of the straight crack in an infinite domain under mixed mode loading will once more be used. Figure 4.22 a) illustrates, that only five crack propagation steps are needed to approach the deflection angle $\theta \approx 83.6°$ of the *S*-criterion for pure mode II loading with less than 2% error. For the following steps, θ stabilizes at approximately 76° which lies between the result for the *S*-criterion and the MCS-criterion. Figure 4.22 b) shows the crack path and the resulting direction of crack propagation for $K_I/K_{II} = 0.5$. In this example only three steps are needed to obtain results between those of the *S*-criterion and the MCS-criterion. Both simulations were performed with $a/L = 0.0125$ and constant crack propagation increments with $\Delta\lambda/a = 1/150$.

5 Analysis of vertical cracks in ice shelves

The vertical propagation of crevasses in glaciers and ice shelves has been a subject of investigation for more than 50 years. Nye (1955) argued that crevasses propagate vertically to the point where the cryostatic pressure neutralizes the flow induced tensile stresses. Weertman (1973) was the first to assume elastic material behavior for the analysis of vertical crevasses in glaciers. He evaluated the characteristics of dry and water-filled single crevasses by using dislocation distribution functions. Methods of linear elastic fracture mechanics for the evaluation of stress intensity factors (SIF) of dry and water filled surface cracks in ice shelves were first applied by Smith (1976). He used a simplified crack geometry and boundary conditions to facilitate the application of tabulated values gained from semi-analytical methods by Tada et al. (1973) and Sih (1973a). His method was adapted and extended by Van Der Veen (1998a,b), who discussed the importance of depth-dependent density profiles and Rist et al. (2002) who additionally analyzed depth-dependent tensile stresses. The approach by Rist et al. (2002) has been repeatedly used for the analysis of bottom and subsurface crevasses, e.g. by Nath and Vaughan (2003) and Luckman et al. (2012), and will be used here as a benchmark for the implemented finite element model.

In this chapter, several types of vertical crevasses are considered as visualized in Fig. 5.1. A valid model geometry for surface cracks in a sufficient distance from the grounding line, the ice front and singular points as ice rises or ice rumples is presented in Sec. 5.1. The influence of geometric dimensions is discussed. In Sec. 5.2 several boundary conditions are presented to demonstrate their influence
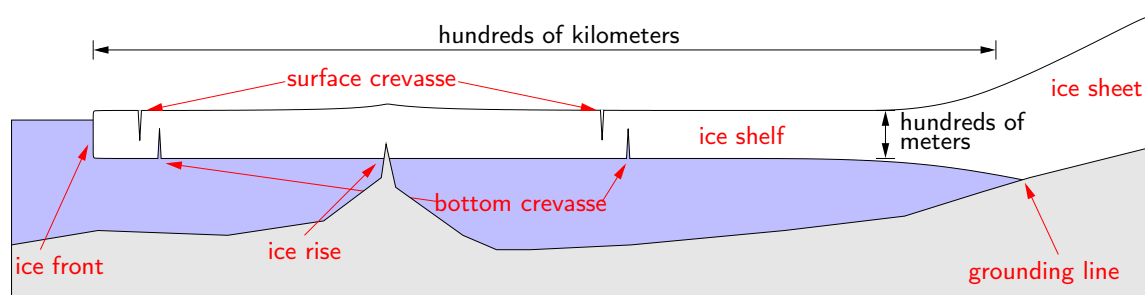

Figure 5.1: Simplified ice shelf model for vertical crack propagation

on the crack criticality. The influence of different elastic material parameters as well as the density is presented in Sec. 5.3. The results on dry surface cracks are compared to the findings of Rist et al. (2002) in Sec. 5.4 before shifting the focus to water-filled surface and bottom cracks in Sec. 5.5. In Sec. 5.6 the simulation of water-filled surface crevasses is extended towards the analysis of frost wedging processes.

5.1 Model setup and geometric dimension

In order to simulate cracks in a specific stress state, the geometric dimensions of the model have to be chosen carefully. Vertical single cracks are local small-scale phenomena, e.g. the crack depth and the crack opening are small in comparison to the lateral extent of ice shelf. For this reason, the length of the model domain has to be sufficiently long to prevent influencing interactions between the vertical boundaries and the crack tip, on the other hand it has to be small in comparison to the characteristic length of the ice shelf.

Fractures tend to align perpendicular to the direction of the first principal stress. This direction is shear-free, hence in-plane shear stresses, leading to a mode II crack opening are neglected for the analysis of vertical crack propagation. Effects as crack closure and contact problems due to compressive stresses will not be considered either.

Figure 5.2 a) shows smoothed flow velocities of the eastern part of the WIS resulting from satellite measurements published in Braun et al. (2009). The resulting
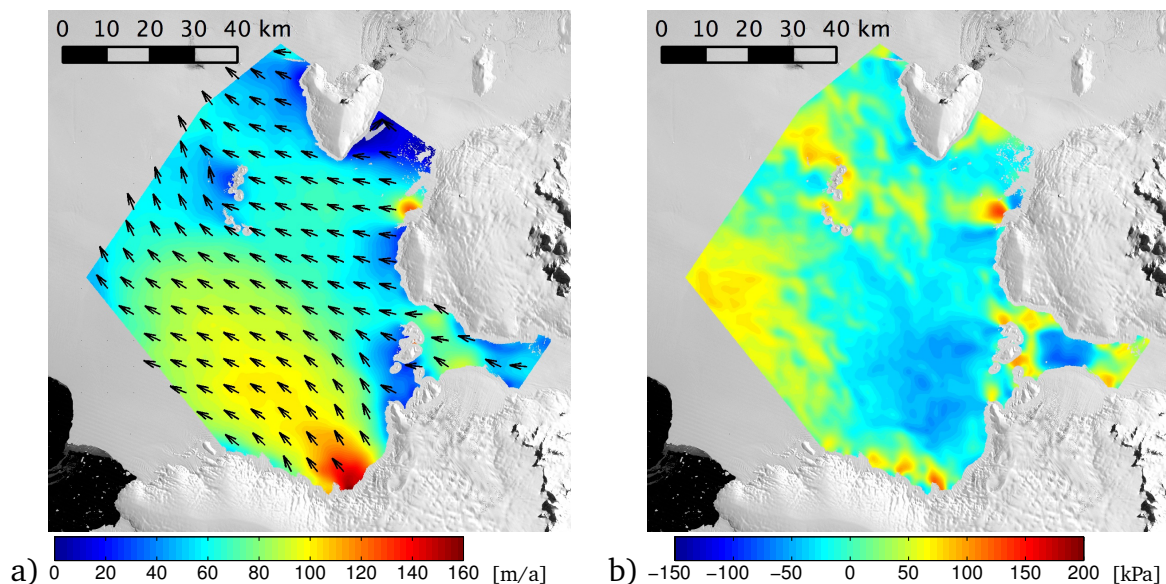

Figure 5.2: a) Horizontal ice flow velocity in [m/a] of the south-western tributaries of the WIS as published in Braun et al. (2009) basing on ERS-1/2 SAR overpasses of March 1994 and March 1996; b) resulting first viscous principal surface stress in [kPa]; background: MOA image from 2003/04 (©NSIDC, Haran et al. 2005)

first principal surface stress, evaluated using the equations in Sec. 2.2.2 with $n = 3$ and $A^{-1/n} \approx 7.4 \cdot 10^7 \text{Pa s}^{1/3}$, is illustrated in Fig. 5.2 b). The value for $A^{-1/n}$ is computed following Greve and Blatter (2009) for an isothermal ice shelf with $T \approx -3°\text{C}$. The relevant tensile stresses range from 0 Pa to 200 kPa, whereupon high stresses only occur at the grounding line or in proximity of ice rises. In freely floating areas, tensile stresses do not exceed 100 kPa. Regions with approximately constant tensile stresses extend only few kilometers.

Braun et al. (2009) published ice shelf thicknesses ranging from 50 m in the North of the WIS to 300 m in the South. This information together with an approximate guess of reasonable domain lengths according to Fig. 5.2 b) motivates an investigation into the influence of the geometric parameters length L and thickness H on crack criticality with respect to the crack depth CD. A third important geometric parameter is the crack opening angle α. Satellite images show crack openings up to several meters, whereupon the associated crack depth and crack geometry are unknown. The variation of the crack opening angle in Sec. 3.2.1 showed negligible differences in the singularity order λ for $\alpha < \pi/10$. Since reasonable crack opening angles are difficult to guess, a wide range of $0 < \alpha < 1/36\pi$ will be simulated. For the two-dimensional FE simulation of vertical single cracks under plane strain conditions, a geometric setup as presented in Fig. 5.3 is used. Computation time is saved by only simulating the symmetric half domain of the problem in analogy to Sec. 4.6.1.
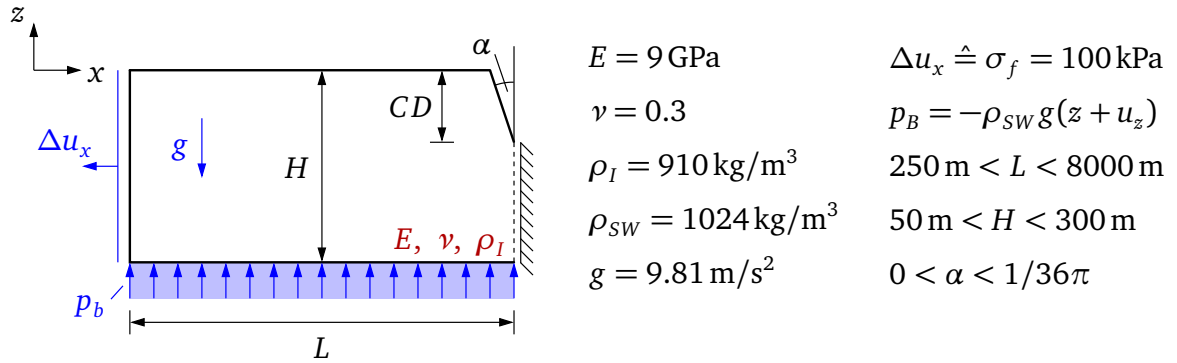

Figure 5.3: Model geometry and boundary conditions for the simulation of dry vertical crack growth; constant material parameters used for the geometric length scale parameter studies

Ice shelves are subjected to gravity and buoyancy forces in the vertical direction. Also the simplified model geometry is loaded by gravity. Buoyancy is realized by a Robin-type pressure boundary condition p_B as a function of the seawater density ρ_{SW}, the gravity constant g, the vertical position z and the vertical displacement u_z at the bottom of the domain.

The horizontal velocities and displacements in a sufficient distance from the ice shelf boundaries are depth-independent, a property widely used in the so-called shallow-shelf-approximation for ice dynamical simulations (Greve and Blatter, 2009). In order to meet this constraint, the vertical boundary is loaded by a prescribed depth-independent displacement Δu_x. For the uncracked homogeneous body, Δu_x can

be related to the horizontal tensile flow stress σ_f using Hooke's law, $\sigma = E'\varepsilon$, with $E' = E$ for plane stress and $E' = E/(1 - \nu^2)$ in the case of plane strain, which will be assumed in the following simulations. Hence

$$\Delta u_x = \varepsilon L = \frac{\sigma_f(1 - \nu^2)}{E} L. \tag{5.1}$$

Unless differently stated, the material parameters E, ν, ρ_I and ρ_{SW}, as well as the remote stress σ_f are kept constant at the values assigned in Fig. 5.3.

In order to make statements about a possible crack depth for given parameter setups, a range of crack depths is simulated and the respective SIF K_I are evaluated from the absolute value of the resulting configurational force using the relation

$$K_I = \sqrt{\frac{\mathscr{G}E}{1 - \nu^2}} \tag{5.2}$$

derived from Eq. (3.7) for mode I loading. Special attention is needed for the interpretation of negative SIFs. With K_I being a function of the square root of the computed configurational forces, which do not distinguish between tensile and compressive stress concentrations, the sign of K_I is determined by an additional evaluation of the relative displacement of the crack faces towards each other in proximity of the crack tip. Hence, negative SIFs represent crack closure. Zero and positive SIFs indicate a potential crack at the respective depth, whereas K_I exceeding the critical SIF K_{Ic} suggests potential crack growth. Rist et al. (2002) published measurements for K_{Ic} ranging from $50\,\text{kPa}\sqrt{\text{m}}$ up to $400\,\text{kPa}\sqrt{\text{m}}$ with very little variation due to a depth increasing density. The region within these limits will in the following be represented by a grey background, a change of sign will be indicated by a black dotted line.

5.1.1 Length L of the model domain

Figure 5.4 a) shows a significant dependence of $K_I(CD)$ on the length L of the model domain regarding a large set of possible crack depths. Zooming into the relevant area of positive SIFs, indicated by the red box in Fig. 5.4 a) however reveals no considerable change in the resulting SIFs for $L > 2000\,\text{m}$ as shown in Fig. 5.4 b). Higher external loads in Fig. 5.4 c) lead to deeper cracks and the influence of the model length on $K_I(CD)$ increases, whereupon the differences for $L > 2000\,\text{m}$ remain negligible. Following simulations will be performed with a domain length of $L = 2000\,\text{m}$. For setups resulting in deep cracks, different values for L may be considered.

5.1.2 Influence of the ice shelf thickness H

Figure 5.5 a) shows $K_I(CD)$ for different ice thicknesses H in the relevant region of positive SIF. Solid and dashed lined represent a displacement load Δu equivalent to $\sigma_f = 100\,\text{kPa}$ and $\sigma_f = 200\,\text{kPa}$, respectively. Relevant differences in $K_I(CD)$ can
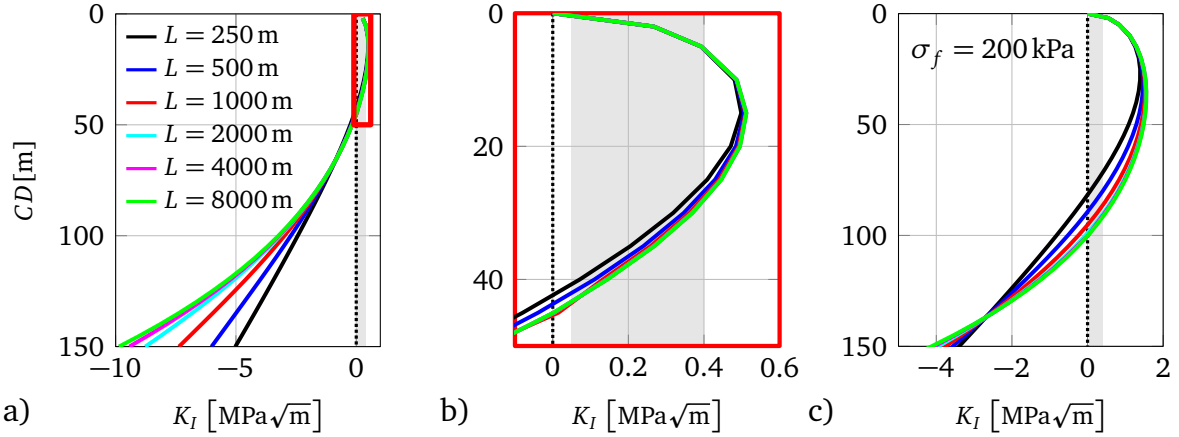
Figure 5.4: a) SIF versus crack depth for different domain lengths L, $H = 250\,\text{m}$, $\alpha = 0°$ and $\Delta u_x \triangleq \sigma_f = 100\,\text{kPa}$; b) zoom into relevant region with positive SIF; c) setup of a) with $\Delta u_x \triangleq \sigma_f = 200\,\text{kPa}$

be observed for both black and blue curves, as well as for the red and the cyan dashed curves. For these setups, positive SIFs exist down to considerably more than one third of the ice shelf thickness. For cases where $\max(CD) < 1/3H$, the dependence on the thickness is smaller. Standard literature in fracture mechanics usually presents K_I as a function of the ratio CD/H in order to use nondimensionalized quantities. By application of body loads, as in the presented case, however the SIF explicitly depends on the crack depth CD and the thickness H as illustrated in Fig. 5.5 b).
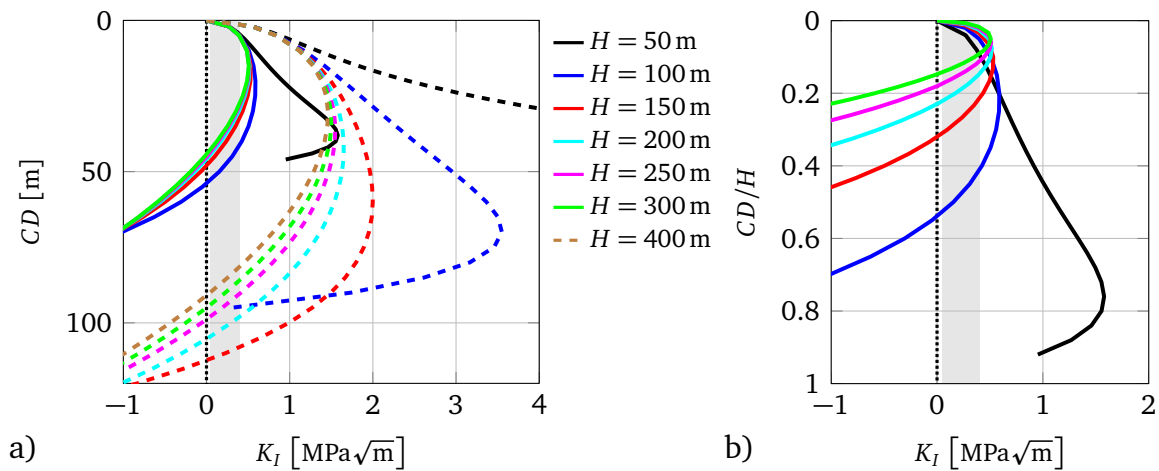

Figure 5.5: a) SIF versus crack depth for different ice shelf thicknesses H, $L = 2000\,\text{m}$ and $\alpha = 0°$; drawn trough lines represent $\Delta u_x \triangleq \sigma_f = 100\,\text{kPa}$, dashed lines represent $\Delta u_x \triangleq \sigma_f = 200\,\text{kPa}$; b) SIF versus ratio CD/H for $\Delta u_x \triangleq \sigma_f = 100\,\text{kPa}$ and different ice shelf thicknesses H

5.1.3 From sharp crack to cracked notch, the influence of α

Several techniques exist to identify cracks in ice shelves. The most nearby method is the analysis of satellite imagery. Depending on the satellite and the mode used, the resolution of the images ranges from $1/2\,\mathrm{m}$ in high-resolution mode (e.g. Terrarar-X spotlight) to several tens of meters. Hence, cracks with openings spanning several pixels on satellite images need to have a crack width of at least several meters. Figure 5.6 a) shows simulated crack top displacements Δu_{xC} e.g. the visible crack width of initially ideally sharp cracks ($\alpha = 0°$) for varying crack depths CD with boundary conditions as introduced in Fig. 5.3 using two different loads. It is obvious that the resulting crack top displacement Δu_{xC} of less than one centimeter cannot explain visible crack openings of several meters. For this reason, open cracks with $\alpha > 0°$ have to be considered whereupon the processes leading to the opening, such as creep or melting, will not be addressed.

Though the existence of a multitude of different crack profiles is possible, only triangular geometries and cracks shaped by quadratic polynomials will be considered in the following. Figure 5.6 b) illustrates the visible crack width Δx_C due to different opening angles α for triangular cracks. As in the example with $\alpha = 0°$, the resulting displacement at the crack opening is insignificant, hence Δx_C only comprises the geometric opening for varying crack depths CD following the equation

$$\Delta x_C = 2CD \tan \alpha. \tag{5.3}$$

By simulating the single edge tension test example illustrated in Fig. 3.5 b) with varying opening angles α it can be shown that in this case the influence of α on K_I is negligible within the considered range of $\alpha \leq 5°$. Only for opening angles $\alpha \geq 10°$ the resulting normalized SIFs considerably decrease as illustrated in Fig. 5.7 a).
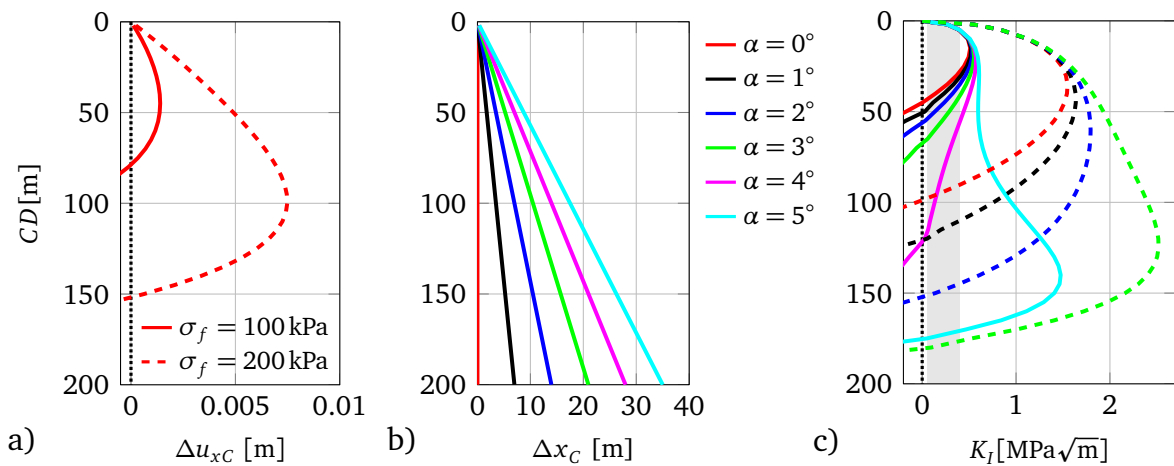

Figure 5.6: a) Total crack top displacement Δu_C versus crack depth for an ideally sharp crack and two different loads; b) geometric crack opening at crack top due to opening angle α versus crack depth; c) SIF versus crack depth for different α, $\Delta u_x \hat{=} \sigma_f = 100\,\mathrm{kPa}$ (solid line) and $\Delta u_x \hat{=} \sigma_f = 200\,\mathrm{kPa}$ (dashed line)

Stress intensity factors for the cracked ice shelf domain with applied body loads and opening angles corresponding to those in Fig. 5.6 b) are shown in Fig. 5.6 c). The influence of even small α is remarkable. Cracks, which under a given loading of $\Delta u_x \triangleq \sigma_f = 100\,\text{kPa}$ arrive at a maximum crack depth of $CD = 45\,\text{m}$ in the $\alpha = 0°$ setup reach down to a crack depth of about $175\,\text{m}$ if $\alpha = 5°$. The corresponding crack width for $CD = 175\,\text{m}$ is $\Delta x_C = 30.6\,\text{m}$. The $\alpha = 1°$ opened crack with $\Delta x_C = 1.75\,\text{m}$ yields a maximum depth of $CD = 50\,\text{m}$. As expected, the influence of α becomes even more apparent for higher loads.

In order to get a better understanding of the influence of the crack profile, a crack geometry modeled with a quadratic polynomial, as illustrated in Fig. 5.7 b), is used. The maximum opening of the spline at the crack top, Δx_C, is defined by the opening angle α_S and the crack depth CD according to Eq. (5.3). The blue area A_S of the spline shaped crack is calculated, as well as the resulting SIF. In a next step a new opening angle α_T of a triangular crack is evaluated to satisfy the condition $A_T = A_S$. This new problem is then simulated to get the associated SIF. Figure 5.7 c) illustrates the computed SIFs for the spline shaped, as well as the triangular shaped crack for $\sigma_f = 100\,\text{kPa}$ and $\sigma_f = 200\,\text{kPa}$. Whereas Fig. 5.6 c) showed a strong difference between the SIF for $\alpha = 3°$ and $\alpha = 5°$ the differences in the present plot for $\alpha_T \approx 2.56°$ and $\alpha_S = 5°$ are hardly visible for the $100\,\text{kPa}$ loading and very small for $\Delta u_x \triangleq \sigma_f = 200\,\text{kPa}$.

This motivates the conclusion, that not the opening angle α itself is the important parameter, but the associated cut out ice mass over the crack tip, whose weight in the case of $\alpha = 0°$ helps to stabilize the crack.

As even small opening angles result in deeper cracks for the given ice shelf thickness of $H = 250\,\text{m}$, the influence of the domain length L and the thickness H will once more be addressed. Figure 5.8 a) shows $K_I(CD)$ for $\alpha = 5°$ and $\Delta u_x \triangleq \sigma_f = 100\,\text{kPa}$
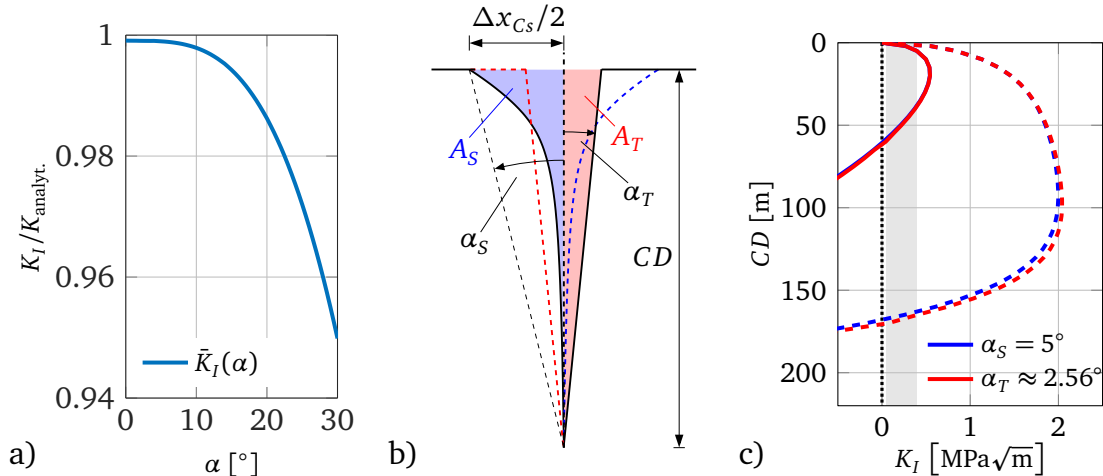

Figure 5.7: a) Resulting normalized SIFs versus opening angle for single edge crack tension test with $a/b = 1/2$; b) quadratic polynomial shaped crack geometry (blue) and associated triangular crack geometry (red); c) resulting SIF versus crack depth for $\Delta u_x \triangleq \sigma_f = 100\,\text{kPa}$ (solid line) and $\Delta u_x \triangleq \sigma_f = 200\,\text{kPa}$ (dashed line)
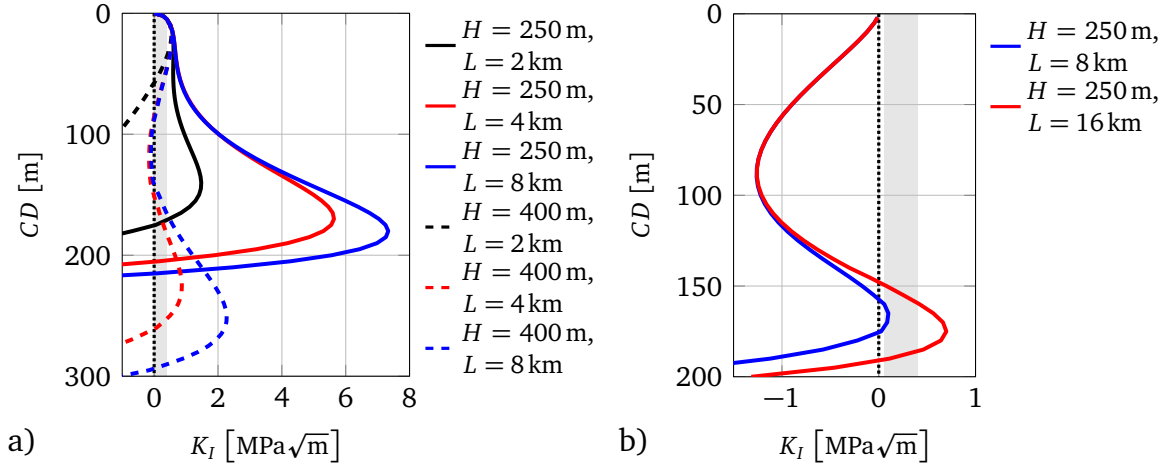
Figure 5.8: SIF versus crack depth for $\alpha_T = 5°$ and a) $\Delta u_x \triangleq \sigma_f = 100\,\text{kPa}$; b) $\Delta u_x \triangleq \sigma_f = 0\,\text{Pa}$

using different domain sizes. Starting from the black solid curve with $H = 250\,\text{m}$ and $L = 2000\,\text{m}$, it shows, that a growing domain length L with fixed thickness H leads to increasing SIF. However, the change in the maximum crack depth is comparatively small and limited by the ice shelf thickness. Going back to the black solid curve and increasing the thickness to $H = 400\,\text{m}$ results in a considerably lower maximum crack depth (black dashed curve). Doubling the domain length to $L = 4000\,\text{m}$ reveals the interesting phenomenon of two separated areas of positive SIF at different depth.

The question may arise if a large opening angle without any tensile remote stress can lead to considerably deep cracks. The answer is YES. For an opening angle of $\alpha = 5°$, an ice shelf thickness $H = 250\,\text{m}$ and a domain length of $L = 8000\,\text{m}$ or $L = 16000\,\text{m}$ positive SIFs occur for crack depths $155\,\text{m} < CD < 175\,\text{m}$ or $145\,\text{m} < CD < 190\,\text{m}$, respectively, as shown in Fig. 5.8 b). The geometric parameters leading to this result might be of rather scientific interest, however they reveal the theoretical possibility of very deep reaching cracks in thick ice shelves under little or zero remote loading and sensitize for the fact that the first stable crack depth must not be mistaken as the maximum possible crack depth.

5.1.4 Summary of the geometric parameter study

In general it can be said, that the influence of the domain length L and the thickness H on $K_I(CD)$ are small as long as the cracks are shallow, e.g. $CD/H < 1/3$. Thin ice shelves tend to be more sensitive to crack growth than thick ones. The most influential geometric parameter is the crack opening angle α, or more precisely, the crack geometry with the associated removed mass over the crack tip. The thickness H of an ice shelf is the only geometric parameter that can be determined to a satisfying extend depending on the global location of the crack situation of interest. The crack geometry and crack depth are hardly known but would be of great value

for the validation of the method and the interpretation of the simulation results. The domain length L must remain a parameter of choice, founded on the mentioned estimations for the chosen boundary conditions. Possible other choices for the lateral boundary conditions will therefore be addressed in the following section.

5.2 Differences in the choice of boundary conditions

The majority of previous studies on crack criticality in ice treated the material as incompressible ($v = 0.5$). The application of a constant or depth-dependent tensile normal stress superimposed by the cryostatic pressure of the ice as vertical boundary condition was widely used. This approach allowed the use of semi-analytical methods for the computation of $K_I(CD)$. Prominent representatives following this approach are Weertman (1973), Van Der Veen (1998a) and Rist et al. (2002). However, this method is restricted to ideally sharp cracks and constant elastic material parameters. Moreover, the applicability of stress boundary conditions for cracks in the ice shelf bulk can be questioned. A variation of the SIFs according to different boundary conditions can be expected and will therefore be investigated in the following section.

5.2.1 Single edge crack tension test

Before applying various boundary conditions to the simplified ice shelf geometry, the general difference between stress and displacement boundary conditions for cracked domains will be shown for the single edge crack tension test. The simulations are performed without additional gravity or bottom pressure in order to ensure compatibility to semi-analytical results. Figure 5.9 shows sketches of the modeled domains with stress, as well as displacement boundary conditions and the resulting deformed shapes with the surface color illustrating the first principal stresses in the domain. Note, that for both cases, the load is equivalent following Eq. (5.1) for the
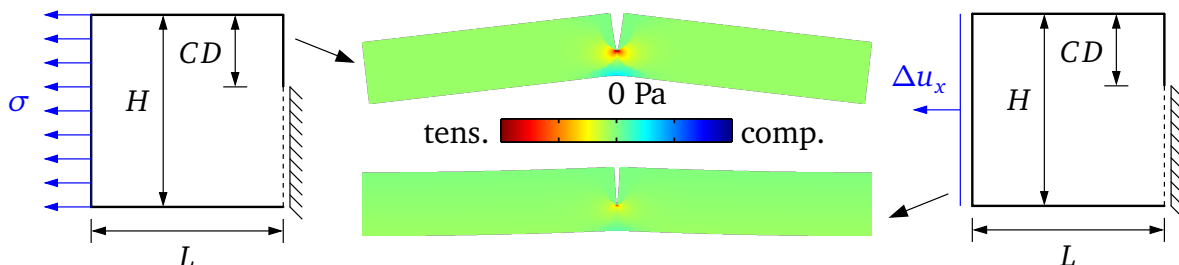

Figure 5.9: Boundary conditions for the single edge crack tension test with stress boundary condition (left) and equivalent displacement boundary condition (right); respective deformed shapes (scale factor 1000) of complete cracked specimen with qualitative values for first principal stress in the middle
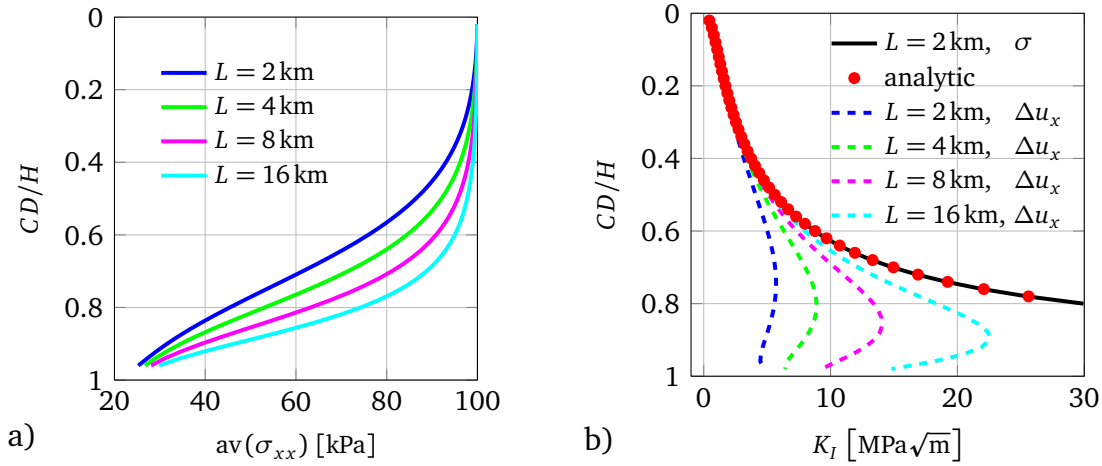
Figure 5.10: a) Averaged reaction stress σ_{xx} at constrained boundary versus CD/H for different domain length L; b) SIF versus CD/H for stress boundary conditions (black line) and displacement boundary conditions (dashed lines) for different domain length L in comparison to semi-analytical results for stress boundary conditions (red dots) following the equations in Fig. 3.5 b)

uncracked domain. The resulting deflections, as well as the principal stresses close to the crack tip are much higher for stress boundary conditions than for the loading by displacements. The difference in the deflections is caused by the fact that boundaries loaded by constrained displacements carry bending moments, which reduce the internal moment in the specimen. The internal moment is related to the bending stress in the domain. Hence, a lower bending moment is one factor causing a reduced stress in the middle of the specimen, where the crack is initiated.

The second factor follows by looking at Fig. 5.10 a) where for the case of constrained displacements, the vertical average of the normal stress at the loaded boundary is plotted versus the normalized crack depth. The initial average stress for the uncracked domain equals the remote stress $\sigma_f = 100\,\mathrm{kPa}$, used for the computation of Δu_x. For growing crack depths, the averaged stress considerably decreases or in other words, crack growth under displacement boundary conditions leads to a softer overall behavior, an effect also known as crack compliance. Increasing the domain length L considerably reduces the influence of the compliance. Figure 5.10 b) presents the resulting SIFs for different boundary conditions and varying domain lengths L. In case of loading by stress boundary conditions, different L yield no deviation in the resulting SIFs, once a minimum length in the order of twice the domain thickness is reached. Therefore, only the results for $L = 2\,\mathrm{km}$ (black line) are plotted. It shows that this length is sufficient to reproduce semi-analytical results for the single edge crack tension test (red dots), which assumes infinitely long domains. In the case of constrained displacements (dashed lines), the influence of the boundary condition reduces with increasing L. Decrescent SIFs for deep cracks result from the just mentioned compliance effect. For $L \rightsquigarrow \infty$, $K_I(CD/H)$ converges to the solution of the problem with stress boundary conditions. Again it appears that for rather shallow cracks ($CD < H/3$) the influence of the boundary conditions

and the domain length on $K_I(CD/H)$ is very small whereas their influence on deeper cracks has to be considered.

5.2.2 Stress and displacement boundary conditions for vertical cracks in ice shelves

The application of displacement boundary conditions on the ice shelf model does not differ from the previous example where Δu_x is computed from the remote stress σ_f for the uncracked situation. However, the loading by stresses needs some additional care. In the case of incompressible material behavior ($\nu = 0.5$), the horizontal normal stress can be computed using $\sigma(z) = \sigma_f + \rho_I g z$ with an upward pointing z-coordinate originating at the ice surface (see Fig. 5.11 for coordinate system). For compressible material behavior, the stress state is not hydrostatic. Hence, the cryostatic pressure acting in vertical direction is not completely transferred to the horizontal direction. In the case of plane strain, the required correction follows from Eq. (2.24) using $\sigma_{yy} = \rho_I g z$ and $\varepsilon_{xx} = 0$. The resulting equation for the boundary stress therefore reads

$$\sigma(z) = \sigma_f + \frac{\nu}{1-\nu}\rho_I g z. \tag{5.4}$$

The influence of different values for ν on the resulting SIFs shall be further emphasized in Sec. 5.3.2. The applied boundary conditions are illustrated in Fig. 5.11 together with the parameters used for the simulations unless differently stated.
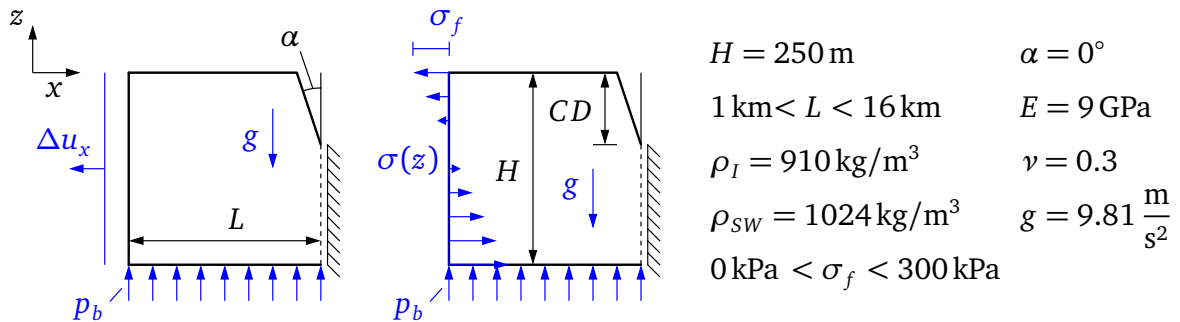

Figure 5.11: Boundary conditions for the ice shelf model with prescribed displacements (left) or equivalent stresses as superposition of the tensile remote stress and an adapted cryostatic pressure (middle); right: parameters used for the simulations

The equations in Fig. 3.5 indicate a linear relation between K_I and the external load σ. This is confirmed by Fig. 5.12 a), where K_I is plotted versus the applied remote stress σ_f for both boundary conditions (indicated by the line color) and at different crack depth (indicated by the line style). Also "unphysical" negative SIFs are shown in order to present the linearity for a wide range of crack depths. As to be expected, differences in the results for stress and displacement boundary conditions predominantly occur for deep cracks. This outcome is supported by Fig. 5.12 b), which shows $K_I(CD)$ for both boundary conditions and a broad spectrum of remote
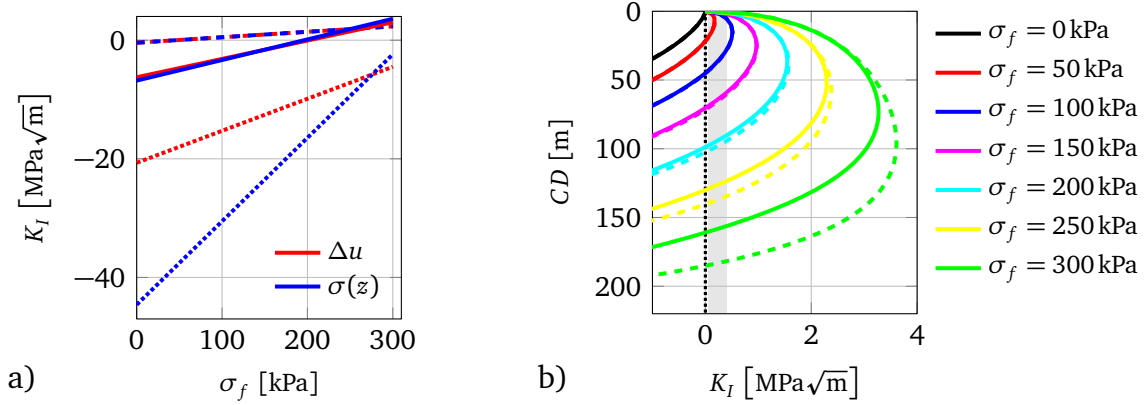
Figure 5.12: a) Linear relation between σ_f and resulting SIFs for both boundary conditions, $L = 2\,\mathrm{km}$, $CD = 20\,\mathrm{m}$ (dashed), $CD = 100\,\mathrm{m}$ (solid), and $CD = 200\,\mathrm{m}$ (dotted); b) SIF versus crack depth for stress boundary conditions (dashed lines) and displacement boundary conditions (solid line), $L = 2\,\mathrm{km}$ and different remote stresses

stresses, concentrating on physical and therefore positive K_I. It appears that in the case of deep cracks, the stress boundary conditions lead to higher $K_I(CD)$ than the equivalent displacement boundary conditions.

The previous chapters show a strong dependence of $K_I(CD)$ on the domain length for deep cracks. In order to verify the influence of the different boundary conditions with respect to the domain length, the set of parameters resulting in the green curves in Fig. 5.12 b) is modeled again with varying L. The simulation results in Fig. 5.13 a) confirm the findings of the single edge crack tension test with both boundary conditions and varying length. Short domain lengths lead to pronounced differences in the resulting K_I. Increasing L reduces the differences between stress boundary conditions and displacement boundary conditions. Not only higher remote stresses but also opening angles of $\alpha > 0$ lead to deeper cracks. Therefore, the differences between stress and displacement boundary conditions are again evaluated for $\sigma_f = 100\,\mathrm{kPa}$ (dark blue curves in Fig. 5.12 b), $\alpha = 5°$, and different domain lengths. The results are illustrated in Fig. 5.13 b). Again it shows, that an increasing domain length considerably reduces the variance in $K_I(CD)$ due to different boundary conditions. The effect of the opening angle together with different boundary conditions however is relevant and has to be taken into account for the choice of a valid boundary condition.

It is appeasing to see, that for the preponderant part of the ice shelf with rather small remote stresses and small opening angles, the choice of the lateral boundary condition has only negligible influence on the resulting K_I. Nevertheless it is important to understand the differences of the boundary condition in order to be able to choose the adequate one in cases where deviations in the results are to be expected. Here, the outcome of both cases with an appropriate domain length and opening angle can be valuable as an upper and lower estimate for the true result. As previously stated, depth-independent horizontal velocities and hence displacements are a key assumption in many ice shelf models. In addition, the crack compliance, only
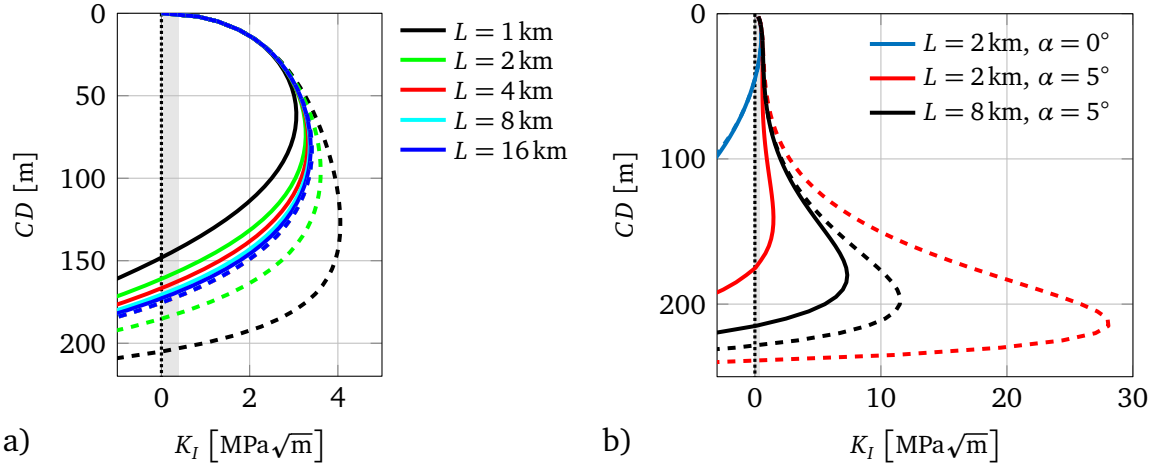
Figure 5.13: SIF versus crack depth for stress (dashed lines) and displacement (solid lines) boundary conditions with a) $\sigma_f = 300\,\text{kPa}$, $\alpha = 0°$ and different domain lengths L; b) $\sigma_f = 100\,\text{kPa}$, $\alpha = 0°$ and $5°$, $L = 2\,\text{km}$ and $8\,\text{km}$

resulting from the application of displacement boundary conditions, is a reasonable feature of the model. Especially in ice dynamical simulations, fractured regions are often implemented as softer domains, in order to be able to reproduce the lower flow stresses in those areas. Hence, unless stated differently, the following simulations of vertical cracks in ice shelves will be performed using displacement boundary conditions in spite of possible dependencies of $K_I(CD)$ on the domain length in the case of deeper cracks.

5.2.3 Neumann or Robin-type boundary condition for the simulation of buoyancy forces

Ice shelves are huge plates that float on the ocean. In order to apply a valid bottom water pressure and to fulfill the vertical equilibrium, two approaches are considered:

$$p_{b1} = \frac{\int\limits_{\Omega} \rho_I(z) g\,\mathrm{d}V}{L_x L_y}, \qquad p_{b2} = \rho_{SW}\, g(z + u_z). \tag{5.5}$$

For p_{b1} the possibly depth-dependent ice density $\rho_I(z)$ and the gravity are integrated over the ice shelf domain and divided by the bottom area (domain length L_x times domain width L_y), which in the two-dimensional case reduces to the domain length L. The vertical equilibrium is fulfilled globally. In the case of varying opening angles and a depth-dependent density, the volume integral has to be evaluated for every crack depth before the solution of the boundary value problem can be started. This additional effort seems unfavorable. However, since the equations to solve are still linear, the integration is quickly carried out within the FE program COMSOL and the overall numerical effort is small.

The Robin-type approach (p_{b2}) fulfills the vertical equilibrium on a rather local scope
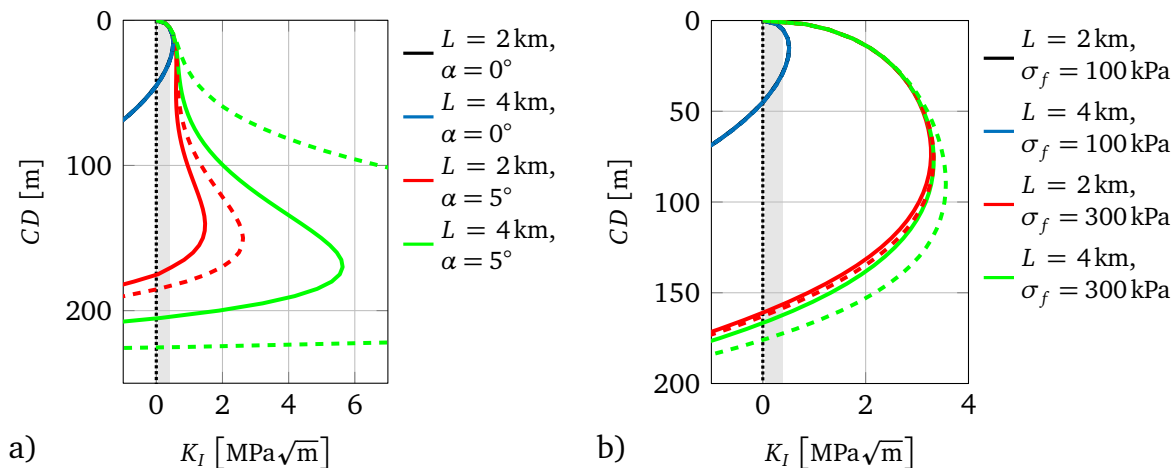
Figure 5.14: SIF versus crack depth for different bottom pressures p_{b1} (dashed lines), p_{b2} (solid lines) and domain length L for a) varying opening angle α using $\Delta u_x \triangleq \sigma_f = 100\,\text{kPa}$ and b) varying remote stress σ_f for the evaluation of Δu_x and $\alpha = 0°$

and is more physically based. This results in a nonlinear system of equations, which will be solved using Newton's method. Fortunately, the increase in computation time is small. An additional benefit of the latter method is the evaluation of the freeboard, which follows as result and can be used as plausibility check for the problem posed. For both boundary conditions, the resulting $K_I(CD)$ are plotted in Fig. 5.14 a) for varying domain lengths and opening angles and in Fig. 5.14 b) for different domain lengths and remote stresses. As already indicated for the vertical boundary conditions in the previous chapter, the type of the boundary condition has no relevant influence on the resulting SIFs for shallow cracks (overlapping blue and black lines). Considerable differences only appear in the case of opening angles $\alpha > 0°$, where an increasing domain length L leads to even more pronounced deviations in the resulting $K_I(CD)$ (Fig. 5.14 a), red and green curves). If deeper cracks result from larger remote stresses, only little influence on the type of bottom boundary condition can be observed, even for longer domain lengths as shown in Fig. 5.14 b).
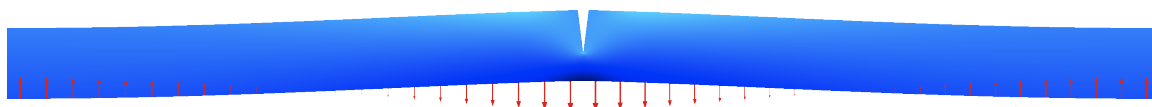

Figure 5.15: Deformed surface plot (first principal stress, scale factor 200) of model loaded by Robin-type bottom pressure p_{b2}; red arrows illustrate $p_{b2} - p_{b1}$.

The reason for the strong influence of the opening angle follows by looking at Fig. 5.15, where the deformed configuration and the difference between the applied bottom pressures p_{b1} and p_{b2} are illustrated. The missing weight of the ice around the crack due to the opening angle results in a local imbalance of vertical forces. This leads to larger displacements in positive z-direction around the crack, the crack is opened and larger SIFs occur. The Robin-type bottom pressure as a function of the vertical displacements attenuates this effect (indicated by the red

arrows). A longer domain length increases the bending moment resulting from the force imbalance around the crack, hence, the stronger the imbalance, the higher is the influence of the domain length.

5.2.4 Summary of the study of different boundary conditions

The influence of the examined boundary conditions on $K_I(CD)$ is strongly related to the geometric parameters domain length L and opening angle α. Whereas shallow cracks in general are insensitive to the type of vertical, as well as horizontal boundary conditions, the influence of different boundary conditions on deeper cracks has to be considered. An opening angle of $\alpha > 0°$ significantly increases the variance due to different vertical and horizontal boundary conditions. Especially striking is the influence of the domain length L: an increasing L results in decreasing differences for changing vertical boundary conditions but in stronger variances in the case of diverse applied bottom pressures. Changing boundary conditions and applied volume forces do not change the linear relation between $K_I(CD)$ and the applied remote stress or equivalent displacement. Unless differently stated, the following simulations are performed using remote displacements at the vertical boundary and a Robin-type boundary condition at the ice shelf bottom.

5.3 The influence of the density and elastic constants

5.3.1 Depth-dependent density profiles

The previous simulations with considerable opening angles showed that the weight of the ice has a strong influence on the resulting SIFs. For this reason it seems obvious to examine the influence of the ice density, the one parameter apart from geometric scales that controls the weight. Rist et al. (2002), Van Der Veen (1998a), Scambos et al. (2000) and Scambos et al. (2009) motivate the application of depth-dependent density profiles for the fracture mechanical analysis of cracks in ice shelves. The WIS experiences regular surface melting, hence, a rather constant density with respect to the depth can be assumed (Braun et al. (2009), Doake (1984)). Nevertheless, in order to study the influence of the density on $K_I(CD)$ in a more general scope, different constant and depth-dependent density profiles are investigated.

Firn densification in the upper ice shelf is dominated by grain settling and packing, depending on the surface temperature and the accumulation rate. Until the density reaches values of $550\mathrm{kg/m}^3$, air cavities within the ice are still connected. Further down, densification is driven by grain growth and sintering. Closed off air bubbles start to form until full pore closure is reached at densities of $820 - 840\,\mathrm{kg/m}^3$. The processes in this regime are not well understood, though the ice temperature

is assumed to be the dominant parameter. Below pore closure, further densification follows by compression of the bubbles.

Firn densification takes place in about the upper $0 - 80\,$m of the ice column. The "bubbly" ice in deeper layers is called meteoric ice. Older layers of meteoric ice might origin from the continental ice sheet. Depending on the location of the ice shelf, the meteoric ice layer can be followed by a layer of clear and bubble-free marine ice formed by freezing of ocean water. The existence of marine ice in the WIS has not been reported (Braun et al., 2009).

One approach, taking into account the different mechanism of densification controlling the density in the depth ranges under consideration here, is the commonly used firn densification model of Herron and Langway (1980). The two-stage model is based on an Arrhenius relation using a time-independent accumulation rate and surface temperature as input. Due to a lack of in-situ measurements of mean surface temperatures and accumulation rates for the WIS, upper and lower bounds are used. Morris and Vaughan (2003) propose the mean annual surface temperature of the WIS to be $-8°\,$C. Seasonal melting and refreezing might increase the mean firn temperature. A drill hole temperature of $-2.5°\,$C at $5.5\,$m depth has been reported by Swithinbank (1988) and will be used as an upper bound. Since the bottom temperature of an ice shelf is limited by the temperature of the ocean ($\approx -2°\,$C), the WIS can be regarded as isothermal. Vaughan et al. (1993) reports an accumulation rate of $a_s = 0.5\,$m/a water equivalent (WE) based on a stake measurement over a short time period. This value will be used as a lower bound. As upper estimate, $a_s = 1\,$m/a will be applied. Figure 5.16 a) presents exponential fits of the density profiles estimated using the method of Herron and Langway (1980). Two additional constant profiles with $\rho_I = 910\,$kg/m^3 (used in previous simulations) and the mean density $\rho_I = 855\,$kg/m^3 of the exponential profile represented by the red solid line are applied in order to compare the results to the findings with constant density. The corresponding SIFs are plotted in Fig. 5.16 b). It shows, that $K_I(CD)$ resulting
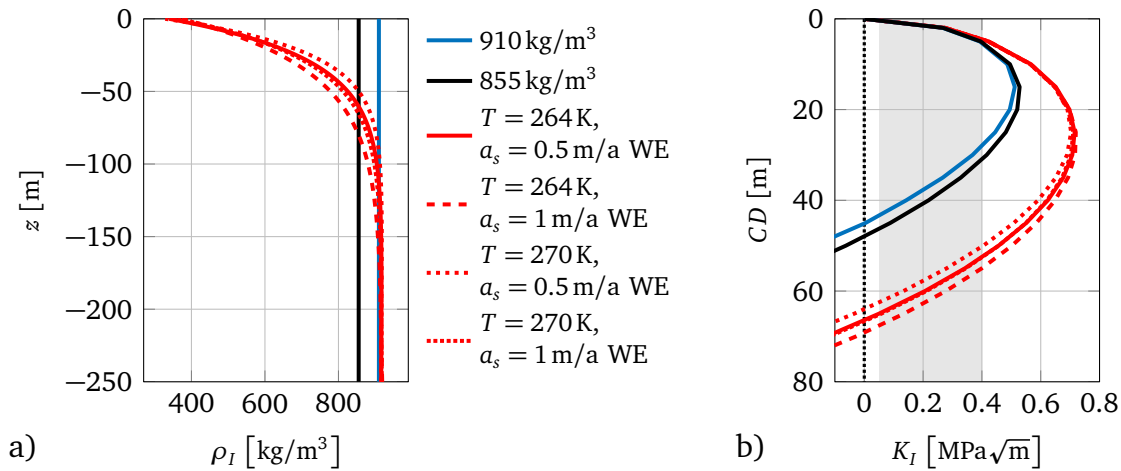

Figure 5.16: a) Applied depth-dependent and constant density profiles; b) resulting SIF versus crack depth for $L = 2000\,$m, $\alpha_T = 0°$, $\Delta u_x \triangleq \sigma_f = 100\,$kPa, $E = 9\,$GPa and $\nu = 0.3$

from different depth-dependent density profiles hardly varies. A slight trend indicates that a density profile with lower curvature $\rho_I(T = 264\,\text{K}, a_s = 1\,\text{m/a WE})$ and hence less ice mass in the upper regime leads to higher $K_I(CD)$ than the profile with the highest curvature $\rho_I(T = 270\,\text{K}, a_s = 0.5\,\text{m/a WE})$. The applied constant profiles lead to considerably lower SIFs. By comparing the black curve with a constant density equivalent to the mean density of the profile $\rho_I(T = 264\,\text{K}, a_s = 0.5\,\text{m/a WE})$ with the results of the associated depth-dependent profile, it appears that not the mean density but the density distribution with respect to the depth has the largest influence on the resulting SIFs. Hence, a lower density in the upper regime leads to less ice overburden pressure at the crack tip and therefore to higher tensile stresses resulting in higher K_I. The presented results reveal the question, how the influence of depth-dependent density profiles interacts with the effects due to different opening angles. The simulation results (not plotted) indicate, that the influence of constant versus depth-dependent density profiles is higher for shallow cracks but declines for deeper cracks.

Rist et al. (2002) and Scambos et al. (2009) suggest density-dependent critical stress intensity factors K_{Ic} ranging from $K_{Ic} = 50\,\text{kPa}\sqrt{\text{m}}$ for low-density firn to $K_{Ic} = 400\,\text{kPa}\sqrt{\text{m}}$ for meteoric ice. More recent measurements of SIFs in ice with a density ranging from 845 to 870 kg/m^3 and resulting mean value of $K_{Ic} = 95\,\text{kPa}\sqrt{\text{m}}$ are published in Christmann et al. (2015). Since the limits of K_{Ic} lead to considerably smaller changes in the consequent crack depth than the different applied density profiles, elastic parameters or opening angles, depth or density-dependent critical SIF will not be considered.

In the following simulations with varying elastic parameters, a constant density of $\rho_I = 910\,\text{kg/m}^3$ is applied. For the study of water-filled cracks, a penetrable upper ice layer together with a distinct pore closure depth is assumed and a depth-dependent density profile will be used.

5.3.2 On the influence of Poisson's ratio

As previously stated, fracture mechanical studies of cracks in ice shelves are often performed using stress boundary conditions instead of volume forces and prescribed displacements. The advantage of this approach follows by the fact that stress boundary value problems and the resulting SIFs are independent on the choice of the elastic parameters E and ν. For this reason, considerations on valid intervals for the elastic parameters in the glaciological community are rare. However, most studies on cracks in ice shelves make an implicit statement via the applied stress boundary condition where the ice overburden pressure is superimposed on a viscous surface stress. Without the application of a correction, as presented in Sec. 5.2, this procedure is only valid for an incompressible material ($\nu = 0.5$). Prominent voices suggesting brittle compressible short time behavior for ice are e.g. Rist et al. (1999), Schulson and Duval (2009), and Hulbe et al. (2010) who use a review of the mechanical properties of snow by Mellor (1975) and Mellor (1977) achieved using
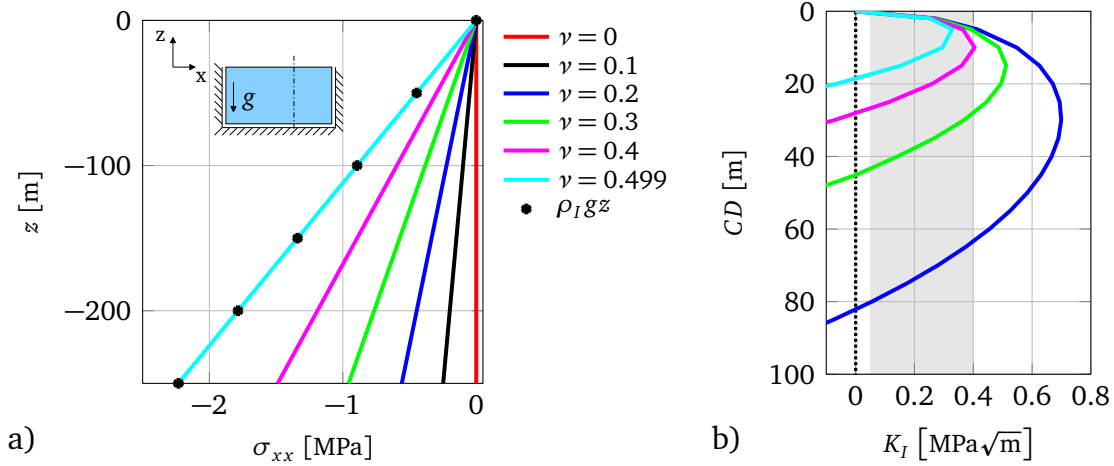
Figure 5.17: a) Horizontal stress σ_{xx} in a constrained uncracked domain under body loads using different Poisson's ratios, hydrostatic pressure (black dots) as reference; b) SIF versus crack depth for different values of Poisson's ratio, $\alpha = 0°$, $L = 2000\,\mathrm{m}$ and $\Delta u_x \triangleq \sigma_f = 100\,\mathrm{kPa}$

wave propagation data. The resulting Poisson's ratios range between $0.2 < \nu < 0.4$. More recent results using $\nu = 0.33$ in the context of viscoelastic modeling of crack initiation at glacier fronts can be found in Koehn and Sachau (2012). Without taking part in the cumbersome discussion on whether, from the fracture mechanical prospective, ice should be treated as solid or viscous fluid, as compressible or incompressible, the aim of the following study with different Poisson's ratios is to sensitize for the huge influence, this material parameter has on the resulting $K_I(CD)$. In addition it should be clarified, that compressibility must not be confused with the durability of a material. The extremely durable diamond with a rather low Poisson's ratio of $\nu = 0.2$ serves as a demonstrative example.

Figure 5.17 a) shows the normal stress σ_{xx} versus the depth z in an isotropic homogeneous body, constrained as illustrated and loaded solely by gravity for different values of Poisson's ratio ν. Additional black dots indicate the ice overburden pressure at the respective depth, $\sigma_{zz} = \rho_I g z$, which is independent of Poisson's ratio. Due to a lack of reliable information on depth or density dependence of Poisson's ratio, only constant values will be used. It shows that only for $\nu \approx 0.5$, the horizontal normal stress equals the cryostatic pressure. The value $\nu = 0.499$ is used as an approximation of the incompressible case ($\nu = 0.5$), which cannot be treated with the applied constitutive law as $\nu = 0.5$ yields an infinite bulk modulus and hence a singular stiffness matrix. For decreasing ν, the horizontal normal stress increases. For $\nu = 0$ (Poisson's ratio of e.g. cork, used for the analytical study in Sec. 4.6.3) the horizontal normal stress disappears. The horizontal and the vertical stress are linked by a constant depending on Poisson's ratio, which in case of plane strain yields $\sigma_{xx} = \frac{\nu}{1-\nu}\sigma_{zz}$, the relation used in Eq. (5.4).

Figure 5.17 b) shows the resulting stress intensity factors $K_I(CD)$ for a displacement load of $\Delta u_x \triangleq \sigma_f = 100\,\mathrm{kPa}$ and a constant density. Note that Poisson's ratio is in-

cluded in the calculation of the displacement boundary condition. As to be expected, $K_I(CD)$ considerably varies for the applied v leading to a maximum crack depth of $CD \approx 20\,\text{m}$ for $v \approx 0.5$ and $CD \approx 80\,\text{m}$ for $v = 0.2$, a change by a factor 4. Lower values for v (not shown here) lead to even larger $K_I(CD)$. The strong variance solely results from the differences in the horizontal stress, induced by the transformation of the cryostatic pressure.

5.3.3 Differences due to depth-dependent Young's moduli

Section 4.6.4 showed a dependence of SIFs on gradients in the elastic material parameters for the single edge crack tension test. The aim for this study is to analyze the influence of depth-dependent Young's moduli on $K_I(CD)$ for the cracked ice shelf model. Rist et al. (2002) and Schulson and Duval (2009) motivate a density related Young's modulus in ice shelf ice ranging from $E \approx 5\,\text{GPa}$ in the upper firn layers to $E \approx 10\,\text{GPa}$ for meteoric ice. According to the exponential fit of the density profile in Fig. 5.16, an exponentially shaped profile for the Young's modulus

$$E(z) = \left[10 - 5\,e^{z/20}\right]\,\text{GPa} \tag{5.6}$$

as visualized in the subplot of Fig. 5.18 a) will be applied. In order to compare the results to the previous findings, two constant values, corresponding to the maximum and the minimum value of the exponential profile, $E = 5\,\text{GPa}$ and $E = 10\,\text{GPa}$, will additionally be used. Though a depth-dependent density causes a depth-dependent Young's modulus, the presented work refrains from a coupled analysis. This approach serves to identify the influence of each parameter separately. Therefore, a constant density of $\rho_I = 910\,\text{kg/m}^3$ and Poisson's ratio $v = 0.3$ are used.

The hitherto constant Young's modulus was used to compute the displacement load according to Eq. (5.1). As equivalent methods for the evaluation of Δu_x in the case of depth-dependent E, two suggestions seem reasonable. The differences between the approaches are visualized in Fig. 5.18 a) by plotting the horizontal normal stress resulting from a simulation of the uncracked domain without applied volume forces. In the subsequent simulations of the cracked specimen, the gravity-induced pressure will naturally be applied.

The first approach regards the surface flow stress resulting from the measured velocity field as given and set. Hence, Young's modulus at the surface, $E(z = 0)$, has to be used for the computation of Δu_x. At the ice shelf surface, the resulting horizontal normal stress (black dashed line) equals the remote stress. Considerably higher tensile stresses appear at lower depth.

In the second approach, Δu_x is chosen such that the averaged horizontal normal stress of the uncracked domain without body forces equals the given surface flow stress. This results in the black solid line in Fig. 5.18 a), where the tensile stress in the upper layers are much lower than the remote stress of $\sigma_f = 100\,\text{kPa}$.

In order to demonstrate the influence of a depth-dependent Young's modulus on
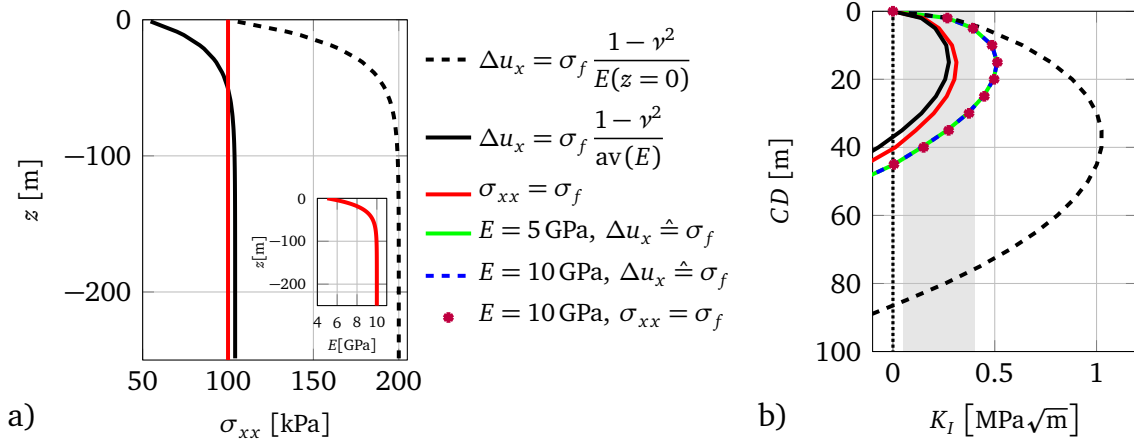
Figure 5.18: a) Horizontal normal stress resulting from simulation of uncracked domain without applied gravity using different boundary conditions and an exponentially shaped Young's modulus (subplot); b) resulting SIF versus crack depth for cracked domain with applied gravity; both plots use $L = 2000\,\text{m}$, $\alpha = 0°$ and $\sigma_f = 100\,\text{kPa}$

$K_I(CD)$ separated from its influence on the displacement boundary condition, the stress boundary condition, as introduced in Eq. (5.4), will be used for comparison. The associated constant normal stress resulting from the simulation without volume forces is illustrated in Fig. 5.18 a) by the solid red line. The horizontal normal stresses resulting from simulations with different constant Young's moduli and displacement or stress boundary conditions (green and blue lines, pink dots) equal the normal stress presented by the solid red line and are not shown in Fig. 5.18 a). In Fig. 5.18 b), the solid green and the overlapping blue dashed lines show, that different constant Young's moduli do not change the outcome of the simulation as long as the boundary displacement Δu_x are adapted. In case of an exponentially shaped Young's modulus the influence on the applied boundary displacement leads to pronounced differences in the resulting $K_I(CD)$. As to be expected, the first approach (dashed black line) with higher tensile stresses leads to considerably higher K_I. The second approach (solid black line) with the lowest stress in the upper range of the ice shelf yields the lowest SIFs.

Also in case of stress boundary conditions, variances due to the gradient in E appear. A comparison of the SIFs resulting from a depth-dependent Young's modulus (red solid line) and those with constant E (pink dots) illustrates the direct influence of $E(z)$ on $K_I(CD)$. It shows, that for the chosen profile, the variance in Young's modulus reduces the resulting SIFs to some extend.

5.3.4 Summary of the studies with different material parameters

The variation of the density, Poisson's ratio, as well as Young's modulus showed a considerable influence on the resulting SIFs. Whereas the consideration of a reason-

able depth-dependent density leads to increasing $K_I(CD)$, the influence of a depth-dependent Young's modulus is linked to the applied boundary condition and needs a more differentiated interpretation. Different constant Poisson's ratios show the strongest influence on the resulting $K_I(CD)$. The decisions about the most reasonable value for ice should be left to experimentalists. Overall it can be said, that under the given load and ice shelf thickness, none of the simulated setups leads to deep or completely penetrating cracks.

5.4 Comparison to the study of Rist et al. (2002)

Now, as the influence of the geometry, the different boundary conditions and the material parameters are well understood, the FE model is compared to the model of Rist et al. (2002). In order to compute SIFs for single surface cracks in the 422 m thick Ronne Ice Shelf, the authors introduce a semi-analytical approach. Therefore, the crack flanks are loaded by a depth-dependent normal stress. Using balance equations, as introduced by Weertman (1957), which include the common power law for the ice flow following Glen (1958), the equation for the crack flank load reads

$$\sigma_{\text{tot.}}(z) = \frac{B}{\int_b^s B \mathrm{d}z} \left\{ g \int_b^s \int_z^s \rho_I(\tilde{z}) \mathrm{d}\tilde{z} \mathrm{d}z - \frac{g}{2\rho_{sw}} \left(\int_b^s \rho_I(z) \mathrm{d}z \right)^2 \right\} - g \int_z^s \rho_I(\tilde{z}) \mathrm{d}\tilde{z}. \quad (5.7)$$

Herein, the depth-dependent density $\rho(z)$ based on measurements of ice cores is parameterized by

$$\rho_I(z) = \left(918 - 539 e^{\frac{z-h}{32.5}} \right) \text{kg/m}^3. \quad (5.8)$$

Note, that with the z-coordinate now originating at sea level, h describes the extent of the freeboard. The letters s and b denote the top and the bottom of the ice shelf, respectively. The seawater density is $\rho_{sw} = 1028\,\text{kg/m}^3$. For further information on the temperature and depth-dependent rate factor $B(z)$, the applied temperature profiles, and experimental measurements of critical SIFs, the reader is referred to the detailed information in Rist et al. (2002). Figure 5.19 a) illustrates the total horizontal normal stress (black line), as well as its tensile and compressive contributions in red and blue, respectively.

For the evaluation of $K_I(CD)$, Rist et al. (2002) apply the weight function method. This approach has been introduced by Bueckner (1970) and was transferred to the problem of a single edge crack in a finite plate using a higher order power shaped load on the crack flanks by Fett et al. (1990). For the application of this method to the presented problem, the exponentially shaped load $\sigma_{\text{tot.}}(z)$ is recast into a polynomial equation of order n reading

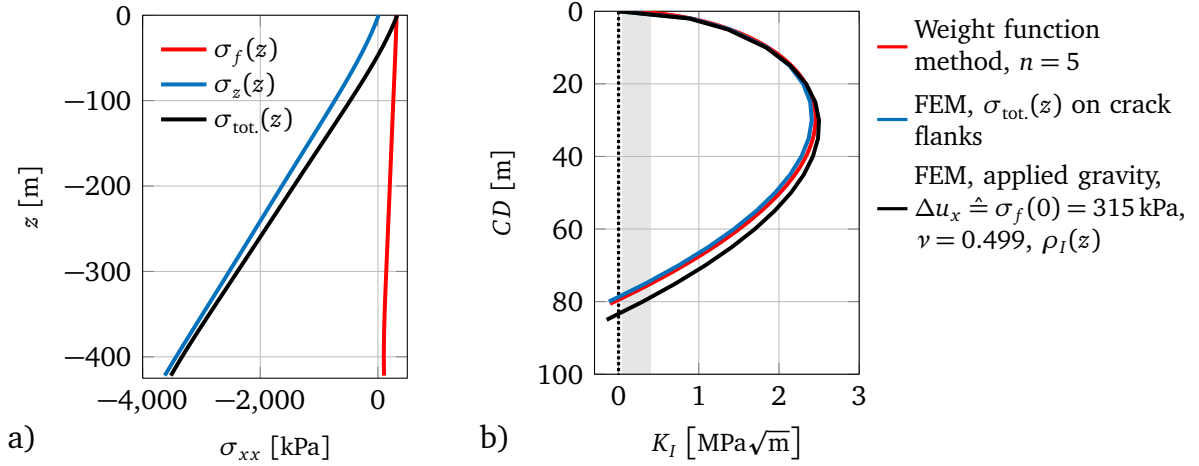$$\sigma_p(a/H) = \sum_n C_n \left(\frac{a}{H} \right)^n, \quad (5.9)$$

Figure 5.19: a) Applied depth-dependent total stress and the contributing components resulting from the ice shelf flow and the cryostatic pressure; b) resulting $K_I(CD)$ using the weight function method and two different FE setups

with the distance from the top surface of the ice shelf, a, and the coefficients C_n. The SIFs are then computed using

$$K_I = \sqrt{CD\pi} \sum_n C_n F_n \left(\frac{CD}{H}\right)^n. \tag{5.10}$$

Therein the coefficients F_n are a set of weighting factors and can be found in Rist et al. (2002) or Fett et al. (1990). Figure 5.19 b) shows the resulting $K_I(CD)$ for $n = 5$ (red line) together with the FE solution of the identical mechanical problem (blue line). Small differences between the semi-analytical method and the FE simulation result from numerical inaccuracies of both methods. The black line shows the results from a FE simulation applying a depth-independent displacement boundary condition, Δu_x, that is computed by use of the tensile stress at the top surface $\sigma_f(z = 0) = 315\,\text{kPa}$. Additionally, gravity with the depth-dependent density profile of Eq. (5.8) and $\nu = 0.499$ are applied. The deviation from the previous findings results from the differences in the models, especially in the depth-varying flow stress $\sigma_f(z)$, which has not been considered in the latter simulation.

The FE simulation with body loads and displacement boundary conditions is in good agreement with results shown by Rist et al. (2002). Additionally it appears, that the computationally fast semi-analytical approach yields very satisfying results for the presented problem. With some further effort, the semi-analytical method could as well be expanded to depth-dependent Young's moduli and compressible material behavior. However, the comprehension of more complex geometries (influence of the opening angle), multiple cracks in a finite geometry, and arbitrary load fields is reserved to numerical methods, e.g. the finite element method, which together with the concept of configurational forces yields promising results.

5.5 Water-filled cracks

The previous sections showed that changing material parameters and loading have a strong influence on the criticality at the crack tip. Nevertheless, dry cracks are very unlikely to penetrate to the bottom of an ice shelf under the given loading, since the weight of the ice tends to close the crevasses at an early stage. Only large opening angles or considerably high remote stresses lead to very deep or even penetrating cracks. However, completely penetrating crevasses in ice shelves have been observed. Therefore, it seems reasonable to consider some additional loading for example due to water of different origin inside the crevasse. This suggestion has first been analyzed by Weertman (1973), was revived by Smith (1976), extended to depth-dependent ice densities by Van Der Veen (1998a) and Rist et al. (2002) and later on applied by e.g. Scambos et al. (2000), Van Der Veen (2007) or Scambos et al. (2009), just to mention a few. All mentioned studies treated ice as incompressible ($\nu = 0.5$), overestimating the influence of the crack closing ice overburden pressure σ_{zz}, as shown in Sec. 5.3.2. Van Der Veen (2007) stated that the water level inside a crevasse must remain near the ice surface to yield deep penetration. The aim of the following study is to show that for $\nu = 0.3$, much less water is needed for deep penetration. In addition, the influence of the opening angle α will again be emphasized. First, the study concentrates on water-filled surface cracks, distinguishing between a filling by meltwater or by brine. In a next step, water-filled bottom cracks are discussed.
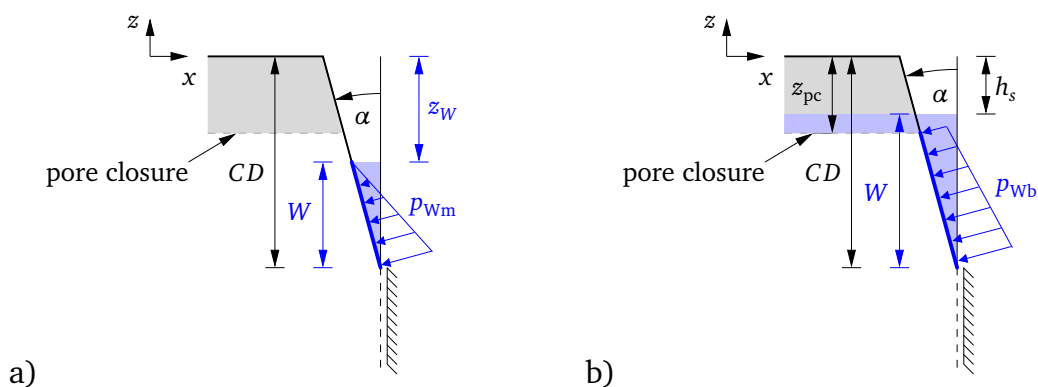
5.5.1 Surface cracks

Figure 5.20: Illustration of the additional pressure boundary condition on the crack faces due to a filling of a) meltwater and b) brine

In order to simulate water-filled surface cracks, a geometry equivalent to Fig. 5.3 with an additional pressure at the crack faces (illustrated in Fig. 5.20 a and b) will be used. A depth-dependent density profile with $T_s = 264\,\text{K}$ and $a_s = 0.5\,\text{m/a}$ (Fig. 5.16 a) and pore closure at approximately $z_{\text{pc}} = -50\,\text{m}$ is applied.
The first setup considers the filling by meltwater. Therefore, the crack depth is kept

constant at the depth for which the SIFs of the unfilled crack changed sign. Different reference situations without water filling using prescribed boundary displacements equivalent to $\sigma_f = 100\,\text{kPa}$ and opening angles of $\alpha = 0°$, $0.1°$, $0.5°$, $1°$ and $2°$ are considered. The associated maximum crack depths are listed in Tab. 5.1.

α	$0°$	$0.1°$	$0.5°$	$1°$	$2°$
CD_{max}	$66\,\text{m}$	$67\,\text{m}$	$70\,\text{m}$	$73\,\text{m}$	$85\,\text{m}$

Table 5.1: Maximum crack depth for dry cracks with prescribed boundary displacement $\Delta u_x \triangleq \sigma_f = 100\,\text{kPa}$, different opening angles α using $\nu = 0.3$ and a depth-dependent density profile $\rho_I(T_s = 264\,\text{K}, a_s = 0.5\,\text{m/a})$. The maximum crack depth CD_{max} is reached when $K_I(CD) < 0$ for all $CD > CD_{\text{max}}$.

The previously stable cracks are simulated with respect to different water levels W up to a maximum level where the water surface reaches pore closure. It is assumed that further meltwater supply disperses through the permeable firn and therefore does not increase the water column inside the cracks. The equation for the depth-dependent additional water pressure inside the crack reads

$$p_{\text{Wm}}(z) = \rho_W g(W - CD - z) \quad \text{for} \quad z < -CD + W, \tag{5.11}$$

with the density of fresh water, $\rho_W = 1000\,\text{kg/m}^3$. Figure 5.21 a) illustrates resulting SIFs with respect to the vertical position of the water surface for an increasing water column inside the crack using different opening angles α. It appears that only a small amount of water is needed to gain SIFs within the range of critical SIFs. A water column of $W \approx 10$ to $12\,\text{m}$ results in SIFs beyond typical critical values and leads to further crack growth.

Figure 5.21 b) demonstrates how deep an ideally sharp crack with varying maximum water supply can grow before a stable situation is reached. Basis for the simulation is a dry, $66\,\text{m}$ deep crack, filled by meltwater. The water level within the crack is on the one hand constrained by pore closure at $50\,\text{m}$ depth, on the other hand by a limited water supply in terms of a maximum water column inside the crack. The blue solid line shows resulting $K_I(CD)$ for unlimited supply. It appears that this condition leads to a complete penetration of the crevasse. If the water supply is limited at a maximum height of $W_{\text{max}} = 50$ or $100\,\text{m}$, the crack propagates considerably deeper than for the unfilled setup. However, the water pressure is not sufficient to result in a complete breaking through of the crevasse. The remaining setup with $W_{\text{max}} = 150\,\text{m}$ was simulated with $\Delta u_x \triangleq \sigma_f = 100\,\text{kPa}$ (solid line) and $\Delta u_x = 0\,\text{m}$ (dashed line). Though it can be argued how a crack is supposed to grow deeper than $50\,\text{m}$ without any external loading before it is eventually filled by meltwater, the plot clearly indicates that also limited water supply can lead to a complete breaking through of a crevasse even in absence of additional external loading. The value $W_{\text{max}} = 3/5H$ which leads to a complete collapse in the presented scope is con-
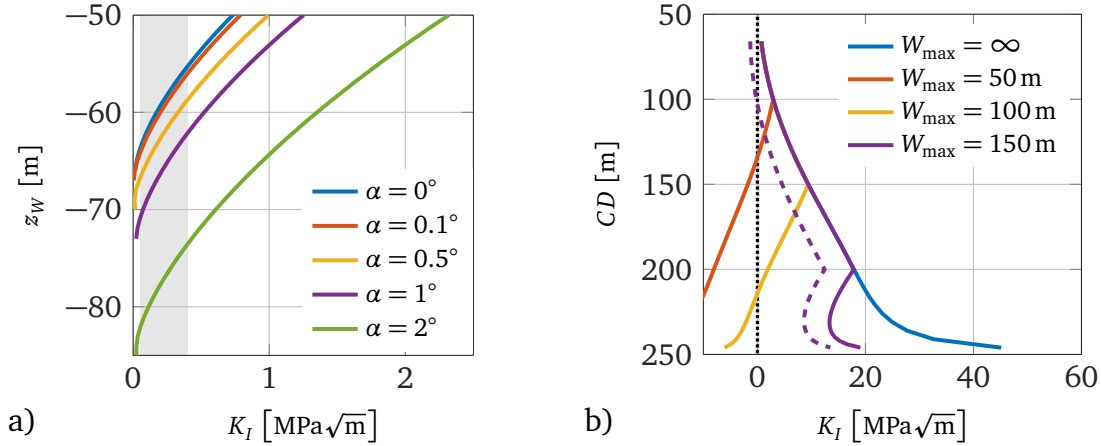
Figure 5.21: a) Resulting SIFs versus position of the water surface $z_W = -CD + W$ for different initially dry starter cracks; b) $K_I(CD)$ for crack growth of an initially 66 m deep crack filled by meltwater up to defined maximum water levels W_{max}; solid lines result from $\Delta u_x \triangleq \sigma_f = 100\,\mathrm{kPa}$, the dashed line from $\Delta u_x \triangleq \sigma_f = 0\,\mathrm{kPa}$

siderably lower than required water levels predicted by Van Der Veen (1998a) and Smith (1976). The reason for this difference is mainly based on the different choice of Poisson's ratio as illustrated in Fig. 5.22 a). Here, $K_I(CD)$ is plotted with respect to the water level W within a 240 m deep crack for constrained lateral boundaries ($\Delta u_x \triangleq \sigma_f = 0\,\mathrm{kPa}$) and compressible (blue line), as well as nearly incompressible material behavior (red line). Whereas the red line supports the general finding by Van Der Veen (1998a), the blue line indicates that the assumption of compressibility results in considerably less water needed for a complete penetration of the crack. A limited water level due to permeable firn above pore closure is ignored in this scope. It should be noted that in the case of an opening angle $\alpha > 0°$, a virtually infinite water supply is available since the crack propagates ideally sharp, and very little water volume is required for a complete fill of the freshly created space.

The second setup analyses crack growth of a single crevasse in areas where brine infiltration occurs. Whereas brine infiltration can usually be found close to the ice front, where seawater drains through the permeable firn layer of the ice shelf, Braun et al. (2009) and Vaughan et al. (1993) report comprehensive brine infiltration at the WIS. Figure 5.20 b) illustrates the boundary conditions used for the simulation. All cracks are filled up to sea level, once the respective crack depth is reached. However, for crack face segments between pore closure and sea level, the pressure of brine inside the ice shelf, as well as on the crack faces compensates and does not increase the stress intensity at the crack tip. The load on the crack faces therefore rises linearly from $p_{\mathrm{Wb}}(z = z_{\mathrm{pc}}) = \rho_{\mathrm{Wb}} g(-h - z_{\mathrm{pc}})$ with the freeboard h to $p_{\mathrm{Wb}}(z = -CD) = \rho_{\mathrm{Wb}} g W$. Scambos et al. (2009) gives the density of brine in equilibrium with ice at a temperature of $T_I = -8°$ to be $\rho_{\mathrm{Wb}} = 1084\,\mathrm{kg/m^3}$ which will be used in the following computation.

Figure 5.22 b) illustrates resulting SIFs versus crack depth for different Poisson's ratios and prescribed lateral displacements. For $CD < -z_{\mathrm{pc}}$, the resulting SIFs are
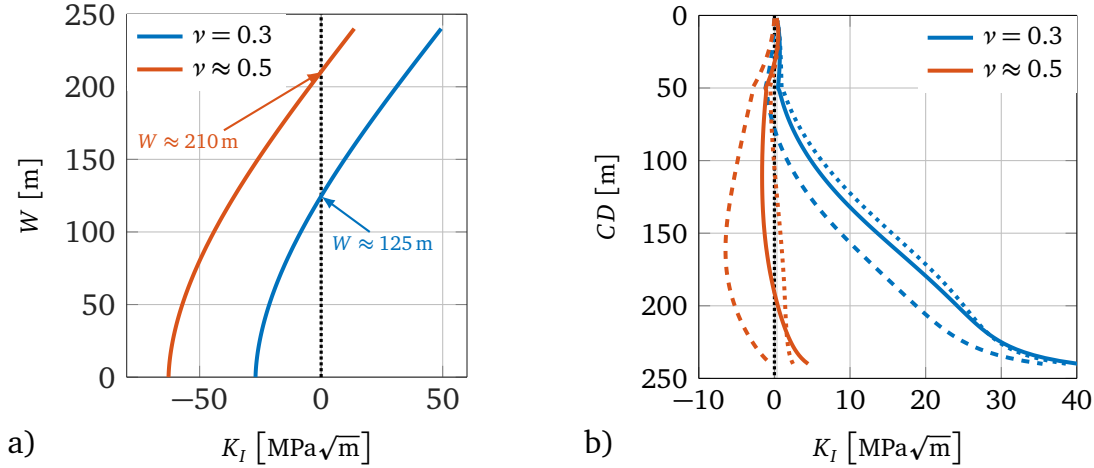
Figure 5.22: a) SIFs versus water level W for ideally sharp crack with $CD = 240\,\text{m}$, $\Delta u_x \triangleq \sigma_f = 0\,\text{kPa}$ using $\nu = 0.3$ (blue line) or $\nu \approx 0.5$ (red line); arrows indicate minimum water level needed to keep the crack open; b) SIFs versus crack depth resulting from the simulation of brine infiltration; line color indicates value for Poisson's ratio, the solid lines represent a constrained boundary displacement $\Delta u_x \triangleq \sigma_f = 100\,\text{kPa}$ and $\alpha = 0°$, the dashed lines $\Delta u_x \triangleq \sigma_f = 0\,\text{kPa}$ and $\alpha = 0°$, the dotted lines $\Delta u_x \triangleq \sigma_f = 100\,\text{kPa}$ and $\alpha = 5°$

equal to those of the dry setup. Once the cracks passes this internal boundary, the influence of the water pressure becomes apparent. The previous results indicated, that surface cracks filled by brine will lead to a breaking through of the crevasse, once the crack tip reaches pore closure. The illustrated SIFs support this suggestion, at least for Poisson's ratio $\nu = 0.3$, indicated by the blue lines. For incompressible material behavior, shown by the red lines, larger external loading, a considerable amount of water or larger opening angles (red dotted line) are needed to result in a breaking through of the crevasse.

5.5.2 Bottom cracks

The first study on the propagation of bottom crevasses in ice can be found in Weertman (1973) and Weertman (1980). A more advanced linear elastic fracture mechanics approach with depth-dependent density was published by Van Der Veen (1998b). Using edge dislocation functions for the semi-infinite domain, Weertman (1980) approximates the depth of a water-filled bottom crevasse in a floating ice shelf with

$$CD_{\text{bottom}} \approx \pi H / 4. \tag{5.12}$$

Therefore, he evaluates the average value of the remote flow stress $\sigma_f = \Delta \rho g H / 2$ applying hydrostatic equilibrium for an incompressible ice shelf. The factor $\Delta \rho$ is the difference between the water and the ice density, whereof the latter is assumed to be constant with depth. Applied to the $H = 250\,\text{m}$ thick ice shelf with an assumed constant density of $\rho_I = 910\,\text{kg/m}^3$ this results in $\sigma_f \approx 110\,\text{kPa}$ and $CD_{\text{bottom}} \approx 196\,\text{m}$. This very simple crevasse depth model will now be compared to the FE simulation
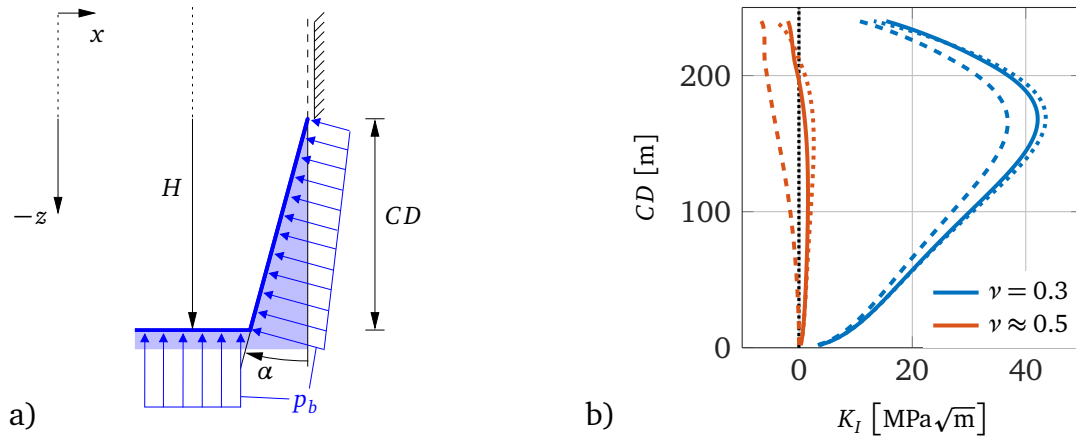
Figure 5.23: a) Pressure boundary conditions for water-filled bottom crack; b) SIFs as a function of the crack depth for water-filled bottom crack, line color indicates value for Poisson's ratio, line style illustrates constrained boundary displacement $\Delta u_x \triangleq \sigma_f = 100\,\text{kPa}$ with $\alpha = 0°$ (solid lines), $\Delta u_x \triangleq \sigma_f = 0\,\text{kPa}$ with $\alpha = 0°$ (dashed lines) or $\Delta u_x \triangleq \sigma_f = 100\,\text{kPa}$ with $\alpha = 5°$ (dotted lines)

using a upside down version of the geometry in Fig. 5.3 with pressure boundary conditions at the ice bottom and the crack faces as illustrated in Fig. 5.23 a). Resulting SIFs as a function of the crack depth are shown in Fig. 5.23 b) for compressible, as well as incompressible material behavior using $\Delta u_x \triangleq \sigma_f = 100\,\text{kPa}$ and $\Delta u_x \triangleq \sigma_f = 0\,\text{kPa}$. It appears that the approximated solution by Weertman (1980) agrees very well to the FE solution for $\nu \approx 0.5$ and $\Delta u_x \triangleq \sigma_f = 100\,\text{kPa}$, leading to crack closure at approximately $CD = 200\,\text{m}$. In addition Fig. 5.23 b) shows, that the incompressible setup without external loading does not result in crack opening at all.

Applying compressible material parameters considerably changes the outcome of the simulation. Independent on the external loading, the crack reaches the upper surface of the ice shelf. This could only be avoided by assumption of a remote backstress, hence applying a compressive remote loading. This was first suggested by Thomas (1973), applied to crevasse penetration by Jezek (1984), and later on used by Van Der Veen (1998b) and Rist et al. (2002).

Previous simulations with dry cracks showed a considerable influence of the crack opening angle α. In order to analyze the impact of the crack opening on bottom cracks, the setup with $\nu \approx 0.5$ and $\Delta u_x \triangleq \sigma_f = 100\,\text{kPa}$ is simulated using $\alpha = 5°$. The associated dotted red line in Fig. 5.23 b) indicates, that this rather pronounced opening angle leads to a small increase of the resulting crack depth but does not affect the overall result.

5.5.3 Discussion on crack healing due to freezing

The previous section showed, that by assuming a compressible material behavior, bottom cracks lead to a complete collapse of the crevasse unless considerable com-

pression on the remote boundaries is applied. Nevertheless, several publications document the existence of stable bottom crevasses that do not reach the surface, e.g. Clough (1974), Jezek et al. (1979), Weeks and Mellor (1978) or more recently Nath and Vaughan (2003) and Luckman et al. (2012). This arises the question, which processes can possibly lead to crack arrest. Weertman (1980) and Van Der Veen (2007) suggest to consider freezing of the water at the faces of a crevasse, which does not only prevent a further penetration of the crack, but eventually might even lead to crack healing. This suggestion is all the more valid if the propagating crack is considered to be ideally sharp and the space between the newly built faces and therefore the water layer in-between very thin. Following Van Der Veen (2007), the thickness d_I with respect to time of a layer of frozen water on an ice surface with the initial temperature T_0 can approximately be computed using

$$d_I = 2\frac{c_p(T_m - T_0)}{\sqrt{\pi}L_h}\sqrt{\frac{k}{\rho_I c_p}t}. \tag{5.13}$$

With the melting temperature of water $T_m = 0°$, an approximated initial temperature of the surrounding ice $T_0 = -3°$, the specific heat of ice $c_p = 2100\,\text{J/(kg\,K)}$, a latent heat of $L = 334000\,\text{J/kg}$, the conductivity of ice $k = 2.1\,\text{W/(m\,K)}$, and the density $\rho_I = 910\,\text{kg/m}^3$, the layer grows approximately $0.2\,\text{mm}$ within the first minute or $1.3\,\text{mm}$ within an hour. These values are negligibly small if opening angles of $\alpha > 1°$ are considered as supposed by Van Der Veen (2007) who assumes crevasse widths of $10\,\text{m}$. Furthermore, Van Der Veen (2007) argues that freezing might be compensated by viscous dissipation. If, in addition, the crack is assumed to propagate very fast, freezing processes might be too slow to dominate. On the other hand, Weertman (1980) argues that ideally sharp crevasses, only opened by elastic deformation, freeze shut after few minutes. Therefore, he considered additional creep opening of the crevasse, which, depending on the thickness of the ice shelf and the temperature difference between the water and the ice, might lead to crevasses with a stable depth.

5.5.4 Summary of the studies on water-filled cracks

The simulation of water-filled cracks demonstrated the considerable impact of the additional load at the crack faces on the resulting SIFs. For the ice shelf without compressive remote stress, with the given geometry, density and compressible material behavior this resulted in a complete penetration of former stable surface crack once the water level W inside the crack exceeded half the ice thickness. Also bottom cracks proved to be highly unstable. The most influencing parameter was Poisson's ratio. For ideally sharp cracks, the possibility of crack arrest due to freezing can be considered but was not further analyzed at this point.

5.6 Frost wedging as reason for ice shelf disintegration

In a glaciological context the term "disintegration" is commonly used for the abrupt collapse of larger ice shelf parts. Well known incidents are the collapse of the Larsen A ice shelf, the disintegration of large parts of Larsen B ice shelf(Glasser and Scambos, 2008), as well as the collapse of parts of the WIS. The initiation of these events is usually linked to meltwater, supra-glacial lakes and a general thinning of the ice shelf. Several ideas exist to explain the sudden collapses such as the suggestion of MacAyeal et al. (2003) and MacAyeal et al. (2009), who link disintegration to a chain reaction of tipping over of thin icebergs and resulting glaciogenic tsunamis. The previous chapter showed the influence of meltwater on crack criticality and confirmed the possibility of water filling in cracks as reason for ice shelf collapse. In addition, it hinted towards the influence of freezing processes within the water-filled crevasse on crack criticality. The direct link between meltwater and disintegration events is confined to events that happened during the melting season in the Antarctic summer. Braun et al. (2009) and Scambos et al. (2009) published very thorough observations of the March 2008 disintegration event at the WIS bridge. Happening at the end of the melt season, Scambos et al. (2009) links this event to meltwater induced propagation of crevasses that opened due to bending of the ice shelf front. Taking into account measured surface temperatures of the corresponding days however reveals the possibility of a more complex frost wedging mechanism.

Figure 5.24 a) shows the WIS. The red box marks the location of the ice shelf bridge. In Fig. 5.24 b), the red area indicates the region before the collapse. The remaining part of the bridge and the floating bridge fragments are shown in Fig. 5.24 c). Further satellite images of lower quality, and hence not shown here, confine the break-up event to the evening of the 28th of February 2008. The solid line in Fig. 5.24 d) (top graph) shows measured dry bulb temperatures at the British research station Fossil Bluff. The location of the station in approximately 240 km distance from the ice shelf bridge is indicated by a red star in Fig. 5.24 a). The pronounced temperature drop at the end of February coincides with the break-up event. Further temperature data from Rothera research station in approximately 420 km distance from the WIS bridge confirms a temperature drop for the respective period but shows considerably larger mean temperatures. Measurements of the wind speed at both stations as illustrated in Fig. 5.24 d) (lower graph) indicate moderate winds during that time. The temperature and weather conditions at the WIS bridge in lower altitude and closer to the open water then Fossil Bluff and less shielded than both stations might differ from the plotted ones, the overall trend, however, can be assumed to be similar.

Since the WIS is known for surface meltwater, the prerequisites for frost wedging as disintegration cause are given and the thermodynamic and mechanical processes involved will be investigated in the following.
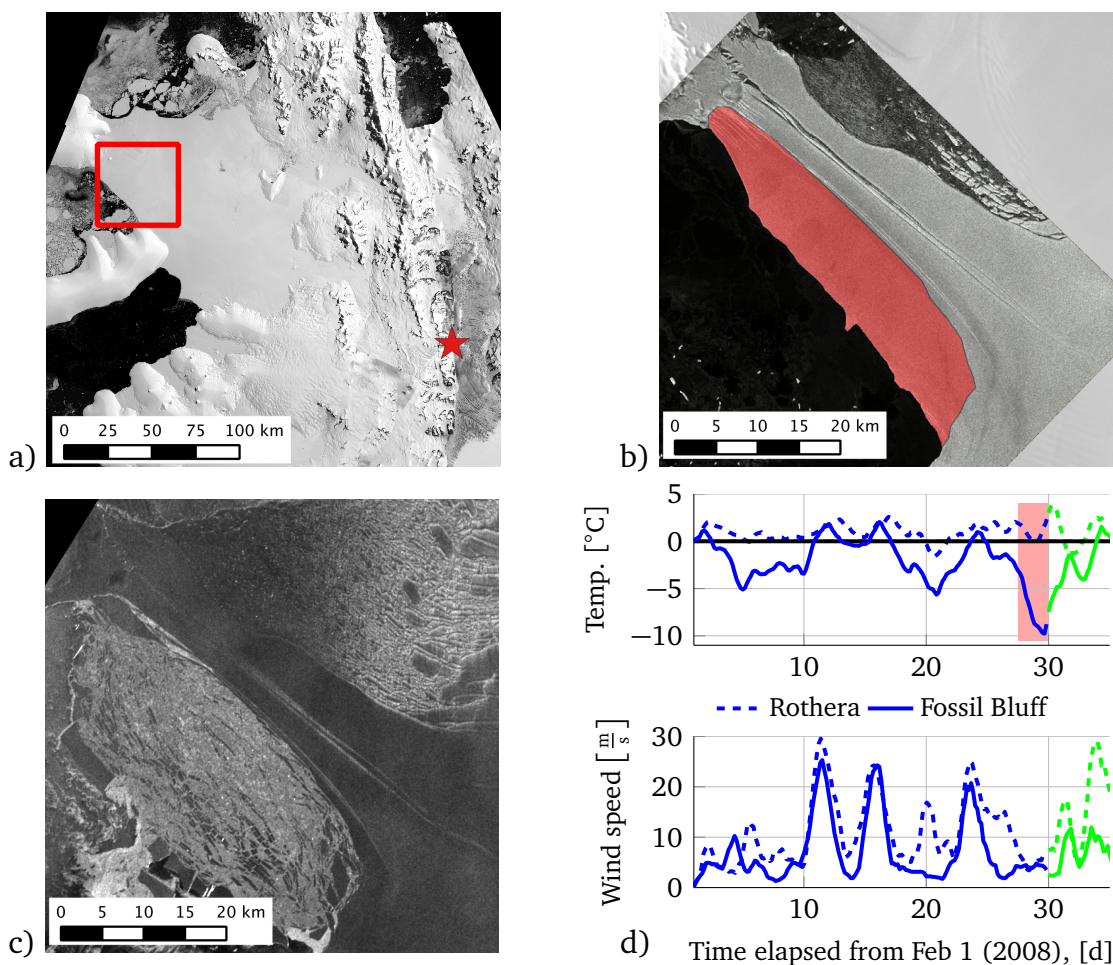
Figure 5.24: a) WIS with ice shelf bridge marked in red (MOA 2003/04, ©NSIDC), red star indicates position of Fossil Bluff station; b) ice shelf bridge, 30.07.2007, (ALOS PAL-SAR, ©TPMO), red area marks zone before collapse; c) ice shelf bridge after collapse, 07.03.2008, (ENVISAT ASAR ©ESA); d) dry bulb temperatures and wind speed at Fossil Bluff Station and Rothera Station, source: BAS, red area marks period of collapse

The general idea of the mechanism is sketched in Fig. 5.25 where a stable dry crack is filled by meltwater during a warm period to an extend that does not cause a breaking through of the crevasse. In a following temperature drop as indicated by Fig. 5.24 d), ice crystals start to grow in the water-filled crevasse. They rise to the water surface due to their lower density and eventually form a closed lid sealing the remaining water. Continuing freezing inside the crevasse now displaces the remaining water, which cannot escape through the closed lid. Hence an additional pressure builds aiming to open the crack, which then leads to further growth of the previously stable crevasse.

Before introducing a fracture mechanical frost wedging model, a thermodynamic investigation including phase transformation is used to estimate the possible ice layer that can form in a water-filled crevasse due to temperatures within the range of those illustrated in Fig. 5.24 d).
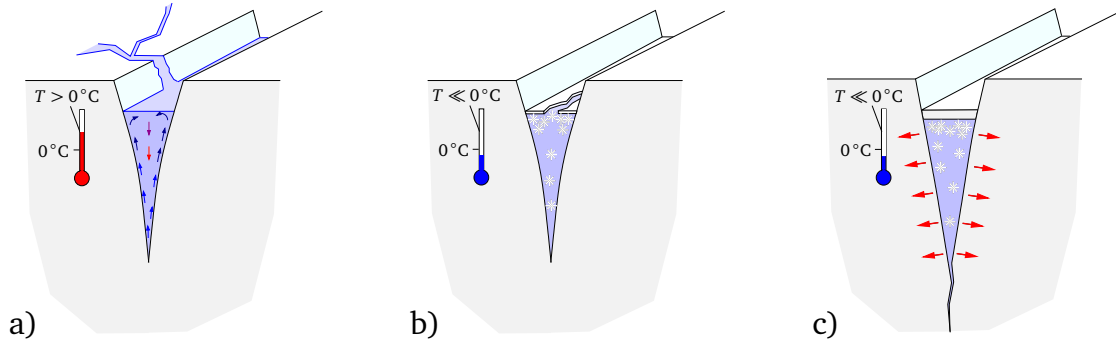
Figure 5.25: Illustration of frost wedging process with a) stable crevasse filled by meltwater during a warm period with estimated flow within the crevasse; b) evolution of an ice lid due to ice crystals rising to the surface; c) crack propagation due to an additional phase transition pressure within the crack

5.6.1 The Stefan problem

Analytic approach

A first special solution of the heat equation with phase transition considering only conduction and neglecting convection goes back to Stefan (1891). He used the resulting equation to describe a growing ice layer on the Polar Sea. Further special solutions of the problem, also less restrictive than the original approach by Stefan (1891), have been found by several authors. An overview of the approaches can be found in Baehr and Stephan (2008). The analytical solution of the one-dimensional two-phase Stefan problem following the paper of Boucíguez et al. (2007) will be used to verify the numerical simulation by COMSOL.

In case of a one-phase Stefan problem, the domain is initially at the phase transition or melt temperature T_M and only shows temperature gradation on one side of the phase boundary. The two-phase Stefan problem deals with temperature gradation on both sides of the phase boundary. The equations to solve are the heat equation for the solid phase (index $_S$)

$$\frac{\partial T_S(x,t)}{\partial t} = \alpha_S \frac{\partial^2 T_S(x,t)}{\partial^2 x} \quad \text{with} \quad \alpha_S = \frac{k_S}{\rho c_S} \quad \text{for} \quad 0 < x < X(t), \quad t > 0, \quad (5.14)$$

the heat equation for the liquid phase (index $_L$)

$$\frac{\partial T_L(x,t)}{\partial t} = \alpha_L \frac{\partial^2 T_L(x,t)}{\partial^2 x} \quad \text{with} \quad \alpha_L = \frac{k_L}{\rho c_L} \quad \text{for} \quad X(t) < x < \infty, \quad t > 0, \quad (5.15)$$

and the equation for the phase transition

$$\rho L_H \frac{\partial X(t)}{\partial t} = -k_L \frac{\partial T_L(X(t)^+,t)}{\partial x} + k_S \frac{\partial T_S(X(t)^-,t)}{\partial x}. \quad (5.16)$$
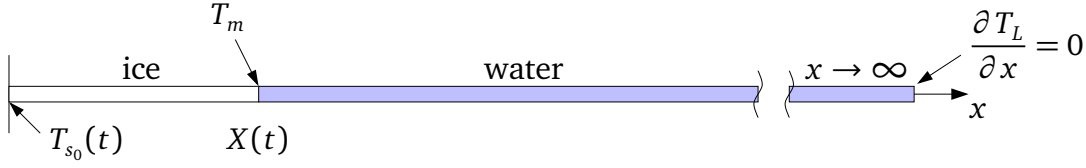
Figure 5.26: Sketch of the one-dimensional semi-infinite domain with applied boundary conditions

Herein the temperature T is dependent on the time t and the coordinate x. The density ρ is assumed as independent of the temperature and the phase. The specific heat capacities c_S and c_L, as well as the heat conductivity k_S and k_L are constant within the phases but different for each. The position of the phase boundary is denoted by $X(t)$, the latent heat by L_H. Provided that the domain is semi-infinite and $T_{S_0}(t) = \text{const.}$ or $T_{S_0}(t) \sim \sqrt{t}$ the problem can be solved using the initial conditions

$$X(t=0) = 0 \quad \text{and} \quad T_L(x,0) = T_{\text{init}} > T_m \quad \text{for} \quad 0 \leq x \leq \infty \tag{5.17}$$

the boundary conditions

$$T_S(0,t) = T_{S_0} < T_m \quad \text{for} \quad t > 0 \quad \text{and} \quad \frac{\partial T_L(\infty, t)}{\partial x} = 0, \tag{5.18}$$

and the transition condition

$$T_S(X(t),t) = T_L(X(t),t) = T_m. \tag{5.19}$$

By choosing an ansatz of the form $T_{S,L}(x,t) = P_{S,L}(\xi)$ and substituting $\xi = x/\sqrt{t}$ for both phases, the derivatives in Eqs. (5.14), (5.15) and (5.16) are transformed to

$$\frac{\partial T(x,t)}{\partial t} = \frac{\partial P}{\partial \xi}\frac{\partial \xi}{\partial t} = -\frac{x}{2\sqrt{t^3}}\frac{\partial P}{\partial \xi},$$

$$\frac{\partial T(x,t)}{\partial x} = \frac{\partial P}{\partial \xi}\frac{\partial \xi}{\partial x} = \frac{1}{\sqrt{t}}\frac{\partial P}{\partial \xi},$$

$$\frac{\partial^2 T(x,t)}{\partial x^2} = \frac{1}{\sqrt{t}}\frac{\partial}{\partial x}\left(\frac{\partial P}{\partial \xi}\right) = \frac{1}{\sqrt{t}}\frac{\partial}{\partial \xi}\left(\frac{\partial P}{\partial \xi}\frac{\partial \xi}{\partial x}\right) = \frac{1}{t}\frac{\partial^2 P}{\partial \xi^2}.$$

Insertion into Eqs. (5.14) and (5.15) yields

$$-\frac{x}{2\sqrt{t^3}}\frac{\partial P_{S,L}}{\partial \xi} = \alpha_{S,L}\frac{1}{t}\frac{\partial^2 P_{S,L}}{\partial \xi^2},$$

$$-\frac{x}{2\sqrt{t}}\frac{\partial P_{S,L}}{\partial \xi} = \alpha_{S,L}\frac{\partial^2 P_{S,L}}{\partial \xi^2} \quad \text{and with} \quad \xi = \frac{x}{\sqrt{t}}$$

$$-\frac{\xi}{2}\frac{\partial P_{S,L}}{\partial \xi} = \alpha_{S,L}\frac{\partial^2 P_{S,L}}{\partial \xi^2}, \tag{5.20}$$

an equation of the form $P'' = f(\xi, P')$ which can be solved using substitution. With $Q(\xi) = P'(\xi)$, Eq. (5.20) transforms to

$$Q'_{S,L}(\xi) = -\frac{\xi}{2\alpha_{S,L}} Q_{S,L}(\xi), \tag{5.21}$$

which can be solved using separation of variables. Since in the following integrations similar steps have to be performed for the solid, as well as the liquid phase using different constants of integration, a side-by-side format will be used for a clear arrangement. The first integration yields

$$\int_{Q_{S_0}}^{Q_S(\xi)} \frac{1}{\tilde{Q}(y)} d\tilde{Q} = -\frac{1}{2\alpha_S} \int_0^{\xi} \tilde{\xi} \, d\tilde{\xi}, \qquad\qquad \int \frac{1}{Q_L(\xi)} dQ_L = -\frac{1}{2\alpha_L} \int \xi \, d\xi,$$

$$\ln\frac{Q_S(\xi)}{Q_{S_0}} = -\frac{1}{4\alpha_S}\xi^2, \qquad\qquad \ln Q_L(\xi) + Q^* = -\frac{1}{4\alpha_L}\xi^2 + \xi^*,$$

$$\rightarrow Q_S(\xi) = Q_{S_0}\, e^{-\frac{1}{4\alpha_S}\xi^2}, \qquad\qquad \rightarrow Q_L(\xi) = c^*\, e^{-\frac{1}{4\alpha_L}\xi^2}. \tag{5.22}$$

Further integration of Eqs. (5.22) leads to

$$P_S(\xi) = P_{S_0} + Q_{S_0} \int_0^{\xi} e^{-\frac{1}{4\alpha_S}\tilde{\xi}^2} d\tilde{\xi}, \qquad P_L(\xi) = P_{L_\infty} - c^* \int_{\xi}^{\infty} e^{-\frac{1}{4\alpha_L}\tilde{\xi}^2} d\tilde{\xi}. \tag{5.23}$$

By substitution of $\Theta^2 = \frac{1}{4\alpha}\tilde{\xi}^2$ with $d\tilde{\xi} = 2\sqrt{\alpha}\,d\Theta$ and the limits $\Theta(0) = 0$, $\Theta(\xi) = \frac{\xi}{2\sqrt{\alpha_L}}$ and $\lim_{\xi\to\infty}\Theta = \infty$, Eqs. (5.23) transform to

$$P_S(\xi) = Q_{S_0} + z_{S_0} 2\sqrt{\alpha_S} \int_0^{\Theta(\xi)} e^{-\tilde{\Theta}} d\tilde{\Theta}, \qquad P_L(\xi) = P_{L_\infty} - c^* 2\sqrt{\alpha_L} \int_{\Theta(\xi)}^{\infty} e^{-\tilde{\Theta}} d\tilde{\Theta}. \tag{5.24}$$

With the definition of the error function and the complementary error function

$$\text{erf}(x) = \frac{2}{\sqrt{\pi}} \int_0^x e^{-t^2} dt \qquad \text{and} \qquad \text{erfc}(x) = \frac{2}{\sqrt{\pi}} \int_x^{\infty} e^{-t^2} dt$$

Eqs. (5.24) take the form

$$P_S(\xi) = P_{S_0} + Q_{S_0}\sqrt{\alpha_S\pi}\,\text{erf}\!\left(\frac{\xi}{2\sqrt{\alpha_S}}\right), \qquad P_L(\xi) = P_{L_\infty} - c^*\sqrt{\alpha_L\pi}\,\text{erfc}\!\left(\frac{\xi}{2\sqrt{\alpha_L}}\right).$$

Application of the boundary conditions $P_{S_0} = P_S(\xi = 0) = T_S(x = 0, t) = T_{S_0}$ and $P_{L_\infty} = P_L(\xi \to \infty) = T(x \to \infty, t) = T(x, t \to 0) = T_{\text{init}}$ leads to

$$T_S(x,t) = T_{S_0} + Q_{S_0}\sqrt{\alpha_S\pi}\,\text{erf}\!\left(\frac{x}{2\sqrt{\alpha_S t}}\right), \qquad T_L(x,t) = T_{\text{init}} - c^*\sqrt{\alpha_L\pi}\,\text{erfc}\!\left(\frac{x}{2\sqrt{\alpha_L t}}\right).$$

The remaining unknowns Q_{S_0} and c^* can be obtained using the transition condition

$T_S(X(t), t) = T_L(X(t), t) = T_M = 0$ (in case of fresh water ice) yielding

$$Q_{S_0} = -\frac{T_{S_0}}{\sqrt{\alpha_S \pi}} \frac{1}{\mathrm{erf}\left(\dfrac{X(t)}{2\sqrt{\alpha_S t}}\right)} \qquad \text{and} \qquad c^* = \frac{T_{\mathrm{init}}}{\sqrt{\alpha_L \pi}} \frac{1}{\mathrm{erfc}\left(\dfrac{X(t)}{2\sqrt{\alpha_L t}}\right)}.$$

The equations for the temperature in both phases hence read

$$T_S(x,t) = T_{S_0} - T_{S_0} \frac{\mathrm{erf}\left(\dfrac{x}{2\sqrt{\alpha_S t}}\right)}{\mathrm{erf}\left(\dfrac{X(t)}{2\sqrt{\alpha_S t}}\right)}, \qquad T_L(x,t) = T_{\mathrm{init}} - T_{\mathrm{init}} \frac{\mathrm{erfc}\left(\dfrac{x}{2\sqrt{\alpha_L t}}\right)}{\mathrm{erfc}\left(\dfrac{X(t)}{2\sqrt{\alpha_L t}}\right)}, \quad (5.25)$$

with the last remaining unknown $X(t)$. By defining $\varsigma = \dfrac{X(t)}{2\sqrt{\alpha_L t}}$ or $X(t) = 2\varsigma\sqrt{\alpha_L t}$ and $\phi = \sqrt{\alpha_L / \alpha_S}$, Eqs. (5.25) can be rewritten as

$$T_S(x,t) = T_{S_0}\left(1 - \frac{\mathrm{erf}\left(\dfrac{x}{2\sqrt{\alpha_S t}}\right)}{\mathrm{erf}(\phi\varsigma)}\right), \qquad T_L(x,t) = T_{\mathrm{init}}\left(1 - \frac{\mathrm{erfc}\left(\dfrac{x}{2\sqrt{\alpha_L t}}\right)}{\mathrm{erfc}(\varsigma)}\right). \quad (5.26)$$

For the evaluation of ς, Eqs. (5.26) are inserted into Eq. (5.16). With

$$\frac{\partial X(t)}{\partial t} = \varsigma\sqrt{\frac{\alpha_L}{t}},$$

$$\left.\frac{\partial T_S(x,t)}{\partial x}\right|_{X(t)} = -\frac{T_{S_0}}{\mathrm{erf}(\nu\lambda)} \frac{e^{-\varsigma^2\phi^2}}{\sqrt{\pi\alpha_S t}} \quad , \text{ and}$$

$$\left.\frac{\partial T_L(x,t)}{\partial x}\right|_{X(t)} = \frac{T_{\mathrm{init}}}{\mathrm{erfc}(\varsigma)} \frac{e^{-\varsigma^2}}{\sqrt{\pi\alpha_L t}},$$

the equation for the phase transition can be transformed to

$$-\varsigma\sqrt{\pi} = \frac{T_{\mathrm{init}} c_L}{L_H} \frac{1}{e^{\varsigma^2}\,\mathrm{erfc}(\varsigma)} + \frac{T_{S_0} c_S}{L_H} \frac{1}{\phi} \frac{1}{e^{\phi^2\varsigma^2}\,\mathrm{erf}(\phi\varsigma)},$$

a nonlinear equation in ς which can be solved numerically using Newton's method.

Numerical approach

A straightforward implementation of the two-dimensional two-phase Stefan problem into COMSOL for paraffin wax is presented in Ogoh and Groulx (2010). The authors use the so-called heat capacity method for the simulation of the phase shift,

where the specific heat capacity during melting or freezing is

$$c_{p_m} = \frac{L_H}{\Delta T_m} + c_p. \tag{5.27}$$

The heat capacity c_p, as well as the heat conductivity k of paraffin wax, shows only little deviation within and between the different phases, enabling the authors to use $c_{p_S} = c_{p_L}$ and $k_S = k_L$. Cuffey and Paterson (2010) give temperature-dependent functions for the specific heat capacity and the conductivity of ice reading

$$c_S(T) = \left(152.5 + 7.122 \, \frac{T}{K} \right) \frac{J}{kg\,K},$$

$$k_S(T) = 9.828 \, e^{-0.0057T/K} \, \frac{W}{m\,K},$$

for T in Kelvin. Material parameters for liquid water at different temperatures and atmospheric pressure can be taken from VDI-Wärmeatlas (2006). For simplicity reasons we refrain from including temperature dependencies of the thermal constants within the phases. The deviation between the phases in case of water and ice though is to strong to be neglected. Unless differently stated, the following simulations will be performed using the thermal constants in Tab. 5.2.

	$\rho\left[\frac{kg}{m^3}\right]$	$c_p\left[\frac{J}{kg\,K}\right]$	$k\left[\frac{W}{m\,K}\right]$	$L_H\left[\frac{J}{kg}\right]$
ice, solid	910	2100	2.1	334000
water, fluid	1000	4200	0.56	–

Table 5.2: Thermal material parameters for ice and water at $T \approx 0°C$ and atmospheric pressure; rounded values of the parameters found in Cuffey and Paterson (2010) and VDI-Wärmeatlas (2006)

Unlike in the analytical case, where the phase shift happens at a distinct temperature, the numerical implementation needs a temperature interval ΔT_m in which melting or freezing occurs. While Ogoh and Groulx (2010) use the smoothly differentiable COMSOL function *flc2hs* for the implementation of $c_p(T)$, we use

$$c_p(T) = \begin{cases} c_S + \frac{L_H}{2\Delta T_m}\left[\tanh(\kappa_c[T - T_m + \Delta T_m]) + 1\right] & \text{if} \quad T <= T_m - \frac{\Delta T_m}{2} \\ c_L - \left[\frac{L_H}{2\Delta T_m} + \frac{c_S - c_L}{2}\right]\left[\tanh(\kappa_c[T - T_m]) - 1\right] & \text{if} \quad T > T_m - \frac{\Delta T_m}{2} \end{cases} \tag{5.28}$$

for a smooth transition between c_L, c_m and c_s. The plot in Fig. 5.27 a) shows $c_p(T)$ for water and ice following Eq. (5.28) using a temperature interval of $\Delta T_m = 2°\,C$ and two different values of the constant κ_c. A comparison of the analytical evaluation and solutions of the FE simulation using different values for κ_c and ΔT_m is shown in Fig. 5.27 b). Since the analytical method requires a constant density, $\rho_S = \rho_L = 1000\,kg/m^3$ is applied. Furthermore, as a phase-dependent

conductivity imposes an additional discontinuity for the numerical simulation, $k_S = k_L = 2.1\,\text{W/(m\,K)}$ is used in this first comparison. The two-dimensional FE simulation is performed using a $1\,\text{m}$ long and $0.02\,\text{m}$ thick geometry in analogy to Fig. 5.26. The domain is meshed using mapped elements, 500 elements in x-direction and 10 elements across the thickness. The boundary conditions and the initial condition follow the sketch in Fig. 5.26 using $T_{\text{init}} = 5°\text{C}$ and $T_{S_0} = \text{const.} = -10°\text{C}$ with additional adiabatic insolation at the long horizontal edges of the domain.

The simulations show that the heat capacity method is able to reproduce the general trend of the analytical solution (black lines) for different points in time very well. A zoom into the red box reveals the inaccuracies due to the smearing of the phase transformation. Simulations with small intervals ΔT_m (green and dark blue lines) show a better approximation of the analytic solution than the larger interval $\Delta T_m = 2°\text{C}$. Unfortunately, bisecting ΔT_m for unchanged κ_c leads to higher discontinuities and results in approximately doubled computation times. The factor κ_c influences the curvature of the smoothed step function. A smaller value for κ_c (red and dark blue lines) attenuates the discontinuity and reduces the computation time with only negligible influence on the accuracy of the simulation result.

In a next step the influence of diverse constant thermal material parameters in the different phases is evaluated. Therefore, $\kappa_c = 10/\text{K}$ and $\Delta T_m = 1°\text{C}$ are used. For a smooth transition between the phases, the heat conductivity now follows the equation

$$k(T) = k_S + \frac{k_L - k_S}{2}\left(\tanh\left[\kappa_k\left(T - T_m + \frac{\Delta T_m}{2}\right)\right] + 1\right), \qquad (5.29)$$

with $\kappa_k = 7/\text{K}$ in order to confine the predominant part of the step to the interval $-1°\text{C} < T < 0°\text{C}$. The phase-dependent density is implemented accord-

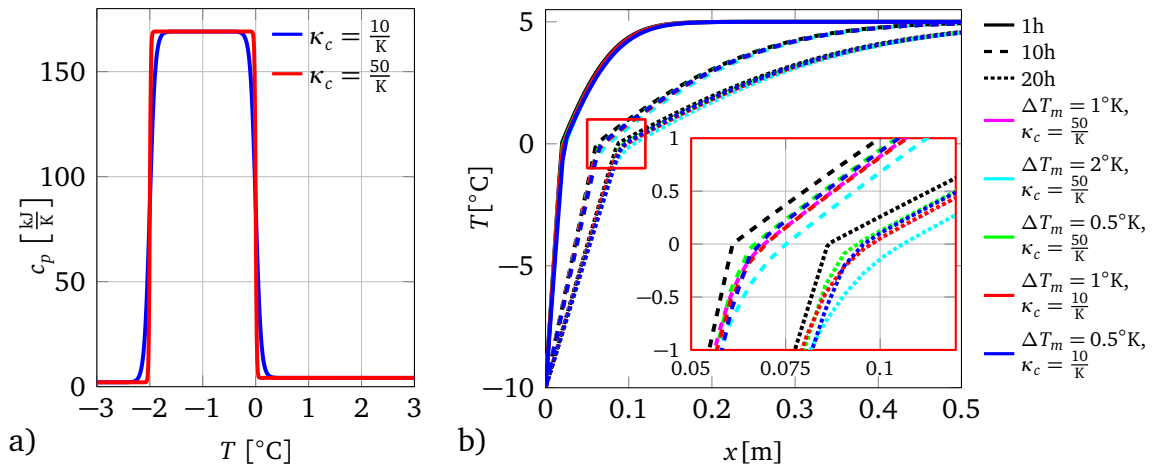Figure 5.27: a) Temperature-dependent heat capacity for different values of the constant κ_c; b) resulting temperatures in comparison to the analytical solution (black lines) for different phase-shift-temperature intervals ΔT_m and constants κ_c; varying line styles indicate different points in time
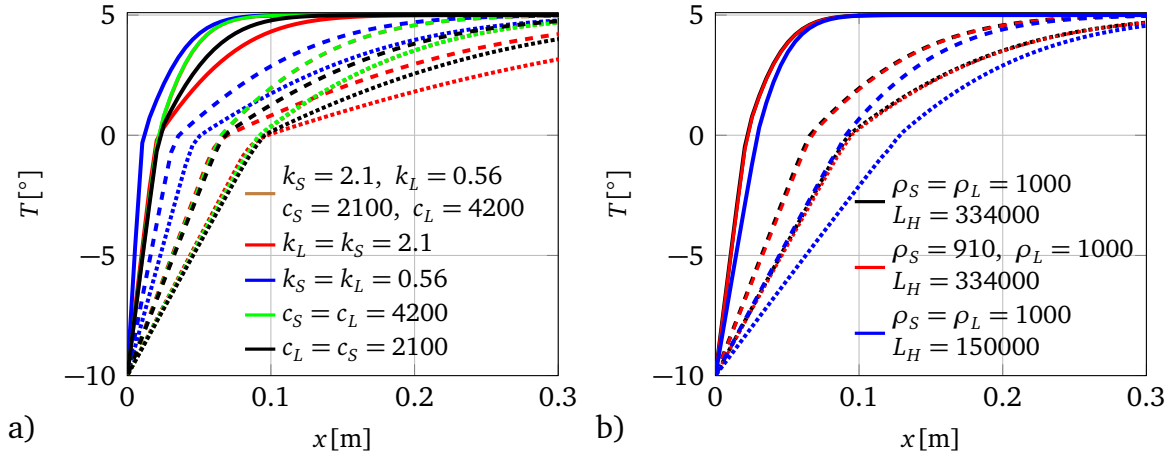
Figure 5.28: Temperatures in the solid and liquid phase due to varying material parameters at different points in time: 1 h (solid line), 10 h (dashed line), 20 h (densely dotted line). Parameters in labels in SI-units according to Tab. 5.2; a) varying k and c_p; b) varying ρ and L_H

ing to Eq. (5.29) using ρ_S and ρ_L from Tab. 5.2. Figure 5.28 a) shows the temperature in both phases for different points in time using a constant density $\rho_S = \rho_L = 1000 \,\text{kg/m}^3$ and $L_H = 334000 \,\text{J/kg}$. The parameters for the heat capacity, as well as the conductivity in the different phases vary. Different line styles represent different points in time as are $t = 1\,\text{h}$ (solid line), $t = 10\,\text{h}$ (dashed line) and $t = 20\,\text{h}$ (densely dotted line). The brown curves describe the most complex parameter setup with different values for c_P and k in both phases. The labels of the subsequent lines show variations from this setup. The brown curves are overlapped by the green lines with $c_S = c_L = 4200 \,\text{J/(kg\,K)}$. Hence, changing the heat capacity of the solid phase does not change the temperatures in this scope. Reducing c_L (black lines) results in decreasing temperatures in the liquid phase but does not change the position of the phase transition, nor the temperatures in the solid phase. An even stronger decrease of the temperatures in the liquid phase results from a larger k_L (red lines). However, the temperatures in the solid phase, as well as $X(t)$ remain unchanged. The only influence on the position of the phase transition and the temperatures in the solid phase appears for the blue lines, where the heat conductivity in the solid phase, k_S, has been reduced.

The influence of a phase-dependent density and varying latent heat is shown in Fig. 5.28 b). A comparison of the black and the red line with constant and phase-dependent density indicates no relevant difference. A different latent heat as depicted by the blue line on the other hand not only shows a considerable influence on the resulting temperatures in the solid, as well as in the liquid phase but also shifts the position of the phase transition for the different points in time.

Application to water-filled surface crevasses

The presented model is now extended to the more complex geometry of a water filled surface crack as shown in Fig. 5.29. Since the model is supposed to represent a water-filled single crevasse far from the external boundaries of the shelf, at first, the geometric parameters H and L have to be identified large enough for different values of T_{ext}, $T_{init,S}$ and $T_{init,L}$ such that their influence on the temperatures within the liquid phase and especially the position of the melting front is reduced. Reasonable values of the external dimensions are also dependent on the amount of water inside the crack. In order to limit the free parameters to a practicable number, the water level is set to $W = 5$m and the opening angle is limited to $\alpha \leq 5°$ in the following simulations.
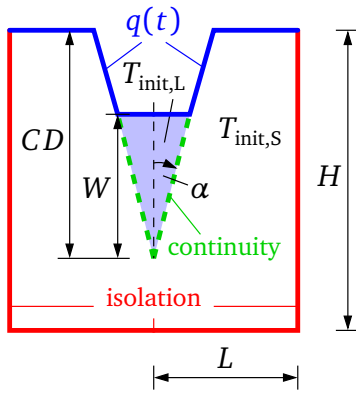

Figure 5.29: Sketch of the two-dimensional water-filled crevasse with the geometric parameters and the applied boundary conditions.

Tedesco et al. (2012) published measurements of the water temperature in two different supra-glacial lakes in western Greenland for June 2010 and June 2011. The measurements were performed at different depth below the water surface. The maximum measured temperatures did not exceed 1.5°C. Since the ratio between the air-water interface and the water-ice-interface is much bigger for supra-glacial lakes than for water-filled surface cracks, the maximum water temperature in cracks is most likely lower than 1.5°C. However, in order to include extreme cases, the maximum initial water temperature is set to $T_{init,L} = 2°C$. Since the simulation neglects the possibility of supercooled water inside the crack, the minimum initial water temperature is set to $T_{init,L} = 0°C$. In order to reduce the amount of discontinuities, the ice-air and the water-air-interface are subjected to a time-dependent heat flux following the equation

$$q(t) = \begin{cases} 0 \, \frac{W}{m^2} & \text{if} \quad t < 1\,\text{d} \\ \frac{100}{1\,\text{d}}(t - 1\,\text{d})(T_{ext} - T) \, \frac{W}{m^2} & \text{if} \quad t \geq 1\,\text{d}, \end{cases} \quad (5.30)$$

with $T_{ext} = -5\,°C$ or $T_{ext} = -10\,°C$. The approach gives time to first smooth out the temperature jump at the ice-water interface before, after one day, the heat flux coefficient increases. This results in a much better convergence than constraining the respective boundaries by a time-dependent temperature.

In the following, different parameter setups are considered. Therefore, step functions for the heat capacity and the thermal conductivity with the parameters for the solid and liquid phase as presented in Tab. 5.2 and $\kappa_c = 10/\text{K}$ and $\kappa_k = 7/\text{K}$ are used. Since the previous simulation indicated negligible influence due to a constant or phase dependent density, $\rho_S = \rho_W = 1000\,\text{kg/m}^3$ is applied.
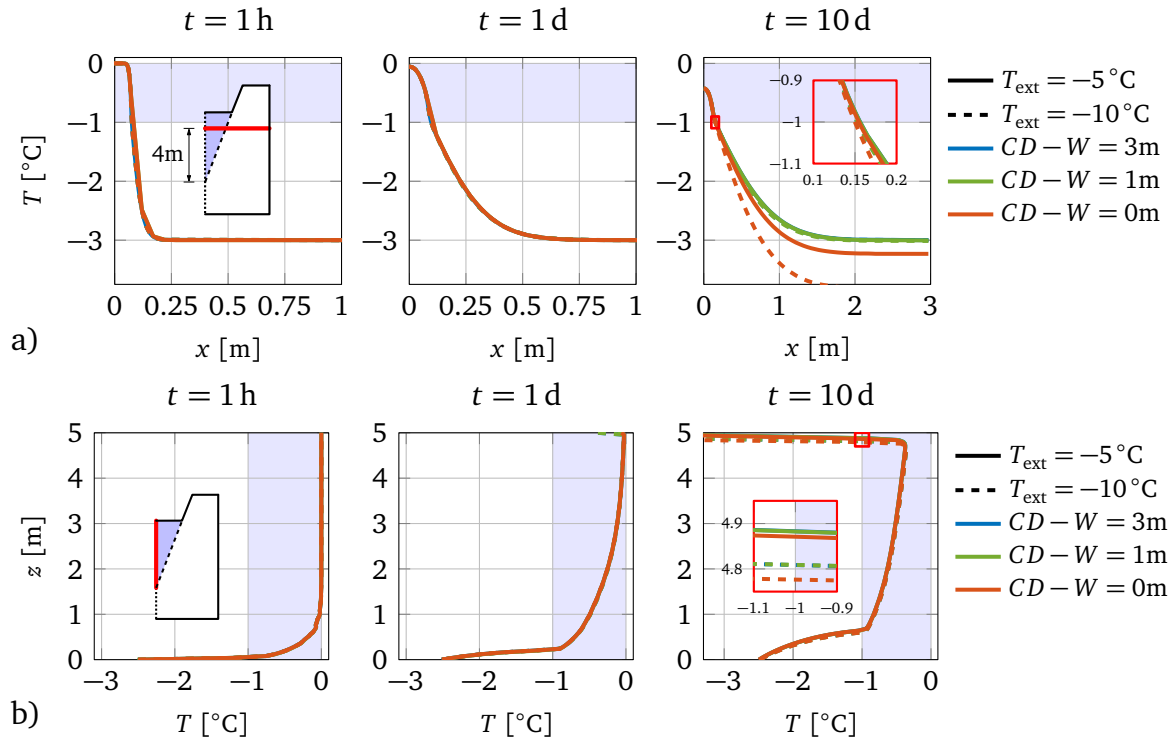
Figure 5.30: Influence of the geometric parameter $CD-W$ and the external temperature for different points in time; a) temperatures along horizontal line 1m below the water surface; b) temperatures along line of symmetry

First, the influence of the freeboard, $CD-W$, together with different values for T_{ext} is analyzed after one hour, one day and ten days using $\alpha = 1°$, $L = 3\,\text{m}$, $T_{\text{init,L}} = 0\,°\text{C}$ and $T_{\text{init,S}} = -3\,°\text{C}$. The resulting temperatures along a horizontal and a vertical intersection are illustrated in Figs. 5.30 a) and b), respectively. Due to symmetry of the resulting temperature profile, the horizontal section only comprises the right half of the domain. The vertical section follows the line of symmetry. Differences in the external temperature are indicated by the line style, varying values for $CD-W$ by the line color. The light blue background marks the temperature interval during which the phase shift occurs. The passing of the colder limit of the temperature interval, associated with phase transition, will in the following be referred to as the position of the phase shift.

The resulting graphs show, that the freeboard has no influence on the temperatures in the system as long as no external heat flux is applied. After $t = 10\,\text{d}$, differences due to the freeboard and due to the external temperatures appear. Especially, the horizontal section illustrates the influence of the freeboard on the temperatures within the solid phase. For $CD-W > 1\,\text{m}$ the differences vanish. Neither the freeboard nor the external temperatures influence the position of the phase boundary along the crack faces as shown by the enlarged view of the lines in vicinity of $T = -1\,°\text{C}$. Considerable freezing independent of $CD-W$ or T_{ext} appears at the crack tip. The ice layer growth at the former water surface is much slower. The zoom in the red box indicates pronounced differences in the thickness of the ice lid
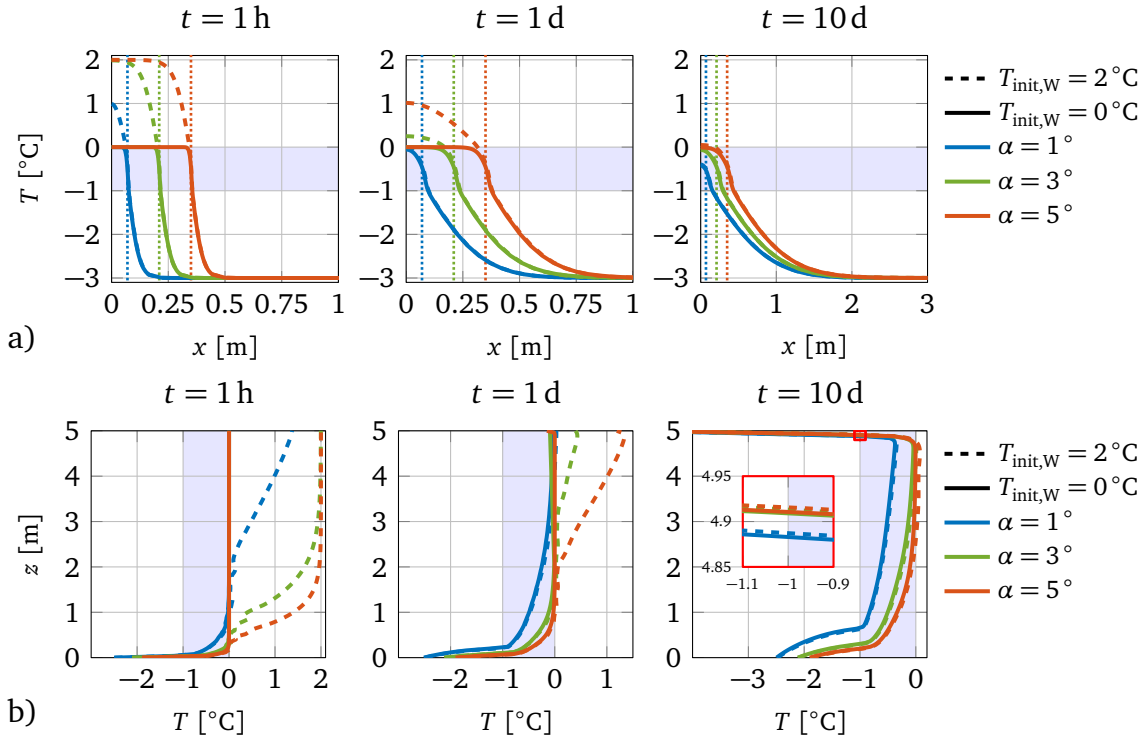
Figure 5.31: Influence of the opening angle α and the initial water temperature on the temperatures along the horizontal (a) and vertical (b) sections in the crevassed domain as indicated in Fig. 5.30 at different points in time

due to T_{ext} after ten days. The influence of $CD - W$ on the lid thickness is comparatively small.

It must be assumed that the influence of the freeboard on the ice-lid thickness is considerably larger for real crevasses, where the heat transfer coefficient is strongly dependent on the air flow within the crevasse and hence on the crevasse spacing, the wind speed and the orientation of the crevasse with respect to the wind direction.

In a next step, the influence of the opening angle and the initial temperature of the water on the resulting temperatures along the sections are analyzed. Therefore, $CD - W = 3\,\text{m}$, $T_{\text{ext}} = -5\,°\text{C}$, $L = 3\,\text{m}$ and $T_{\text{init,S}} = -3\,°\text{C}$ are used. The dashed and the solid lines in Fig. 5.31 a) illustrate the temperatures along the horizontal section for $T_{\text{init,L}} = 2\,°\text{C}$ and $T_{\text{init,L}} = 0\,°\text{C}$, respectively. Differences in the opening angle are referred to by the line color. Already after $t = 1\,\text{h}$ it appears that the narrow crack with $\alpha = 1°$ is considerably less able to keep the warmer temperatures in the water than cracks with larger opening angles. This finding is supported by the results after $t = 1\,\text{d}$. However, after $t = 10\,\text{d}$, the deviations due to different initial water temperatures almost vanish for all opening angles used. Furthermore, for the illustrated points in time, the initial water temperature has no influence on the position of the phase transition.

The prescribed opening angle affects the initial position of the phase boundary at the crack flanks. This can by seen in the plots of the temperatures along the horizon-
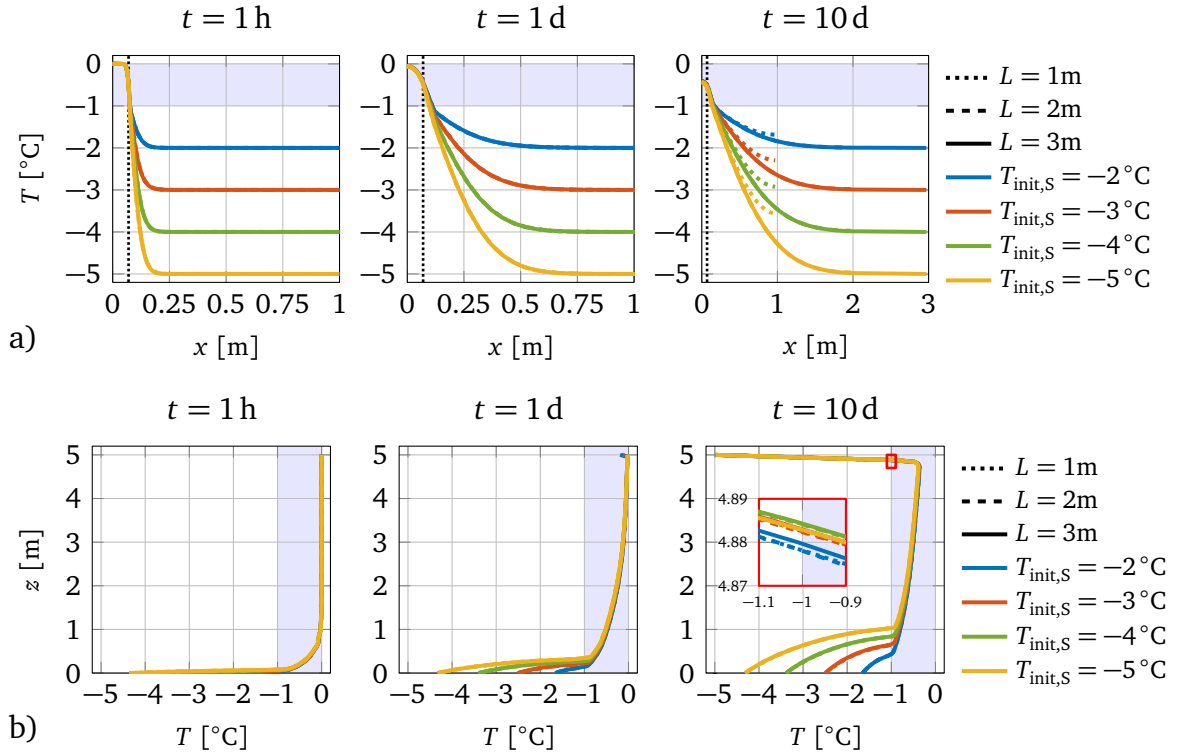
Figure 5.32: Influence of the domain length L and the initial ice temperature on the temperatures in the crevassed domain at different points in time; therefore $CD - W = 3$m, $H - CD = 3$m and $T_{\text{bdy}} = -5$°C; a) temperatures along horizontal line 1m below the water surface; b) temperatures along line of symmetry

tal section, where vertical, thin, densely dashed lines point out the corresponding initial phase boundary one meter below the water surface. The temperatures along the vertical section are therefore more appropriate to demonstrate the influence of the opening angle on the evolution of the phase shift position. After one hour, only the very tip of the crack is frozen. The deviations due to the opening angle in the resulting solid phase and in the transition zone are very small. Stronger differences due to opening angle and initial water temperature can be seen in the remaining liquid phase. After $t = 1$d the deviations due to the initial water temperature decrease and stronger differences due to the opening angle in the solid phase and transition zone appear. These differences become even more pronounced after $t = 10$d. Here, the impact of the initial water temperature becomes negligibly small, especially for sharper opening angles. The deviation in the lid thickness due to the opening angles and initial water temperatures after $t = 10$d comprises only few centimeters as illustrated in the enlarged view of the phase boundary position.

Next, the influence of the domain length L and the initial ice temperature $T_{\text{init,S}}$ is analyzed using $CD - W = 3$ m, $\alpha = 1°$, $T_{\text{ext}} = -5$ °C and $T_{\text{init,L}} = 0$ °C. The resulting temperatures along the introduced sections are illustrated in Figs. 5.32 a) and b) where the line color represents different $T_{\text{init,S}}$, the line style different L.

The plots show that significant differences due to varying $T_{\text{init,S}}$ along the horizon-
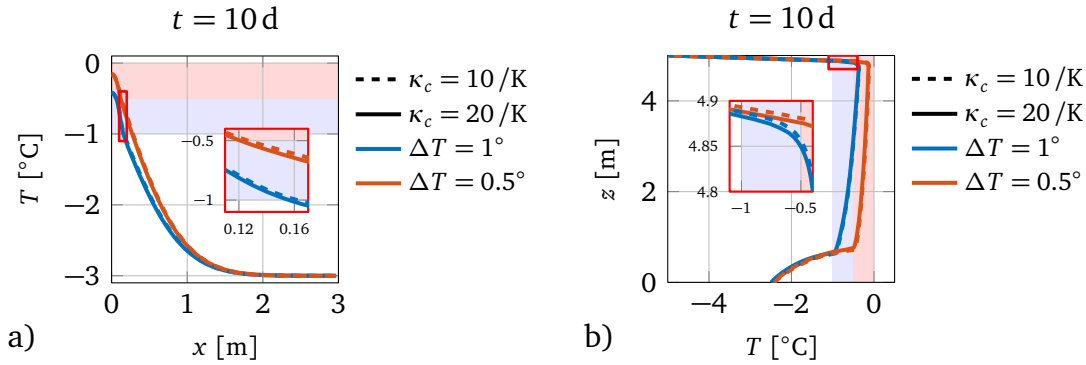
Figure 5.33: Influence of the width of the phase transition interval and the curvature parameter k_c on the resulting temperatures along the horizontal (a) and vertical (b) section after $t = 10\,\mathrm{d}$

tal section 4 m below the water surface are restricted to the initially solid area, right from the vertical, densely dotted line which indicates the initial position of the phase boundary. Also differences due to the length of the domain only appear in major distance of the water-ice interface and after a considerable amount of time. It shows that the length $L \geq 2\,\mathrm{m}$ is sufficient to represent the surrounding ice mass for $\alpha = 1°$. The previous plot with different opening angles indicated that $L = 3\,\mathrm{m}$ is long enough for the considered larger opening angles up to $\alpha = 5°$. The temperatures along the vertical section in Fig. 5.32 b) are completely independent on the domain length L but show variances due to different $T_{\mathrm{init,S}}$ around the crack tip. The resulting lid thickness is nearly independent on the initial ice temperature as shown by the enlarged view in the red box where the differences in the vertical position are within the range of millimeters.

Figure 5.27 b) showed that the influence of the size of the temperature interval for the phase shift, as well as the curvature parameter κ_c on the temperatures in the one-dimensional setup was very small. In order to check whether this trend can be transferred to freezing within a water-filled crack, the model domain in Fig. 5.29 is simulated using $CD - W = 3\,\mathrm{m}$, $L = 3\,\mathrm{m}$, $\alpha = 1°$, $T_{\mathrm{ext}} = -5\,°\mathrm{C}$, $T_{\mathrm{init,L}} = 0\,°\mathrm{C}$ and $T_{\mathrm{init,S}} = -3\,°\mathrm{C}$ with different values for ΔT and κ_c. The resulting temperatures along the horizontal and the vertical section after $t = 10\,\mathrm{d}$ are illustrated in Figs. 5.33 a) and b), respectively. Changes in ΔT are indicated by the line color, variations in κ_c by the line style. The light red background hints towards the phase transition interval for $\Delta T = 0.5\,°\mathrm{C}$. Whereas the differences due to diverse κ_c are negligible, a considerable influence of the ΔT on the resulting temperatures appears. However, a closer look at the associated phase shift positions reveals, that the influence of ΔT on the lid thickness is negligibly small. Stronger differences in the resulting phase shift position appear along the crack faces, where the smaller value for ΔT displaces the phase boundary by approximately 4 cm inwards. In general it can therefore be said, that the application of a phase transition zone slightly underestimates the freezing process.

The enlarged views of the phase boundaries along the vertical sections after $t = 10\,\mathrm{d}$ for all tested setups indicate that the extent of the developed ice layer at the surface spans only few tens of centimeters whereas the ice growth at the crack tip is considerably larger. Influence within the range of centimeters could be seen due to different opening angles. Stronger deviations only occurred due to different external temperatures. Since the model ignores the influence of convection, the transport of colder and less dense water from the tip to the top is disabled, leading to an overestimate ice growth at the crack tip and an underrated lid growth at the surface.

The influence of convection

Thus far, heat transport due to fluid movement has been excluded in the simulations. However, Taylor (2004) stated for melt ponds in sea ice, that even small temperature differences lead to turbulent flow. An influence of convective heat transfer within the crevasse must therefore be assumed. In case of natural convection, the flow regime can be characterized by the Grashof number, which describes the ratio between the time scales for viscous diffusion and internal buoyancy forces in the fluid. It is defined as

$$\mathrm{Gr}_L = \frac{g\,\alpha_T (T_{\mathrm{wall}} - T_{\mathrm{fluid}}) L^3}{(\eta/\rho)^2}, \tag{5.31}$$

with the coefficient of thermal expansion α_T and the characteristic length of the problem L. For a setup as illustrated in Fig. 5.34, the material parameters are evaluated at $(T_{\mathrm{fluid}} - T_{\mathrm{wall}})/2 = 2°\,\mathrm{C}$ and read $\alpha_T = -0.0324\cdot 10^{-3}\,\mathrm{1/K}$, $\eta = 1730.9\cdot 10^{-6}\,\mathrm{Pa\,s}$ and $\rho = 999.94\,\mathrm{kg/m^3}$. With $L = 0.1\,\mathrm{m}$ the Grashof number yields $\mathrm{Gr}_L = 4.2430\cdot 10^5$. This value is much lower than the critical value of $\mathrm{Gr}_L = 10^9$ which denotes the transition between laminar and turbulent flow in case of free convection, hence laminar flow behavior can be assumed. A FE simulation of the simple setup illustrated in Fig. 5.34 supports this finding. Within the FE program COMSOL, the built-in modules for laminar or turbulent flow are coupled with a heat transfer in fluids module using the multiphysics node. Following the notation in the COMSOL user manual, the temperature T results from the solution of the heat transfer equation

$$\rho c_p \left(\frac{\partial T}{\partial t} + (\boldsymbol{v}\cdot\nabla)T \right) = -(\nabla\cdot\boldsymbol{q}) + \boldsymbol{\sigma}:\mathbf{L} - \frac{T}{\rho}\left.\frac{\partial\rho}{\partial t}\right|_p \left(\frac{\partial p}{\partial t} + (\boldsymbol{v}\cdot\nabla)p \right) + Q, \tag{5.32}$$

with the given velocity $\boldsymbol{v}$, the velocity gradient $\mathbf{L}$, the conductive heat flux vector $\boldsymbol{q}$ and the pressure p. The scalar Q contains heat sources other than viscous dissipation. The viscous stress in case of a Newtonian fluid takes the form

$$\boldsymbol{\sigma} = 2\eta\mathbf{L} - \frac{2}{3}\eta(\nabla\cdot\boldsymbol{v})\mathbf{1}. \tag{5.33}$$

The temperature is transferred to the fluid flow module to compute the temperature-dependent material parameters such as the density, the viscosity, the conductivity

and the specific heat capacity. In the fluid flow module the Navier-Stokes equations

$$\frac{\partial \rho}{\partial t} + \nabla \cdot (\rho \boldsymbol{v}) = 0 \tag{5.34}$$

$$\rho \frac{\partial \boldsymbol{v}}{\partial t} + \rho (\boldsymbol{v} \cdot \nabla) \boldsymbol{v} = \nabla \cdot (-p\boldsymbol{1} + \boldsymbol{\sigma}) + \boldsymbol{f} \tag{5.35}$$

are solved for the velocity $\boldsymbol{v}$ and the pressure p.
By application of turbulent flow approximations using the common $K - \epsilon$-model, Eq. (5.35) is transformed to

$$\rho \frac{\partial \boldsymbol{v}}{\partial t} + \rho (\boldsymbol{v} \cdot \nabla) \boldsymbol{v} = \nabla \cdot \left(-p\boldsymbol{1} + 2(\eta + \eta_T)L - \frac{2}{3}(\eta + \eta_T)(\nabla \cdot \boldsymbol{v})\boldsymbol{1} - \frac{2}{3}\rho K \boldsymbol{1} \right) + \boldsymbol{f} \tag{5.36}$$

and two additional transport equations have to be introduced for the turbulent kinetic energy, K, and the turbulent dissipation rate, ϵ, reading

$$\rho \frac{\partial K}{\partial t} + \rho \boldsymbol{v} \cdot \nabla K = \nabla \cdot \left(\left(\eta + \frac{\eta_t}{c_K} \right) \nabla K \right) + P_K - \rho \epsilon, \tag{5.37}$$

with the production term

$$P_K = \eta_T \left(2\nabla \boldsymbol{v} : \mathbf{L} - \frac{2}{3}(\nabla \cdot \boldsymbol{v})^2 \right) - \frac{2}{3}\rho K \nabla \cdot \boldsymbol{v} \tag{5.38}$$

and

$$\rho \frac{\partial \epsilon}{\partial t} + \rho \boldsymbol{v} \cdot \nabla \epsilon = \nabla \cdot \left(\left(\eta + \frac{\eta_t}{c_\epsilon} \right) \nabla \epsilon \right) + c_{\epsilon 1} \frac{\epsilon}{K} P_K - c_{\epsilon 2} \rho \frac{\epsilon^2}{K}, \tag{5.39}$$

respectively. Herein, $\eta_T = \rho c_\eta K^2 / \epsilon$ is the turbulent viscosity. The constants $c_K = 1$, $c_\epsilon = 1.3$, $c_{\epsilon 1} = 1.44$, $c_{\epsilon 2} = 1.92$ and $c_\eta = 0.09$ are literature values, determined from experimental data, fitting a wide range of turbulent flows. The resulting velocity field is given back to the heat transfer module. All equations are solved fully cou-
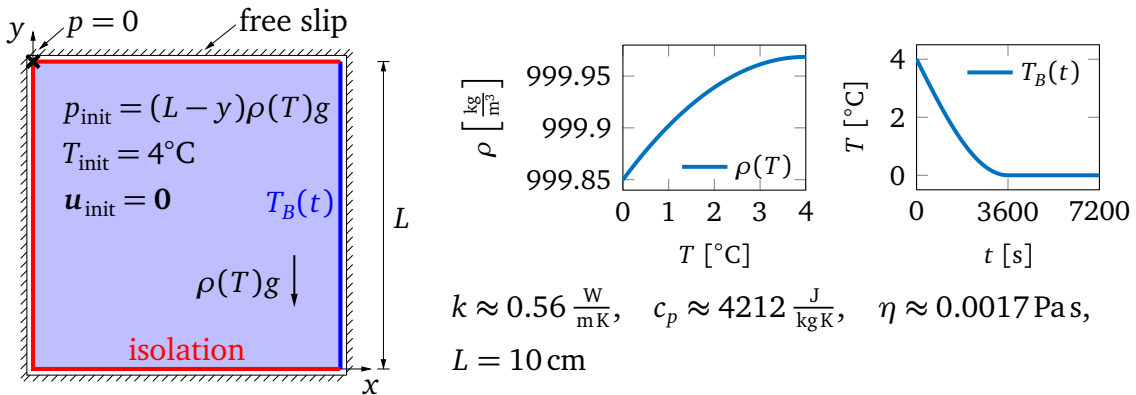

Figure 5.34: Geometric setup with initial values, boundary conditions and material parameters for the evaluation of the appropriate flow model

pled.

Figure 5.34 illustrates the quadratic domain used for the determination of the appropriate flow regime. The initial temperature of the water is set to $T_{\text{init}} = 4° \text{C}$, the water is at rest and the initial pressure equals the hydrostatic pressure. Free slip is enabled at all boundaries. For a well-posed problem, the pressure has to be fixed at one point. The domain is loaded by gravity using the illustrated temperature-dependent density profile. The right lateral boundary is continuously cooled using the time-dependent temperature profile

$$T_B(t) = \left(T_{\text{init}} - 4\,\text{K}\sin\left(\frac{t}{3600\,\text{s}}\frac{\pi}{2}\right)\right)(t \leq 3600\,\text{s}) + (T_{\text{init}} - 4\,\text{K})(t > 3600\,\text{s}) \quad (5.40)$$

as illustrated in Fig. 5.34. The remaining boundaries are isolated. Temperature-dependent built-in COMSOL functions for liquid water are used for all material parameters but the density, which follows a polynomial fit of literature values

$$\rho(T) = -0.007471(T - T_m)^2 \frac{\text{kg}}{\text{m}^3\,\text{K}^2} + 0.05953(T - T_m)\frac{\text{kg}}{\text{m}^3\,\text{K}} + 999.85\,\frac{\text{kg}}{\text{m}^3} \quad \forall\ T > T_m,$$
$$(5.41)$$

in order to represent the negative thermal expansion of water below $4° \text{C}$. Average values of the remaining material parameters in the indicated temperature interval are shown in Fig. 5.34. The laminar, as well as the turbulent study are performed with the same mesh consisting of approximately 28300 elements with considerable refinement along the boundaries.

Figures 5.35 a) and b) show isothermal contours of both simulations at distinct points in time. The general temperature distribution appears to be very similar.
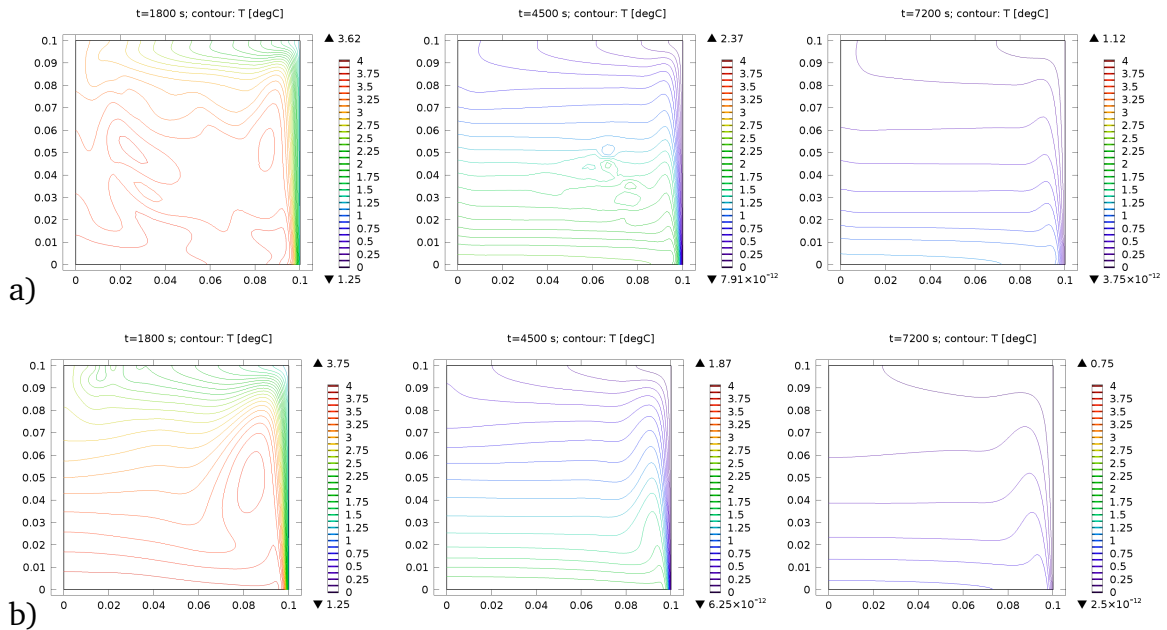

Figure 5.35: Isocontours of the resulting temperature for a) a laminar flow model and b) a turbulent flow model

After $t = 1800\,\text{s}$ the contours of the turbulent flow simulations seem slightly more sorted than those of the laminar simulation. The maximum and minimum temperatures are about the same. A considerably larger difference in the maximum temperature appears after $t = 4500\,\text{s}$, the structure of the isolines however is very similar. At $t = 7200\,\text{s}$, the differences in the maximum temperature reduce.

It appears that the application of a turbulent flow model results in a faster mixing of the fluid and hence lower maximum temperatures after two hours. It has to be noted that for a larger domain, e.g. a real crevasse, the characteristic length, which is set by the water level inside the crevasse, can be much higher than the simulated 10 cm. Hence, the Grashof number most likely exceeds the critical value of 10^9 and turbulent flow has to be assumed. Since on the other hand, turbulent flow leads to a rapid mixing of the fluid, the temperature difference will decrease very fast which eventually results in $\text{Gr}_L < 10^9$, allowing to use the computationally much less expensive laminar model for the simulation of the phase transition.

In a next step, the phase transition process using the heat capacity method is included into the coupled heat transfer - laminar flow - simulation. Due to the complexity of the problem, a downsized version of the geometry in Fig. 5.29 with $W = 0.5\,\text{m}$, $H = 1.8\,\text{m}$, $CD-W = 0.3\,\text{m}$, $L = 1.5\,\text{m}$ and $\alpha = 5°$ is used. For comparability to previous results the heat flux following Eq. (5.30) with $T_{\text{ext}} = -5\,°\text{C}$ is applied. Within the initially liquid phase now the coupled system of Navier-Stokes equations and heat transfer equations is solved. In order to save computation time, only the heat transfer equation is solved in the initially solid phase, hence the domain remains solid even if temperatures exceed $T = -1\,°\text{C}$. The heat capacity is evaluated using Eq. (5.28), the conductivity follows Eq. (5.29) with $\kappa_k = 7/\text{K}$. Other than in previous simulations with phase transition, now also the equations for the density and the viscosity have to meet the jump at the phase boundary and therefore read

$$
\rho(T) = \begin{cases} \rho_S + \dfrac{\rho_{T_m} - \rho_S}{2}\left[\tanh\left(\kappa_\rho\left[(T - T_m) + \dfrac{\Delta T_m}{2}\right]\right) + 1\right] & \forall\ T < T_m \\[2mm] -0.007471(T - T_m)^2\,\tfrac{\text{kg}}{\text{m}^3\,\text{K}^2} + 0.05953(T - T_m)\,\tfrac{\text{kg}}{\text{m}^3\,\text{K}} + 999.85\,\tfrac{\text{kg}}{\text{m}^3} & \forall\ T \geq T_m \end{cases}
$$

with $\rho_s = 910\,\tfrac{\text{kg}}{\text{m}^3}$ and

$$
\rho_{T_m} = \frac{\rho_s(\tanh(\kappa_\rho \Delta T_m) - 1) + 2 \cdot 999.85}{1 + \tanh(\kappa_\rho \Delta T_m)}
$$

to ensure a smooth transition between both temperature intervals, as well as

$$
\eta(T) = \eta_S + \frac{\eta_L - \eta_S}{2}\left[\tanh\left(\kappa_\eta\left[(T - T_m) + \Delta T_{\text{shift}}\right]\right) + 1\right]
$$

with $\eta_S = 5000\,\text{Pa}\,\text{s}$, $\eta_L = 2 \cdot 10^{-3}\,\text{Pa}\,\text{s}$. In order to yield convergence, the viscosity for the solid phase, η_S, is chosen extremely low in comparison to measured viscosities of ice, which are about eleven to thirteen orders of magnitude higher. However,
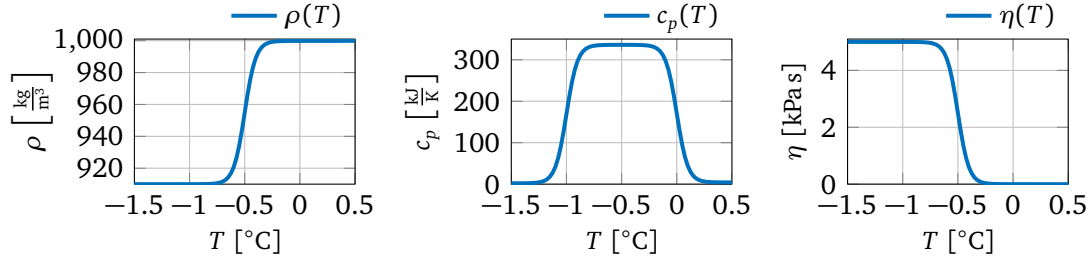
Figure 5.36: Temperature-dependent material parameters for $\Delta T = 1\,°\text{C}$ and $\kappa_\rho = \kappa_c = \kappa_\eta = 10/\text{K}$

the simulation shows negligibly small velocities in the solid phase and considerably larger velocities in the liquid phase, hence this rather daring guess can be accepted. If a larger jump in the viscosity is desired, a different approach with separated solid and liquid phases and a moving boundary in between can be used.

Resulting plots of the density, the heat capacity and the viscosity for $\Delta T = 1\,°\text{C}$, $\Delta T_{\text{shift}} = 0.5\,°\text{C}$ and $\kappa_\rho = \kappa_c = \kappa_\eta = 10/\text{K}$ are shown in Fig. 5.36. Figures 5.37 a) and b) show graphs of the normalized relevant material parameters for different ΔT_m to illustrate their location along the temperature axis with respect to the phase transition interval. The associated temperatures along the vertical section after $t = 5\,\text{d}$ are shown in Figs. 5.37 c). The solution of the heat transfer equation with phase shift, in the following abbreviated with HT are visualized by red lines, the solution of the coupled problem of heat transfer and laminar flow also known as non-isothermal flow (NITF) are illustrated in blue. For $\Delta T = 1\,°\text{C}$, no relevant differences between HT and NITF appear. By using $\Delta T = 0.5\,°\text{C}$, $\kappa_\rho = \kappa_\eta = 30/\text{K}$ and $\kappa_\eta = 10/\text{K}$, the resulting temperatures for NITF are slightly changed such that the lid thickness is increased and freezing at the crack tip is reduced.
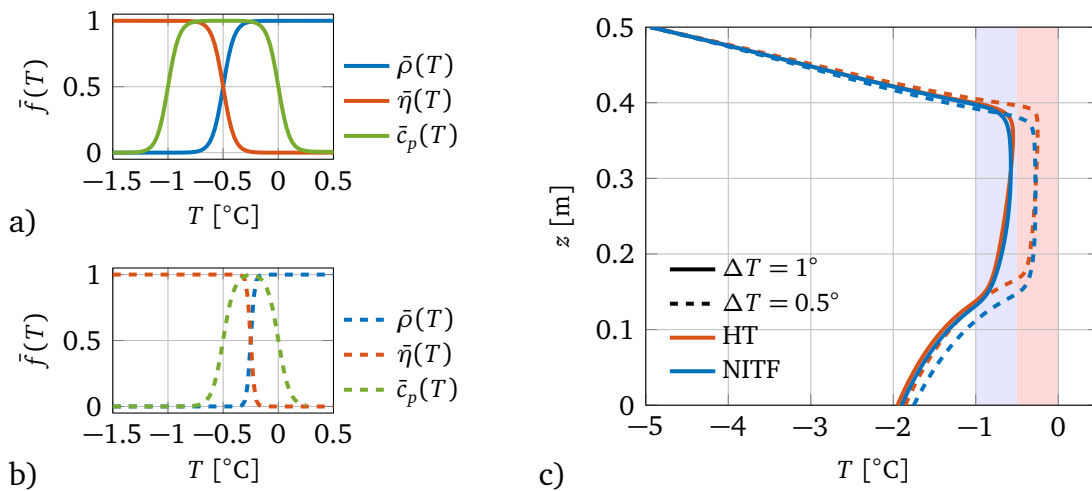

Figure 5.37: Normalized material parameters for a) $\Delta T = 1\,°\text{C}$ and $\kappa_\rho = \kappa_c = \kappa_\eta = 10/\text{K}$, as well as b) $\Delta T = 0.5\,°\text{C}$ and $\kappa_\rho = \kappa_\eta = 30/\text{K}$ and $\kappa_\eta = 10/\text{K}$ using $\Delta T_{\text{shift}} = \Delta T/2$; c) resulting temperatures after $t = 5\,\text{d}$ along vertical section for HT and NITF
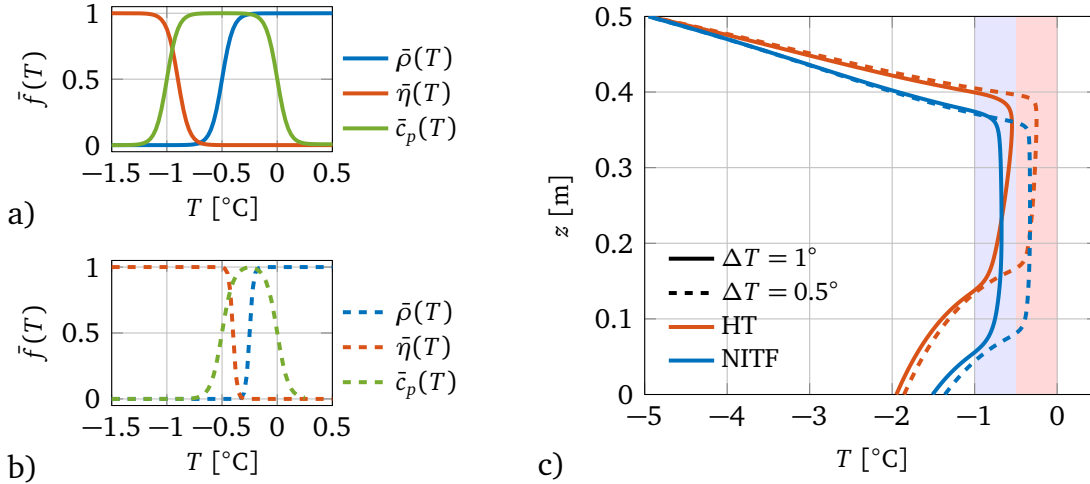
Figure 5.38: Normalized material parameters for a)$\Delta T = 1\,°C$, $\Delta T_{\text{shift}} = 0.9\,°C$ and $\kappa_\rho = \kappa_c = \kappa_\eta = 10/\text{K}$, as well as b) $\Delta T = 0.5\,°C$, $\Delta T_{\text{shift}} = 0.4\,°C$ and $\kappa_\rho = \kappa_\eta = 30/\text{K}$ and $\kappa_\eta = 10/\text{K}$; c) resulting temperatures after $t = 5\,\text{d}$ along vertical section for HT and NITF

The reason for this unexpectedly little difference between HT and NITF follows by a closer look at the material parameters in Figs. 5.37 a) and b). The flow in the crack is solely forced by buoyancy, which is triggered by gradients in the density. Since the predominant part of the density transition coincides with an already considerably increased viscosity, the expected transport of "ice crystals" to the surface is hindered.

In a next step the parameter ΔT_{shift} in the equation for $\eta(T)$ is varied such that $\Delta T_{\text{shift}} = 0.9\,°C$ for $\Delta T_m = 1\,°C$ and $\Delta T_{\text{shift}} = 0.4\,°C$ for $\Delta T_m = 0.5\,°C$. Plots of the resulting normalized material parameters with respect to the temperature are shown in Figs. 5.38 a) and b). The consequent temperatures along the vertical section are illustrated in 5.38 c). It appears that the shifted viscosity profile considerably reduces freezing at the crack tip and increases the lid growth at the surface. A more physical value for ΔT_{shift} could be found by fitting the simulation to experimental results.

The presented model shows that the simulation of phase transition within a water-filled crevasse by only modeling conductive heat transfer overestimates freezing at the tip and underestimates the resulting lid thickness. Nevertheless, also the setups including the influence of convection only lead to small lid thicknesses in the considered period of time.

5.6.2 A frost wedging model

The previous section gave a rough estimate of possible lid thicknesses due to freezing. Now, the fracture mechanical frost wedging process itself is modeled. Starting point for the simulation is a crevasse, opened by the angle α and the remote loading $\Delta u_x \triangleq \sigma_f = 100\,\text{kPa}$. The remaining parameters and boundary condition are equivalent to the setup of the crack filled by meltwater presented in
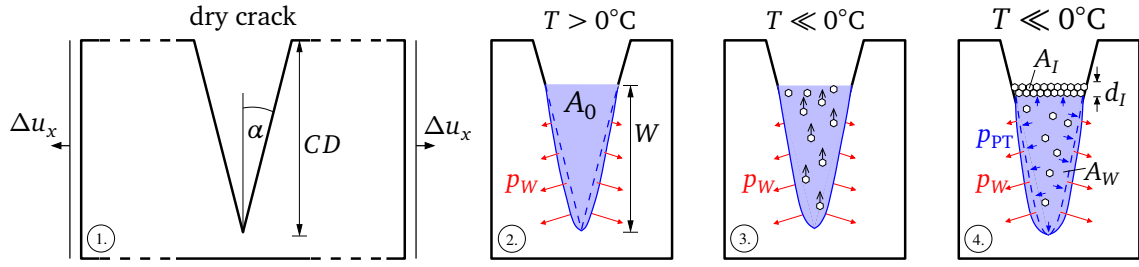
Figure 5.39: Illustration of frost wedging process with 1. a stable dry crack opened due to the opening angle α and external loading; 2. still stable crevasse filled by meltwater during a warm period, 3. evolution of an ice lid due to ice crystals rising to the surface, 4. crack propagation due to additional phase transition pressure within the crack

Sec. 5.5 using $L = 2000\,\text{m}$, $H = 250\,\text{m}$ and $E = 9\,\text{GPa}$. The simulations only consider compressible behavior for ice applying $\nu = 0.3$. A depth-dependent density profile as shown by the solid red line in Fig. 5.16 a) is assumed. This leads to maximum stable depths CD of the dry cracks with respect to the opening angle as presented in Tab. 5.1. The crack is filled by meltwater up to a level W that results in K_I below the critical value of $K_{Ic} = 400\,\text{kPa}\sqrt{\text{m}}$ used in this context. The area of water filling A_0 inside the crack is evaluated with respect to the deformed shape of the domain. Next, the first lid increment is inserted.
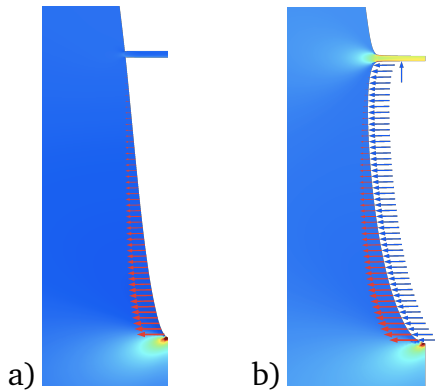

Figure 5.40: Qualitative countour plots of first principal stress in cracked domain with scaled deformation with a) loading by water pressure, unloaded lid due to eigenstrain; b) additional loading by phase transition pressure, load also carried by the lid

The lid is supposed to grow within a crevasse that is already deformed by the external loading and the water filling, bearing only the additional load due to the phase transition pressure acting on the crack faces. Two approaches were made to capture this process. In a first attempt, the lid area was not explicitly included into the simulation. The effect of the lid however was approximated by constraining the horizontal displacements of the fictitious crack face - lid - interface at the values resulting from the simulation of the water-filled crack. This resulted in a very rigid representation of the lid and therefore in an exaggerated shielding of the crack tip from the additional load due to the phase transition pressure.

In the second attempt, the ice lid is modeled explicitly. In order to have the lid bear only the additional load due to freezing, it is subjected to an eigenstrain $\varepsilon_{xx}^{\text{eig}}$ fulfilling the equation

$$\sigma_{\text{av}} = \text{av}\left(\sigma_{xx}^{\text{lid}}(\varepsilon_{xx}^{\text{eig}}, p_{\text{PT}} = 0)\right) = 0. \tag{5.42}$$

Herein, $\text{av}(\ldots)$ denotes the evaluation of the average stress in the lid area carried out in COMSOL. Equation (5.42) is solved numerically using a Newton's iteration

scheme. This approach needs more computational effort for the solution but yields a more accurate representation of the overall process. A qualitative plot of the loaded crack with relaxed first lid increment is shown in Fig. 5.40 a).

In a next step, the deformed area A_I of the inserted lid increment and the resulting required area of the remaining water under the lid

$$A_W = A_0 - A_I \frac{\rho_I}{\rho_W} \tag{5.43}$$

can be computed. The phase transition pressure p_{PT} then follows by solving

$$A_{W_{\mathrm{sim.}}}(p_{\mathrm{PT}}) = A_W \tag{5.44}$$

employing once more Newton's iteration scheme. The surface plot in Fig. 5.40 b) illustrates the first principal stress within the deformed geometry. The red arrows indicate the depth-dependent water pressure, the blue arrows the additional phase transition pressure. Considerable stresses now appear in the lid increment. If the average horizontal stress in the lid, which now is a function of the applied eigenstrain and the phase transition pressure, exceeds a given threshold $\sigma_{\mathrm{av}}^{\mathrm{max}}$, the lid breaks.

Weeks and Mellor (1978) report a tensile strength of about $2\,\mathrm{MPa}$ for small intact laboratory freshwater ice specimens. Reeh (1968) states that the tensile strength of glacier ice must be considerably smaller due to inhomogeneities in the bulk and assumes a value of less than $1\,\mathrm{MPa}$ to be reasonable. In addition, he argues that the tensile strength depends on the strain rate, as well as on the temperature. This is confirmed by a study of Wilhelms et al. (2007) who measured the force needed to break ice cores at different depth and temperatures. For temperatures around $T = -5\,^{\circ}\mathrm{C}$ the resulting tensile strength was approximately $1\,\mathrm{MPa}$.

If the lid breaks, the phase transition pressure is set back to zero and the surplus water spills through the lid and freezes at the surface. The resulting increased lid thickness follows the equation

$$A_I(d_I, \varepsilon_{xx}^{\mathrm{eig}}) = \frac{\rho_W}{\rho_I}(A_0 - A_{\mathrm{sim}}(p_{\mathrm{PT}} = 0)), \tag{5.45}$$

which is solved using Newton's iteration scheme. A configuration with subcritical lid stress is then used to compute the configurational force and the resulting SIF at the crack tip. If the resulting K_I exceed the critical value, the crack is allowed to grow. The crack growth increment is set with respect to the value of K_I such that the number of growth steps is reduced without resulting in configurations with negative K_I. For every growth step, the pressure p_{PT} has to be evaluated. If the resulting K_I falls below the critical limit, the lid thickness is increased by the increment Δd_I. Since the new lid part is supposed to grow within the already stretched crevasse, the eigenstrain as evaluated from Eq. (5.42) has to be adapted. For simplicity, we refrain from the computation of a depth-dependent eigenstrain but state, that the resulting force transmitted by the crack face - lid - interface is supposed to be equal

before and after the lid growth. This can be approximated by using

$$\sigma_{\mathrm{av}}\left(\varepsilon_{xx}^{\mathrm{eig,\,new}}, p_{\mathrm{PT}}^{\mathrm{old}}\right) = \sigma_{\mathrm{av}}\left(\varepsilon_{xx}^{\mathrm{eig,\,old}}, p_{\mathrm{PT}}^{\mathrm{old}}\right) \frac{d_I^{\mathrm{old}}}{d_I^{\mathrm{old}} + \Delta d_I}, \tag{5.46}$$

which is solved for $\varepsilon_{xx}^{\mathrm{eig,new}}$ applying Newton's iteration scheme. The phase transition pressure used for the iteration is the one computed for the last crack growth step. Hence the inserted increment is still assumed to be part of the water area. The part of former crack face area that is now covered by the new lid increment is not loaded any more. Next, the new deformed lid area and the required area of remaining water are computed, followed by a new evaluation of the phase transition pressure. During this iterative sequence of crack growth and lid growth, the situation can occur that the new area due to the chosen crack growth $A_{W_{\mathrm{sim.}}}$ even without additional phase transition pressure is larger than the required area. Then the maximum crack for which $A_{W_{\mathrm{sim.}}} = A_W$ for $p_{\mathrm{PT}} = 0$ is determined. If a new crack depth can be found and $K_I < K_{Ic}$, the ice lid will grow. If $K_I > K_{Ic}$, the crack is will to grow further, allowing for an air-filled gap between the water surface and the bottom of the ice lid. Since for $\alpha > 0°$ the available water is considerably larger than the water needed to fill the space between the newly created crack flanks, this situation leads to a complete penetration of the crack. A sketch of the complete crack growth algorithm can be found in Fig. 5.41.

Figure 5.42 illustrates the phase transition pressure, the average lid stress, the stress intensity factor and the resulting crack depth for a growing ice lid thickness using $\alpha = 2°$ and lid growth increments of $\Delta d_I = 0.05\,\mathrm{m}$. Application of a maximum average lid stress of $\sigma_{\mathrm{av}}^{\mathrm{max}} = 2\,\mathrm{MPa}$ in Fig. 5.42 a) as indicated by the red dashed line in the graph of the resulting average lid stress results in breaking of the lid for the first two lid growth steps. For these instances, the stress intensity factor is set to zero and the ice lid thickness comprising the surplus water is computed. Every simulation step directly following a breaking of the lid leads to resulting stress intensity factors with respect to the adapted ice lid thickness, the newly computed eigenstrain $\varepsilon_{xx}^{\mathrm{eig,new}}$, $p_{\mathrm{PT}} = 0\,\mathrm{Pa}$ and $\sigma_{\mathrm{av}} \approx 0\,\mathrm{Pa}$. With the addition of a third lid increment, the resulting phase transition pressure does not break the ice lid but leads to crack growth due to which the phase transition pressure and the resulting stress intensity factors are reduced until eventually the stress intensity factors fall below the critical value of $K_{Ic} = 400\,\mathrm{kPa}\sqrt{\mathrm{m}}$ as indicated by the red dashed line. With the insertion of another lid increment the phase transition pressure and the resulting K_I rise again leading to further crack growth. Thus far, crack growth led to a decreasing phase transition pressure and decreasing K_I. At a crack depth of approximately $97\,\mathrm{m}$, a turning point is reached. Now, further crack growth leads to increasing stress intensity factors even without additional phase transition pressure. Since the opening angle of $\alpha = 2°$ offers a quasi-infinite water supply to fill the geometrically ideally sharp crack, the fissure will propagate to the bottom of the ice shelf. After few meters of crack propagation, the critical stress in the lid is reached again. This however is ignored in the ongoing simulations as a breaking of the lid at this stage would

simulate water filled crack with pseudo lid increment

Newton's iteration to find $\varepsilon_{xx}^{\text{eig}}$ fulfilling $\text{av}\,(\sigma_{xx}^{\text{lid}}(\varepsilon_{xx}^{\text{eig}})) = 0$

evaluate A_0 and A_I in deformed shape

compute required area of remaining water under lid: $A_W = A_0 - A_I \rho_I / \rho_W$

Newton's iteration to find p_{PT} fulfilling $A_{W_{\text{sim}}}(p_{\text{PT}}) = A_W$

evaluate $\sigma_{\text{av}}^{\text{old}} = \text{av}\,(\sigma_{xx}^{\text{lid}}(\varepsilon_{xx}^{\text{eig}}, p_{\text{PT}}))$

if $\sigma_{\text{av}}^{\text{old}} \le \sigma_{\text{av}}^{\text{max}}$

if $\sigma_{\text{av}}^{\text{old}} > \sigma_{\text{av}}^{\text{max}}$

surplus water exits through lid

$\Rightarrow \; p_{\text{PT}} = 0$

Newton's iteration to find d_I fulfilling

$A_I(d_I, \varepsilon_{xx}^{\text{eig}}) = \frac{\rho_W}{\rho_I}(A_0 - A_{\text{sim}}(p_{\text{PT}} = 0))$

evaluate K_I

if $K_I > K_{Ic}$

if $K_I \le K_{Ic}$

set $d_I = d_I + \Delta d_I$

Newton's iteration to find $\varepsilon_{xx}^{\text{eig}}$ with

$\sigma_{\text{av}}^{\text{new}}(\varepsilon_{xx}^{\text{eig}}, p_{\text{PT}}^{\text{old}}) = \frac{d_I}{d_I + \Delta d_I} \sigma_{\text{av}}^{\text{old}}$

if $p_{\text{PT}} \ne 0$

if $p_{\text{PT}} = 0$

set $CD = CD + \Delta CD$

set $p_{\text{PT}} = 0$

compute $A_{W_{\text{sim}}}(p_{\text{PT}} = 0)$

set $CD = CD + \Delta CD$

Newton's iteration to find W

with $A_{W_{\text{sim}}}(W) = A_W$

if $A_{W_{\text{sim}}} < A_W$

if $A_{W_{\text{sim}}} \ge A_W$

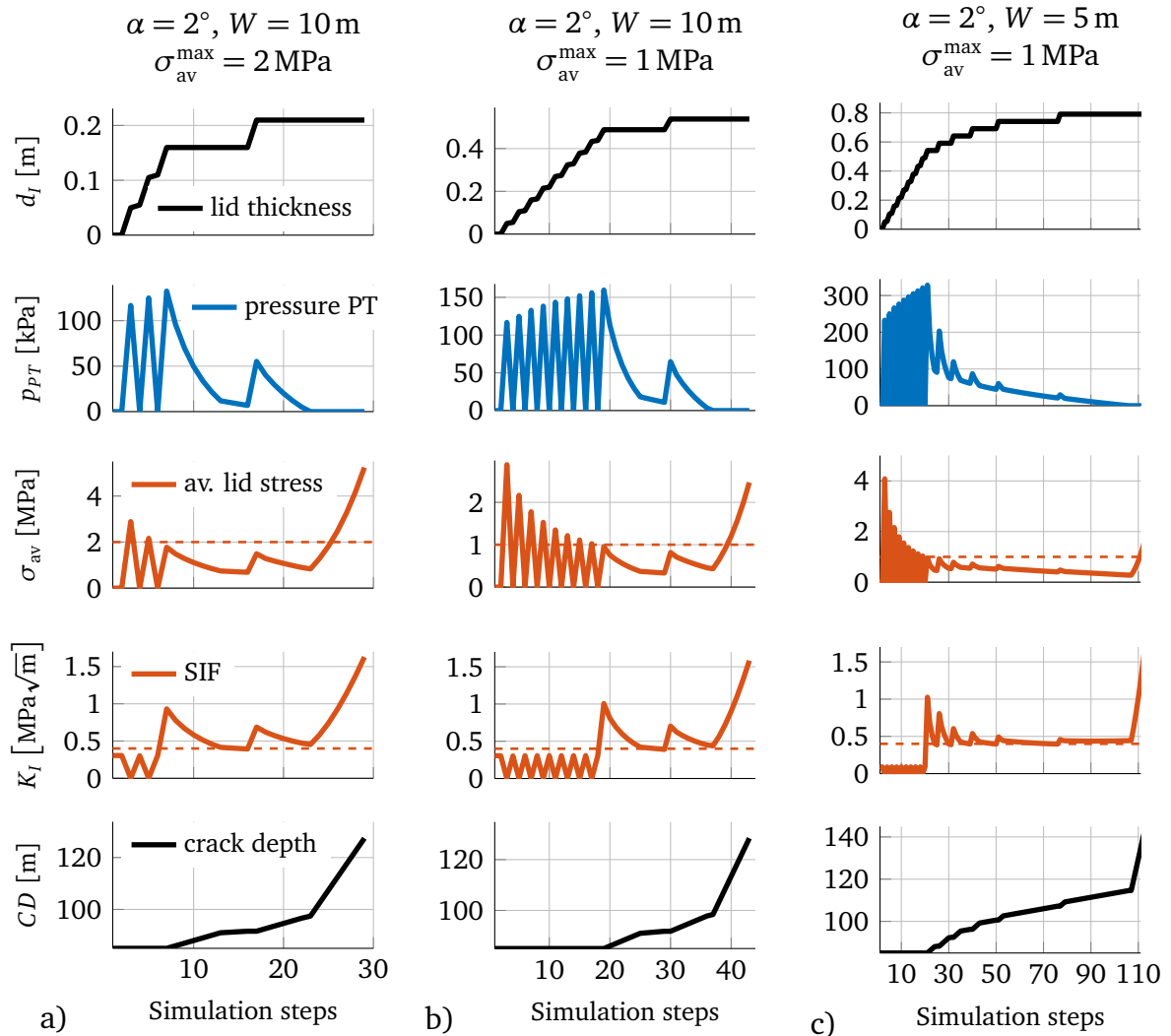Figure 5.41: Workflow for simulation of freezing-induced crack propagation

Figure 5.42: Lid thickness and resulting phase transition pressure, average lid stress, stress intensity factor and crack depth with respect to simulation step of frost wedging process for $\alpha = 2°$ using different values for the water level or the maximum average lid stress

only increase the stress at the crack tip and therefore accelerate crack propagation. The simulation with equal water level but reduced maximum average tensile stress as shown in Fig. 5.42 b) needs several more lid growth steps before a stable lid geometry is reached. The results in Fig. 5.42 c) show, that the same lid growth increments of $\Delta d_I = 0.05\,\text{m}$ as in the previous simulations lead to a considerably higher phase transition pressure and resulting average lid stress if a reduced water level of $W = 5\,\text{m}$ is used. A lower water level slightly reduces the amount of dispersed water for equal lid increment thickness. However, since a lower water level implies a smaller ice water interface, which can move to make room for the dispersed water, the displacements along the interfaces have to be considerably larger and hence a higher phase transition pressure is needed. With $d_I \approx 0.55\,\text{m}$, a stable lid geometry is reached and crack propagation starts. A lid thickness of $d_I \approx 0.8\,\text{m}$ leads to a complete penetration of the crack. Further simulations with $\alpha = 2°$, $W = 5\,\text{m}$ and

$\sigma_{\text{av}}^{\text{max}} = 2\,\text{MPa}$ (results not plotted) show crack propagation with $d_I \approx 0.214\,\text{m}$ and lead to a complete penetration of the crack with $d_I \approx 0.41\,\text{m}$.

The plots in Figs. 5.43 and 5.44 show the results for comparable setups using $\alpha = 1°$ and $\alpha = 0.5°$. Since a smaller opening angle considerably reduces the dispersed water per lid growth increment, the resulting phase transition pressure and the average lid stress decrease. In the case of $W = 10\,\text{m}$, where the stress intensity factors of the water-filled crack without ice lid are close to the critical level, less lid increments are needed for a stable lid configuration, hence the lid thickness which eventually leads to a complete penetration of the crevasse also decreases. This trend cannot be observed for $W = 5\,\text{m}$ where a decreasing opening angle leads to an equal or even increasing lid thickness needed for a complete penetration of the crevasse. In further simulations not presented here with $\alpha = 0.1°$ and $\Delta d_I = 0.05\,\text{m}$ the resulting
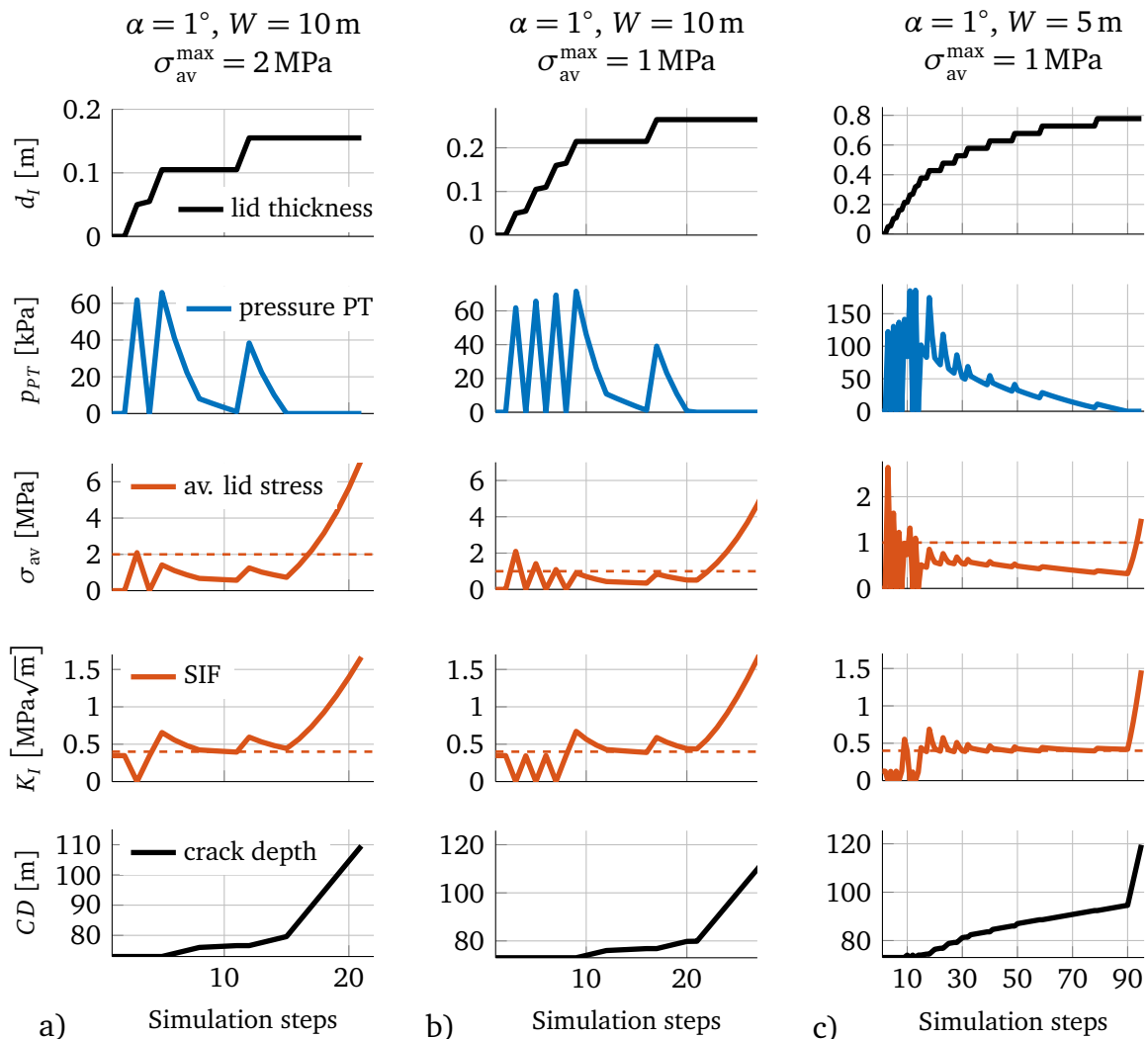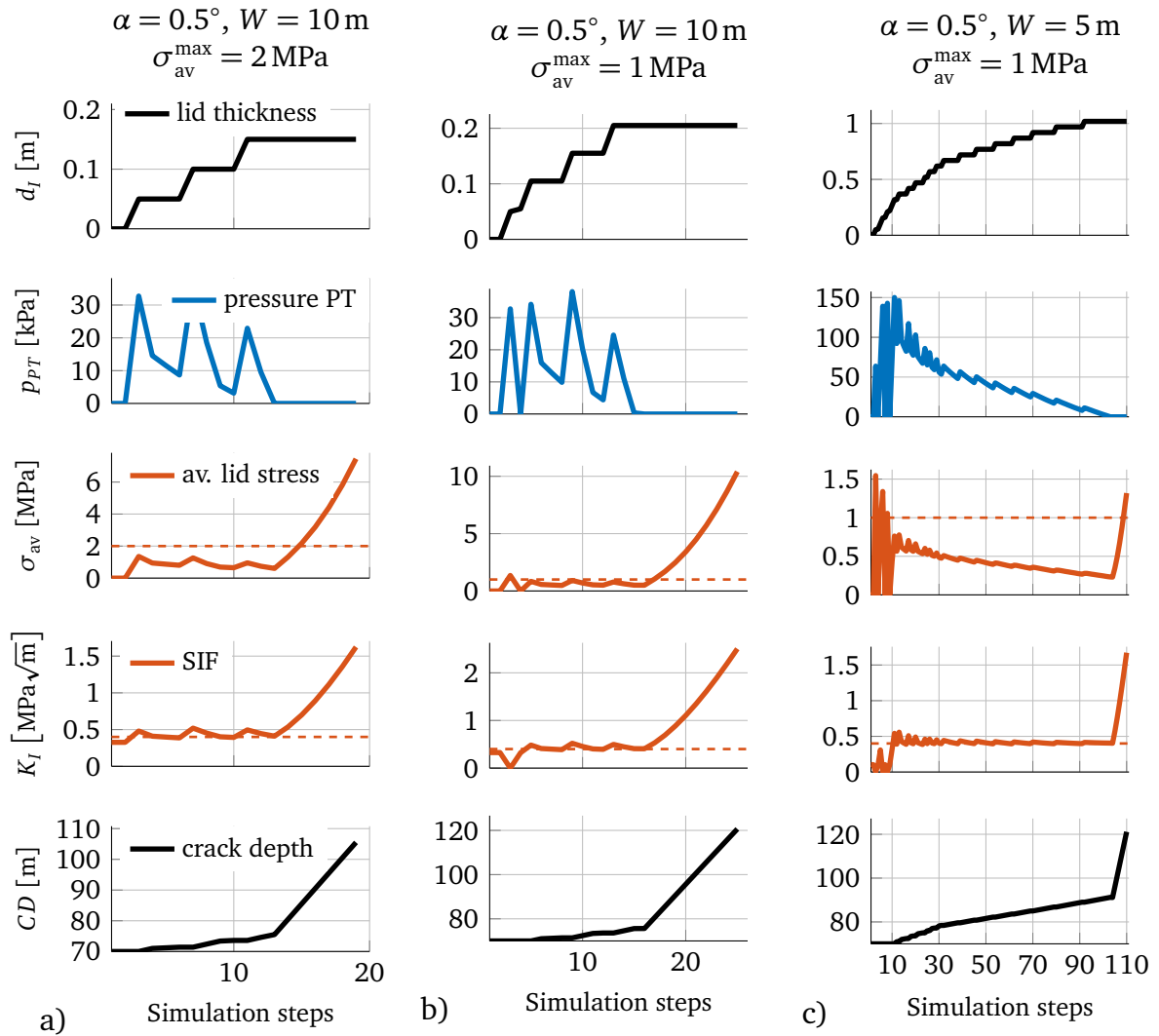

Figure 5.43: Lid thickness and resulting phase transition pressure, average lid stress, stress intensity factor and crack depth with respect to simulation step of frost wedging process for $\alpha = 1°$ using different values for the water level or the maximum average lid stress

Figure 5.44: Lid thickness and resulting phase transition pressure, average lid stress, stress intensity factor and crack depth with respect to simulation step of frost wedging process for $\alpha = 0.5°$ using different values for the water level or the maximum average lid stress

average stress in the lid does does not exceed 1 MPa. Nevertheless, water-filled cracks with small opening angles need considerably more lid growth steps until the crack penetrates to the bottom of the ice shelf. Ideally sharp cracks completely freeze before the crack tip reaches the bottom of the shelf since the water supply is very small.

Although freezing in a crack is a continuous process, all presented simulations were performed with incremental lid growth, accepting that the results consequently also depend on the growth increment Δd_I. Simulations with $\Delta d_I = 0.02$ m show, that smaller increments considerably reduce the ice lid thickness needed for a complete penetration of the crack. Exemplarily for $\sigma_{av}^{max} = 1$ MPa, $d_I \approx 0.16$ m is needed for $\alpha = 2°$ and $W = 10$ m, $d_I \approx 0.1$ m suffices for $\alpha = 1°$ and $W = 10$ m and also the lid thickness needed for the crack with $\alpha = 2°$ and $W = 5$ m can be reduced from
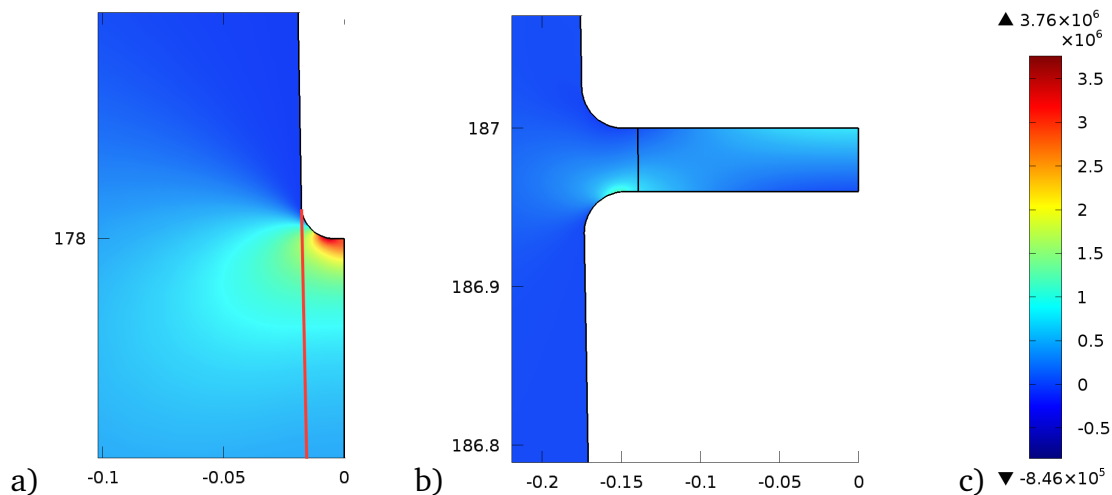
Figure 5.45: Snapshot of the stress component σ_{xx} for a) a rounded tip due to freezing at the crack tip, b) a rounded ice lid with the associated colorbar with units in Pa in c)

$d_I \approx 0.8\,\mathrm{m}$ for $\Delta d_I = 0.05\,\mathrm{m}$ to $d_I \approx 0.57\,\mathrm{m}$ using $\Delta d_I = 0.02\,\mathrm{m}$. Since even these small increments lead to a breaking of the lid in the first few steps, the results still present a upper limit of the ice lid thickness needed for complete penetration.

The simulations of the phase transition process indicated considerable freezing at the crack tip. Figure 5.45 shows qualitative plots of the stress component σ_{xx} at a rounded crack tip and a rounded lid for $\alpha = 2°$ and $W = 10\,\mathrm{m}$. The crack tip is rounded such that freezing of the first meter of water at the tip is represented whereas freezing from the crack faces is ignored. The red line in Fig. 5.45 a) illustrates the former crack face. The lid - crack face - interface is rounded in order to prevent stress concentrations at unphysical edges. It appears that even at a rounded crack tip, the stress component σ_{xx} is higher than the measured tensile strength for ice. Hence the initiation of a new crack can be expected. The stresses in the lid are considerably smaller.

5.6.3 Summary of the simulation of frost wedging processes

The analysis of the phase transition process within a water-filled crevasse revealed that only small ice lid thicknesses ranging from $d_I = 10\,\mathrm{cm}$ to $d_I = 20\,\mathrm{cm}$ can be expected for the applied external temperatures, geometries and the considered time span. The most influencing parameter on the resulting lid thickness is the external temperature. Considerable freezing at the crack tip could be observed. The consideration of fluid movement inside the crevasse reduced the freezing at the tip and increased the lid thickness. The consequent simulation of the frost wedging process showed that for situations where without additional freezing the stress concentration at the tip of the water-filled crack is close to the critical value, the lid thicknesses

resulting from the thermodynamical model suffice to let the crack penetrate the ice shelf. Also freezing at the tip cannot prevent high stresses due to the phase transition pressure that eventually lead to new crack initiation. In case of crevasses where the stress intensity due to the water is far below the critical level or in case of very sharp cracks, crevasse penetration due to frost wedging is unlikely since lid thicknesses of more than 50 cm are needed. If the crevasse is ideally sharp, the crack can only propagate few meters before it completely freezes.

Many prerequisites are needed to start a frost wedging process: very cold external temperatures, water-filled crevasses that have not penetrated by only the water load, complete sealing of the crevasses due to the ice lid and a crack propagation speed that is faster then freezing processes at the tip that might lead to crack healing. Therefore, it is daring to assume that all disintegration events that coincide with a drop of the external temperatures considerably below 0 °C are triggered by frost wedging. Nevertheless the simulations show that the presented process is possible.

6 Simulation of horizontal rift propagation in ice shelves

Besides the analysis of vertical crack propagation for the estimation of crack depths, the availability of high-resolution images of crevassed ice shelf surfaces also revealed the interest to study the propagation of rifts. The term "rift" in this context is commonly used for horizontally propagating cracks that are assumed to penetrate the complete thickness of the ice shelf. Hence, the faces of the rift below the water level are suspect to water pressure. In satellite pictures, the water surface within larger rifts is often covered with ice gravel or sea ice.

The analysis of rift propagation is of high scientific interest since the direction of the rift, the speed of the propagation and also potential rift arrest reveal information on the structure of the ice shelf. Furthermore, the analysis of rift propagation can be used to predict the iceberg size resulting from large calving events. Apart from the purely scientific interest, the estimation of a most probable rift propagation direction helps to plan routes for field campaigns in the respective region.

First descriptions of rifts in Antarctic ice shelves are based on areal photography. This method for capturing surface structures in Antarctica dates back to the beginning of the 20th century (Roscoe, 1956). Examples can be found in Rignot (2002) for PIG or in Neuburg et al. (1959) who describe the Grand Chasm, a major rift in the Filchner-Ronne Ice Shelf whose final propagation in 1986 resulted in an iceberg with an area of 11500 km^2 (Van Der Veen, 2002). With the development of space borne measurement tools in the 1970's, ice shelves could be monitored on a regular base, enabling scientists to describe rift propagation. Rignot (2002) describes the calving front, the grounding line and two major calving events with the preceding rifts of PIG for the 1947 - 2000. His observations are complemented by MacGregor and Catania (2012) who describe rifting and ice front retreat in the Amundsen Sea Embayment between 1972 and 2011. Fricker (2005), Bassis (2005), Bassis et al. (2007) and Bassis et al. (2008) published a thorough analysis of the growth of a single rift in the Amery Ice Shelf from 2002 to 2006 with the aim to identify the major forces that drive rift propagation. Further rift propagation eventually leading to calving of larger ice shelf parts is documented for e.g. the Ronne Ice Shelf (Larour et al., 2004a,b), the Brunt Ice Shelf (Khazendar et al., 2009) and the WIS (Braun et al., 2009). An overview of ice shelves with past or present rift propagation can be found in Walker et al. (2013).

Different approaches have been followed in order to simulate rifted ice shelves. On the one hand models were built to predict the location of crevasses and rifts based

on the flow stress resulting from simulated or measured ice shelf velocities. Examples can be found in Rist et al. (1999) where LEFM is used to connect principal flow stresses and the critical fracture toughness. An extra variable for fractured or rifted zones depending on the shear stress and influencing the velocity field was introduced by Sandhäger (2003) and further developed by Sandhäger et al. (2005). Weis et al. (1999) implemented a comparable approach, using a so-called enhancement factor to increase the velocities in rifted zones. Both models were applied for the Brunt Ice Shelf and the results compared to measured surface velocities in Humbert et al. (2009). The approaches of Rist et al. (1999) and Sandhäger et al. (2005) were combined by Jansen et al. (2010). Albrecht and Levermann (2012) introduced a new field variable, the fracture density field, which allows for crack initiation, crack transportation and crack healing.

The thus far mentioned methods describe fractured or rifted areas as weak zones within the ice shelf continuum. This is different in the approaches of Larour et al. (2004a) and Larour et al. (2004b), as well as Hulbe et al. (2010), where rifts in the ice shelf are treated as geometric features. Both, Larour et al. (2004a) and Hulbe et al. (2010) analyze rift propagation using small excerpts of the complete ice shelf. Hulbe et al. (2010) assumes rift propagation to happen on a linear elastic time scale and therefore solves the elastic boundary value problem of the excerpt domain using the Boundary Element Method. The required stress boundary conditions are taken from the viscous surface stress computed from measured ice shelf velocities. Crack propagation is evaluated using the maximum circumferential stress criterion. Also Larour et al. (2004a) uses linear elastic fracture mechanics to evaluate whether the rift propagates. However, the direct solution of the elastic boundary value problem is omitted and the crack propagation velocity is computed directly from the crack opening rate evaluated from the ice dynamical simulation. In Larour et al. (2004b) this method is transferred to a simulation of the entire Ronne Ice Shelf using different assumptions on the filling of the rifts, as are water or ice mélange of which the latter helps to prevent further crack growth.

The modest number of models explicitly describing the horizontal propagation of geometric rifts in flowing ice shelves is symbolic for the difficulties that arise when the stresses of the dynamic simulation, solving for the ice velocity, have to be transferred to a linear elastic model that is based on displacement fields. A comprehensive solution of the full problem could only be achieved by application of a viscoelastic material law with a transient simulation of the problem. Depending on the complexity of the ice shelf, a satisfying solution of only the steady state velocities already requires extensive knowledge on the geometry in three dimensions, the boundary conditions and the material parameters of the domain in combination with further external parameters as e.g. the accumulation and melting rate, as well as the air and ocean temperatures. Therefore, a complete viscoelastic solution of the problem will be omitted. Instead, the following section proposes a new method to relate the viscous answer of the ice shelf to an adequate forcing for the linear elastic model, which is then used for the analysis of horizontal rift propagation. The performance of the

approach is first demonstrated for a simplified box-like geometry with constructed velocity fields before it is applied to rifts at PIG and WIS.

6.1 From viscous flow to elastic fracture by means of viscous volume forces

A suitable viscoelastic model to describe the rheology of ice is that of a viscoelastic fluid. The one-dimensional representation of the most elementary viscoelastic fluid, the Maxwell model, consists of a spring and a dashpot in series connection as illustrated in Fig. 6.1 a). In order to meet the specifications known for ice, the spring symbolizes linear elastic material behavior, while the dashpot represents the highly nonlinear flow behavior of ice using Glen's flow law as introduced in Sec. 2.2.2. Simple equilibrium considerations show, that the stresses in the spring, as well as in the dashpot have to be equal. The respective strains on the other hand sum up to a total strain. Hence, assuming an external stress σ yields $\sigma_e = \sigma_v = \sigma$ and $\varepsilon_{ve} = \varepsilon_e + \varepsilon_v$ with the subscripts referring to the elastic and the viscous contribution, respectively. Previous publications on rift propagation (Larour et al., 2004a) indicate, that even
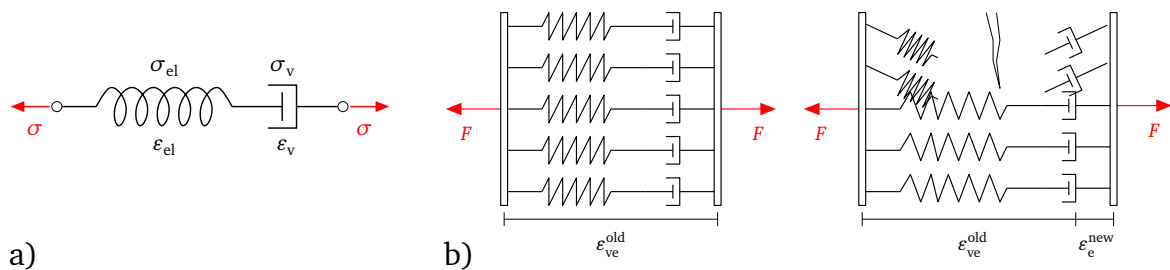

Figure 6.1: a) One-dimensional representation of a Maxwell model; b) schematic sketch of a crack in a Maxwell material

though viscous creep dominates the overall behavior of ice shelves on the longer time scale, rift growth can be assumed to happen on a short time scale enabling the use of linear elastic fracture mechanics also for the analysis of horizontally propagating cracks. The general idea of the fracture process is sketched in Fig. 6.1 b). The material, experiencing an external load F, deforms on the long time scale with a resulting viscoelastic strain ε_{ve}. If now, due to a sudden incident a crack initiates, the external load is distributed on a smaller area and the consequent increase in strain is predominantly generated by the elastic part, yielding higher stresses that lead to further fracture.

The extension of the stress to three dimensions results in

$$\boldsymbol{\sigma}_e = \boldsymbol{\sigma}_v \quad \text{and hence} \quad \text{div}\,\boldsymbol{\sigma}_e - \text{div}\,\boldsymbol{\sigma}_v = 0. \tag{6.1}$$

The definition,

$$\boldsymbol{f}_v = -\text{div}\,\boldsymbol{\sigma}_v, \tag{6.2}$$

yields a so called viscous volume force f_v which can then be used as load for the linear elastic simulation solving

$$\text{div } \sigma_e + f_v = 0, \tag{6.3}$$

for the displacement field.

In case of measured velocity fields as input for the computation of the viscous volume force, the exact boundary condition (e.g. inflow from glaciers, friction at the bedrock along the grounding line), the material parameters, as well as the geometry can not be completely distinguished. For this reason, also without the insertion of starter cracks, the resulting elastic stresses for an approximated geometry with estimated stress or displacement boundary conditions can not equal the previously computed viscous stresses. This violates the assumptions made in Equ. (6.1). Nevertheless, qualitative features such as regions with tensile or compressive stresses and shear bands can be resolved. This is all the more important as no predictions on the certainly existing spatial distribution of the material parameters in the ice have to be made.

Figure 6.2 a) shows the sketch (not to scale) of a simplified quadratic ice shelf ramp with the horizontal extend $L = 100$ km. The thickness varies from $H = 300$ m at $x = 0$ m and $y = L/2$ to $H = 150$ m at $x = L$ and $y = -L/2$. The velocities along the grounding line ($x = 0$) are constrained. Along the lateral boundaries at $y = -L/2$ and $y = L/2$, only the velocities in normal direction are hindered. An idealized ice rise (blue) is inserted in the lower part of the ramp. The velocities along the boundaries of the ice rise are fixed. This constraint overestimates the decelerating effect of real ice rises and is used for simplicity. The ice domain is loaded by gravity. The two-dimensional Stokes equations are solved for the ice shelf velocities using the shallow shelf approximations with the parameters $n = 3$ and $A^{-1/n} = 7.6 \cdot 10^7$ Pa s$^{1/3}$. For further information on the solution of ice dynamical problems, the reader is referred to e.g. Greve and Blatter (2009) or Schmitt (2011). In a first simulation, the ice rise is ignored. The resulting horizontal velocities are illustrated in Fig. 6.2 b). The first principal viscous surface stress with the resulting viscous volume forces is shown in Fig. 6.2 c). The viscous stresses, as well as the viscous volume forces are computed using difference quotients in MATLAB. The elastic boundary value problem is solved for the horizontal two-dimensional ice shelf plane using the plane stress approximation as introduced in Sec. 2.2.1. The spatial variability of the ice shelf thickness hurts the assumptions made for a plane stress simulation but can be accepted due to the dimensions of the domain, where changes in the thickness of several meters occur on a horizontal scale of several kilometers.

Figure 6.2 d) illustrates the first principal elastic stress resulting from the linear elastic simulation forced by the viscous volume forces. Since the geometry and the boundary conditions correspond to those of the ice dynamical simulation, the resulting viscous and elastic stresses almost match. Small differences are of numerical origin.

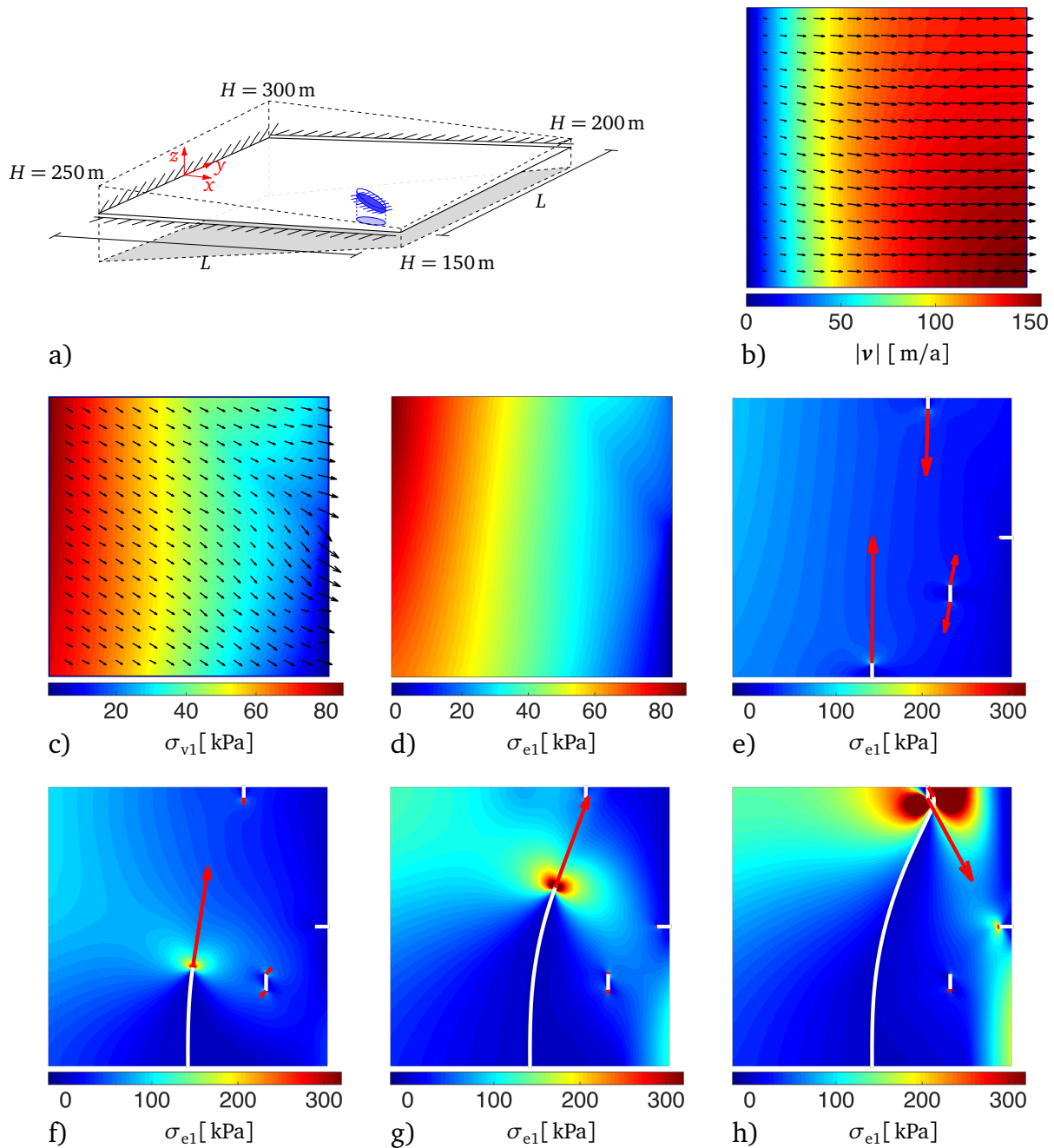The first principal elastic stress after the insertion of the initial cracks with the re-

Figure 6.2: a) Sketch of idealized ice shelf ramp with ice rise (not to scale); b) ice shelf speed (color) and direction (black arrows) resulting from ice dynamical simulation without ice rise; c) resulting first principal viscous surface stresses (color) and viscous volume forces (black arrows); d) first principal elastic stress due to application of viscous volume forces in a linear elastic simulation without initial cracks; e) first principal elastic stress after insertion of initial cracks (green lines) and resulting configurational forces at the crack tips (red arrows, scaled); f)-h) crack path after 20 and 40 and 67 growth steps

sulting configurational crack tip forces is demonstrated in Fig. 6.2 e). Even though the maximum stresses at the crack tips exceed 1000 kPa, the color range is fixed at the values indicated by the color bar to point out spatial changes in the stresses.

The resulting crack paths after 20, 40 and 67 crack growth steps are illustrated in Fig. 6.2 f) to h). Unlike in the benchmark example after Bouchard et al. (2003) in Sec. 4.6.6, where both cracks are allowed to grow at the same time, now only the crack with the highest value of J propagates by a defined increment depending on the change of the crack direction angle $\Delta\theta$. No threshold for crack initiation is applied.

In a next step, the ice shelf ramp with ice rise is simulated. Figure 6.3 a) shows the resulting horizontal velocities. As to be expected, the ice rise not only considerably decelerates the ice velocities in the lower part of the ice shelf but also reduces the maximum velocity, which now appears at the upper right corner of Fig. 6.3 a). The first principal viscous and elastic stresses, as well as the viscous volume forces are illustrated in Figs. 6.3 b) and c). Strong tensile viscous stresses now appear downstream of the ice rise. This characteristic is also well captured by the first principal elastic stress. The viscous volume forces show considerable fluctuations around the
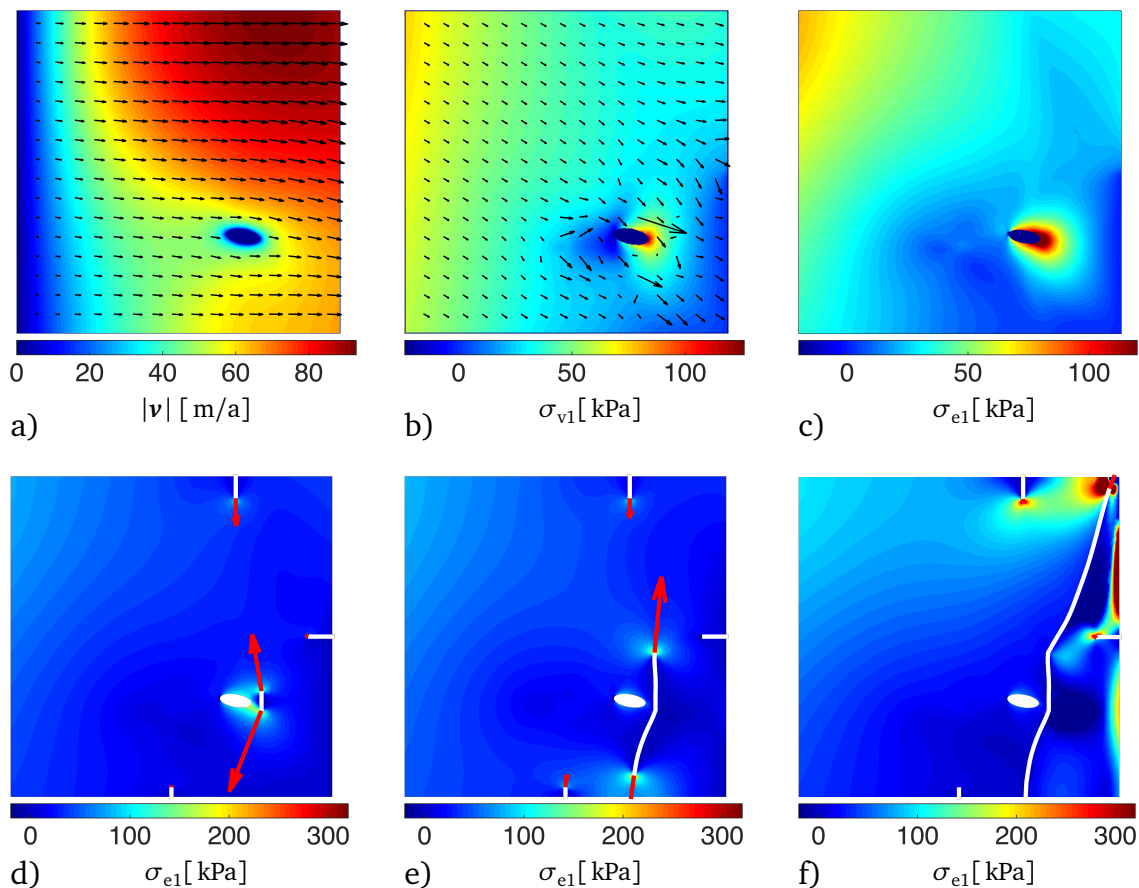

Figure 6.3: a) Ice shelf speed and direction resulting from ice dynamical simulation with ice rise; b) resulting first principal viscous surface stresses and viscous volume forces (black arrows); c) first principal elastic stress due to application of viscous volume forces in a linear elastic simulation without initial cracks; d)-f) first principal elastic stress and crack path for initial configuration and after 40 and 85 growth steps, scaled red arrows show configurational crack tip force
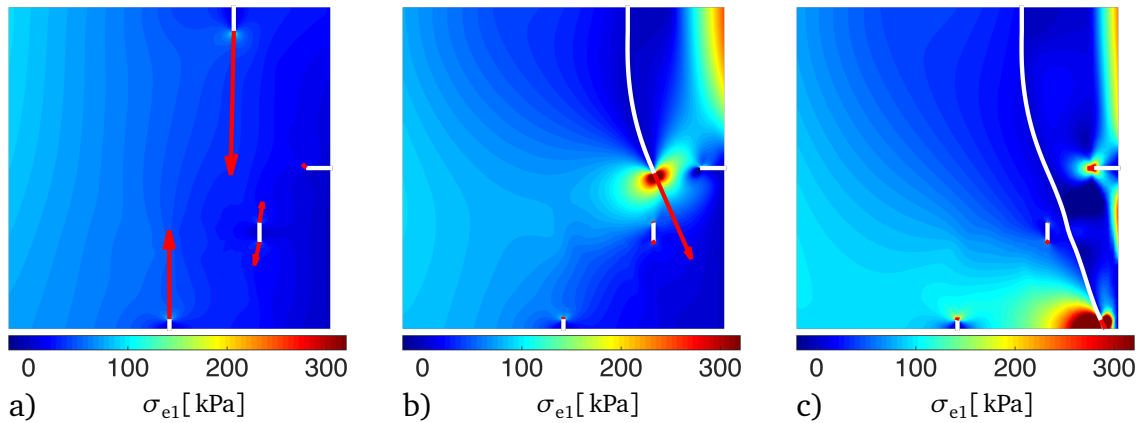
Figure 6.4: First principal elastic stress, configurational crack tip force and crack path for viscous volume force resulting from ice dynamical simulation with ice rise applied to fracture mechanical model without ice rise; a) initial setup; b) crack path after 40 steps; c) crack path after 79 steps

ice rise. This is caused by the successive derivatives using difference quotients that are needed for the computation. Slight discontinuities or stronger gradients in the velocity profile hence amplify with each derivative and lead to the demonstrated result. The viscous volume forces in some distance from the ice rise are similar to those in Fig. 6.2 c). Figures 6.3 d) to f) show the crack path and the resulting configurational forces at the crack tip for the initial state and after 40 and 85 iterations. Unlike in the previous example without ice rise, now the crack in the ice shelf bulk shows the strongest criticality and propagates first towards the closer boundary, then towards the upper right corner.

In order to demonstrate the influence of an accordance between the geometry and boundary conditions used for the evaluation of the velocity profile and those applied for the fracture mechanical problem, the viscous volume forces resulting from
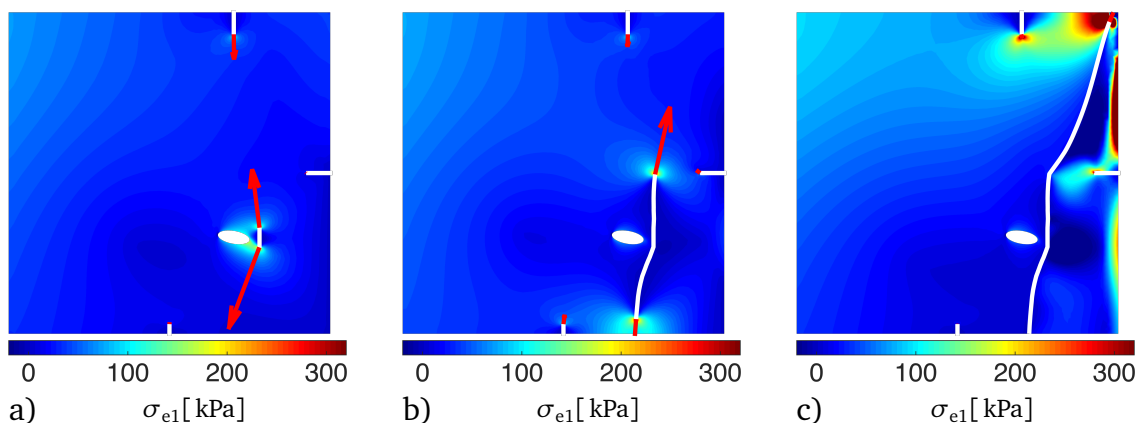

Figure 6.5: First principal elastic stress, configurational crack tip force and crack path for viscous volume force resulting from ice dynamical simulation without ice rise applied to fracture mechanical model with ice rise; a) initial setup; b) crack path after 40 steps; c) crack path after 85 steps

the ice dynamical simulation with ice rise are applied to the linear elastic model without ice rise. The resulting crack path as shown in Figs. 6.4 a) to c) completely differs from the previous two simulations. If on the other hand, the viscous volume forces of the simulation without ice rise are applied to the fracture mechanical model with ice rise (results shown in Fig. 6.5), only slight variations in the resulting crack path appear in comparison to the example with compatible volume forces. Hence, the crack path in an ice shelf model, loaded by viscous volume forces, is influenced by the overall trend of the volume forces and by the geometry with the associated boundary conditions. Local trends in the viscous volume forces only play a secondary role but can tip the scale if several crack tips show similar criticality as can be seen by comparing Fig. 6.2 e) and Fig. 6.4 a).

6.2 Rift propagation at Pine Island Glacier

Pine Island Glacier is one of the longest and fastest flowing glacier of Antarctica (Rignot et al., 2011b). It is located in the Amundsen Sea embayment in Western Antarctica as indicated by the red box in Fig. 6.6 a). The floating part of the glacier is divided into a northern, a central and a southern ice shelf (Rignot, 2002) from which only the central part will be considered in the following study. The ice shelf is known to produce large tabular icebergs with a surface area of several hundreds of km^2 on a quasi-regular base. The rift propagation leading to the most recent calving event was first observed autumn 2011 and documented by Howat et al. (2012). The rift is illustrated in Fig. 6.6 b). The final iceberg break-off occurred in autumn 2013. The availability of high resolution satellite data from the ice shelf prior and after the
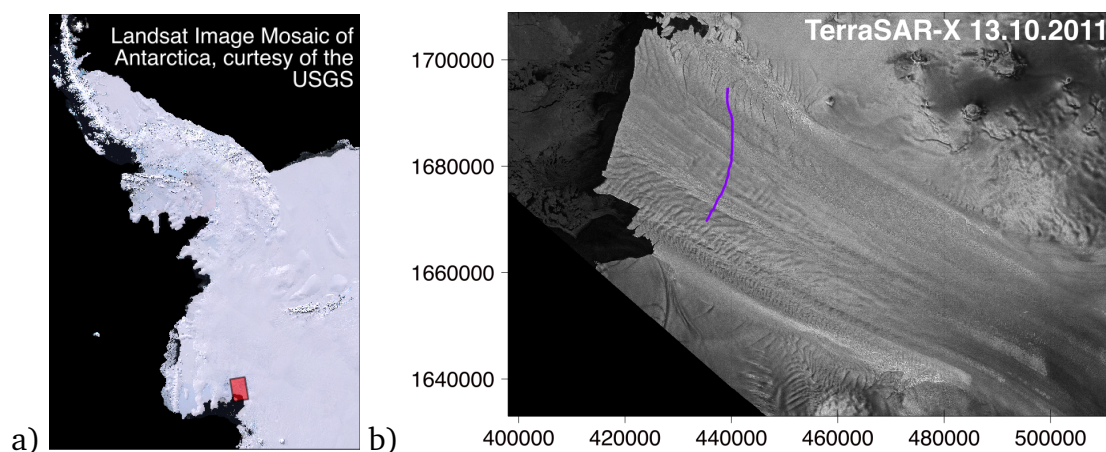

Figure 6.6: a) Landsat Image Mosaic of Western Antarctica in polarstereographic projection; red box indicates location and extend of following images of PIG; b) TerraSAR-X image of PIG taken on October 13th in 2011 with coordinates (in meters) in Universal Transverse Mercator (UTM) projection using zone 14S; the crack highlighted in purple leads to the 2013 calving event

crack growth motivated the presented fracture mechanical analysis of horizontal rift propagation in ice shelves.

Rignot (2002) documented the position of the calving front, as well as several calving events of PIG from 1947 to 2000. A detailed analysis of the 2001 calving event is published in Bindschadler and Rignot (2001). Further information on e.g. the calving fronts in the Amundsen Sea embayment from 1972 to 2011 can be found in MacGregor and Catania (2012).

Figure 6.7 illustrates the position of the calving front and the initial cracks, which eventually propagate leading to iceberg break-off and the resulting calving event from January 2004 to November 2013. Shaded lines illustrate crack or calving front
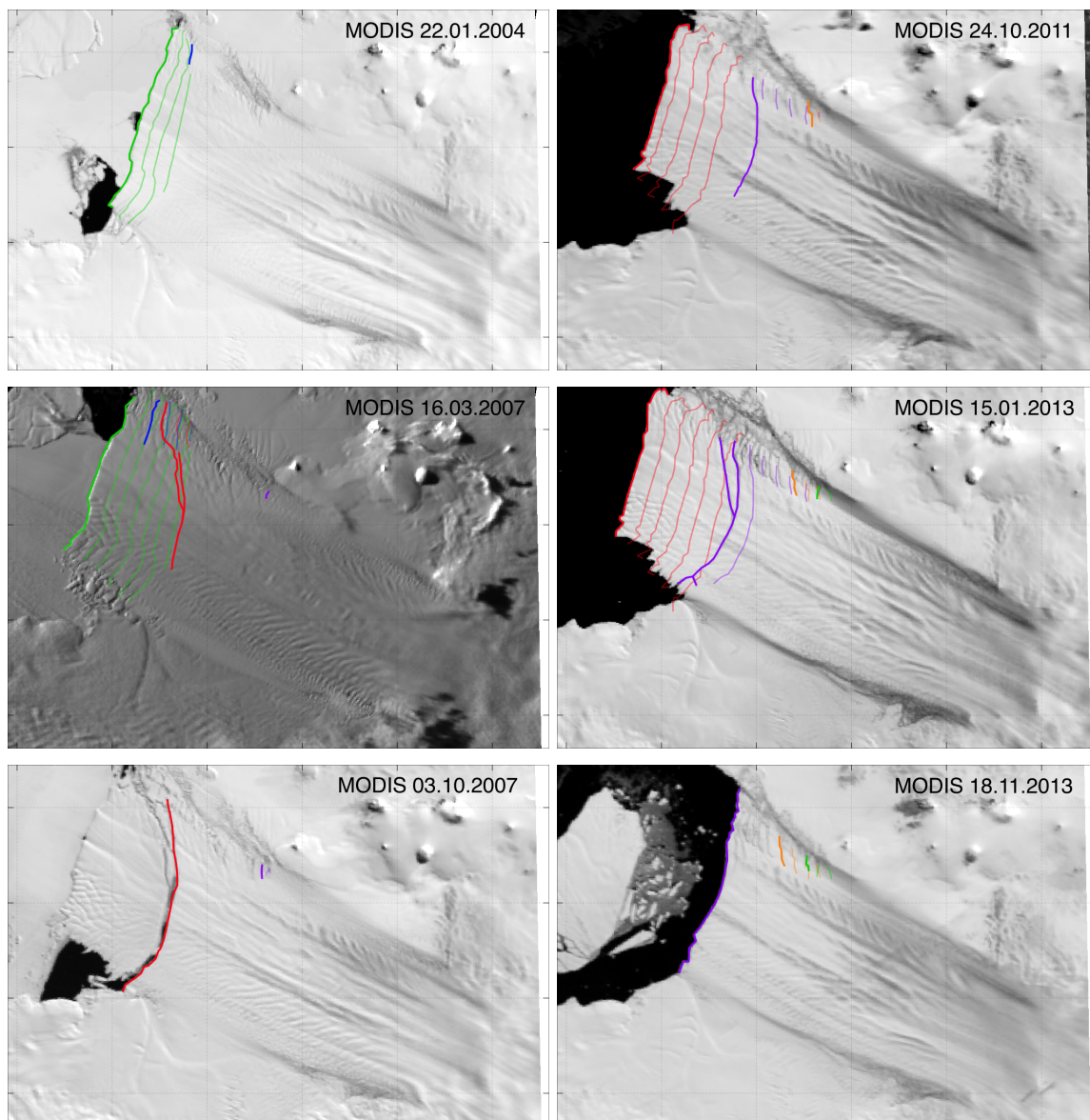

Figure 6.7: Series of annual calving front positions and rift paths that eventually lead to major calving events superimposed on associated MODIS image (Scambos et al., 2015); coverage and axes equivalent to Fig. 6.6 b)

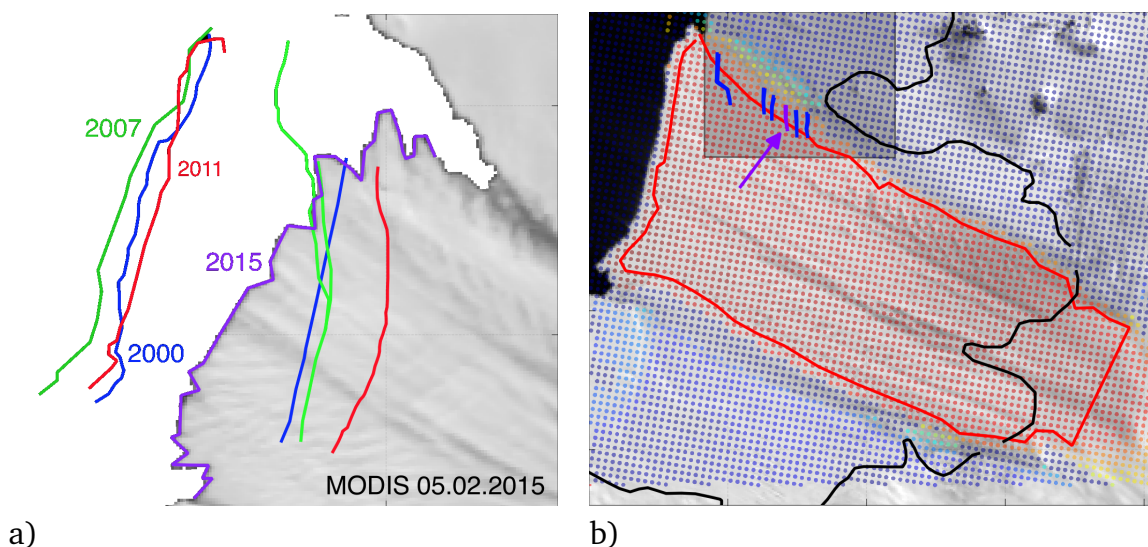a)   b)

Figure 6.8: a) Calving front positions associated with major rift propagation leading to the last three calving events in 2013, 2007 and 2001 superimposed on MODIS image of PIG front in February 2015 (Scambos et al., 2015) with associated calving front; b) point plot of velocity field grid data generated by Ian Joughin using ALOS Palsar images of 2006 and 2008 superimposed on MODIS image of October 2008; red line shows geometry used for fracture mechanical simulation; black lines illustrate DInSAR grounding line data (Rignot et al., 2011a); initial cracks, generated from MODIS images, are indicated in blue and purple; the purple initial crack led to the 2011 rift propagation and the consequent 2013 calving event; gray box indicates extent of rifted ice shelf margin in Fig. 6.11

positions from previous points in time. The timespan between the shaded lines is approximately one year. Several authors, e.g. Rignot (2008) and Joughin et al. (2010) describe the continuous thinning and acceleration of PIG in the recent years. Especially the latter can be observed by looking at the annual advance of the calving front in the images of January 2013 and March 2007 presented in Fig. 6.7. It shows that the distance between the annual snapshots of the calving front in January 2013 is considerably larger than in the image of March 2007. Figure 6.8 a) illustrates the position of the calving front at the time of rift propagation for the last three calving events superimposed on the most recent image in visible mode of PIG from February 2015. It appears that the position of the front associated with rift propagation hardly changes. Rignot (2002) reports one further advance of the calving front to the indicated position in 1966. If this advance was directly followed by a calving event is not known. One further small calving event in 1992 happened with a calving front considerably further upstream. The last three calving events indicate a slightly increasing iceberg size.

The solid purple line in Fig. 6.8 a) illustrates the calving front in February 2015. Even though the terminus associated with calving for the last events is by far not reached, the calving front shows signs of ongoing smaller scale calving resulting in the somewhat frayed appearance of the front.

At the beginning of the presented analysis of rift propagation, the amount of up
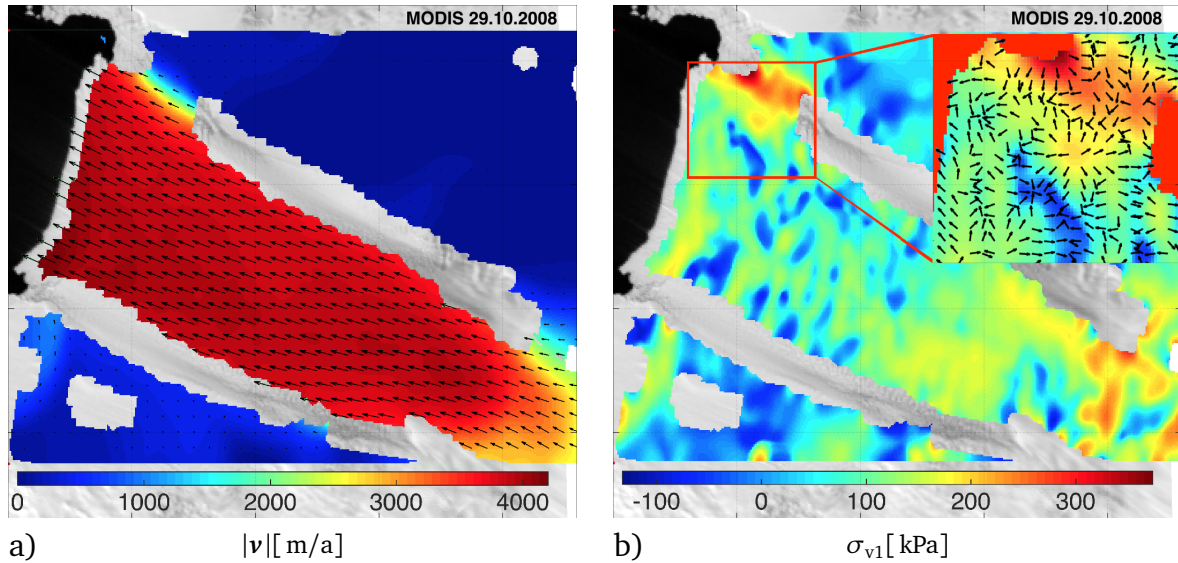
Figure 6.9: a) Raster plot of smoothed ice shelf speed (color) with flow direction indicated by black arrows; b) resulting first principal viscous surface stress with zoom into smaller ice shelf part to show direction of normalized viscous volume forces pointing from tensile to compressive areas

to date velocity fields of PIG was very limited. The following analysis is therefore based on measured velocities of Ian Joughin (personal communication) resulting from ALOS Palsar images from 2006 and 2008 and confined to the geometry of October 2008. Taking into account the large time interval used with one major calving event happening in 2007, the resulting velocity field must be considered as rather rough indicator for the real velocities in October 2008.

The dotted field in Fig. 6.8 b) illustrates the resolution and coverage of the applied original velocity data projected in the required UTM coordinate system together with the geometry and the initial cracks used for the fracture mechanical simulation. The initial crack paths are picked from a MODIS image of October 2008. The purple initial crack eventually propagated in 2011 and led to the 2013 calving event.

The original velocity data contains strong gradients resulting from the coarse resolution, from the tracking process used to build the velocity field or from natural origin. Due to the use of difference quotients these strong gradients lead to jumps in the viscous stresses and especially in the resulting viscous volume forces. In order to reduce the jumps, the velocity field is smoothed in MATLAB using the NaN preserving filtering algorithm *ndnanfilter* by Carlos Aguilera. The resulting smoothed ice shelf speed is shown in Fig. 6.9 a). Black arrows indicate the flow direction. The consequent first principal viscous surface stress in shown is Fig. 6.9 b). A zoom into the northwestern part of the ice shelf illustrates normalized viscous volume forces. As to be expected, the volume forces point from regions with tensile stresses to those with compressive stresses.

Before the viscous volume forces can be used as load for the fracture mechanical analysis, suitable boundary conditions have to be found. The fast flowing central
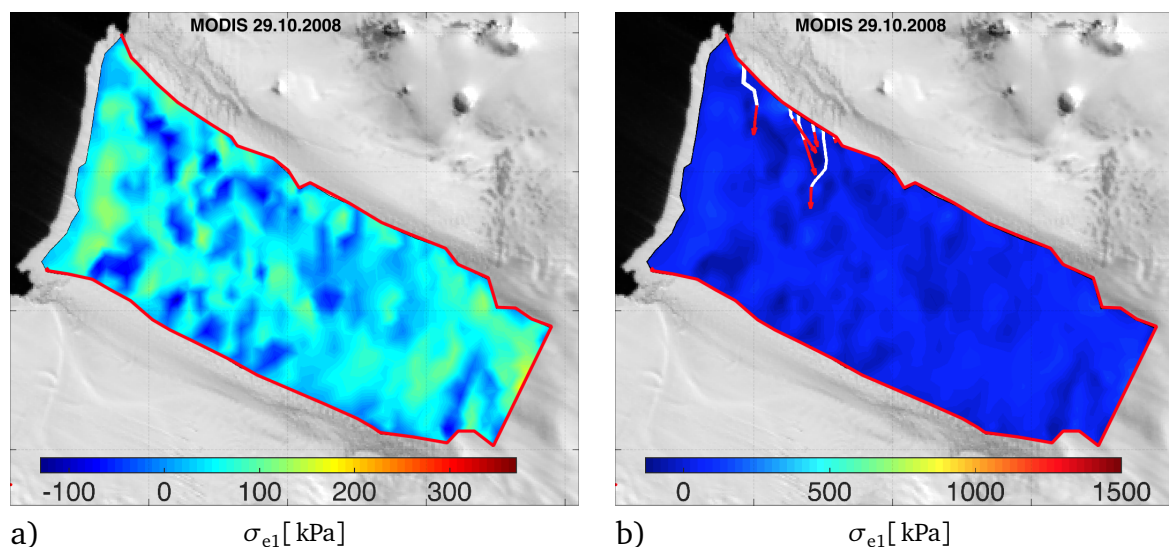
Figure 6.10: First principal elastic stress for a) an ice shelf domain completely constrained along both lateral margins and along the inflow without initial cracks and b) the ice shelf after some crack propagation steps

ice shelf is connected to the considerably slower flowing northern and southern ice shelf along the lateral margins. Especially along the northern margin, ice rises and grounded ice shelf parts influence the ice shelf velocities. A gray box in Fig. 6.8 b) highlights the part of the grounding line (black line) that is responsible for most initial rifts. The ice flow along the lateral margins is neither free, nor fully constrained but might be best described by a contact and friction boundary condition where the friction coefficient depends on the location. However, for the sake of simplicity, as well as due to a lack of knowledge about the spatial distribution and the value of suitable friction coefficients, this rather sophisticated approach is dismissed in favor of four different setups with free or fully constrained boundary conditions. A comparison of the resulting first principal elastic stress without initial cracks to the first principal viscous stress in Fig. 6.9 b) is used to evaluate the plausibility of the setup. Therefore, the color range of the following plots without initial crack is fixed at the limits used in Fig. 6.9 b) even though much higher and lower stresses, depending on the boundary conditions, will locally be reached. Also for the following plots with inserted cracks, the color range is fixed to point out the influence of the different boundary conditions.

In a first simulation, the displacements along all boundaries but the calving front are constrained in x and in y direction, as indicated by the red line in Fig. 6.10 a). The resulting distribution of areas with lower or higher stresses coincides very well with the internal structure of stresses in Fig. 6.9 b), the stress values however are too small. The resulting crack paths after few simulation steps with the associated configurational crack tip forces are shown in Fig. 6.10 b). As in the previous example with the artificial velocity field, only the crack with the largest configurational crack tip force is allowed to grow per simulation step. No threshold for crack prop-

agation is applied. The propagation algorithm was stopped after the merging of crack 2 and 3 (counted from left to right) since a new geometry without the cut out ice shelf fragment in between both cracks needs to be inserted to continue the simulation.

The kinking of the cracks towards the ice shelf inflow is not an unphysical process. Figure 6.11 shows a close up of the strongly rifted area downstream of the grounding line indicated in Fig. 6.8 b). The kinks first appeared in December 2004 during a period where the water in front of PIG was covered with sea ice.

It can be assumed that also the rifts were filled with sea ice or ice mélange and hence at least partly frozen to the northern ice shelf part. The boundary conditions along the northern margin might have been similar to the simulated setup. No kinking however can be seen for the cracks along the northern margin in 2008 hence completely fixed displacements along both margins seem unlikely.

Next, only the displacements along the boundary representing the inflow are constrained. The resulting first principal elastic stress without and with initial cracks is shown in Fig. 6.12 a) and b). Again, the constrained boundary is marked in red. Due to the resulting bending of the ice shelf, exaggerated tensile and compressive stresses appear at the northern and southern part of the constrained boundary, respectively.
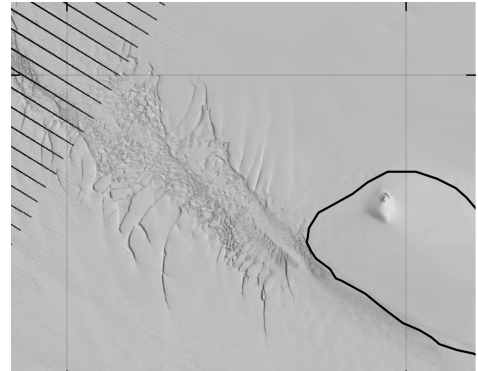

Figure 6.11: Crack kinking along strongly rifted and debris-filled ice shelf margin in December 2006; LandSat image provided by USGS
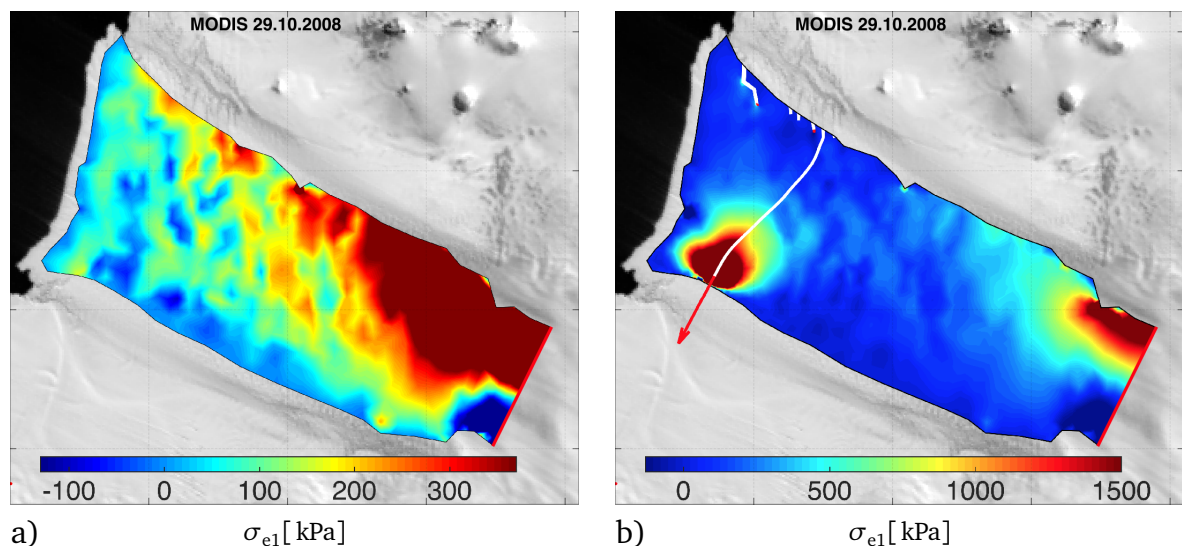

Figure 6.12: First principal elastic stress for a) an ice shelf domain only constrained along the inflow boundary without initial cracks; b) the ice shelf after complete penetration of crack 5
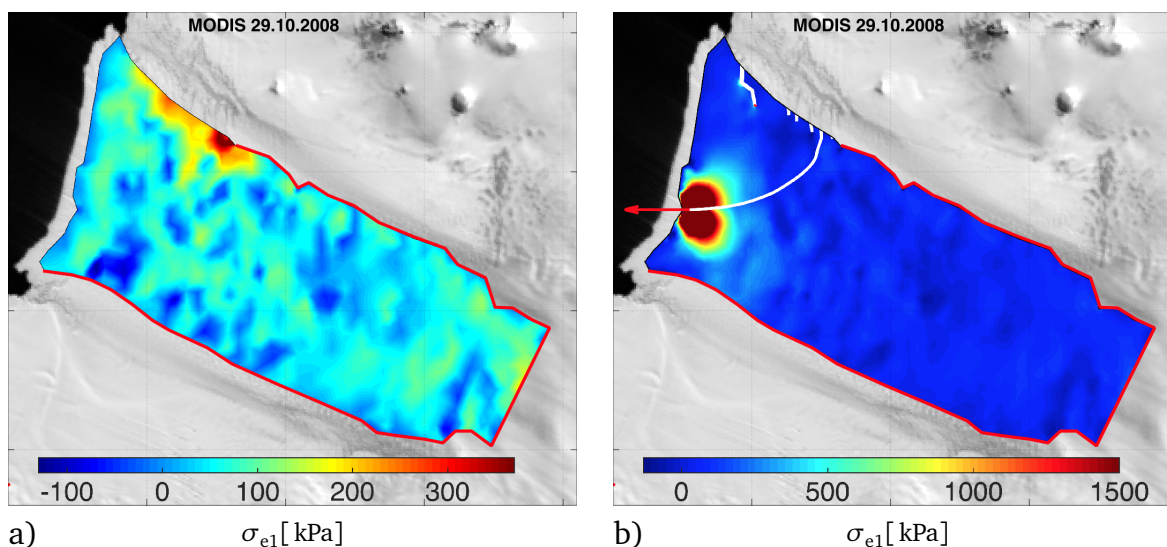
Figure 6.13: First principal elastic stress for a) an ice shelf domain partly constrained along the northern lateral boundary and completely constrained along the inflow and the southern lateral boundary without initial cracks; b) the ice shelf after complete penetration of crack 5 towards the calving front

The setup somewhat captures the stress distribution in the last third of the ice shelf (regarded from inflow to the front) with stronger compressive stressed along the southern lateral boundary. Even though one more initial crack further upstream, as well as one considerably longer crack at the ice front exists, the fifth crack (counted from the left) starts to propagate and eventually crosses the entire ice shelf from north to south. In view of the timespan used to compute the velocity field, this is in good agreement with observed propagating rift, which is one crack further left. The crack path however does not seem reasonable in comparison to observable calving events.

The following two setups aim to approximate the less constrained rifted margin downstream of the grounding line (compare to Fig. 6.11). Therefore, the displacements along the grounded area, the boundaries further upstream, as well as the inflow boundary are constrained, the calving front, as well as the boundaries in the rifted margin are free. In a first try, the displacements along the southern lateral boundary are fully constrained. The resulting first principal elastic stress without initial crack as illustrated in Fig. 6.13 a) shows a better fit to the illustrated viscous surface stress than the previous setups. Now, considerable tensile stresses along the northern margin downstream of the grounded area appear. The tensile stresses in the remaining ice shelf bulk however are still too small. As in the previous setup with the completely free northern lateral boundary, the fifth crack starts to propagate. Since the southern boundary is constrained, the crack propagates towards the closest free boundary, the ice front. This result agrees well with common knowledge about crack propagation, however it does not fit the observed crack paths. Therefore, it must be assumed that also the southern lateral boundary is only partly constrained. This is realized in the last setup as visualized by the red highlighted
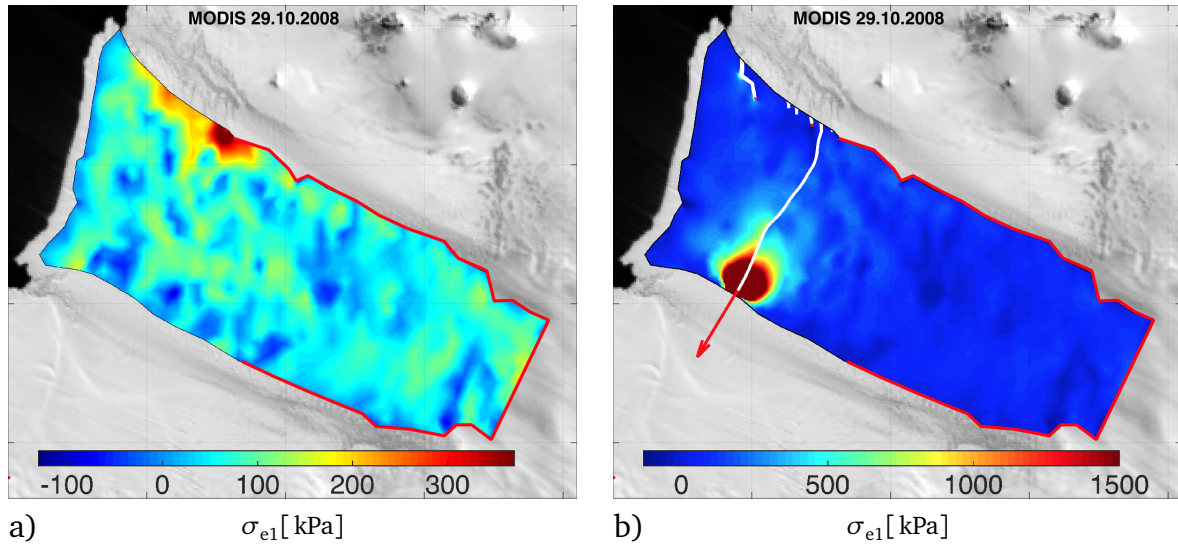
Figure 6.14: First principal elastic stress for a) an ice shelf domain partly constrained along the northern and the southern lateral boundary and completely constrained along the inflow without initial cracks; b) the ice shelf after complete penetration of crack 5 towards the southern lateral boundary

boundaries in Fig. 6.14. Again, the largest tensile stresses in the setup without initial crack appear at the transition from free boundary conditions to constrained boundary conditions along the northern lateral boundary. The stresses in the ice shelf bulk are slightly higher than in the previous example and hence show the best fit to the viscous stresses. Also the resulting crack path in Fig. 6.14 b) represents the best approximation of the observed crack path, which leads to the 2013 calving event.

A closer look at the calving events in Fig. 6.7 demonstrates that a complete separation of the iceberg only occurs when the crack reaches the unconstrained section of the southern lateral boundary, hence open water. This state however cannot be modeled with the given velocity profile and the associated geometry. The boundary conditions of the last setup therefore represent a good approximation of the real situation.

In 2012, more up to date velocity fields of PIG were produced. Unfortunately, most fields contain huge gaps, which cannot be filled by the speckle-tracking algorithm used. Fig. 6.15 a) illustrates the only available velocity field prior to the rift opening in 2011 provided by Dana Floricioiu from DLR Earth Observation Centre. The field is computed using TerraSar-X images of 19.05.2011 and 30.05.2011. Considerable interpolation and smoothing is needed to obtain the filled velocity field in Fig. 6.15 b). In addition, the field is slightly shifted towards the upper left to fit the TerraSar-X image produced five month later (02.10.2011), which is used for the generation of the geometry and the initial cracks. The overall image of the smoothed velocity field seems reasonable. However, a look at the resulting first principal viscous stress in Fig. 6.16 a) reveals localized areas of tensile and compressive stresses in the ice shelf bulk that most likely result from the interpolation and smoothing algorithm.

Figure 6.16 b) illustrates the geometry and the initial cracks used for the fracture

a) $|\mathbf{v}|[\,\mathrm{m/a}]$ b) $|\mathbf{v}|[\,\mathrm{m/a}]$
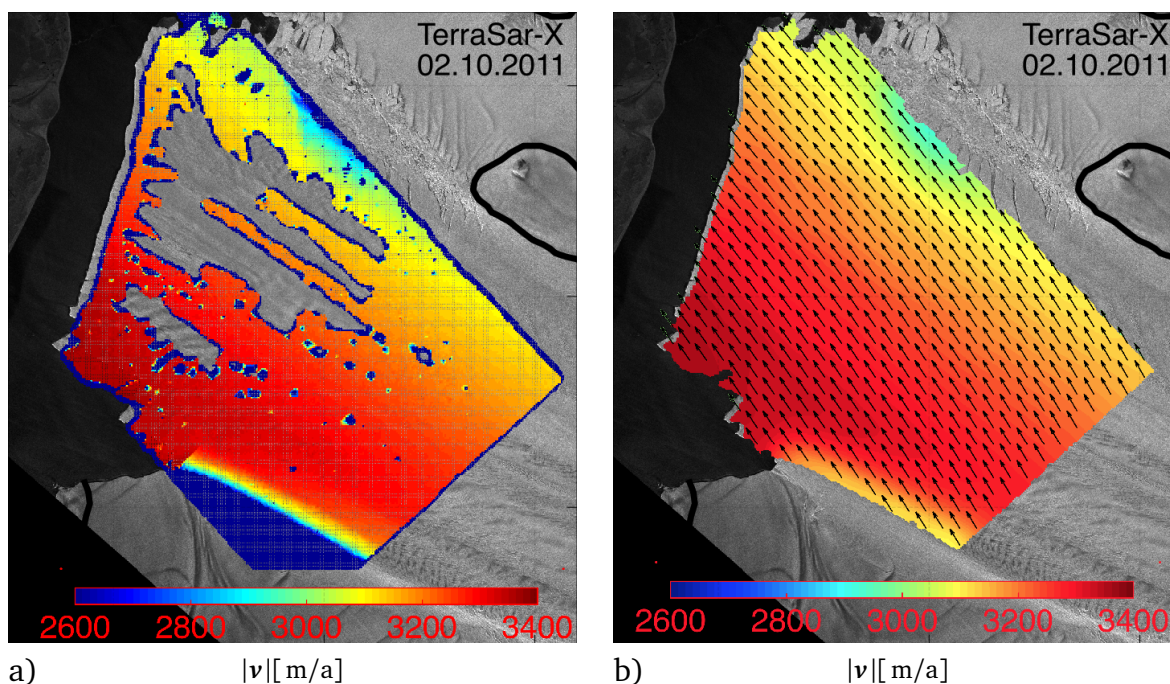
Figure 6.15: a) Plot of original flow speed data in May 2011; b) raster plot of interpolated and smoothed ice shelf speed (color), black arrows indicate the flow direction

a) $\sigma_{\mathrm{v1}}[\,\mathrm{kPa}]$ b) $\sigma_{\mathrm{v1}}[\,\mathrm{kPa}]$

Figure 6.16: a) First principal viscous stress (color) with black arrow indicating the resulting viscous volume forces; b) model geometry with initial cracks superimposed on viscous stress; red and blue lines indicate fixed and free boundaries; the purple arrow marks the initial crack which leads to the 2013 calving event

mechanical simulation. The purple arrow points towards the initial crack that eventually led to the 2013 calving event.

Neither the velocity field, nor the resulting viscous stresses give a strong implication for why the purple crack propaga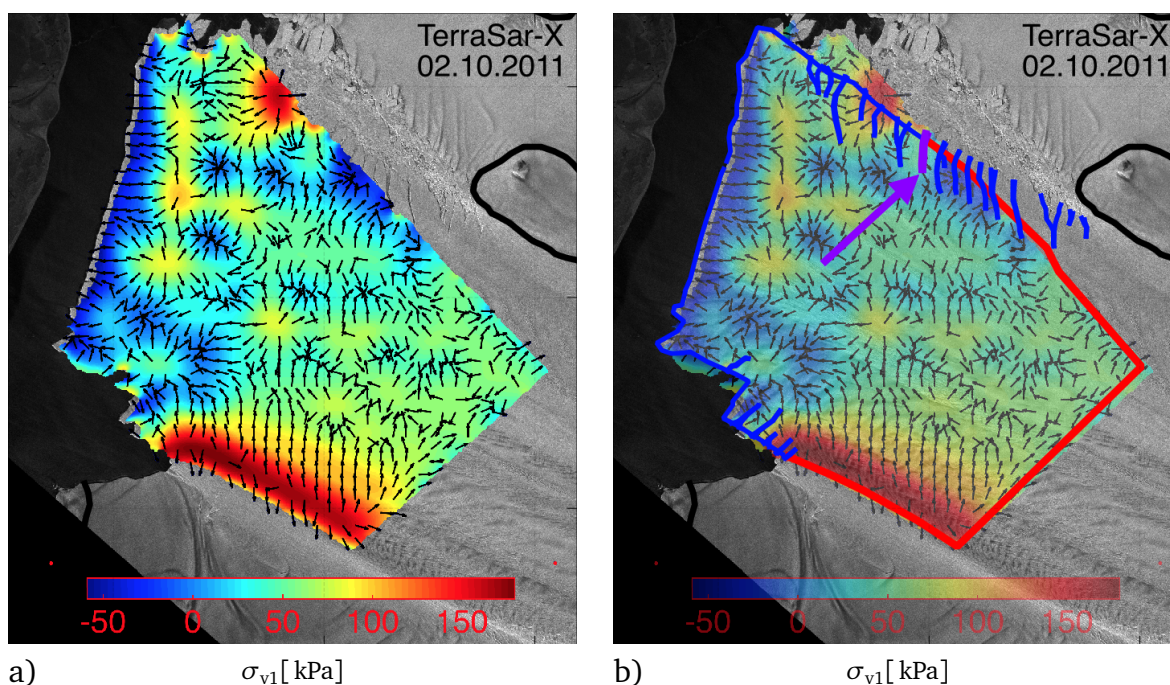tes five month later and not any of the surrounding cracks. Only slightly higher tensile stresses along the crack faces in comparison to the direct neighbors can be observed. Considerably higher tensile stresses however appear further downstream. Several setups with different fixed and free boundary conditions are used for the simulation of the rift propagation. The only setup leading to the propagation of the purple initial crack without any adjustment of the initial crack length is illustrated in Fig. 6.16 b) where the red and the blue lines indicate fixed and free boundaries, respectively. The zone of compressive stresses, upstream of the purple crack, motivates this setup. A comparison of the satellite images from the 02.10.2011 and 13.10.2011, hence right prior and after rift propagation, however shows no implication for a constrained boundary along this rifted area, since movement of the ice masses can be observed. The resulting crack path is shown in Fig. 6.17 a) in comparison to the rift path (purple dashed line) that was observed on 13.10.2011.

Slight adjustment of the length of the black initial crack is sufficient to yield crack propagation at the desired location without the previous strong requirements on the boundary conditions. Figure 6.17 b) illustrates the original initial crack (solid black line), the adjusted crack path (pink tip), as well as the constrained boundaries used
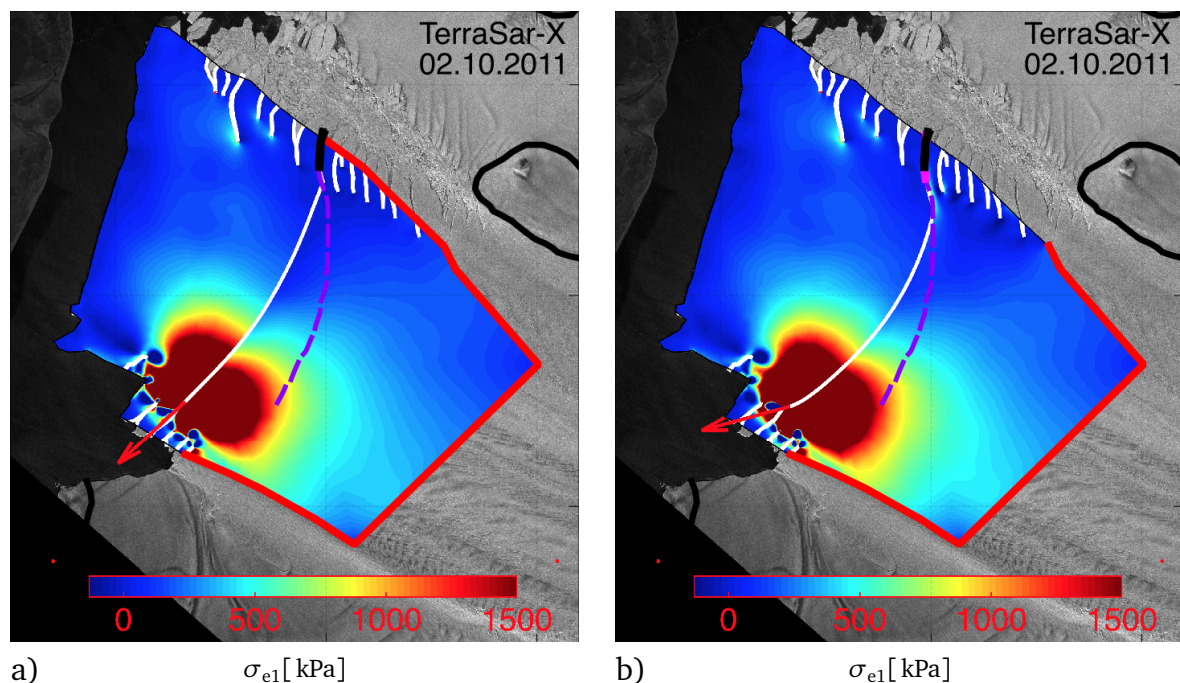

Figure 6.17: Resulting crack path in comparison to observed rift for a) original initial cracks as observed on the TerraSar-X image of 02.10.2011 and constrained boundary upstream of black initial crack; b) slightly elongated initial crack (black with pink tip) and less restrictive boundary conditions

for the new simulation. The therewith obtained crack path shows a slightly better fit to the observed rift illustrated by the dashed purple line.

The presented results leave several potential reasons for the propagation of the purple crack. It is possible that the velocity field considerably changed during the austral summer of 2011. Also a sudden change in the boundary conditions can be responsible for the propagation of the rift. Local changes in the ice thickness that are not captured by the velocity field can also serve as reason for crack propagation at the specific location. Furthermore, different initial crack lengths than observed on the satellite image of 02.10.2011 or frozen ice mélange in the longer crack further downstream can serve as reason for the propagation of the purple crack. A last and rather daring option is that the purple crack propagated earlier, closed again and left a zone of weaker ice, which opened for good in 2011. The latter suggestion is supported by the previous simulation with the 2008 geometry and velocities, where an initial crack next to the purple one propagates for different sets of boundary conditions.

6.3 Rift propagation at Wilkins Ice Shelf

Wilkins Ice Shelf is located at the western side at the Antarctic Peninsula as shown in Fig. 6.18 a). With a surface area of formally $16200\,\mathrm{km}^2$ and average surface veloc-

a)   b)
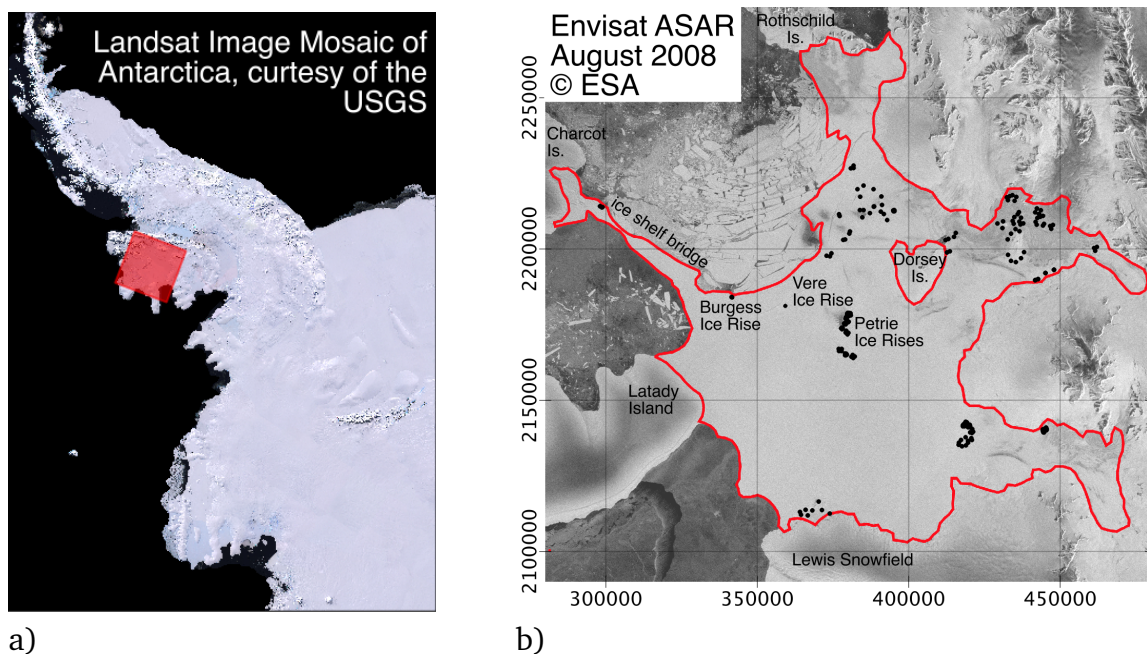
Figure 6.18: a) Landsat Image Mosaic of Western Antarctica; red box indicates location and extend of the following images of WIS; b) Envisat ASAR image of WIS in August 2008 with names of important landmarks, red lines indicate boundary of floating ice shelf part (provided by Melanie Rankl), black dots point out locations of ice rises (provided by Angelika Humbert), coordinates in kilometers

ities of $30-90$ m/a (Vaughan et al., 1993), the WIS is one of the lager and very slow moving ice shelves of the Antarctic Peninsula. The ice shelf gained special attention within the glaciological community due to major break-up events discovered since 1991 (Braun et al., 2009; Cook and Vaughan, 2010) with the collapse of the ice shelf bridge in 2009 (Humbert et al., 2010) as thus far last major break-up. This event reduced the ice shelf area to a total of 11100 km^2. A special feature of the WIS is the large number of small ice rises (173) as indicated in Fig. 6.18 b) that pin the ice shelf. Braun et al. (2009) state that although ice rises are generally regarded as stabilizing elements of ice shelves, they play an important role in the past break-up record of WIS. Braun et al. (2009) observe that after all major break-up events, considerable rift growth occurred, mostly extending from smaller cracks downstream of ice rises. The WIS therefore represents an interesting candidate for the application of the viscous volume forces approach to the fracture mechanical analysis of rift propagation.

Despite the availability of a large number of satellite images of WIS within the last decade, the generation of high-resolution velocity fields covering the whole area of interest prior to the bridge collapse proved to be a difficult task. Especially the sometimes larger time interval between the images available, as well as considerable surface melt during austral summers, hindered the application of interferometric methods for the computation of the surface velocities by remote sensing specialists. In spite of the mentioned difficulties a high-resolution snapshot of the velocities of the whole WIS for autumn 2008 could be provided by Melanie Rankl (Friedrich-Alexander-Universität, Erlangen-Nürnberg).
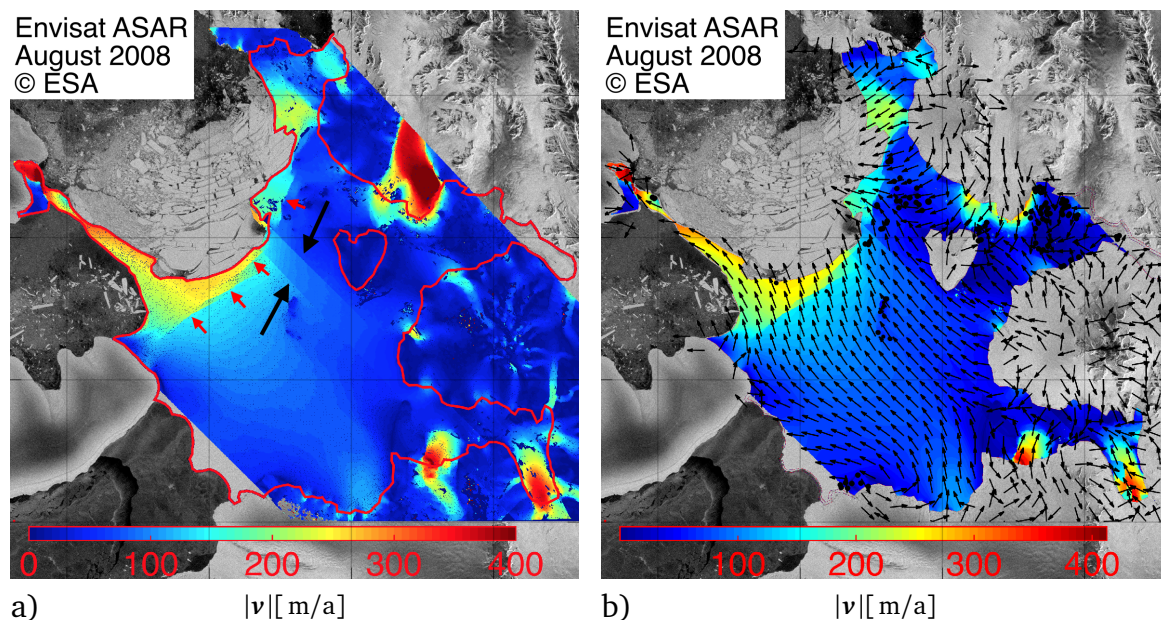

Figure 6.19: a) Raster plot of the assembled original velocity fields; black arrows indicate the suture zone between the individual pictures; red arrows indicate jumps in the velocities due to crack opening; b) assembled, filled and smoothed ice shelf speed (color) with black arrows indicating the flow direction

Figure 6.19 a) illustrates the original velocity data with a spatial resolution of 100 m in x and y direction. Dark points, visible as noise especially in the bridge part of the field, result from NaNs in the original data. Black arrows indicate sharp bands that traverse the image from the upper left to the lower right. These stripes indicate unnatural jumps in the velocity field, which arise due to the assembling of the data using satellite images of two different orbits from different time intervals. The lower left field results from ALOS Palsar pictures taken on 28.09.2008 and 23.11.2008, the upper right field from pictures taken on 22.10.2008 and 07.12.2008. Differences between the velocities of the individual fields at locations within the suture zone are up to 150 m/a. The field in Fig. 6.19 a) uses the mean value of the individual fields within the suture zone. Further high jumps in the velocities appear due to opening cracks close to the calving fronts as indicated by red arrows in Fig. 6.19 a). Even though resulting from natural origin (unlike the discontinuities at the suture zone) also these jumps need special care during the evaluation of the viscous volume forces. The previously applied order of filling and smoothing of the velocities with ensuing computation of the viscous stresses and volume forces would result in smeared jumps in the velocities and hence extended regions of high stresses. However, since the velocity jumps result from crack opening, high stresses across the crack faces are unphysical, whereas high stresses at the crack tips are likely to appear.

Several sequences of NaN filling, smoothing with and without structure preservation, differentiation, and assembling of the individual fields have been tested. The most promising order will be described in the following.

First, unphysical high or low values are removed from the individual velocity fields and filled with NaNs. Then the NaNs are filled applying the MATLAB routine *ndnanfilter* already used for PIG. All not-NaN data is preserved. In a next step, the structure

a) $\sigma_{v1}[\,\mathrm{kPa}]$ b) $|f_v|[\,\mathrm{N/m^3}]$ c) $\sigma_{v1}[\,\mathrm{kPa}]$
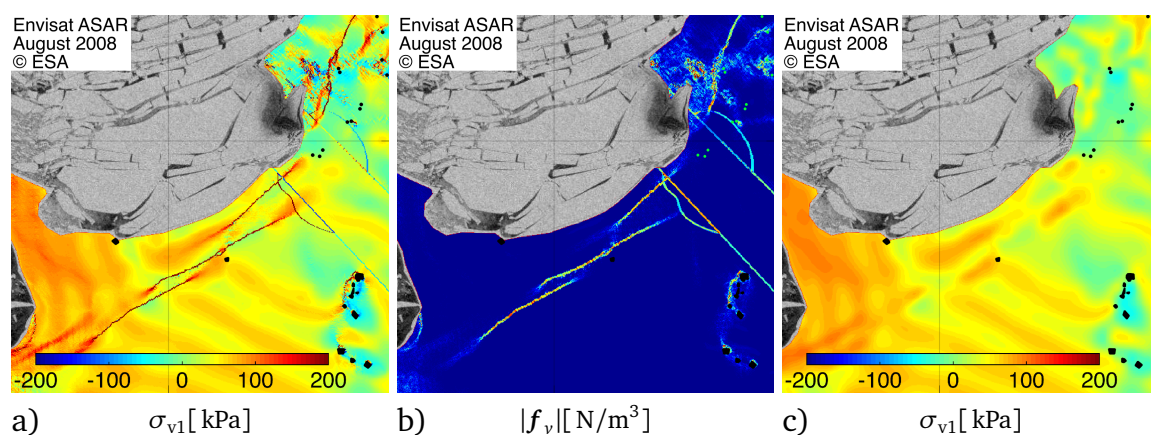
Figure 6.20: Enlarged view of box marked in Fig. 6.21 a) with a) first principal viscous surface stress with exaggerated stresses across crack faced and suture zones; b) absolute value of viscous volume force resulting from non-smoothed viscous stresses; c) smoothed first principal viscous surface stress after elimination and filling of unphysical values; ice rises are indicated in black

preserving bilateral MATLAB filter *bfilter2* implemented by Douglas Lanman and inspired by the work of Tomasi and Manduchi (1998) is used to smooth the velocities in the ice shelf bulk, preserving the sharp jumps across the crack flanks. Only then, the two individual fields are assembled. As for the original velocities in Fig. 6.19 a), the mean values of both fields are used in the suture zone. Figure 6.19 b) illustrates the smoothed ice shelf speed with black arrows indicating the flow direction. The assembled velocity field is then used to compute the viscous surface stresses.

As to be expected, the jumps in the velocity field across the crack faces and the suture zone result in sharp lines of high stresses as shown in the enlarged view of the area between the Petrie ice rises and the ice shelf bridge in Fig. 6.20 a). Further differentiation yields the resulting viscous volume forces whose absolute value $|\boldsymbol{f}_v|$, as illustrated in Fig. 6.20 b), is an even better indicator for locations of unphysical stresses. In combination with the associated satellite picture, $|\boldsymbol{f}_v|$ can be used to find active rifts that are likely to propagate further.

In order to remove unphysical stresses, NaNs are included into all stress components at those locations where $|\boldsymbol{f}_v|$ exceeds a certain threshold. In a further step the NaNs are filled and the field is slightly smoothed by another application of *ndnanfilter*. The resulting first principal viscous surface stress is shown in Fig. 6.20 c). The components of the viscous stress tensor are then used to compute the viscous volume forces, which are applied to the fracture mechanical simulation.

Figure 6.21 a) illustrates the first principal viscous surface stress in the complete ice shelf, as well as the direction of the viscous volume forces indicated by black arrows

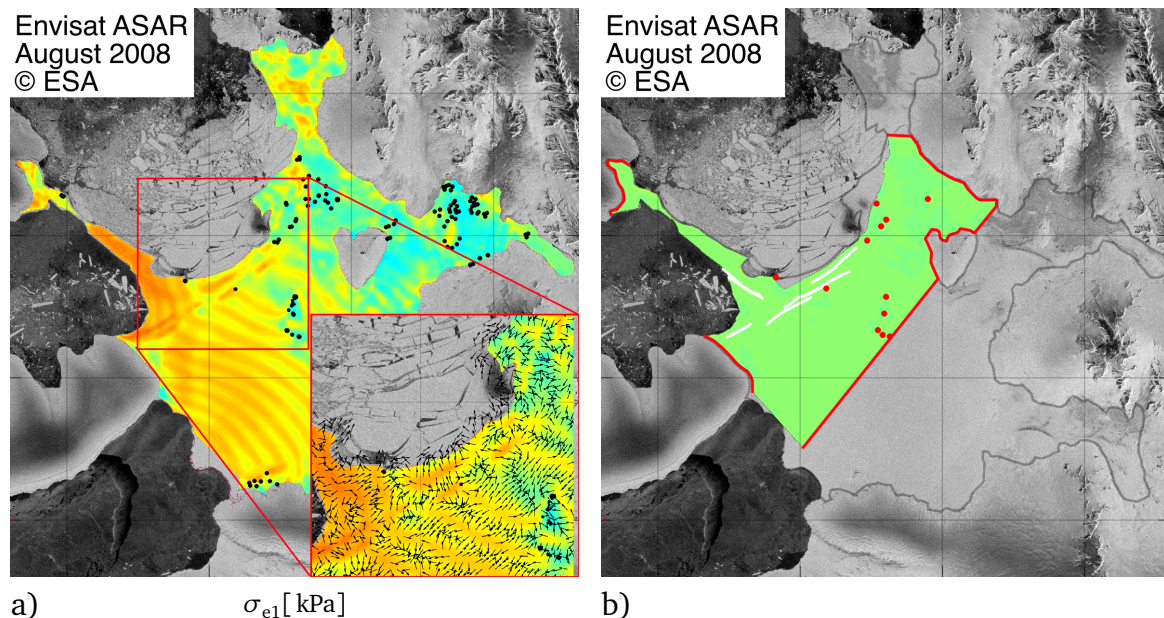a)　　　　　　　$\sigma_{e1}[\,\mathrm{kPa}\,]$　　　　b)

Figure 6.21: a) First principal viscous surfaces stress with normalized viscous volume forces in enlarged view; b) geometry for fracture mechanical simulation with initial cracks in white and ice rises, as well as constrained boundaries in red

in the enlarged view. Striking features are the long stripes, predominantly appearing between Latady Island, Lewis Snowfield and the Petrie Ice Rises but also in different orientation along the bridge. Similar features have not been observed at other ice shelves. Since the stripes already appear in the original data, it can be assumed that they result from the image capturing process itself or from the successive processing to obtain the velocity data. As the undulations across the stripes are within the same order of magnitude as the variation of the stresses from natural origin, an influence on the resulting crack path in the fracture mechanical simulation must be assumed. Unfortunately, remote sensing specialists have not found ways to remove or reduce the stripes up to now.

Larger rifts in the WIS are predominantly found in the upper left of a line, crossing the ice shelf from Latady Island to Dorsey Island. In order to reduce the computation time, therefore only the upper left part of the ice shelf, as illustrated in Fig. 6.21 b), is used for the fracture mechanical simulation. Red lines indicate the grounding line and the section through the ice shelf where the displacements are fixed. In a first simulation also the displacements along the boundaries of the ice rises are

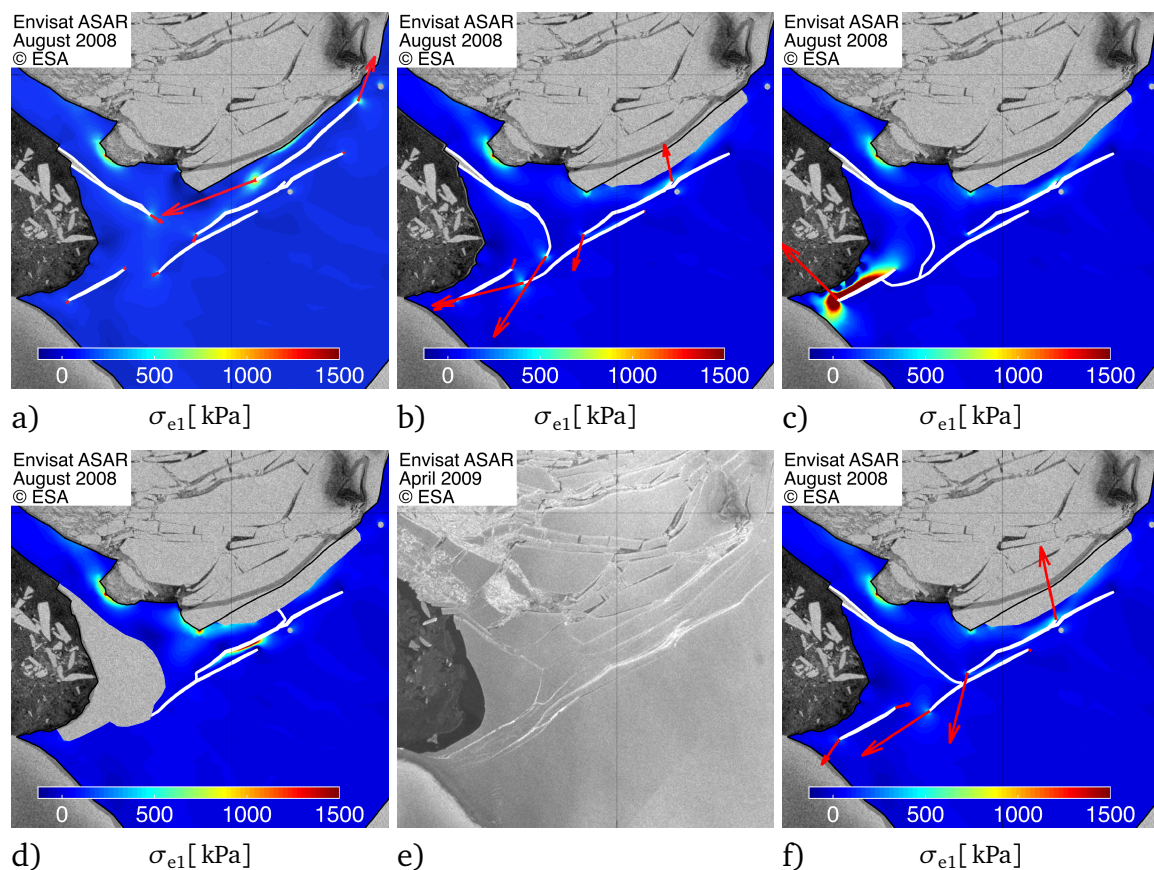Figure 6.22: Resulting crack path and configurational crack tip forces at the WIS using constrained boundaries at the ice rises a) for the initial configuration; b) after 60 iterations; c) after 80 iterations; d) after 102 iterations; e) observed cracks during collapse of the bridge in April 2009; f) crack path and configurational crack tip force after 50 iterations with unconstrained boundaries at the ice rises

constrained. All remaining boundaries, as well as the flanks of the initial cracks as indicated by white lines, are free. The lengths and the locations of the initial cracks results from the plot of $|f_\nu|$ in combination with an ALOS Palsar image of 28.09.2008.

Figure 6.22 a) illustrates the configurational crack tip forces after the first computation step. As in the previous example only the crack tip with the highest value of J is allowed to grow. After several growth steps, first one, then the other of the most critical crack tips in Fig. 6.22 a) reaches the front and the first block calves off. Figure 6.22 b) illustrates the situation after 60 iterations. At this stage, the rift emerging from the bridge, as well as the rift farthest away from the calving front grow by turns and eventually merge into the rift to the left as shown in Fig. 6.22 c). The left tip of the left rift then propagates towards the calving front and one further block detaches from the ice shelf. Figure 6.22 d) demonstrates the situation after 102 steps. The two remaining rifts merge and the right one penetrates the ice front, detaching the bridge from the ice shelf.

The resulting crack patterns are in good agreement with the real crack paths, which can be seen on a satellite image of August 2009 after the collapse of the bridge as illustrated in Fig. 6.22 e). Especially the turning of the rift emerging from the bridge towards the lower left of the picture is very well captured. Even better results can be expected by application of more physical boundary conditions along the grounding line along Latady Island. Here, the completely fixed boundary imposes a very restrictive constraint and deflects the crack propagation towards the ice front.

One further simulation is performed with free displacements along the boundaries of the ice rises. The resulting crack path after 50 iterations is illustrated in Fig. 6.22 f). Unlike in the previous simulation, the crack emerging from the bridge does not turn towards the lower left but directly propagates inwards the ice shelf. This is not in agreement with the observed crack paths and therefore once more emphasizes the influence of the applied boundary conditions.

6.4 Summary and outlook for the simulation of horizontal rift propagation

Viscous volume forces as means to transfer the viscous surfaces stresses in the ice shelf into a forcing for the fracture mechanical simulation prove to be a very comfortable approach with promising results in comparison to actual fracture patterns. The most important feature of the approach is that no information on the spatial distribution of the material parameters or the ice shelf thickness are needed. Furthermore, if the resolution of the measured velocity data is sufficient, information on the location and length of active rifts results as by-product of the evaluation of the viscous volume forces.

The applicability of the method is limited by the quality and resolution of the velocity fields, as well as by the knowledge and applicability of the appropriate

boundary conditions. Furthermore, the method is thus far only able to simulate likely crack paths but does not tell if and under which conditions a crack will propagate. In order to gain this information, simulations of a three-dimensional cracked specimen with the associated boundary conditions are needed. Also a thorough comparison of satellite data to aerial photography or field observations of cracks will help to distinguish between those cracks visible in satellite pictures that are actual rifts and those that are only surface cracks.

The simulations of rifts in the WIS motivate to also consider criteria for crack initiation. High tensile stresses in the bulge of the bridge hint towards the evolution of new cracks in this area, which also appear on satellite pictures prior to the complete collapse of the bridge.

Criteria for crack initiation are also needed for a viscoelastic simulation of rift propagation, which can be a future project for the analysis of the regular calving events at PIG. Due to the fast flow speed it is likely that the velocities in the last third of the glacier, close to the calving front, continuously change as the lateral boundaries become less constrained. A combination of viscous flow simulation and fracture mechanical analysis might be able to capture the ongoing small rifting at the transition of clamped to free boundary and possibly can be capable to indicate after which distance or time an initial rift may lead to a major calving event.

7 Conclusion and outlook

The aim of this work was the analysis of different fracture scenarios in Antarctic ice shelves using the concept of configurational forces in conjunction with FE simulations.

The evaluation of configurational forces is based on field variables that are computed in the course of the FE simulation of a boundary value problem. Algorithms for the computation of configurational forces can therefore be included into standard FE procedures as a post-processing step, without much additional effort. In the presented work, the linear elastic boundary value problem was solved using the commercial FE program COMSOL. The evaluation of the configurational forces followed in post-processing routines in MATLAB.

Since volume forces, pressurized crack faces, spatially distributed material parameters, as well as mixed mode loading situations characterize the various fracture situations in Antarctic ice shelves, the main focus of this work was the implementation of a configurational force approach that enables a precise computation of $\mathscr{G}$ without the limitations of path dependence. The developed two-dimensional algorithm therefore computes resulting configurational crack tip forces using additional area integrals to eliminate the error invoked by volume forces and spatially distributed material parameters, as well as additional line integrals along the crack faces to exclude inaccuracies due to pressurized crack faces and mixed mode loading. The computed resulting configurational crack tip forces showed less than 0.1% error in comparison to analytical and semi-analytical results, as well as literature values. Also the implemented algorithm for crack path prediction based on the resulting configurational forces proved a very good agreement to standard benchmark tests as e.g. by Bittencourt et al. (1996) or Bouchard et al. (2003).

The algorithm was applied for the study of vertical dry cracks emerging from the ice shelf surface using an idealized two-dimensional ice shelf domain with a centered single crack. Different values of geometric and material parameters, as well as several types of boundary conditions were analyzed. The most important geometric parameter was the crack opening angle α. With the same external loading, an opening of $\alpha = 5°$ led to 400% deeper cracks in comparison to the ideally sharp crack setup. The influence of α has been completely ignored in previous studies.
The influence of stress versus displacement boundary conditions along the lateral boundaries representing the remaining ice shelf bulk was small and only relevant for deep reaching cracks. Significant differences due to stress boundary conditions

versus Robin-type boundary conditions to represent buoyancy forces along the bottom boundary were only observed for large opening angles α.

As shown in previous studies by e.g. Rist et al. (2002), the application of a depth-dependent density profile considerably increased the resulting crack depth in comparison to the application of a constant mean density. Even more pronounced was the influence of Poisson's ratio, resulting in considerably deeper cracks for the compressible case with $\nu = 0.3$ than for the application of incompressible material behavior with $\nu = 0.5$. This is all the more important as many publications treat ice as incompressible, also for fracture mechanical analyses even though compressible behavior for ice on the short time scale has been repeatedly reported (Schulson and Duval, 2009).

The study of the criticality of vertical cracks was extended towards water-filled cracks emerging from the top, as well as from the bottom of the ice shelf. As shown in previous studies, e.g. Van Der Veen (1998a,b) the additional water pressure on the crack faces considerably increased the resulting crack depth and could result in the complete penetration of an initially stable crack. As in the previous studies of dry cracks, the choice of Poisson's ratio strongly influenced the outcome of the simulations.

The study of vertical cracks was completed by a simulation of possible frost wedging processes within a water-filled crevasse. A coupled simulation of fluid flow and heat transfer with phase shift yielded possible ice lid thicknesses on the water depending on the external temperature applied. The resulting ice lid thicknesses were used for the fracture mechanical analysis with additional phase transition pressure along the crack - water interface. It was shown, that reasonable ice lid thicknesses could result in the complete penetration of an initially stable water-filled crevasse, depending on the opening angle α.

The crack path prediction algorithm based on configurational forces was applied for the propagation of horizontal rifts in ice shelves. A new approach of transferring the viscous surface stresses resulting from measurements of the ice shelf speed into an adequate loading for the fracture mechanical analysis via viscous volume forces was introduced. The resulting crack paths agreed well with observed crack paths from satellite imagery. This is remarkable, as no information on the spatial distribution of the ice properties was needed. However, the approach strongly depends on the quality and resolution of the applied measured velocity fields, as well as on the knowledge of adequate boundary conditions for the fracture mechanical analysis.

In summary, the configurational force approach along with FE simulations proved to be a very robust and flexible tool for the evaluation of crack criticality and crack propagation directions in various fracture scenarios of Antarctic ice shelves. However, the computational effort especially due to the generation of a new mesh with every crack growth step is a drawback of this method. In the presented quasi static simulations where each configuration was independent of the previous step, repeated remeshing functioned well. Nevertheless, the existence of more elegant

mesh adaption techniques also in collaboration with configurational forces (Miehe and Gürses, 2007) should be mentioned.

Future analyses of vertical crack growth and large scale calving events might use time-dependent viscoelastic material laws with large deformations for which more advanced remeshing strategies have to be applied. Especially projection algorithms for history variables on the newly inserted mesh nodes will be needed. Also the coupling of fracture mechanics to the ice dynamical simulations is desired. A possible framework to cover large deformations due to ice shelf flow, a changing topology and fractures could be the particle finite element method as described in Oñate et al. (2004). Also the switch to a continuous formulation of cracks as e.g. the application of a phase field model for fracture, presented in Bourdin et al. (2000), can be considered.

For a better differentiation between surface crevasses and rifts, a three-dimensional analysis of fractures in ice shelves will be needed. This will also help to find a valid critical stress intensity factor for the two-dimensional horizontal analysis of rift propagation.

Further field measurements of crevasse depth and elastic material parameters, as e.g. an averaged Young's modulus over a larger ice shelf region, as well as Poisson's ratio under steady state loading, could help to solidify the parameter basis for the fracture mechanical simulations.

Bibliography

T. Albrecht and A. Levermann. Fracture field for large-scale ice dynamics. *Journal of Glaciology*, 58(207):165–176, 2012.

H. Altenbach. *Kontinuumsmechanik: Einführung in die materialunabhängigen und materialabhängigen Gleichungen*. Springer, 2012.

H. D. Baehr and K. Stephan. *Wärme- und Stoffübertragung*. Springer, 2008.

J. L. Bamber, J. L. Gomez-Dans, and J. A. Griggs. A new 1 km digital elevation model of the Antarctic derived from combined satellite radar and laser data–Part 1: Data and methods. *The Cryosphere*, 3(1):101–111, 2009.

J. L. Bamber, R. E. M. Riva, B. L. A. Vermeersen, and A. M. LeBrocq. Reassessment of the Potential Sea-Level Rise from a Collapse of the West Antarctic Ice Sheet. *Science*, 324(5929):901–903, 2009.

A. F. Banwell, M. Caballero, N. S. Arnold, N. F. Glasser, L. M. Cathles, and D. R. MacAyeal. Supraglacial lakes on the Larsen B ice shelf, Antarctica, and at Paakitsoq, West Greenland: a comparative study. *Annals of Glaciology*, 55(66):1–8, 2014.

J. N. Bassis. Episodic propagation of a rift on the Amery Ice Shelf, East Antarctica. *Geophysical Research Letters*, 32(6):1–5, 2005.

J. N. Bassis, H. A. Fricker, R. Coleman, and Y. Bock. Seismicity and deformation associated with ice-shelf rift propagation. *Journal of Glaciology*, 53(183):523–536, 2007.

J. N. Bassis, H. A. Fricker, R. Coleman, and J. Minster. An investigation into the forces that drive ice-shelf rift propagation on the Amery Ice Shelf, East Antarctica. *Journal of Glaciology*, 54(184):17–27, 2008.

W. Becker and D. Gross. *Mechanik elastischer Körper und Strukturen*. Springer, 2002.

D. Bergez. Determination of stress intensity factors by use of path-independent integrals. *Mechanics Research Communications*, 1(3):179–180, 1974.

R. A. Bindschadler and E. Rignot. "Crack!" in the Polar Night. *Eos, Transactions American Geophysical Union*, 82(43):497–505, 2001.

Bibliography

T. N. Bittencourt, P. A. Wawrzynek, A. R. Ingraffea, and J. L. Sousa. Quasi-automatic simulation of crack propagation for 2D LEFM problems. *Engineering Fracture Mechanics*, 55(2):321–334, 1996.

P. O. Bouchard, F. Bay, and Y. Chastel. Numerical modelling of crack propagation: automatic remeshing and comparison of different criteria. *Computer Methods in Applied Mechanics and Engineering*, 192(35-36):3887–3908, 2003.

A. C. Boucíguez, R. F. Lozano, and M. A. Lara. About the exact solution in two phase-stefan problem. *Engenharia Térmica*, 6(2):70–75, 2007.

B. Bourdin, G. A. Francfort, and J. J. Marigo. Numerical experiments in revisited brittle fracture. *Journal of the Mechanics and Physics of Solids*, 48(4):797–826, 2000.

M. Braun, A. Humbert, and A. Moll. Changes of Wilkins Ice Shelf over the past 15 years and inferences on its stability. *The Cryosphere*, 3:41–56, 2009.

H. F. Bueckner. A novel principle for the computation of stress intensity factors. *Zeitschrift für Angewandte Mathematik und Mechanik*, 50(9):529–546, 1970.

G. P. Cherepanov. Crack propagation in continuous media. *Journal of Applied Mathematics and Mechanics (Engl. transl. of PMM 31 476-488)*, 31(3):503–512, 1967.

J. Christmann, R. Müller, and K. G. Webber. Measurement of the fracture toughness of polycrystalline bubbly ice from an Antarctic ice core. *Earth System Science Data*, 7(1):87–92, 2015.

J. W. Clough. RISP radio-echo soundings. *Antarctic Journal of the United States*, 9 (4):159–159, 1974.

A. J. Cook and D. G. Vaughan. Overview of areal changes of the ice shelves on the Antarctic Peninsula over the past 50 years. *The Cryosphere*, 4:77–98, 2010.

B. Cotterell. On brittle fracture paths. *International Journal of Fracture*, 1(2):96–103, 1965.

K. M. Cuffey and W. S. B. Paterson. *The physics of glaciers*. Academic Press, 2010.

H. De Angelis. Glacier Surge After Ice Shelf Collapse. *Science*, 299(5612):1560–1562, 2003.

R. Denzer, F. J. Barth, and P. Steinmann. Studies in elastic fracture mechanics based on the material force method. *International Journal for Numerical methods in Engineering*, 58(12):1817–1835, 2003.

C. S. M. Doake. Ice-shelf densities from a comparison of radio echo and seismic soundings. *Annals of Glaciology*, 5:47–50, 1984.

F. Erdogan. Fracture Mechanics of Functionally Graded Materials. *Composites Engineering*, 5(7):753–770, 1995.

F. Erdogan and G. C. Sih. On the Crack Extension in Plates Under Plane Loading and Transverse Shear. *Journal of Basic Engineering*, 85(4):519–525, 1963.

F. Erdogan and B. H. Wu. The surface crack problem for a plate with functionally graded properties. *Journal of Applied Mechanics*, 64(3):449–456, 1997.

J. D. Eshelby. The force on an elastic singularity. *Philosophical Transactions of the Royal Society of London. Series A, Mathematical and Physical Sciences*, 244(877): 87–112, 1951.

T. Fett, D. Munz, and J. Neumann. Local stress intensity factors for surface cracks in plates under power-shaped stress distributions. *Engineering Fracture Mechanics*, 36(4):647–651, 1990.

P. Fretwell, H. D. Pritchard, D. G. Vaughan, J. L. Bamber, N. E. Barrand, R. Bell, C. Bianchi, R. G. Bingham, D. Blankenship, G. Casassa, G. A. Catania, D. Callens, H. Conway, A. J. Cook, H. F. J. Corr, D. Damaske, V. Damm, F. Ferraccioli, R. Forsberg, S. Fujita, Y. Gim, P. Gogineni, J. A. Griggs, R. C. A. Hindmarsh, P. Holmlund, J. W. Holt, R. W. Jacobel, A. Jenkins, W. Jokat, T. A. Jordan, E. C. King, J. Kohler, W. Krabill, M. Riger-Kusk, K. A. Langley, G. Leitchenkov, C. Leuschen, B. P. Luyendyk, K. Matsuoka, J. Mouginot, F. O. Nitsche, Y. Nogi, O. A. Nost, S. V. Popov, E. Rignot, D. M. Rippin, A. Rivera, J. Roberts, N. Ross, M. J. Siegert, A. M. Smith, D. Steinhage, M. Studinger, B. Sun, B. K. Tinto, B. C. Welch, D. Wilson, D. A. Young, C. Xiangbin, and A. Zirizzotti. Bedmap2: improved ice bed, surface and thickness datasets for Antarctica. *The Cryosphere*, 7(1):375–393, 2013.

H. A. Fricker. Multi-year monitoring of rift propagation on the Amery Ice Shelf, East Antarctica. *Geophysical Research Letters*, 32(2):1–5, 2005.

N. F. Glasser and T. A. Scambos. A structural glaciological analysis of the 2002 Larsen B ice-shelf collapse. *Journal of Glaciology*, 54(184):3–16, 2008.

J. W. Glen. The flow law of ice. *International Association of Hydrological Sciences Publications*, 47:171–183, 1958.

P. A. Gradin. A note on the J-Integral for thermal stress crack problems. *International Journal of Fracture*, 27(2):59–60, 1985.

R. Greve and H. Blatter. *Dynamics of Ice Sheets and Glaciers*. Springer, 2009.

A. A. Griffith. The Phenomena of Rupture and Flow in Solids. *Philosophical Transaction of the Royal Society A*, 221:163–198, 1920.

D. Gross and T. Seelig. *Fracture Mechanics, with an Introduction to Micromechanics*. Springer, 2002.

Bibliography

D. Gross, S. Kolling, R. Müller, and I. Schmidt. Configurational forces an their application in solid mechanics. *European Journal of Mechanics*, 22:669–692, 2003.

M. E. Gurtin and P. Podio-Guidugli. Configurational forces and the basic laws for crack propagation. *Journal of the Mechanics and Physics of Solids*, 44(6):905–927, 1996.

M. E. Gurtin and P. Podio-Guidugli. Configurational forces and a constitutive theory for crack propagation that allows for kinking and curving. *Journal of the Mechanics and Physics of Solids*, 46(8):1343–1378, 1998.

M. E. Gurtin and M. M. Shvartsman. Configurational forces and the dynamics of planar cracks in three-dimensional bodies. *Journal of Elasticity*, 48(2):167–191, 1997.

T. Haran, J. Bohlander, T. A. Scambos, T. Painter, and M. A. Fahnestock. MODIS Mosaic of Antarctica 2003-2004 (MOA2004), 2005.

M. M. Herron and C. C. Langway. Firn densification: an empirical model. *Journal of Glaciology*, 25(93):373–385, 1980.

G. A. Holzapfel. *Nonlinear solid mechanics: A continuum approach for engineering*. John Wiley & Sons, 2000.

I. M. Howat, K. C. Jezek, M. Studinger, J. A. MacGregor, J. Paden, D. FlorIcioiu, R. Russel, M. Linkswiler, and R. Dominguez. Rift in Antarctic Glacier: A Unique Chance to Study Ice Shelf Retreat. *Eos, Transactions American Geophysical Union*, 93(8):77–88, 2012.

T. J. R. Hughes. *The finite element method.* linear static and dynamic finite element analysis. Dover Publications, Inc., 2000.

C. L. Hulbe, C. LeDOUX, and K. Cruikshank. Propagation of long fractures in the Ronne Ice Shelf, Antarctica, investigated using a numerical model of fracture propagation. *Journal of Glaciology*, 56(197):459–472, 2010.

A. Humbert, T. Kleiner, C. Mohrholz, C. Oelke, R. Greve, and M. Lange. A comparative modeling study of the Brunt Ice Shelf/Stancomb-Wills Ice Tongue system, East Antarctica. *Journal of Glaciology*, 55(189):53–65, 2009.

A. Humbert, D. Gross, R. Müller, M. Braun, R. S. W. van de Wal, M. R. van den Broeke, D. G. Vaughan, and W. J. van de Berg. Deformation and failure of the ice bridge on the Wilkins Ice Shelf, Antarctica. *Annals of Glaciology*, 51(55):49–55, 2010.

M. A. Hussain, S. L. PU, and J. H. Underwood. Strain Energy Release Rate for a Crack under Combined Mode I and II. *ASTM STP*, 560:2–28, 1974.

M. Ichikawa and S. Tanaka. A critical analysis of the relationship between the energy release rate and the stress intensity factors for non-coplanar crack extension under combined mode loading. *International Journal of Fracture*, 18(1):19–28, 1982.

G. R. Irwin. Analysis of Stresses and Strains Near the End of a Crack Traversing a Plate. *Journal of Applied Mechanics*, 24:361–364, 1957.

D. Jansen, B. Kulessa, P. R. Sammonds, A. J. Luckman, E. KING, and N. F. Glasser. Present stability of the Larsen C ice shelf, Antarctic Peninsula. *Journal of Glaciology*, 56(198):593–600, 2010.

K. C. Jezek. A Modified Theory of Bottom Crevasses Used as a Means for Measuring the Buttressing Effect of Ice Shelves on Inland Ice Sheets. *Journal of Geophysical Research*, 89(B3):1925–1931, 1984.

K. C. Jezek, C. R. Bentley, and J. W. Clough. Electromagnetic sounding of bottom crevasses on the Ross Ice Shelf, Antarctica. *Journal of Glaciology*, 24:321–330, 1979.

I. Joughin and R. B. Alley. Stability of the West Antarctic ice sheet in a warming world. *Nature Publishing Group*, 4(8):506–513, 2011.

I. Joughin, B. E. Smith, and D. M. Holland. Sensitivity of 21st century sea level to ocean-induced thinning of Pine Island Glacier, Antarctica. *Geophysical Research Letters*, 37(20):1–5, 2010.

M. Khalaquzzaman, B. X. Xu, and R. Müller. Computational Homogenization of Piezoelectric Materials using FE2 to determine Configurational Forces. *Technische Mechanik*, 32(1):21–37, 2012.

A. Khazendar, E. Rignot, and E. Larour. Roles of marine ice, rheology, and fracture in the flow and stability of the Brunt/Stancomb-Wills Ice Shelf. *Journal of Geophysical Research*, 114(F4):1–9, 2009.

R. Kienzler and G. Herrmann. *Mechanics in Material Space: with Applications in Defect and Fracture Mechanics (Engineering Online Library)*. Springer, 2000.

R. Kienzler, L. Rohde, R. Schröder, and K. Kutz. Treating mixed-mode problems with path-independent integrals. *Engineering Fracture Mechanics*, 77(18):3604–3610, 2010.

J.-H. Kim and G. H. Paulino. Finite element evaluation of mixed mode stress intensity factors in functionally graded materials. *International Journal for Numerical methods in Engineering*, 53(8):1903–1935, 2002.

J. K. Knowles and E. Sternberg. On a Class of Conservation Laws in Linearized and Finite Elastostatics. *Archive for Rational Mechanics and Analysis*, 44(3):187–211, 1972.

Bibliography

D. Koehn and T. Sachau. Two-dimensional numerical modeling of fracturing and shear band development in glacier fronts. *Journal of Structural Geology*, 61:133–142, 2012.

S. Kolling and R. Müller. On configurational forces in short-time dynamics and their computation with an explicit solver. *Computational Mechanics*, 35(5):392–399, 2004.

G. V. Kolosov. Über eine Anwendung der Funktionentheorie mit komplexen Veränderlichen auf ebene Probleme der mathematischen Elastizitätstheorie (in Russisch). *Druckerei K. Mattisina*, 1909.

C. Kuhn. *Numerical and Analytical Investigation of a Phase Field Model for Fracture*. PhD thesis, Techn. Univ., Lehrstuhl für Techn. Mechanik, 2013.

C. Kuhn, R. Lohkamp, F. Schneider, J. C. Aurich, and R. Müller. Finite element computation of discrete configurational forces in crystal plasticity . *International Journal of Solids and Structures*, 56-57:62–77, 2015.

M. Kuna. *Numerische Beanspruchungsanalyse von Rissen*. Vieweg + Teubner, 2008.

E. Larour, E. Rignot, and D. Aubry. Processes involved in the propagation of rifts near Hemmen ice rise, Ronne ice shelf, Antarctica. *Journal of Glaciology*, 50(170): 329–341, 2004.

E. Larour, E. Rignot, and D. Aubry. Modelling of rift propagation on Ronne Ice Shelf, Antarctica, and sensitivity to climate change. *Geophysical Research Letters*, 31(16): 1–4, 2004.

A. M. Le Brocq, A. J. Payne, and A. Vieli. An improved Antarctic dataset for high resolution numerical ice sheet models (ALBMAP v1). *Earth System Science Data*, 2(2):247–260, 2010.

K. K. Lo. Analysis of Branched Cracks. *Journal of Applied Mechanics*, 45(4):797–802, 1978.

A. J. Luckman, D. Jansen, B. Kulessa, E. C. King, P. R. Sammonds, and D. I. Benn. Basal crevasses in Larsen C Ice Shelf and implications for their global abundance. *The Cryosphere*, 6(1):2035–2060, 2012.

D. R. MacAyeal, T. A. Scambos, and C. L. Hulbe. Catastrophic ice-shelf break-up by an ice-shelf-fragment-capsize mechanism. *Journal of Glaciology*, 49(164):22–36, 2003.

D. R. MacAyeal, A. Emile, and C. Richard. Seismic observations of glaciogenic ocean waves (micro-tsunamis) on icebergs and ice shelves. *Journal of Glaciology*, 55 (190):193–206, 2009.

J. A. MacGregor and G. A. Catania. Widespread rifting and retreat of ice-shelf margins in the eastern Amundsen Sea Embayment between 1972 and 2011. *Journal of Glaciology*, 58(209):458–466, 2012.

R. Mahnken. Material forces for crack analysis of functionally graded materials in adaptively refined FE-meshes. *International Journal of Fracture*, 147(1-4):269–283, 2008.

G. A. Maugin. *Material Inhomogeneities in Elasticity*, volume 3. CRC Press, 1993.

G. A. Maugin. *Configurational Forces: Thermomechanics, Physics, Mathematics, and Numerics (Modern Mechanics and Mathematics)*. Chapman and Hall/CRC, 2010.

M. Mellor. A review of basic snow mechanics. In *International Association of Hydrological Sciences Publication*, pages 251–291, 1975.

M. Mellor. Engineering properties of Snow. *Journal of Glaciology*, 19(19):15–66, 1977.

C. Miehe and E. Gürses. A robust algorithm for configurational-force-driven brittle crack propagation with R-adaptive mesh alignment. *International Journal for Numerical methods in Engineering*, 72(2):127–155, 2007.

C. Miehe, E. Gürses, and M. Birkle. A computational framework of configurational-force-driven brittle fracture based on incremental energy minimization. *International Journal of Fracture*, 145(4):245–259, 2007.

E. M. Morris and D. G. Vaughan. Spatial and temporal variation of surface temperature on the antarctic peninsula and the limit of viability of ice shelves. In *Antarctic Peninsula Climate Variability: Historical and Paleoenvironmental Perspectives*, pages 61–68. American Geophysical Union, 2003.

R. Müller. *Configurational Forces in Defect Mechanics and in Computational Methods*. Inst. für Mechanik, TU Darmstadt, 2006.

R. Müller and G. A. Maugin. On material forces and finite element discretizations. *Computational Mechanics*, 29(1):52–60, 2002.

R. Müller, S. Kolling, and D. Gross. On configurational forces in the context of the Finite Element Method. *International Journal for Numerical methods in Engineering*, 53(7):1557–1574, 2002.

R. Müller, D. Gross, and G. A. Maugin. Use of material forces in adaptive finite element methods. *Computational Mechanics*, 33:421–434, 2004.

N. I. Muskhelishvili. *Some basic problems of the mathematical theory of elasticity* . Noordhoff International Publishers, 1975.

Bibliography

B. Näser, M. Kaliske, H. Dal, and C. Netzker. Fracture mechanical behaviour of visco-elastic materials: application to the so-called dwell-effect. *Zeitschrift für Angewandte Mathematik und Mechanik*, 89(8):677–686, 2009.

P. Nath and D. G. Vaughan. Subsurface crevasse formation in glaciers and ice sheets. *Journal of Geophysical Research*, 108(B1):2020–2031, 2003.

H. Neuburg, E. Thiel, and P. T. Walker. The Filchner ice shelf. *Annals of the Association of American Geographers*, 49(2):110–119, 1959.

R. J. Nuismer. An energy release rate criterion for mixed mode fracture. *International Journal of Fracture*, 11(2):245–250, 1975.

J. F. Nye. Comments on Dr. Loewe's letter and notes on crevasses. *Journal of Glaciology*, 2(17):512–514, 1955.

W. Ogoh and D. Groulx. Stefan's Problem: Validation of a One-Dimensional Solid-Liquid Phase Change Heat Transfer Process. In *Excerpt from the Proceedings of the COMSOL Conference 2010 Boston*, pages 1–6, 2010.

E. Oñate, S. R. Idelsohn, and F. Del Pin. The particle finite element method - an overview. *International Journal of Computational Methods*, 2004.

N. Reeh. On the Calving of Ice from floating Glaciers and ice shelves. *Journal of Glaciology*, 7(50):215–232, 1968.

J. R. Rice. A path independent integral and the approximate analysis of strain concentration by notches and cracks. *Journal of Applied Mechanics*, 35(2):379–386, 1968.

H. A. Richard, M. Fulland, and M. Sander. Theoretical crack path prediction - RICHARD - 2004 - Fatigue & Fracture of Engineering Materials & Structures - Wiley Online Library. *Fatigue and Fracture of Engineering Materials and Structures*, 28:3–12, 2005.

E. Rignot. Ice-shelf changes in Pine Island Bay, Antarctica, 1947-2000. *Journal of Glaciology*, 48(161):247–256, 2002.

E. Rignot. Changes in West Antarctic ice stream dynamics observed with ALOS PALSAR data. *Geophysical Research Letters*, 35(12):1–5, 2008.

E. Rignot, J. Mouginot, and B. Scheuchl. Antarctic grounding line mapping from differential satellite radar interferometry. *Geophysical Research Letters*, 38(L10504), 2011a.

E. Rignot, J. Mouginot, and B. Scheuchl. Ice Flow of the Antarctic Ice Sheet. *Science*, 333(6048):1427–1430, 2011b.

E. Rignot, S. Jacobs, J. Mouginot, and B. Scheuchl. Ice-Shelf Melting Around Antarctica. *Science*, 341(6143):266–270, 2013.

M. A. Rist, P. R. Sammonds, S. A. F. Murrell, P. G. Meredith, C. S. M. Doake, H. Oerter, and K. Matsuki. Experimental and theoretical fracture mechanics applied to Antarctic ice fracture and surface crevassing. *Journal of Geophysical Research*, 104(B2):2973–2987, 1999.

M. A. Rist, P. R. Sammonds, H. Oerter, and C. S. M. Doake. Fracture of Antarctic shelf ice. *Journal of Geophysical Research*, 107(B1):1–13, 2002.

J. Roscoe. Antarctic Photogeography. In A. P. Crary, L. M. Gould, E. O. Hulburt, H. Odishaw, and W. E. Smith, editors, *Antarctica in the International Geophysical Year*, pages 18–22, Washington, 1956.

H. Rott, W. Rack, P. Skvarca, and H. De Angelis. Northern Larsen Ice Shelf, Antarctica: further retreat after collapse. *Annals of Glaciology*, 34(1):277–282, 2002.

M. H. Sadd. *Elasticity: Theory, Applications, and Numerics*. Elsevier, 2005.

H. Sandhäger. Numerical study on the influence of fractures and zones of weakness on the flow regime of Larsen Ice Shelf. In *FRISP Report*, pages 1–7, 2003.

H. Sandhäger, W. Rack, and D. Jansen. Model investigations of Larsen B Ice Shelf dynamics prior to the breakup. In *FRISP Report*, pages 1–8, 2005.

T. A. Scambos. Glacier acceleration and thinning after ice shelf collapse in the Larsen B embayment, Antarctica. *Geophysical Research Letters*, 31(18):1–4, 2004.

T. A. Scambos, C. L. Hulbe, M. A. Fahnestock, and J. Bohlander. The link between climate warming and break-up of ice shelves in the Antarctic Peninsula. *Journal of Glaciology*, 46(154):516–530, 2000.

T. A. Scambos, H. A. Fricker, C.-C. Liu, J. Bohlander, J. Fastook, A. Sargent, R. Massom, and A.-M. Wu. Ice shelf disintegration by plate bending and hydro-fracture: Satellite observations and model results of the 2008 Wilkins ice shelf break-ups. *Earth and Planetary Science Letters*, 280:51–60, 2009.

T. A. Scambos, B. Raup, and J. Bohlander. Images of Antarctic ice shelves (2004-2015). Natl. Snow and Ice Data Cent., Boulder, Colorado, 2015. `http://nsidc.org/data/iceshelves_images/pine.html`.

R. Schmitt. Finite Element Implementation of a Model for Antarctic Ice Shelves. Master's thesis, TU Kaiserslautern, 2011.

E. M. Schulson and P. Duval. *Creep and Fracture of Ice*. Cambridge University Press, 2009.

Bibliography

H. Schütte. Curved crack propagation based on configurational forces. *Computational Materials Science*, 46(3):642–646, 2009.

H. Schütte. On curved crack paths in finite strain fracture mechanics. *International Journal of Fracture*, 166(1-2):145–151, 2010.

G. C. Sih. *Handbook of Stress Intensity Factors for Researchers and Engineers*. Institute of Fracture and Solid Mechanics, Lehigh University, Bethlehem, Pennsylvania, 1973.

G. C. Sih. *Application of the Strain-Energy-Density Theory to Fundamental Fracture Problems*. Air Force Office of Scientific Research, 1973.

R. A. Smith. The Application of Fracture Mechanics to the Problem of Crevasse Penetration. *Journal of Glaciology*, 17(76):223–228, 1976.

J. Stefan. Über die Theorie der Eisbildung, insbesondere über die Eisbildung im Polarmeere. *Wiedemann Ann. Phys. u. Chem.*, 42:269–286, 1891.

P. Steinmann and G. A. Maugin. *Mechanics of Material Forces (Advances in Mechanics and Mathematics)*. Springer, 2010.

C. W. M. Swithinbank. Satellite image atlas of glaciers of the world: Antarctica. *United States Geological Survey Professional Paper*, 1386-B:1–278, 1988.

H. Tada, P. C. Paris, and G. R. Irwin. *The Stress Analysis of Cracks Handbook*. Del. Research Corp., St. Louis, 1973.

P. D. Taylor. A model of melt pond evolution on sea ice. *Journal of Geophysical Research*, 109(C12):1–19, 2004.

M. Tedesco, M. Lüthje, and K. Steffen. Measurement and modeling of ablation of the bottom of supraglacial lakes in western Greenland - Tedesco - 2012 - Geophysical Research Letters - Wiley Online Library. *Geophysical Research Letters*, 39(2):1–5, 2012.

R. H. Thomas. The creep of ice shelves: Theory. *Journal of Glaciology*, 12:45–53, 1973.

C. Tomasi and R. Manduchi. Bilateral filtering for gray and color images. In *Computer Vision*, pages 839–846, 1998.

C. J. Van Der Veen. Fracture mechanics approach to penetration of surface crevasses on glaciers. *Cold Regions Science and Technology*, 27(1):31–47, 1998.

C. J. Van Der Veen. Fracture mechanics approach to penetration of bottom crevasses on glaciers. *Cold Regions Science and Technology*, 27(3):213–223, 1998.

C. J. Van Der Veen. Calving glaciers. *Progress in Physical Geography*, 26(1):96–122, 2002.

C. J. Van Der Veen. Fracture propagation as means of rapidly transferring surface meltwater to the base of glaciers. *Geophysical Research Letters*, 34(1):1–5, 2007.

D. G. Vaughan, D. R. Mantripp, J. Sievers, and C. S. M. Doake. A synthesis of remote sensing data on Wilkins Ice Shelf, Antarctica. *Annals of Glaciology*, 17:211–218, 1993.

VDI-Gesellschaft Verfahrenstechnik und Chemieingenieurswesen (GVC). *VDI-Wärmeatlas*. Springer, 10th edition, 2006.

C. C. Walker, J. N. Bassis, H. A. Fricker, and R. J. Czerwinski. Structural and environmental controls on Antarctic ice shelf rift propagation inferred from satellite monitoring. *Journal of Geophysical Research: Earth Surface*, 118(4):1–11, 2013.

W. F. Weeks and M. Mellor. Some elements of iceberg technology. *CRREL Report*, 78 (2):1–38, 1978.

J. Weertman. Deformation of floating ice shelves. *Journal of Glaciology*, 23(3): 38–42, 1957.

J. Weertman. Can a water-filled crevasse reach the bottom surface of a glacier? *International Association of Scientific Hydrology Publication*, 95:139–145, 1973.

J. Weertman. Bottom crevasses. *Journal of Glaciology*, 25(91):185–188, 1980.

M. Weis, R. Greve, and K. Hutter. Theory of shallow ice shelves. *Continuum Mechanics and Thermodynamics*, 11:15–50, 1999.

J. Weiss. Subcritical crack propagation as a mechanism of crevasse formation and iceberg calvig. *Journal of Glaciology*, 50(168):109–115, 2004.

F. Wilhelms, S. G. Sheldon, I. Hamann, and S. Kipfstuhl. Implications for and Findings from Deep Ice Core Drillings - an Example: the Ultimate Tensile Strength of Ice at High Strain Rates. In *The Royal Society of Chemistry Special Publication*, pages 635–639, 2007.

W. K. Wilson and I. W. Yu. The use of the J-integral in thermal stress crack problems. *International Journal of Fracture*, 15(4):377–387, 1979.

P. Wriggers. *Nonlinear Finite Element Methods*. Springer, 2008.

O. C. Zienkiewicz and R. L. Taylor. *The finite element method*. Butterworth- Heinemann, 5 edition edition, 2000.

D. Zimmermann. *Material Forces in Finite Inelasticity and Structural Dynamics: Topology Optimization, Mesh Refinement and Fracture*. PhD thesis, Stuttgart, 2008.

Curriculum Vitae

Name:	Carolin Plate
Geburtsort:	Lüdenscheid

08.1991 – 07.1995	Grundschule Unnau
08.1995 – 07.2004	Konrad-Adenauer-Gymnasium, Westerburg
	Abschluss: Allgemeine Hochschulreife
10.2004 – 09.2009	Studium Mechanik an der Technischen Universität Darmstadt
	Diplomarbeit: *An implementation of Halley's method in the* *finite element solution of elasticity problems*
	Abschluss: Diplom Ingenieurin
seit 10.2009	Wissenschaftliche Mitarbeiterin am Lehrstuhl für Technische Mechanik, Fachbereich Maschinenbau und Verfahrenstechnik der Technischen Universität Kaiserslautern